INFLUENCE OF MESOSCALE FEATURES OF THE RESERVOIR-CAPROCK INTERFACE ON FLUID TRANSMISSION INTO AND THROUGH CAPROCK

by

Stefan P. Raduha

Submitted in Partial Fulfillment
of the Requirements for the

Masters of Science in Geology

New Mexico Institute of Mining and Technology
Department of Earth and Environmental Science

Socorro, New Mexico
May 2013

ABSTRACT

The reservoir-caprock interface is often considered a no-flow boundary in reservoir models; however, when deformation features (e.g., faults or fracture networks) are present at the interface, reservoir fluids can potentially use these features as pathways to travel into and through the caprock. Structural features that are commonly present at such interfaces in my study area on the east side of the San Rafael Swell include joints and zones of deformation bands in reservoir lithologies that transition to opening-mode fractures in caprock lithologies. The goal of this study is to describe these features in detail at the outcrop scale, and to determine their potential effect on geologic sequestration of CO_2 and petroleum migration. Geologic units examined include the Navajo Sandstone, the Carmel Formation, and the Entrada Sandstone.

Methods for this project include selecting detailed study sites, mapping the sedimentary and structural features, measuring the permeability of different lithologies using both a field permeameter and mercury injection capillary pressure, analyzing thin sections optically and using a microprobe, analyzing the stable isotopes of carbonate cements, using X-ray diffraction to determine cement mineralogy, and creating conceptual geologic and permeability models based on field data.

Field reconnaissance yielded multiple outcrops containing evidence of bleaching within the caprock, demonstrating that reducing fluids penetrated the overlying caprock via fractures. Outcrops demonstrating partial seal bypass were made into conceptual

models. These models are designed to be used as the framework for single- and multi-phase (brine-CO_2) hydrologic modeling.

Paragenesis and geochemistry were used to constrain the types of fluids that moved through the system and the timing of fluid migration. Bleaching and pyrite mineralized fractures inside the Earthy Member of the Entrada Sandstone demonstrate strongly reducing conditions during at least some of the fracture mineralization. The presence of hydrocarbon-filled fluid inclusions in the Carmel Formation suggest the reducing conditions may have been caused by hydrocarbons. Eventually most of the fractures were cemented closed with iron oxide, barite, kaolinite, and/or calcite cement. $\delta^{18}O_{SMOW}$ of the calcite fractures in both the Carmel Formation and the Earthy Member of the Entrada Sandstone range from 14.35 to 17.47‰. The $\delta^{13}C_{PDB}$ of the fracture-filling calcite in the Co-op Creek Member of the Carmel Formation ranges from -2.37 to 1.66‰, and in the Winsor Member of the Carmel Formation and the Earthy Member of the Entrada Sandstone ranges from -6.61 to -3.59‰. These results indicate that the calcite may have formed in either high temperature burial conditions and/or low temperature uplift conditions.

Permeability for units of interest was determined using field and laboratory measurements. Field measurements were obtained using a TinyPerm II field minipermeameter, capable of measuring the permeabilities between 10 and 10,000 mD. Mercury injection capillary pressure (MICP) was used to calculate the permeability of zones of deformation bands that are below the lower measurement limit of the field permeameter. The permeability of the zones of deformation bands ranges from 0.416 to

16.10 mD. MICP results also show that the zones of deformation bands are capable of trapping a 3 m column of supercritical CO_2, oil, or gas.

Mesoscale interface features such as those described in this study, have the potential to compromise geologic carbon sequestration projects. If a caprock contains leakage pathways associated with these features there may be negative consequences, such as CO_2 contaminating freshwater aquifers or escaping back to the atmosphere. The low permeability of the zones of deformation bands intersecting the caprock can lead to reservoir compartmentalization, which could lead to lower than anticipated injectivity and difficulties in pressure management.

Keywords: Mesoscale features; reservoir; caprock; interface; deformation bands; fractures; Navajo Sandstone; Carmel Formation; Entrada Sandstone; San Rafael Swell

ACKNOWLEDGEMENTS

First, I would like to thank my family for all their support they have given me throughout graduate school. In the midst of homework, research, and trying to find a job; being able to have a friendly Skype conversation at the end of the week with my family is always comforting. It has also been reassuring to know that you guys were always there for me.

Second, I would like to thank my advisor Dr. Peter Mozley. During my time in graduate school Peter did a great job mentoring me by providing me with excellent feedback on any questions I had. Thank you very much for selecting me to be a part of the interface project; it has been a great experience.

Third, I would like to thank everyone else involved with the interface project. I was very fortunate to be able to work with some great people from New Mexico Tech, Utah State University, and Sandia National Laboratories. I would particularly like to thank David Butler for doing a great job creating hydrologic models based upon the conceptual models produced for this thesis. I would also like to thank Dr. James Evans, Dr. Jason Heath, Dr. Thomas Dewers, Dr. Mark Person, Alex Urquhart, and Elizabeth Petrie for their help on this project. I would especially like to thank Santiago Flores and Leslie Clayton their help with field work under the unrelenting sun of the San Rafael Desert.

Fourth, I would like to thank the faculty at New Mexico Tech. The professors I have studied under and the coursework I have taken had a huge positive impact on the project. In particular I would like to thank Dr. Andrew Campbell for his help with stable isotope analysis. I would also like to thank Dr. Dana Ulmer-Scholle for her help with carbonate thin sections and fluorescent microscopy.

Fifth, I would like to thank the faculty at the New Mexico Bureau of Geology and Mineral Resources. I would like to thank Lynn Heizler for her help with the electron microprobe analysis. I would also like to thank Dr. Virgil Lueth and Zachary Vance for their help with the X-ray diffraction analysis.

I would also like to thank the staff of the Department of Earth and Environmental Science at New Mexico Tech. All of you are great hard working people, and without you the department would surely be chaos. I would particularly like to thank Pat Valentine for helping me the large amount of paperwork required for this project. I would also like to thank Erik Weiss for all the computer assistance he provided.

I would like to thank the companies who performed services. Wagner Petrographic © did an excellent job creating the thin sections, and PoroTechnology did a great job with the zone of deformation bands mercury injection capillary porosimetry.

A special thanks to Shane Butler and Dr. William Roy at the Illinois State Geological Survey (ISGS) for first introducing me to carbon sequestration by giving me the chance to work on the joint ISGS/ADM carbon sequestration project in Decatur, IL. Without this background experience there is a good chance I would not have been involved in this project. An additional thanks to Shane Butler for all the advice he gave me for getting in to graduate school.

I would also like to thank my friends and fellow students at New Mexico Tech.

Funding for this research was provided by the U.S. Department of Energy National Energy Technology Laboratory grant number DE-FE0004844.

TABLE OF CONTENTS

LIST OF FIGURES

LIST OF TABLES

This thesis is accepted on behalf of the
Faculty of the Institute by the following committee:

Advisor

5/24/2013

Dr. Peter S. Mozley — Date

Committee Members

Andrew Campbell 5/15/2013

Dr. Andrew R. Campbell — Date

5/23/2013

Dr. James P. Evans — Date

Jason Heath 5/22/13

Dr. Jason E. Heath — Date

I release this document to the New Mexico Institute of Mining and Technology.

Stefan P. Raduha 5/24/2013

Stefan P. Raduha — Date

CHAPTER 1. INTRODUCTION

Focus and Significance of Research

The focus of the research is the influence of mesoscale features at the reservoir-caprock interface on carbon capture, utilization, and storage (CCUS). The features of interest are zones of deformation bands and fractures.

This research is important for several reasons. Understanding the impact mesoscale reservoir-caprock interface features have on fluid flow is very important when determining how well a caprock will perform as a seal for a geologic carbon sequestration project. If a caprock contains leakage pathways there may be several negative consequences, such as CO_2 contaminating freshwater aquifers or escaping back to the atmosphere. Understanding mesoscale interface features is also important to enhanced oil recovery. Mesoscale interface features may contribute to the loss of CO_2 in thief zones of oil fields undergoing tertiary recovery.

Background

What is the Mesoscale?

The mesoscale refers to the size between the microscale and the macroscale, usually referred to a being between 0.01 to 10 m. Geologic structures with less than 12 m of offset are too small to be detected by modern 3-D seismic techniques, often causing them to be overlooked (Gauthier and Lake, 1993). The main mesoscale features that I focus on in this thesis are fractures and deformation bands.

Fractures

There are three types of fractures: opening-mode, sliding-mode, and tearing-mode (Kanninen and Popelar, 1985). Opening-mode fractures form due to extension whereas sliding-mode and tearing-mode fractures form due to shear stress (Fig. 1). All three types of fractures have the potential to form in rocks that have undergone deformation. Rocks that are usually stiff and low porosity are especially prone to fractures (Fossen et al., 2007).

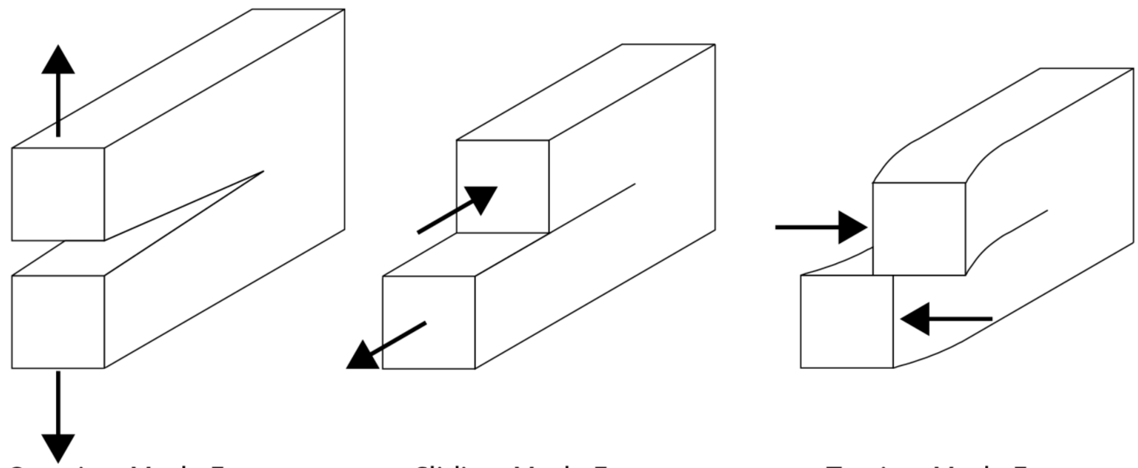

Figure 1. Three types of fractures: opening-mode, sliding-mode, and tearing-mode. Modified from Kanninen and Popelar (1985).

When a fracture opens it becomes a zone of increased permeability. Fluids flow through a fractured rock at increased speeds compared to a rock with no fractures. This is especially true in a low permeability caprock where fluids could use fractures to penetrate and completely bypass impermeable zones (Cartwright et al., 2007).

Deformation Bands

Three types of strain localization are commonly present in high porosity sandstones: deformation bands, zones of deformation bands, and slip surfaces (Aydin and

Johnson, 1978; Fig. 2). A good definition of deformation bands is from Fossen et al. (2007):

> "Deformation bands in porous rocks are low-displacement deformation zones of millimeters to centimeters thickness that tend to have enhanced cohesion and reduced permeability compared with ordinary fractures."

The maximum amount of displacement from a single deformation band ranges from a few millimeters to a few centimeters (Aydin, 1978). A zone of deformation bands (also known as a deformation band cluster) is made up of two or more closely spaced, individual deformation bands that are parallel to subparallel (Aydin and Johnson, 1978; Fig. 3). Thickness and displacement of zones of deformation bands varies based on the number of bands present. The maximum thickness and displacement is roughly 0.5 m and 0.3 m, respectively (Aydin and Johnson, 1978). Aydin and Johnson (1978) define a slip surface as "a through-going, discrete surface of discontinuity". These occur on the margins of zones of deformation bands where they are sometimes referred to as faulted deformation bands and can be identified by slickensides and striations (Aydin and Johnson, 1978). These zones contain much more shear displacement than zones of deformation bands, with a maximum possible displacement of several meters.

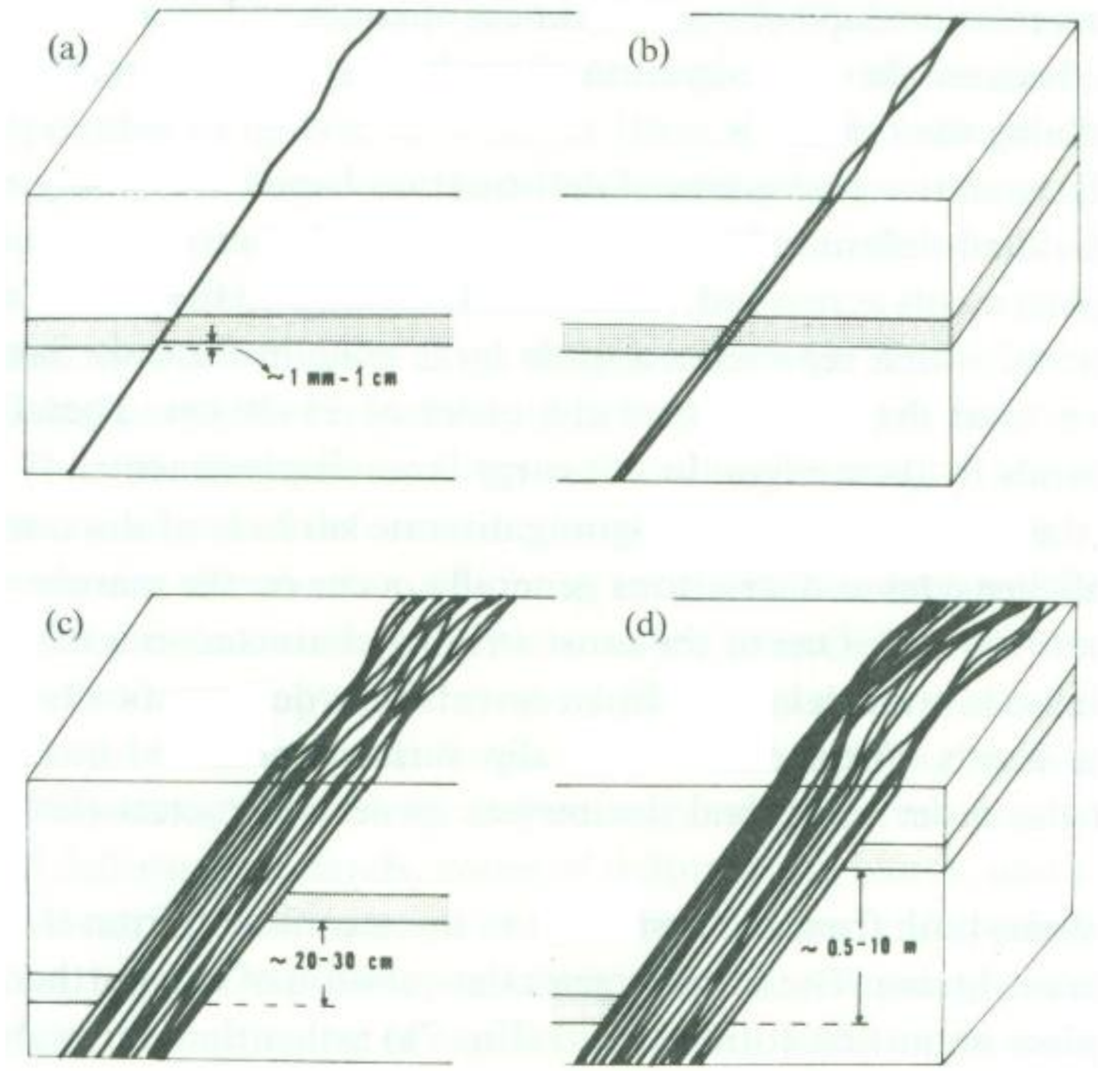

Figure 2. Diagram showing the different types of deformation mechanisms in high porosity sandstones (a) deformation band (b) two deformation bands (c) zone of deformation bands (d) slip surface forming on the border of a zone of deformation bands. From Aydin and Johnson (1978).

Figure 3. A zone of deformation bands in the Entrada Sandstone at the Iron Wash Study site. San Rafael Swell in background.

Deformation bands can form in both convergent and divergent tectonic conditions (Fig. 4).

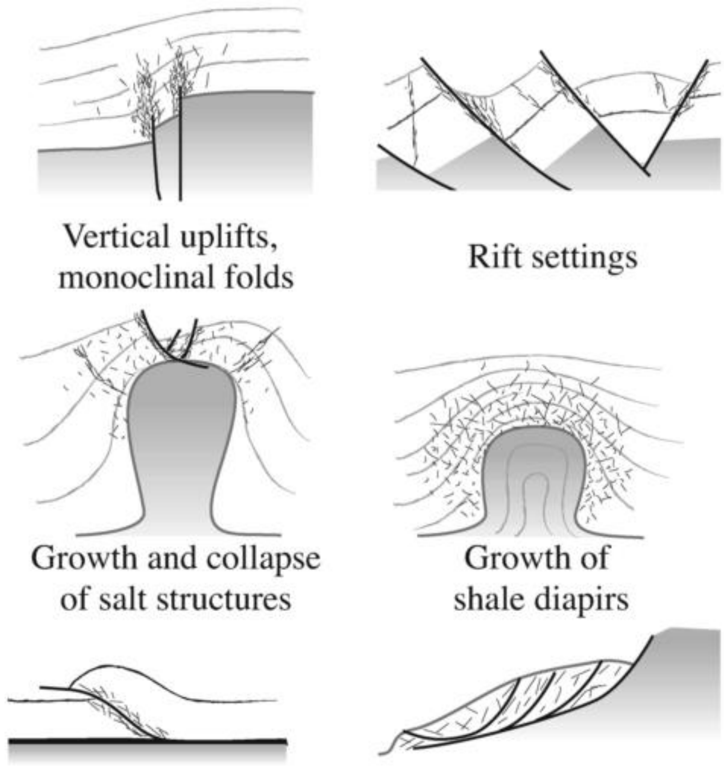

Figure 4. The various tectonic conditions in which deformation bands can form. From Fossen et al. (2007).

Deformation bands have been classified by their kinematics as well as by the deformation mechanism. When classifying deformation bands kinematically, three main types are present: shear bands, compaction bands, and dilation bands (Aydin et al., 2006; Fig. 5a). Shear bands form when grains slide against each other. Compaction bands form when grains undergo compression. Dilation bands form when grains undergo extension. Compaction and dilation bands can have a shear component to them as well. The most common of the three types is one that has a combination of both compaction and shear (Fossen et al., 2011). When classifying deformation bands by their deformation mechanism four main types are present: disaggregation bands, phyllosilicate bands, cataclastic bands, and solution bands (Fossen et al., 2007; Fig. 5b). Disaggregation bands occur when grains slide or roll against each other but do not break

(Fossen et al., 2007). Phyllosilicate bands occur when an abundant amount of clay and sheet silicate minerals cause grains to slide instead of undergoing cataclasis (Fossen et al., 2007). Cataclasis bands occur when grains grind against each other and fracture (see Aydin, 1978 for some of the early work describing this type of band). The fracturing of grains produces clean chemically reactive mineral surfaces, which are more prone to forming overgrowth cement (Fossen et al., 2007). Solution bands contain tightly packed grains with little to no evidence of fracturing (Gibson, 1998). Grains in these bands are often cemented and aligned parallel to pressure solution induced dissolution seams (Gibson, 1998).

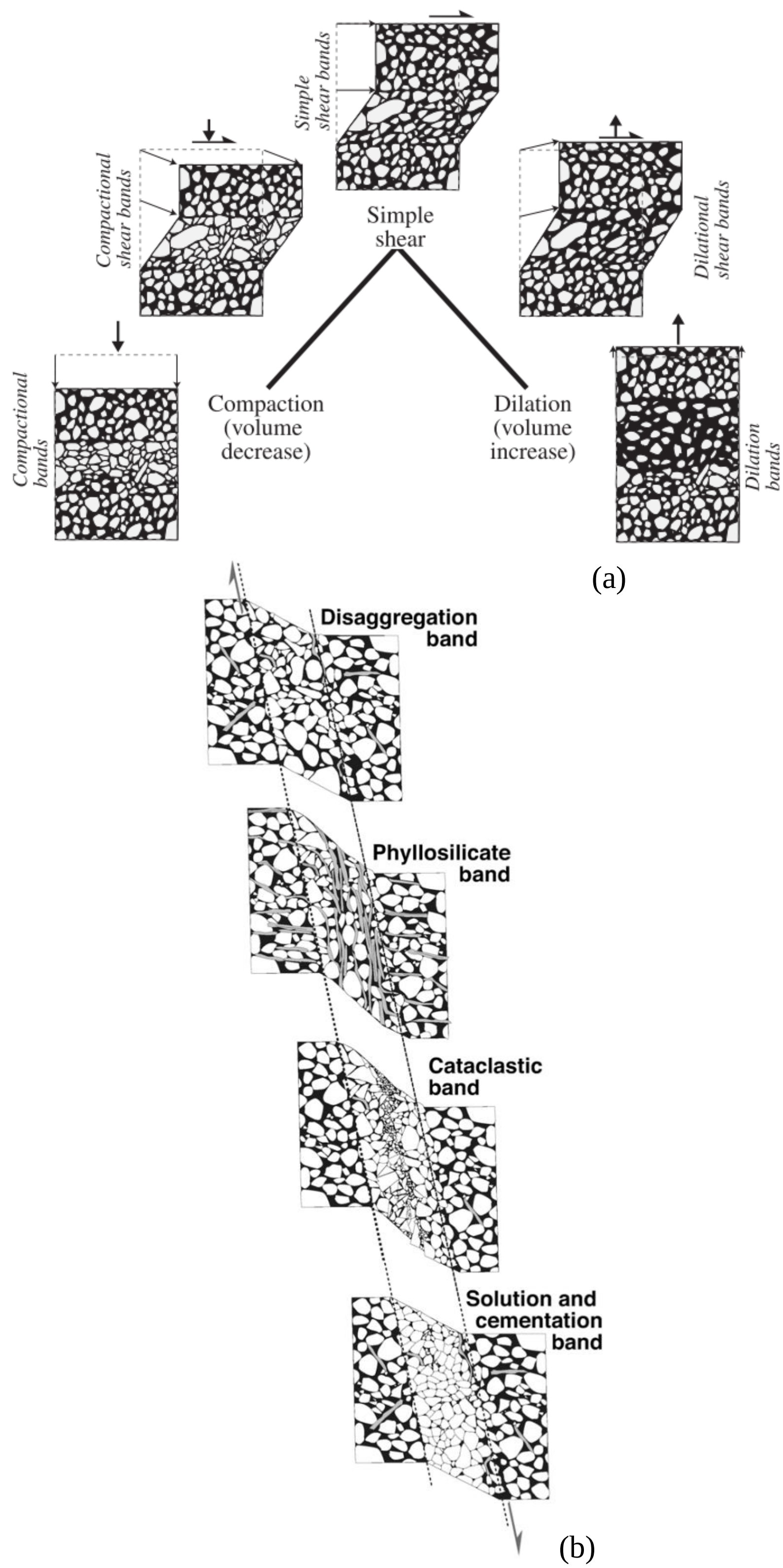

Figure 5. Classification of deformation bands based on (a) kinematic classification and (b) deformation mechanism classification (from Fossen et al. 2007).

CHAPTER 2. GEOLOGIC SETTING

Stratigraphy and Depositional Environments

Three stratigraphic units are present in the study area: the Navajo Sandstone, the Carmel Formation, and the Entrada Sandstone. These units range from lower to middle Jurassic in age (Doelling, 2002).

Navajo Sandstone

The oldest unit of interest in the study area is the Navajo Sandstone (Figs. 6 and 7). This unit mainly consists of large-scale cross-bedded sandstone. The sandstone beds are made up of fairly uniform feldspathic quartz arenite. In addition to sandstone, lenticular beds of limestone and dolomite are present locally (Parry et al., 2009). The unit is present throughout the Colorado Plateau (Freeman and Visher, 1975). The top of the Navajo Sandstone is truncated by the J-2 unconformity (Pipiringos and O'Sullivan, 1978).

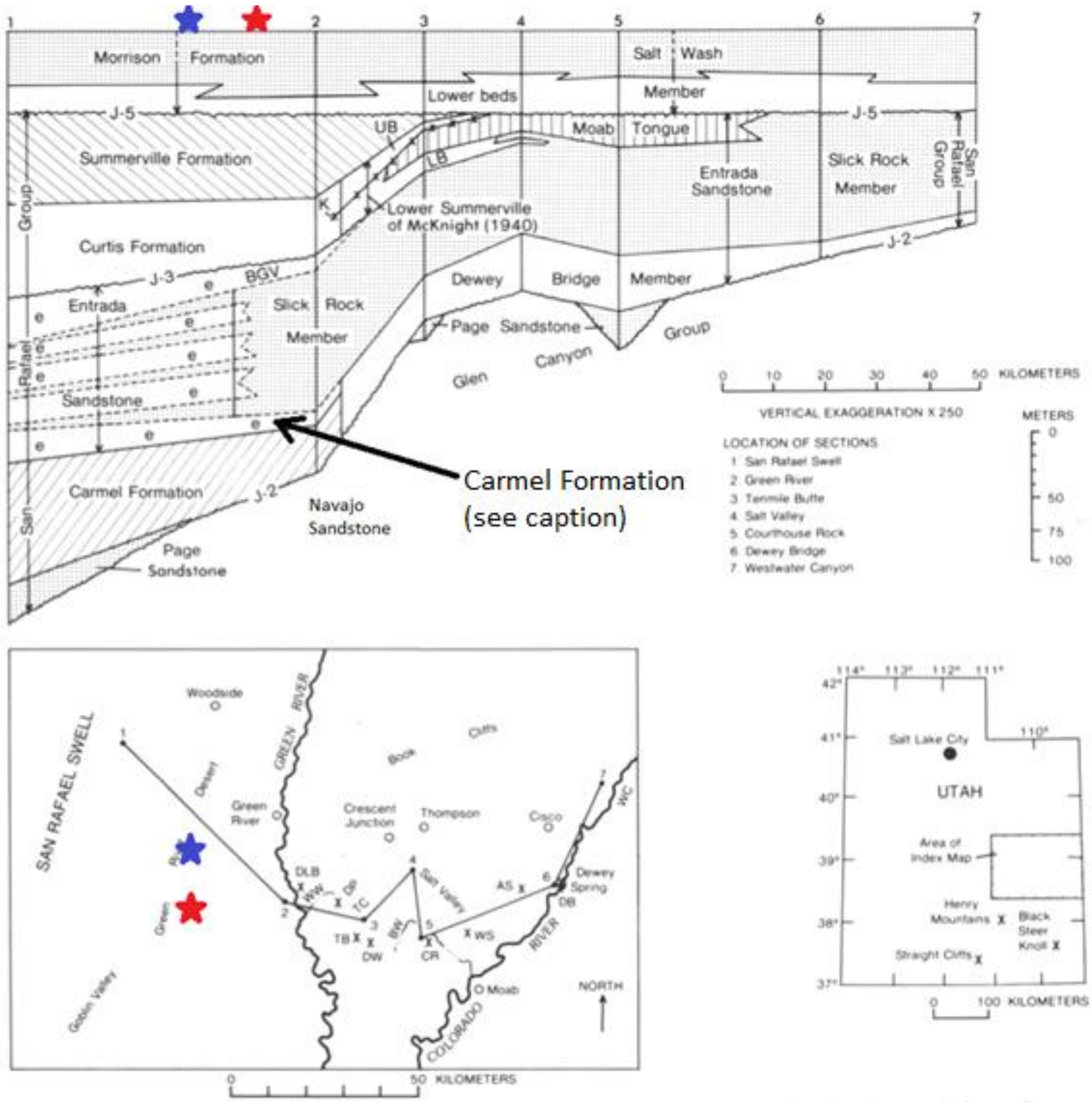

Figure 6. Map and stratigraphy of study area. The study area is located between the San Rafael Swell (1) and Green River (2). The red star is the approximate location of the Iron Wash study site, the blue star the approximate location of the Uneva Mine Canyon study site. The lowermost portion of the Earthy Member of the Entrada Sandstone is likely the Banded Unit of the Winsor Member of the Carmel Formation as described by Doelling and Kuehne (2008). When describing units at the Iron Wash study site this unit is considered part of the Carmel Formation. Modified from O'Sullivan (1981).

Figure 7. Detailed index map of the study area. Map from Google Earth. Fault information from Doelling (2002).

In the past the depositional environment of the Navajo Sandstone was controversial, with some workers concluding the cross-bedded sandstone was deposited in marine and tidal environments (Freeman and Visher, 1975). However, these arguments have since been refuted (Folk, 1977; Picard, 1977; Steidtmann, 1977; Ruzyla, 1977) and reinforced with evidence that the large-scale cross-bedded sandstones were deposited by eolian dunes. Associated carbonate deposits likely formed in interdune lakes, which formed during periods of high water table (Parry et al., 2009).

Page Sandstone

Although the Page Sandstone is not present in the study area, other workers have found it in nearby regions (Doelling and Kuehne, 2008). The unit is often reported as being a less than 3 m thick sandstone layer, containing iron oxide and calcite cement, and in some locations containing dead oil (Doelling and Kuehne, 2008). The depositional environment of the Page Sandstone near the study area is either eolian or beach (Blakey et al., 1983).

Carmel Formation

The Carmel Formation is a very diverse unit consisting of siliciclastic, carbonate, and evaporite lithologies. In the study area the Carmel Formation consists of four members; starting from oldest, these members are: the Co-op Creek Member, the Crystal Creek Member, the Paria River Member, and the Winsor Member. Differentiating among the members has caused problems in the past, with authors incorrectly interpreting Carmel Formation members as part of the Entrada Sandstone (Cashion, 1967). However, adding to the Entrada-Carmel confusion is the Dewey Bridge Member to the east. This unit is considered part of the Entrada Sandstone although it is contemporaneous with the deposition of the Carmel Formation (O'Sullivan, 1981; Fig. 4). Further confusion arises when considering the relationship between the Carmel Formation and the Entrada Sandstone. The uppermost layers of the Winsor Member of the Carmel Formation may have been confused with the Earthy Member of the Entrada Sandstone (O'Sullivan, 1981; Fig. 4).

Co-op Creek Member

The Co-op Creek Member consists of interbedded shale, siltstone, sandstone, limestone, and dolomite lithologies (Doelling and Kuehne, 2008). This wide range of lithologies is due to the shifting depositional environment, reflecting changes in the shoreline of the Jurassic Carmel Seaway, which entered from the north into what would later become Utah (Fig. 8). The Carmel Seaway produced multiple transgression-regression cycles, leading to variable depositional environments for this member including marine, tidal, and beach (Blakey et al., 1983).

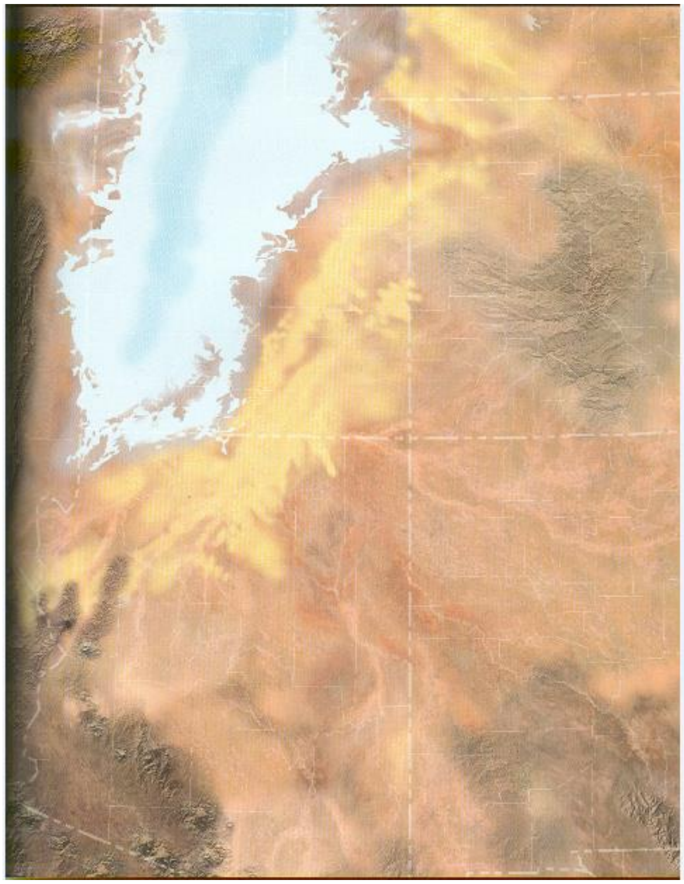

Figure 8. Paleogeographic reconstruction of the Carmel Seaway during the middle Jurassic (170 Ma). Eolian dunes to the east of the Carmel Seaway were responsible for the deposition of the Page Sandstone. From Blakey and Ranney (2008).

Crystal Creek Member

The Crystal Creek Member mainly consists of red-brown siltstone, with lesser amounts of sandstone (Doelling and Kuehne, 2008). Bedding of this member is indistinct and locally contorted (Doelling and Kuehne, 2008). Blakey et al. (1983) concluded the Crystal Creek Member formed in a subtidal-shoreface-beach environment.

Paria River Member

The Paria River Member consists of interbedded calcisiltite, calcarenite, sandstone, limestone, and marl (Doelling and Kuehne, 2008). Some beds in this member contain pelecypod casts and are dolomitic. Blakey et al. (1983) interprets the limestone of the Paria River Member as forming in a marine environment. They indicate that the dolomite and sandstone lithologies formed in a sabkha under regressive conditions.

Winsor Member

The lower portion of this unit contains interbedded sandstone, siltstone, and gypsum, whereas the upper portion contains only interbedded siltstone and sandstone (Doelling and Kuehne, 2008). Blakey et al. (1983) indicate that the Carmel Seaway was undergoing regression during the deposition of this interval. This caused a shift in environments from tidal marine/carbonate dominated to terrestrial/siliciclastic sabkha dominated (Blakey et al., 1983).

<u>Entrada Sandstone</u>

The Entrada Sandstone in a mainly siliciclastic dominated unit. In the study area the Entrada Sandstone is broken up into two main members, the Earthy Member and the Slick Rock Member. These members interfinger with each other, with the Earthy Member becoming more dominant to the west of the study area and the Slick Rock Member becoming more dominant to the east of the study area (Fig. 4).

Slick Rock Member

This unit consists of massive and cross-bedded sandstone beds (Doelling, 2002). The cross-bedded sandstone beds of the Slick Rock Member are eolian in origin (O’Sullivan, 1981). The massive sandstone beds may have formed from multiple conditions, including bioturbation, deposition of wind-blown sand into still water, postdepositional liquefaction, or deposition by mass-flow events (Eschner and Kocurek, 1986).

Earthy Member

This member consists mainly of red-brown, silty, very-fine grained sandstone (Doelling, 2002). The depositional environment for the Earthy Member was near-shore marine (Baker, 1946; O'Sullivan, 1981). The shoreline went through multiple transgression-regression cycles, producing intertonguing between the Slick Rock and Earthy Members (Fig. 4; O'Sullivan, 1981).

Tectonic Setting

The units in the study area have undergone extensive deformation. Early workers attributed the formation of the San Rafael Swell to the late Cretaceous Laramide orogeny (Baker, 1935). However, more recent work indicates that the orientation of the San Rafael Swell is not compatible with the northeast-southeast Laramide orogeny, suggesting other unknown forces may have been involved in forming the San Rafael Swell (Fischer and Christensen, 2004).

Several normal faults are present in the study area. The origin of normal faulting in the San Rafael Swell is still uncertain, although it likely formed due to uplift related to the Laramide orogeny (Shipton and Cowie, 2001; Shipton, 1999).

Small deformation features such as fractures and deformation bands are also present throughout the study area. Fischer and Christensen (2004) reported fracture systems in the Carmel Formation in the San Rafael Swell, which are composed of multiple joint sets, faulted joints, conjugate fault sets, and minor cleavage. These fracture systems formed due to folding and were possibly influenced by rotation or shearing from slip along an underlying basement fault (Fischer and Christensen, 2004). Davatzes et al. (2003) found cataclastic deformation bands and jointing inside the Navajo Sandstone of the San Rafael Swell. They concluded that the deformation bands were developed around maximum burial of the Navajo Sandstone, with the joints forming later possibly during uplift (Davatzes et al., 2003). Torabi and Fossen (2009) reported seeing dissolution and cataclastic bands within the Entrada Sandstone at the San Rafael Swell which were also attributed to forming around maximum burial.

CHAPTER 3. METHODS

Field Work

This project required the selection of detailed study sites that could be used as natural analogs for subsurface conditions. Study sites of interest include those along the reservoir-caprock interface that contain conduits for and barriers to flow (i.e. fractures, faults, and zones of deformation bands).

Upon selection of a study site the sedimentary and structural features were mapped and sampled for lab analysis. Maps showing the spatial relationships among the various features were made on photomosaics of each site (Fig. 9).

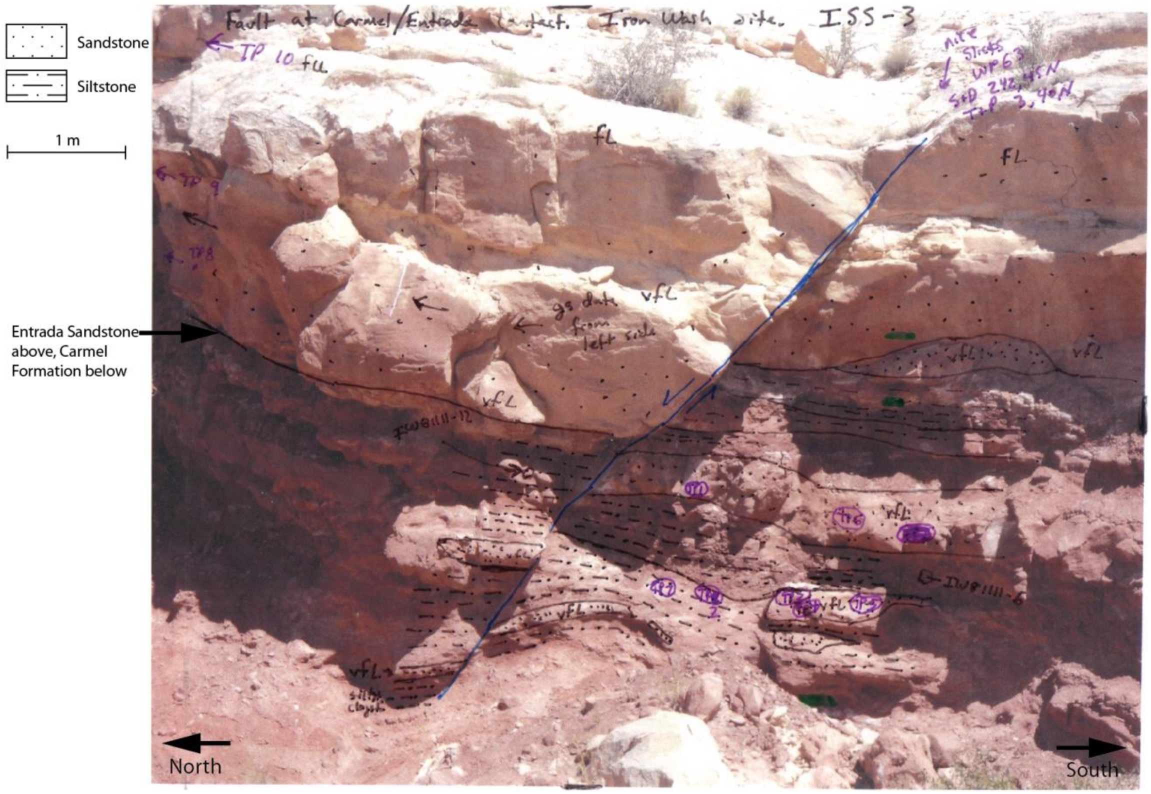

Figure 9. Example of how each study site was described. Includes lithologies, structures, sample locations, and other important notes.

Stratigraphic sections were measured at each of the main study areas to determine unit thicknesses and produce stratigraphic columns.

Field Permeability Measurements

The permeability of the different lithologies was measured using a New England Research, Inc TinyPerm II Portable Air Permeameter (Fig. 10). This device has an operating range from approximately 10 millidarcys to 10 darcys (TinyPerm II Portable Air Permeameter User's Manual, New England Research, Inc). To use the permeameter the user places the device against the rock surface then compresses a plunger to create a vacuum. Air travels through the rock into the device until the vacuum reaches atmospheric pressure. The status of the vacuum reaching atmospheric pressure is displayed on a LCD screen. The amount of time needed for the vacuum to reach atmospheric pressure ranges from a few seconds to several minutes depending on the permeability of the rock. Once the vacuum reaches atmospheric pressure the device displays a number that can be used to determine the permeability of the rock. In order to avoid the effects of weathering, only fresh surfaces were used in measuring permeability. Fresh surfaces were obtained through excavation and scraping the rock surface. A brush and compressed air were used clear debris from the fresh surface prior to measuring the permeability.

Figure 10. Using the TinyPerm II to gather permeability measurements in the field.

The greatest source of error in use of the permeameter is accidental leakage of air past the seal tip, which will produce a measured permeability that is erroneously high. To reduce this source of error, an additional soft seal (a doughnut of either a kneaded rubber eraser or Silly Putty®) was placed around the TinyPerm II nozzle. This piece of material was reformed after each measurement to prevent leakage. In addition, each sample was measured three times and the lowest permeability measurement was used.

Sandstone plug standards with a known permeability determined through air-based laboratory measurements were used to check the accuracy of the factory calibration of TinyPerm II. A total of 35 sandstone plug standards, with permeabilities ranging from 0.01 to 3,551 mD, were measured using TinyPerm II and the values compared. The TinyPerm II values obtained using the factory calibration have a higher permeability than those obtained using conventional core plug permeametry, especially for samples >100 mD (Fig. 11ab). This is consistent Fossen et al. (2011) whom concluded TinyPerm II is ~1.8 times the air-based laboratory standard plug permeability value. The following calibration equations, which were experimentally derived from the sandstone plug standards, are used to correct TinyPerm II measurements.

For samples >100 mD:

original TinyPerm II value in mD = 3.5754*(actual value in mD) - 440.55 mD

For samples <100 mD

original TinyPerm II value in mD = 1.3647*(actual value in mD)

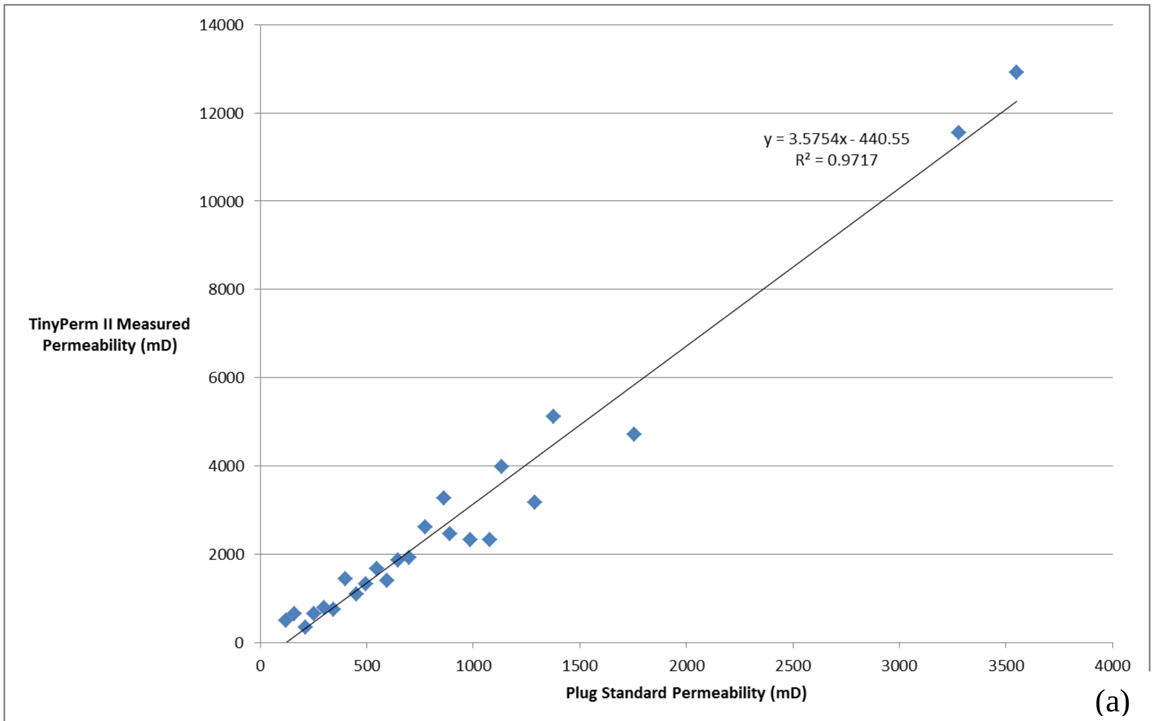

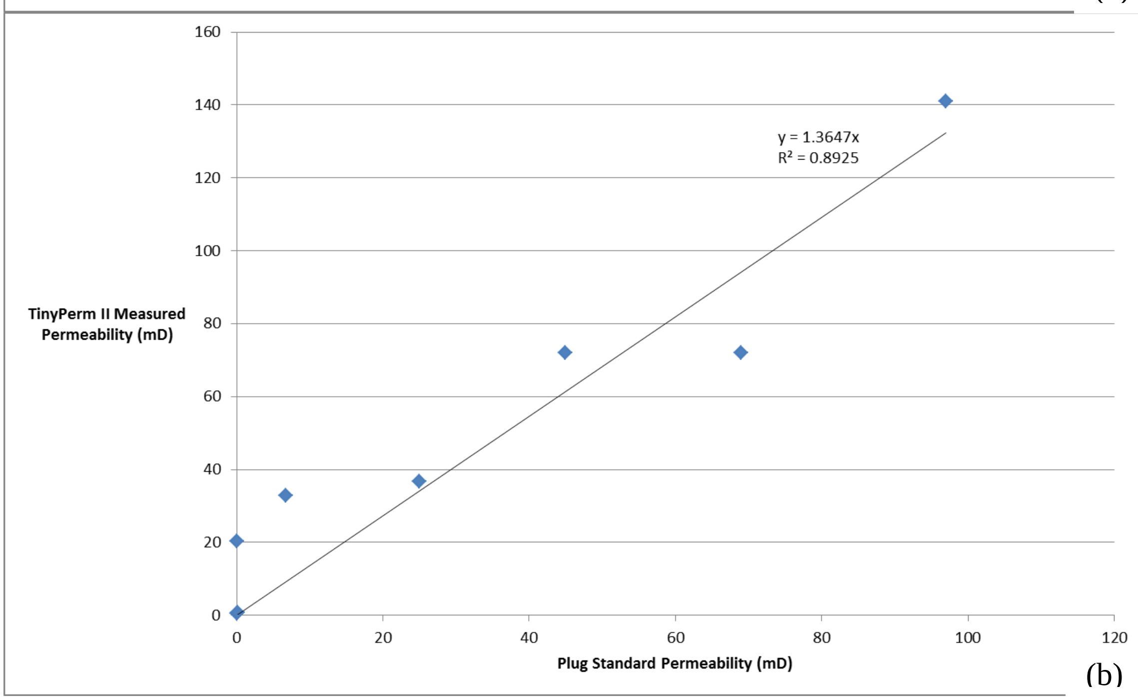

Figure 11. Graphs showing the relationship between sandstone plug standards and their corresponding TinyPerm II value for values >100 mD (a) and values <100 mD (b).

Because TinyPerm II uses vacuum and time based measurements to determine the permeability of a sample, the sample size and geometry may have an effect on the permeability measurement. This phenomenon is referred to as the "shape factor" (Grover 1955; Liang et al. 1995). Small samples, such as plugs, should ideally offer the least air resistance to the TinyPerm II (Fig. 12). Hand samples and outcrop samples should offer the greatest amount of air resistance as there is more rock for air to travel through. To assess this potential source of error I compared TinyPerm II measurements among outcrops, hand samples, and plugs to determine a sample size-permeability relationship for improved TinyPerm II calibration. Unfortunately the results of this experiment were inconclusive. The majority of the measurements did the opposite of what was expected, with the outcrop samples having the largest permeability and the plugs having the smallest permeability (Fig. 13). This may be due to the mobilization of fines on the outside of plugs and hand samples upon trimming with a rock saw. However, not all rocks were cut down to size with a trim saw, some were fractured with a rock hammer or rock press. Another factor that may have affected the results was that TinyPerm II was serviced in the middle of data collection.

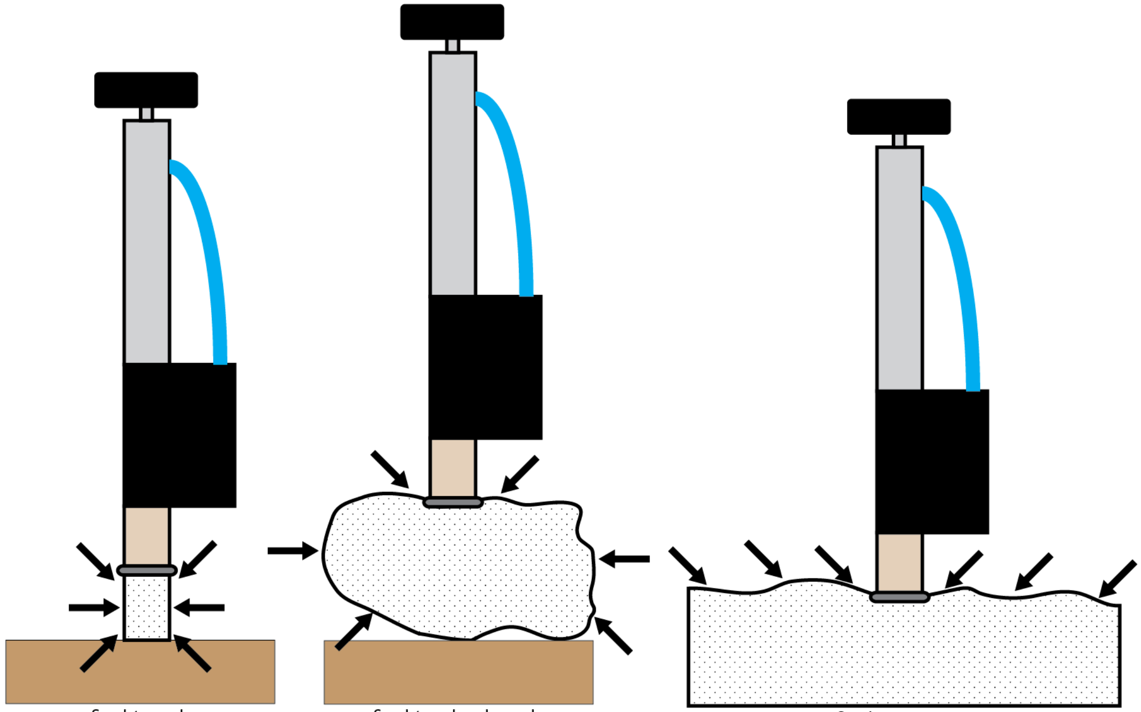

Figure 12. Sample size and geometry likely affect the permeability measurement of TinyPerm II. Small plugs are likely offer the least resistance to airflow while outcrop samples are likely the most resistant.

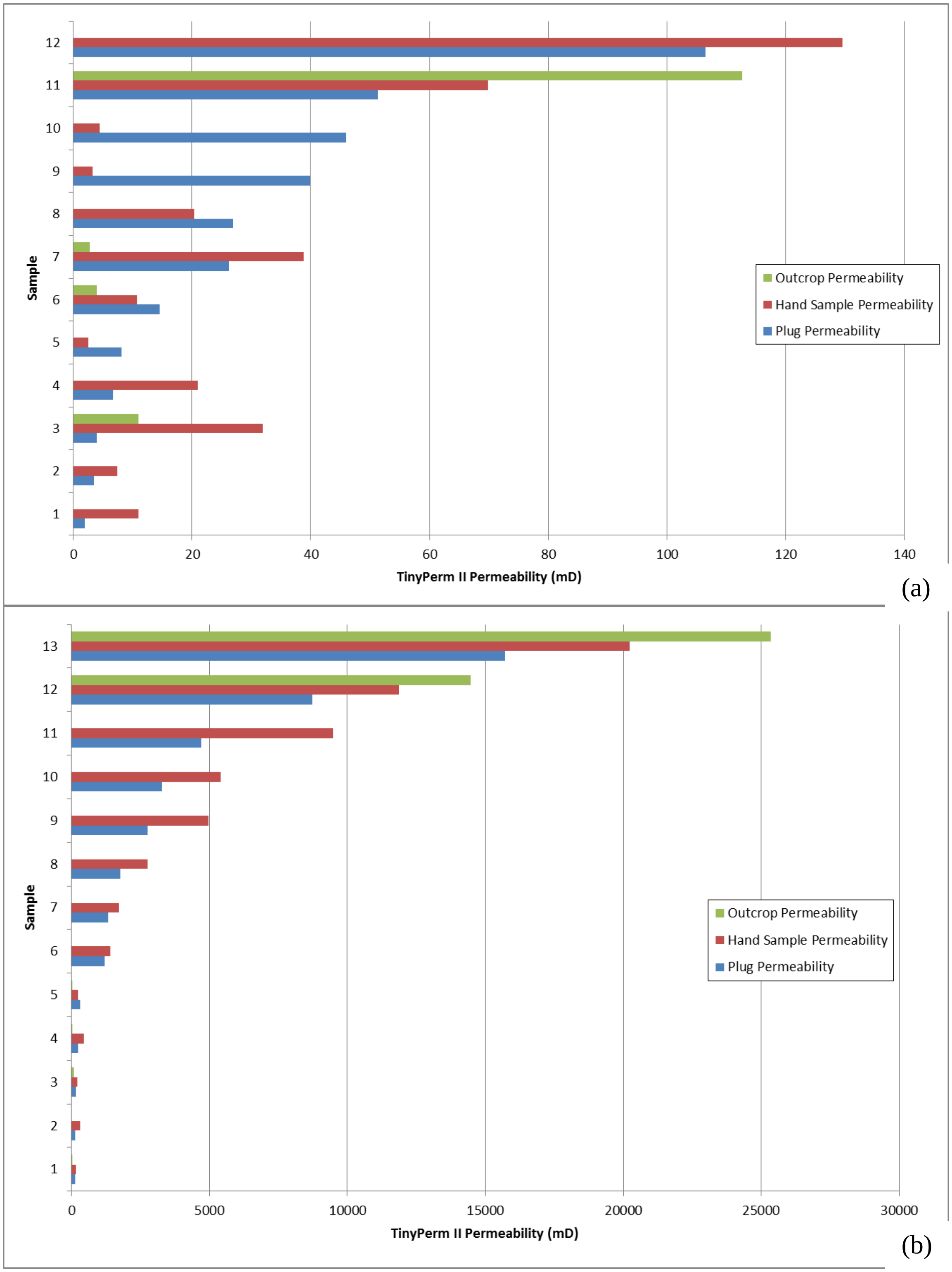

Figure 13. Comparison of plug, hand samples, and outcrop permeability measurements using TinyPerm II for samples (a) <140 mD and (b) > 140 mD.

Mercury Injection Capillary Pressure (MICP)

MICP analysis involves injecting mercury into a plug while measuring the pressure necessary to do so. This provides data on pore-throat size distribution and porosity. This analysis was carried out on zones of deformation bands, allowing for the calculation of the permeability and breakthrough pressure of a non-wetting phase. The latter is necessary in calculating the maximum column of CO_2, oil, or gas zones of deformation bands can contain. Samples were cut into plugs that were no larger than 0.75 inches in diameter and 0.75 inches thick. The plugs were then sent to Poro-Technology where they were jacketed with epoxy and underwent MICP analysis.

Geologic and Permeability Conceptual Models

Conceptual geologic models were made for each study site to document the structural and lithologic variation. Key data recorded includes lithofacies and the geometry of structural elements, such as fractures and deformation bands. Data were recorded on outcrop photographs. These models were modified to create permeability models using minipermeameter, fracture aperture, laboratory and literature data. Adobe Illustrator® CS5 was used to create the models.

Petrography

Selected samples were cut into billets using a diamond coated rock saw and sent to Wagner Petrographic © to make 24x46 mm thin sections. Two types of thin sections were prepared, standard thin sections meant for only optical analysis and polished thin sections meant for both optical and microprobe analysis. All thin sections were impregnated with epoxy containing a red Rhodamine dye to allow differentiation of real porosity from apparent porosity produced during thin-section preparation.

Optical petrography was performed on a standard petrographic microscope equipped with a digital camera. Photomicrographs were used to document mineralogy and textural properties. The modal abundance of constituents was determined for siliciclastic samples using a 300-point count. An additional 100-point (pores only) count was also performed to document the types of porosity present. For samples that do not contain abundant porosity, the types of porosity were estimated visually. Point counting was not performed on limestones, samples that were too small (< 2 cm^2), or samples of poor thin-section quality (thin sections made from billets damaged during transport).

Electron Microprobe Analysis

Polished thin sections were analyzed using a CAMECA ® SX-100 electron microprobe equipped with back-scattered and secondary electron detectors, and three WDS spectrometers for quantitative chemical analysis. Prior to analysis, each polished thin section was coated with carbon. Because results of the quantitative analysis of carbonate cements are given in Wt% oxide recalculated as carbonate, the data were converted to mol% using dimensional analysis and then normalized to 100%. Wt% oxide totals were used to exclude bad data; specifically, carbonate analyses differing more than 2% from a sum of 100% were considered inaccurate and not reported. All quantitative analyses were performed using a 15 kV beam. The beam diameter used for the majority of the analyses was 20 μm, although a beam diameter of 10 μm was used on some locations too small for 20 μm.

X-ray Diffraction Analysis

Iron oxide cement was analyzed using a PANalytical X'Pert PRO X-ray diffractometer. Heavily iron oxide cemented whole rock and fracture-fill samples were ground to a fine powder using a mortar and pestle. The powder was analyzed on the X-ray diffractometer from 6 to 70 °2θ. Mineral peaks were identified using X'Pert High Score plus.

Stable Isotope Analysis

Stable isotope (oxygen and carbon) analysis of fracture-filling calcite was performed using a Thermo Finnigan Delta Plus XP mass spectrometer. Analysis was performed under continuous flow conditions with a helium carrier gas. The samples were first extracted from the veins using a Dremel® Tool with ~1 mm drill bit. Roughly 0.25 mg of the sample was then weighed and placed in a small vial. The vials were closed with a cap and septum to prevent leakage. Next each vial was injected with helium gas for two minutes; this was done using a specifically designed needle that contains one hole for injecting helium and another for removing air. Ten drops of phosphoric acid was then placed inside each the vial. Next the vials were put into a heating block and given time to equilibrate to 50º C. Once at 50º C, each sample was run ten times on the mass spectrometer. Standards were run to check for accuracy and to correct the raw data. CO_2 lab standards (blanks) were run every five samples to check for accuracy and machine drift during the sample run. Duplicate samples were run to check for variability in isotopic signatures among veins. The $\delta^{18}O$ of the duplicates were within 0.03 to 2.11‰ of each other, while the $\delta^{13}C$ were within 0.36 to 1.79‰ of each other. All duplicate samples were averaged. Calcite from the same vein but from a slightly different location were also run to check for isotopic variability. The $\delta^{18}O$ of calcite from the same vein but from a slightly different location were within 0.45 to 0.54‰ of each other, while the $\delta^{13}C$ were within 0.31 to 1.48‰ of each other.

CHAPTER 4. RESULTS

Study Sites and Conceptual Models

Two main study sites were examined during this project, the Uneva Mine Canyon study site (UMS) and the Iron Wash study site (ISS). Both are located within 20 km of each other (Figs. 6 and 7).

Uneva Mine Canyon Study Site (UMS)

Units found at this study site include the Navajo Sandstone and the Carmel Formation. All four members of the Carmel Formation are present at this site, although only the lowermost are described in detail because the reservoir-caprock interface is the main concern of this study. Two detailed study sites were selected for analysis at this location: Uneva Mine Canyon study site #1 (UMS-1) and Uneva Mine Canyon study site #3 (UMS-3).

Navajo Lithofacies

Previous authors have broken the Navajo Sandstone into two main groups of facies, dune and interdune (Dalrymple and Morris, 2007; Parry et al., 2009). Dalrymple and Morris (2007) broke down the dune facies into three lithofacies, large trough cross-stratified, small trough-cross stratified, and reworked eolian. The large and small trough cross-stratified lithofacies are both present at the Uneva Mine Canyon study site; however in this thesis both of these lithofacies are combined for simplicity and called the cross-bedded sandstone lithofacies. Instead of recognizing the reworked eolian lithofacies at this study site I instead chose to recognize a deformed sandstone lithofacies.

I feel "deformed" is a more appropriate name compared to "reworked eolian" because water reworking would not form the massive beds found in this lithofacies (see below). No interdune facies were observed in the upper portion of the Navajo Sandstone measured at this site, although this facies is lower in the section.

The cross-bedded sandstone lithofacies contains 2.0 to 7.2 m thick beds of tan, medium upper (average) grained, well sorted, calcareous sandstone (see APPENDIX A for the stratigraphic column of the study site). Large-scale trough cross-bedding in this lithofacies is consistent with an eolian origin.

The deformed sandstone lithofacies contains 0.6 to 4.7 m thick beds of tan, medium lower (average) grained, moderately-well sorted sandstone. It is characterized by massive and convolute bedding. The massive sandstone beds may have formed from multiple conditions, including bioturbation, deposition of wind-blown sand into still water, post depositional liquefaction, or deposition by mass-flow events (Eschner and Kocurek, 1986).

Co-op Creek Member Lithofacies

Blakey et al. (1983) broke the Judd Hollow Member (equivalent to the Co-op Creek Member) of the Carmel Formation into seven different lithofacies. These lithofacies are: gypsiferous mudstone, algal-laminated dolomicrite, pelmicrite, oosparite, biomicrite, terrigeneous mudstone, and basal sandstone. I recognized all but the gypsiferous mudstone lithofacies at the study site. In this thesis, the algal-laminate dolomicrite, pelmicrite, and biomicrite lithofacies are combined for simplicity and called the micritic mudstone lithofacies. In addition, the oosparite lithofacies is called the oolitic bivalve grainstone lithofacies, in order to maintain consistent Dunham (1962) nomenclature. To avoid confusion using the Dunham (1962) nomenclature, in this thesis the terrigeneous mudstone lithofacies is called the shale lithofacies. Sandstone units are present throughout the Co-op Creek Member and not just at the base of the unit. Because of this the basal sandstone lithofacies is called the sandstone lithofacies. Different from Blakey et al. (1983) I chose to recognize a siltstone lithofacies for this unit.

The micritic mudstone lithofacies contains 1 to 6.5 m thick beds of tan, sandy, micritic mudstone. Structures include asymmetrical ripple marks, parallel lamination, and cross lamination. Several zones have undergone dolomitization. Given the presence of micrite, this lithofacies likely formed in a low-energy marine environment. This is consistent with the interpretations of the three micritic lithofacies described by Blakey et al. (1983). Blakey et al. (1983) concluded the dolomicrite lithofacies formed along a low-energy carbonate shoreline, the pelmicrite lithofacies was deposited by near-shore marine processes on a protected shelf, and the biomicrite lithofacies formed on a low-energy basin slope.

The oolitic bivalve grainstone lithofacies contains 0.5 to 0.7 m thick beds of maroon oolitic bivalve grainstone. The unit contains abundant stylolites. Given the presence of ooids, this facies likely formed in a high-energy marine environment. Blakey et al. (1983) interpreted this lithofacies as forming as offshore bars and tidal channel mouth bars along a shelf margin.

The sandstone lithofacies contains 0.2 to 1.3 m thick beds of tan to gray calcareous, silty, fine lower (average) grained, well sorted sandstone. Structures include asymmetrical ripple marks, symmetrical ripple marks, convolute bedding, and load casts. This unit's close proximity to the limestone units suggests a highly variable depositional environment, such as a tidal flat or beach environment. Blakey et al. (1983) interpreted this unit as reworked deposits from the underlying Navajo Sandstone. However, since the unit is present throughout the Co-op Creek Member and not just the base this is probably not the case.

The siltstone lithofacies contains 0.5 to 3.5 m thick beds of tan to red, calcareous, sandy siltstone. Structures include asymmetrical ripple marks, symmetrical ripple marks, parallel lamination, cross lamination, wave ripple lamination, convolute bedding, and load casts. Several zones of the lithofacies have undergone dolomitization. This unit's close proximity to the limestone units and the presence of various ripple structures suggests a low to moderate energy marginal marine depositional environment.

The shale lithofacies contains 0.1 to 2.0 m thick beds of red, calcareous shale. Structures include parallel lamination and sandstone lenses. This unit's close proximity to the limestone units and its parallel lamination likely indicates some sort of low energy marine to marginal marine depositional environment. This is consistent with Blakey et al. (1983) who interpreted the terrigenous mudstone lithofacies was deposited in a low-energy marine environment.

Uneva Mine Canyon Study Site #1 (UMS-1)

This study site is located just south of the entrance to Uneva Mine Canyon (12 S, 547208, 4303956, WGS 84 datum). The site has an excellent exposure of the interface between the Navajo Sandstone and the Carmel Formation (Figs. 14ab). This site was chosen based on the large amount of bleaching associated with fractures at and above the interface (Fig. 14c). Almost all of the Carmel Formation is exposed at this study site, except for the upper portion of the Winsor Member.

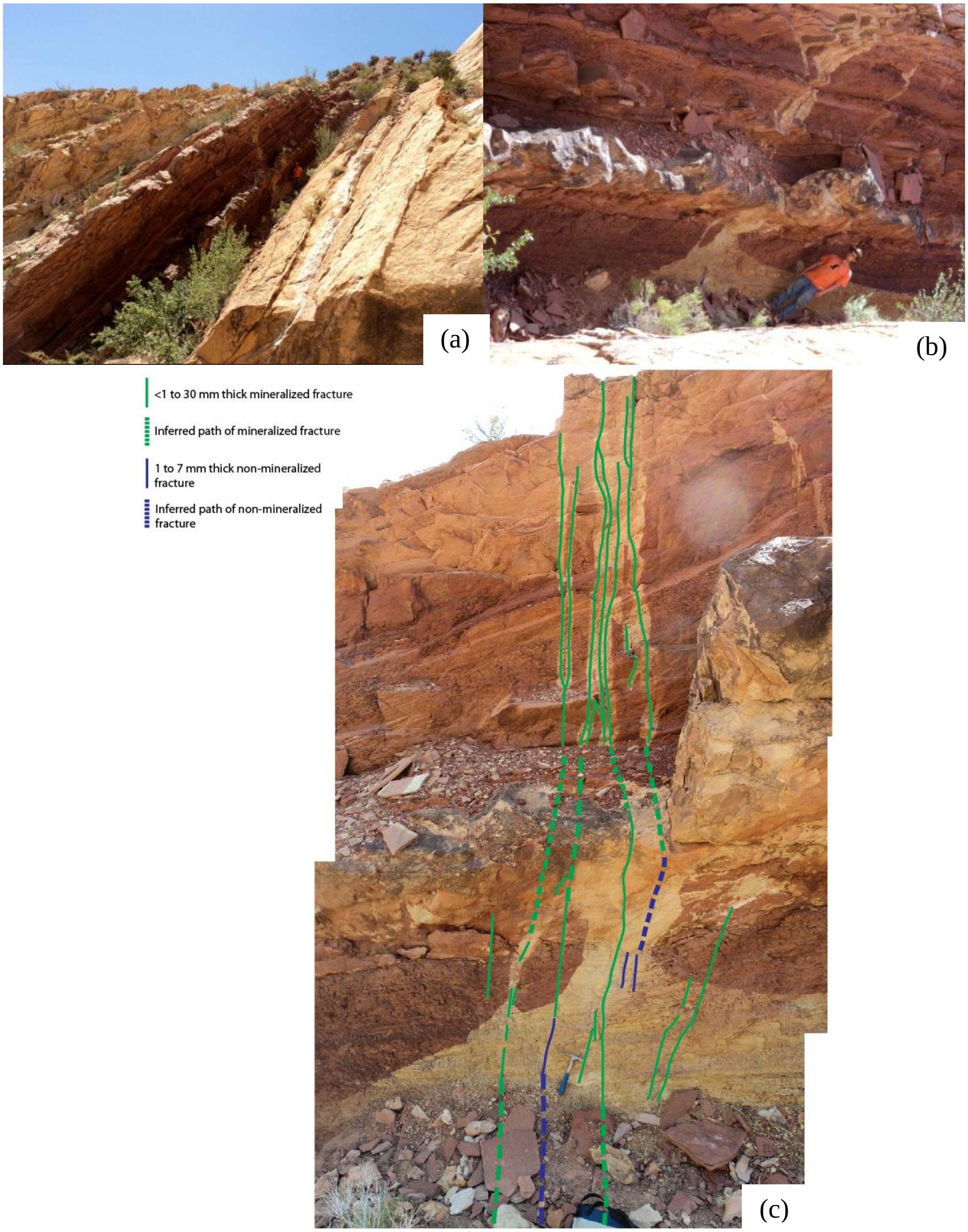

Figure 14. (a) Overview of UMS-1, 6 ft./1.83 m person for scale. On the right side of the image is the Navajo Sandstone, while to the left is the Co-op Creek Member of the Carmel Formation. The person wearing an orange t-shirt marks the location of the reservoir-caprock interface. (b) Overview of the bleached zone, 6 ft./1.83 m person for scale. (c) Bleached fracture network of UMS-1 with annotations, hammer for scale. Fractures cut through the Navajo Sandstone into the Carmel Formation. The bleached fractures make it easy to trace the fracture network.

Interface Structural Features

Structural features of interest at UMS-1 are a set of fractures going from the Navajo Sandstone into the Carmel Formation (Fig. 15). Fractures of the Navajo Sandstone are opening-mode. The majority of the fractures in the Carmel Formation are opening-mode with minor amounts of sliding-mode fractures. Fracture thickness varies from <1 to 30 mm. The fracture network penetrates 17.7 m into the Carmel Formation before it can no longer be traced. Bleaching is associated with most fractures close to the interface, but bleaching is no longer visible on mineralized fractures farther away from the interface. The Navajo Sandstone and the base of the Carmel Formation are bleached, with an increased concentration of bleaching in close proximately to the fracture networks.

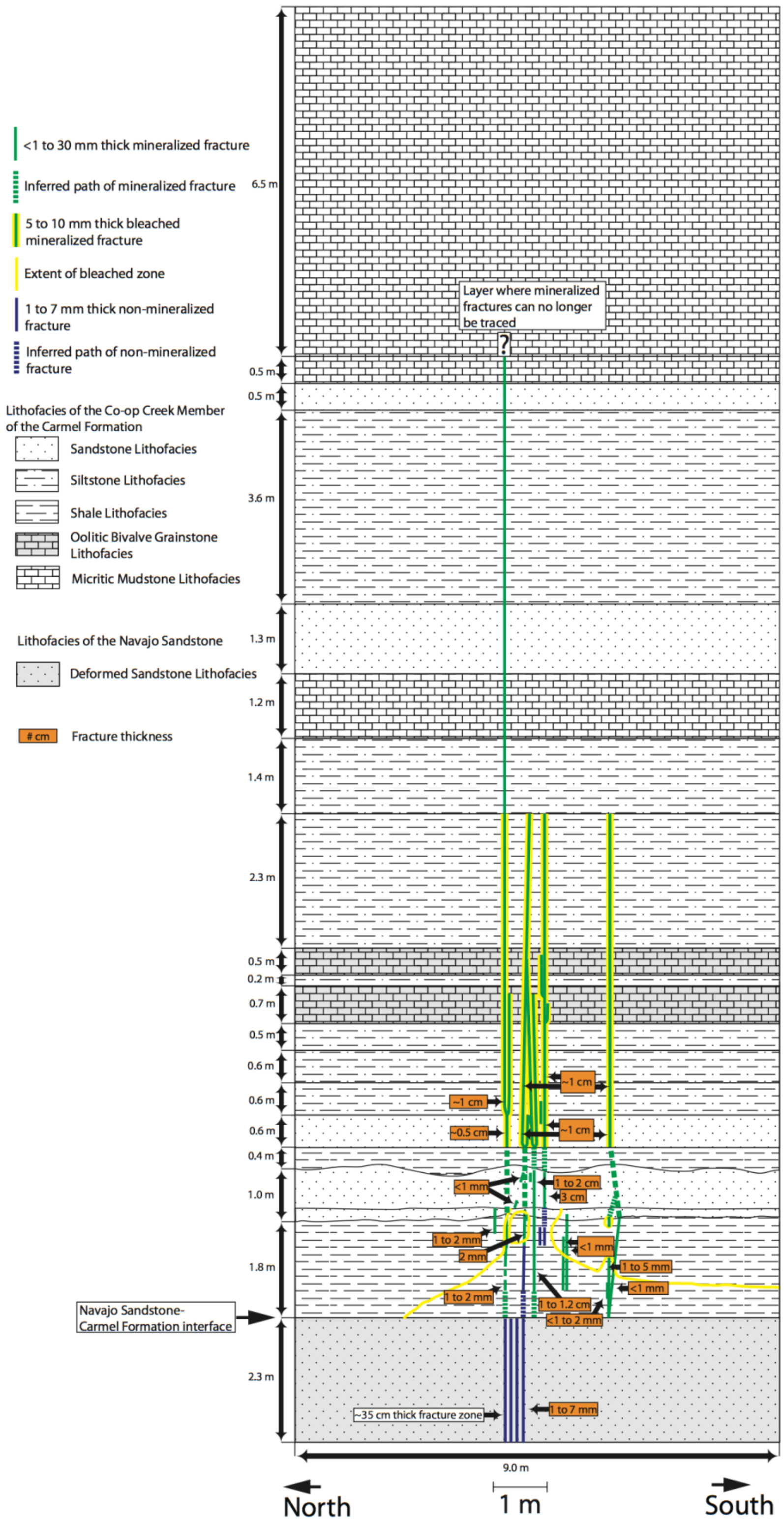

Figure 15. Geologic conceptual model of UMS-1. Fractures cut through the Navajo Sandstone into the Carmel Formation. Bleaching fluids from the Navajo Sandstone used the factures to penetrate the caprock, bleaching the fractures in the process. Fractures penetrate the Carmel Formation for 17.7 m until they can no longer be traced.

Permeability Variations

The permeability of the deformed sandstone lithofacies of the Navajo Sandstone and the sandstone lithofacies of the Carmel Formation at UMS-1 were assigned values using corrected TinyPerm II field measurements. The permeability of the deformed sandstone lithofacies, the average of three measurements taken at various locations within this lithofacies, is 237 mD (Fig. 16; see APPENDIX B for TinyPerm II data). The permeability of the sandstone lithofacies, based on one measurement, is 7 mD.

The permeability of the micritic mudstone and oolitic bivalve grainstone lithofacies of the Carmel Formation at UMS-1 were both assigned the value of 0.019 mD. This is average of two measurements obtained from Payne (2011) using mercury injection capillary pressure data to calculate the permeability of limestones from the Co-op Creek Member at a study area also located in the San Rafael Swell.

The permeability of the siltstone and shale lithofacies of the Carmel Formation at UMS-1 were both assigned the value of 0.000133 mD. This is the average of two measurements obtained from Payne (2011) using tight rock analysis to determine the permeability of shales and siltstones from the Co-op Creek Member at a study area also located in the San Rafael Swell.

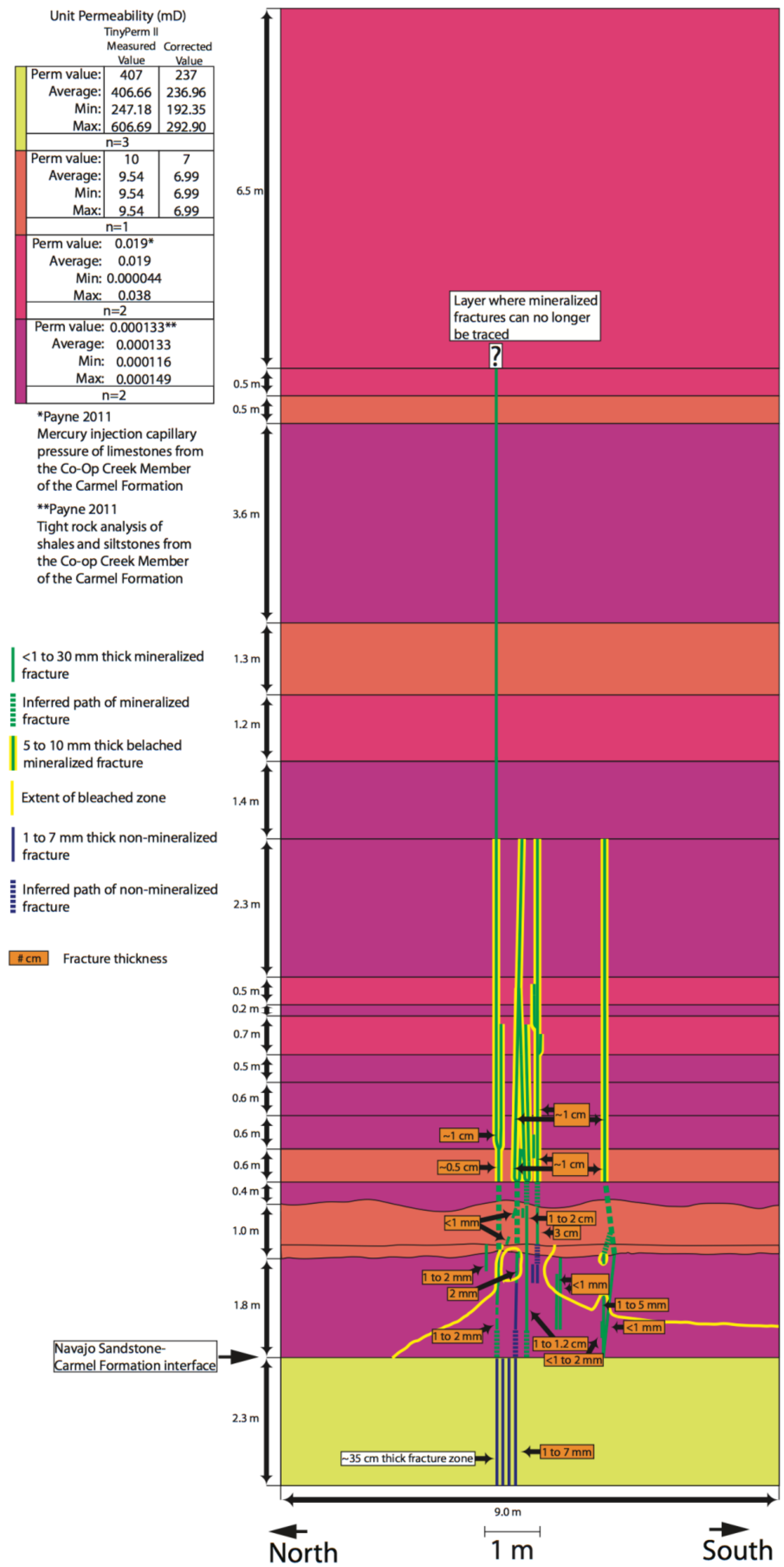

Figure 16. Permeability conceptual model of UMS-1. The color of each lithofacies corresponds to a different permeability, as listed above. Permeability was determined using a combination of TinyPerm II measurements and laboratory permeability measurements from existing authors.

Uneva Mine Canyon Study Site #3 (UMS-3)

This study site is about 200 m north of the canyon entrance (12 S 0547245, 4304151, WGS 84 datum). The site has a partially exposed outcrop of the interface between the Navajo Sandstone and the Carmel Formation. Unfortunately, the area where the interface is located is covered with debris, although there are good outcrops directly above and below. This site was chosen based on the large amount of bleaching associated with structural features at the interface (Fig. 17abc).

(a)

Figure 17. (a) A zone of deformation bands in the Navajo Sandstone near the Carmel Formation interface at UMS-3, 6 ft./1.83 m person for scale. (b) Enlarged view the zone of deformation bands, broom for scale. (c) A heavily bleached and fractured zone slightly above the interface at UMS-3, hammer for scale. Note the large zone of bleaching associated with mineralized fractures.

Interface Structural Features

Structural features of interest at UMS-3 are a zone of deformation bands in the Navajo Sandstone transitioning into a set of opening-mode fractures into the Carmel Formation (Fig. 18). The zone of deformation bands is roughly 15 cm thick. Fracture thickness varies from <1 to 20 mm. The fracture network can be tracked for roughly 5.4 m into the Carmel Formation before it can no longer be traced due to cover. Bleaching is associated with most fractures close to the interface. The Navajo Sandstone and the base of the Carmel Formation is bleached, with an increased concentration of bleaching in close proximately to the fracture networks (Fig. 17c).

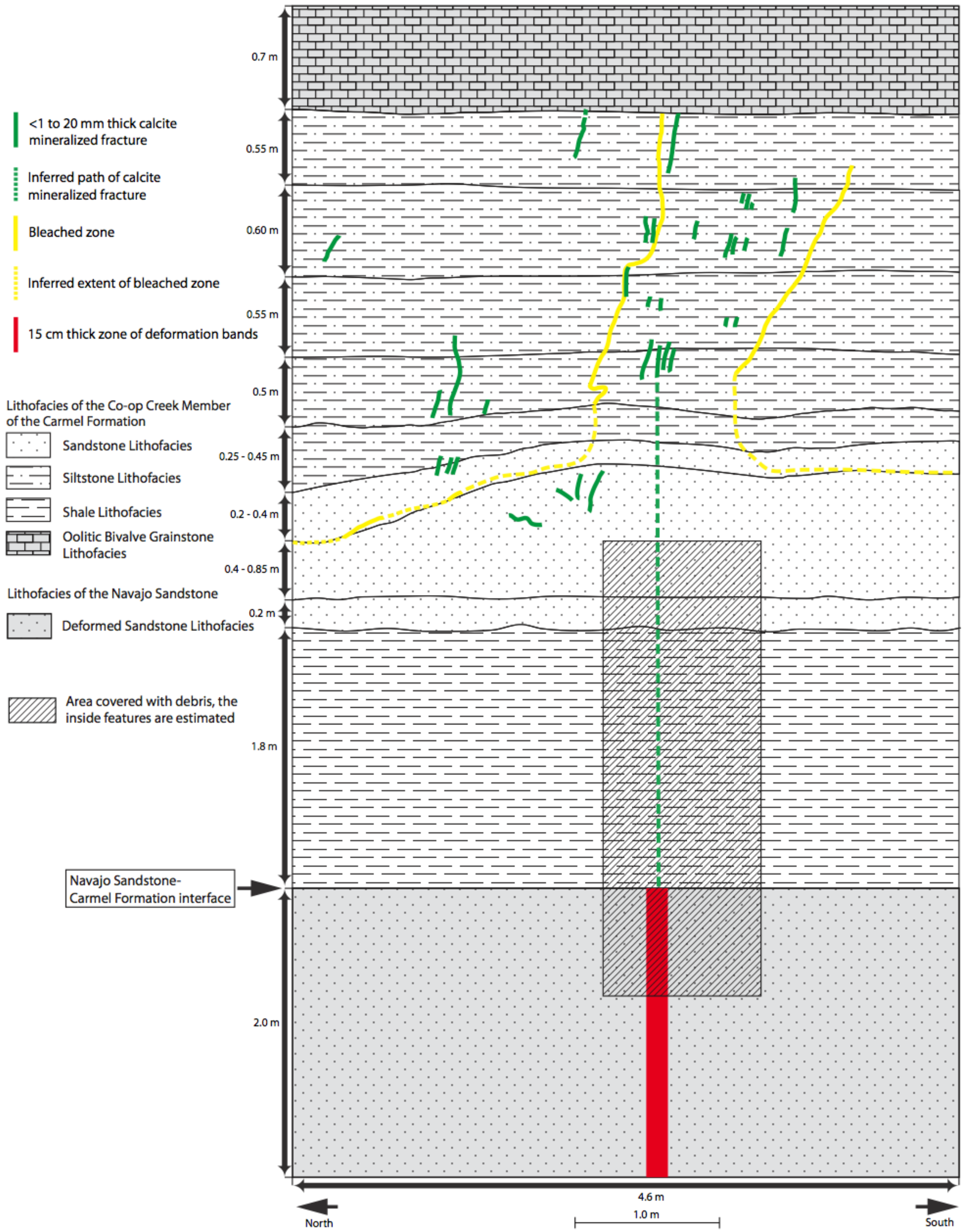

Figure 18. Geologic conceptual model of UMS-3. A zone of deformation bands in the Navajo Sandstone transition into a set of fractures in the Carmel Formation. Bleaching fluids from the Navajo Sandstone used the factures to penetrate the caprock, bleaching the fractures in the process. Fractures penetrate the Carmel Formation for 5.4 m until they can no longer be traced.

Permeability Variations

The deformed sandstone lithofacies of the Navajo Sandstone and the sandstone lithofacies of the Carmel Formation at UMS-3 were assigned permeability values using corrected TinyPerm II field measurements. The permeability of the deformed sandstone lithofacies, the average of four measurements taken at various locations within this lithofacies, is 524 mD (Fig. 19). The permeability of the sandstone lithofacies, the average of two measurements taken at various locations within this lithofacies, is 8 mD.

The permeability of the oolitic bivalve grainstone, siltstone, shale lithofacies are assigned the same values as were assigned at UMS-1.

Due to the relative similarity between the Navajo Sandstone and the Entrada Sandstone, the permeability of the zone of deformation bands at UMS-3 is assigned the same value as those from ISS-1 (see ISS-1 section for more details). These permeability measurements are consistent with measurements of previous authors working on cataclasis bands in the Navajo Sandstone, which range from 2 to 6.9 mD (Torabi et al., 2008).

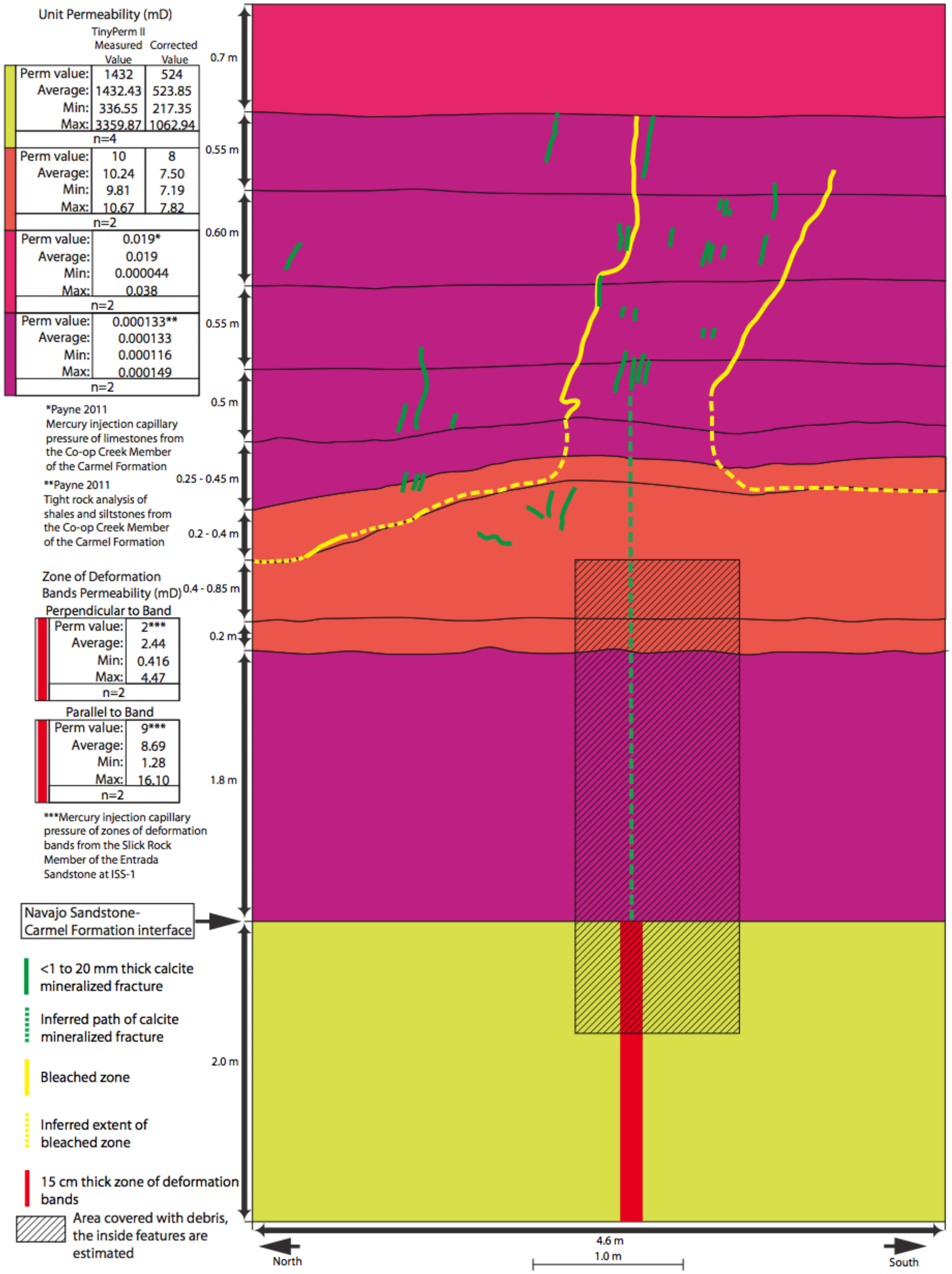

Figure 19. Permeability conceptual model of UMS-3. The color of each lithofacies corresponds to a different permeability, as listed above. Permeability was determined using a combination of TinyPerm II measurements, laboratory permeability measurements, and laboratory permeability measurements from existing authors.

Iron Wash Study Site

This study site is located west of mile marker 146 on Utah State Route 24. Units found at this study site include the Carmel Formation and the Entrada Sandstone. Only the uppermost member of the Carmel Formation is present at this study site. Four detailed study site were selected for analysis at this location: Iron Wash study site #1 (ISS-1), Iron Wash study site #3 (ISS-3), Iron Wash study site #4 (ISS-4), and Iron Wash study site #5 (ISS-5).

Banded Unit of the Winsor Member Lithofacies

Blakey et al. (1983) states that moving east from the San Rafael Swell to the Green River the majority of the upper unnamed member (equivalent to the Winsor Member) consists of the redbed facies. Blakey et al. (1983) describes the unit as a calcareous to dolomitic fine-grained reddish-orange sandstone interbedded with reddish-brown mudstone. This is consistent with what is present at the Iron Wash study site, except instead of mudstone the unit consists of siltstone. Due to the grain size and permeability differences between beds, I decided to break this unit into two lithofacies, the sandstone and siltstone lithofacies. I did not include a shale facies because little shale is present in the Winsor Member at the study sites.

The siltstone lithofacies contains 0.1 to 2.0 m thick beds of reddish-brown, semi-calcareous siltstone. Structures include sandstone lenses. Blakey et al. (1983) attributed the mudstone of the redbed facies to a high intertidal and supratidal-sabkha setting. Although the siltstone at this study site may have a slightly larger grain size than the mudstone described by Blakey et al. (1983), it seems logical to assume both formed through similar processes.

The sandstone lithofacies contains 0.1 to 0.8 m thick beds of reddish-brown, very fine lower (average) grained, well sorted sandstone. Some portions of the lithofacies have undergone dolomite cementation. Structures include sandstone lenses, which may have originated as channels associated with a tidal flat depositional environment.

Slick Rock Member of the Entrada Sandstone

Marino (1992) identified nine lithofacies in the Entrada Sandstone in the northern part of the San Rafael Swell. These lithofacies include green mudstone, oolitic sandstone, polydirectional dune sandstone, sigmoidal bundle sandstone, angular and fine-grained sandstone, "stone baby" silty sandstone, red silty mudstone, wavy sandstone, and cross-bedded sandstone. Within the Slick Rock Member the cross-bedded sandstone, wavy sandstone, and red silty mudstone lithofacies are present. To be consistent with the Navajo Sandstone, the wavy sandstone lithofacies shall be known as the deformed sandstone lithofacies.

The cross-bedded sandstone lithofacies contains 0.3 to 8.9 m thick beds of gray to yellow, medium lower (average) grained, moderate to well sorted, calcareous sandstone. Structures include trough and low-angle cross-bedding. The large-scale bedding of this facies likely indicates an eolian origin, as noted by Marino (1992).

The deformed sandstone lithofacies contains 0.2 to 1.5 m thick beds of gray to yellow, medium lower (average) grained, moderately-well sorted sandstone. Structures include massive and convolute bedding. As stated previously with the deformed sandstone lithofacies in the Navajo Sandstone, multiple conditions may be responsible for forming this lithofacies.

The red silty mudstone lithofacies contains 0.1 to 0.3 m thick beds of red shale and siltstone. Structures include parallel lamination. This unit is interbedded with the sandstone beds of the Slick Rock Member. Given this facies is interbedded with eolian sandstone, it likely formed during a wet interdune period.

Earthy Member Lithofacies

The majority of the nine lithofacies described by Marino (1992) for the Entrada Sandstone in the northern part of the San Rafael Swell are present in the Earthy Member. However, for the sake of simplicity I decided to combine several of his lithofacies into three main facies. The first lithofacies known as the sandstone lithofacies consists of the angular and fine-grained sandstone, polydirectional dune sandstone, sigmoidal bundle sandstone, and “stone baby” silty sandstone lithofacies. The second, known as the shale lithofacies consists of the green mudstone and red silty mudstone lithofacies. The third lithofacies, known as the siltstone lithofacies, is a combination of the silty components associated with the red silty mudstone and “stone baby” silty sandstone lithofacies. The oolitic sandstone lithofacies was not observed at this study site.

The sandstone lithofacies contains 0.1 to 1.4 m thick beds of dark red, fine lower (average) grained, moderately sorted, calcareous, silty sandstone. Structures include convolute, massive, and low-angle cross-bedding. Marino (1992) interpreted eolian, tidal flat, foreshore, and shore face depositional environments for the lithofacies that make up this composite facies.

The siltstone lithofacies contains 0.6 to 4.0 m thick beds of brownish-red, sandy siltstone. Structures include parallel lamination. Marino (1992) interpreted the silty lithofacies formed from a tidal flat depositional environment

The shale lithofacies contains 0.1 to 0.2 m thick beds of red, gray, tan, and green shale with some layers of sandstone. Structures include parallel lamination. The different colored shales may represent different environments, with the greenish shale forming in reducing offshore marine conditions and the reddish shales oxidizing tidal flat conditions (Marino, 1992). Thin sections show that some portions of this lithofacies are litharenites made up of shale fragments and quartz grains (Fig. 20). Marino (1992) interpreted this as a storm deposit resulting from the mixing of shoreline dunes and offshore mudstones.

Figure 20. Thin-section photomicrograph mosaic of the "shale" lithofacies. The rock is not actually a shale, but instead a litharenite, composed of shale fragments and quartz grains. The rip-up clasts together with the quartz grains suggests this may have been a storm deposit. Stratigraphic up is located on the side opposite of the scale bar (left side of image). The abundant fractures and complex clay fabric are likely the result of deformation. IW8911-9b, Earthy Member of the Entrada Sandstone, plane polarized light.

Iron Wash Study Site #1 (ISS-1)

The UTM coordinates for the study site are 12 S 0546085, 4288762, WGS 84 datum. The site has an excellent exposure of the interface between the Slick Rock Member of the Entrada Sandstone and the Earthy Member of the Entrada Sandstone (Fig. 21ab). It was chosen because it contains a zone of deformation bands intersecting a reservoir-caprock interface.

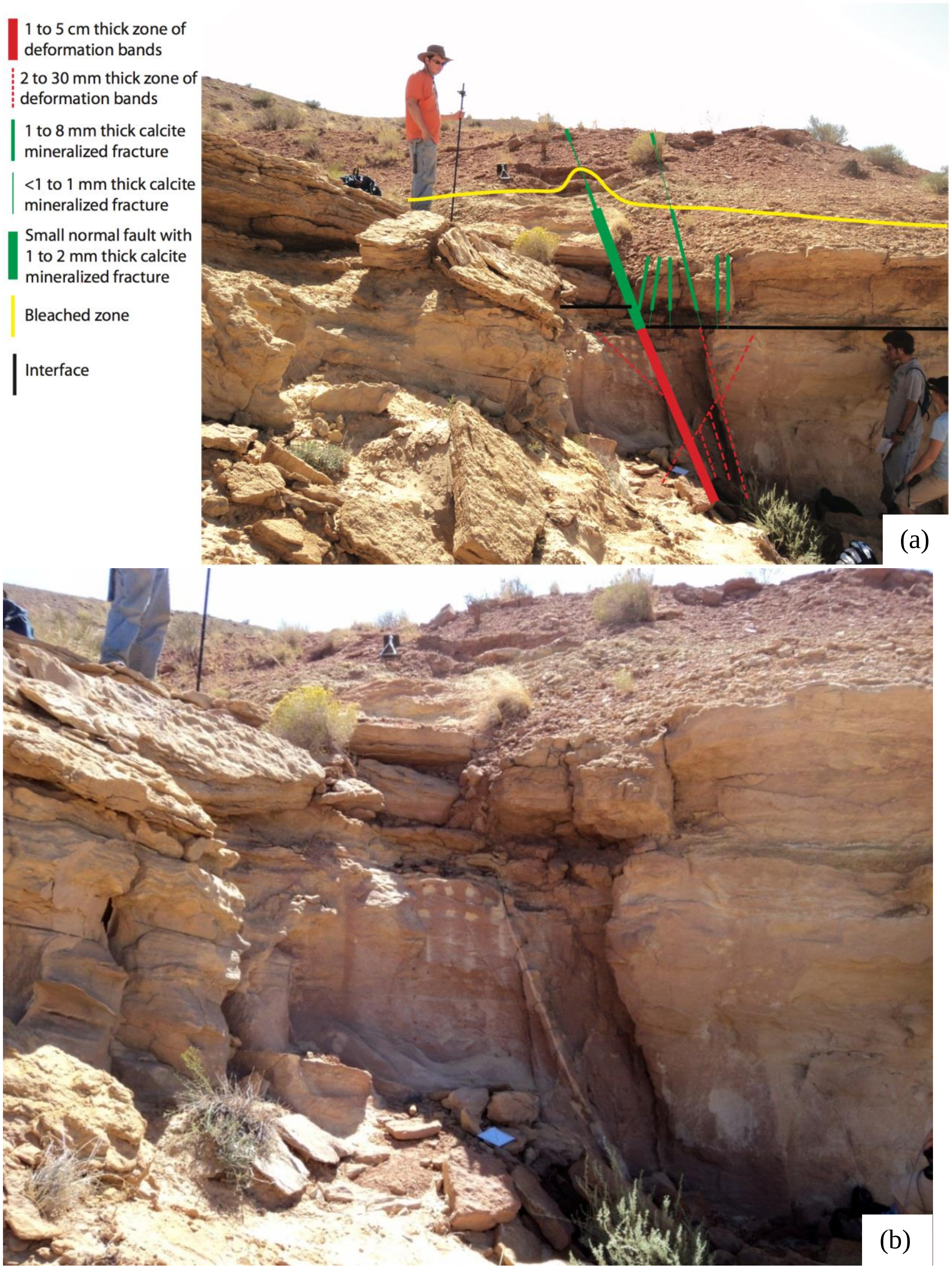

Figure 21. (a) Overview of ISS-1 with annotations, 6 ft./1.83 m person for scale. The black line marks the interface between the Slick Rock Member and Earthy Member. A zone of deformation bands in the Slick Rock Member transitions into a set of fractures in the Earthy Member. The fracture network and the base of the earthy Member is bleached. (b) Enlarged view of ISS-1 zone of deformation bands, 6 ft./1.83 m person for scale.

Interface Structural Features

Structural features of interest at ISS-1 are zones of deformation bands in the Slick Rock Member transitioning to a set of opening-mode fractures in the Earthy Member (Fig. 22). The main zone of deformation bands is 1 to 5 cm thick, becoming thinner as it approaches the interface. Smaller zones of deformation bands are also present at the interface ranging in thickness from 2 to 30 mm, also becoming thinner as they approach the interface.

The thickness of the Earthy Member fractures varies from <1 to 8 mm. The fracture network can be tracked for 3 m into the Earthy Member before it can no longer be traced due to erosion. Bleaching is associated with some of the fractures close to the interface. The Slick Rock Member and base of the Earthy Member is bleached, with an increased concentration of bleaching in close proximately to the fracture network.

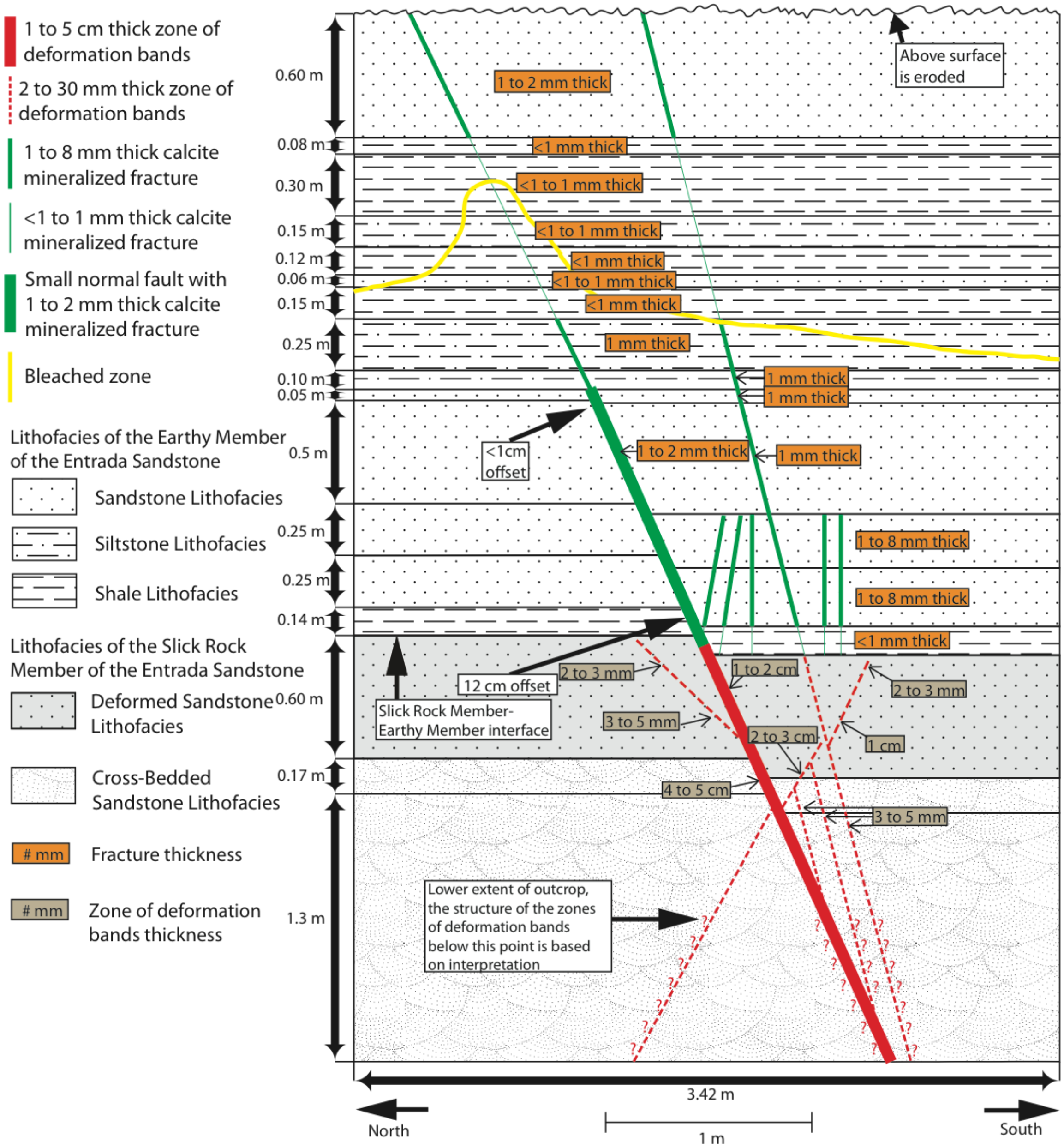

Figure 22. Geologic conceptual model of ISS-1. A zone of deformation bands in the Slick Rock Member transition into a set of fractures in the Earthy Member. Bleaching fluids from the Slick Rock Member used the factures to penetrate into the caprock, bleaching the fractures in the process. Fractures penetrate the Earthy Member for 3 m until they can no longer be traced.

Permeability Variations

The permeability of the deformed sandstone and the cross-bedded sandstone lithofacies of the Slick Rock Member and the sandstone lithofacies of the Earthy Member at ISS-1 was assigned using corrected TinyPerm II field measurements. The permeability of both the deformed sandstone lithofacies and the cross-bedded sandstone lithofacies, the average of 26 measurements taken at various locations within these lithofacies, is 3,528 mD (Fig. 23). The permeability of the sandstone lithofacies was assigned two different values based on their position. Based on one measurement, the lower sandstone beds located next to the interface adjacent to the mineralized fractures were assigned the value of 1 mD. Based on the average of 12 measurements at various locations, all other sandstones were assigned the value of 56 mD. Field observations show an increased amount of cementation adjacent to the mineralized fractures in sandstone near the interface, likely contributing to the decrease in permeability at this location.

The permeability of the siltstone and shale lithofacies of the Earthy Member are below the lower measurement limit of TinyPerm II, so they were assigned a permeability of 0.0055 and 0,0005 mD, respectively. These values are the average permeability for siltstones and shales from Brace (1980). These values have a higher permeability than the siltstone and shale samples measured by Payne (2011) in the Carmel Formation using tight rock analysis, which ranged from 0.000116 mD to 0.000267 mD.

The permeability of the main zone of deformation bands at ISS-1 was calculated using mercury porosimetry data. Based on the average of two measurements, when moving parallel to a zone of deformation bands the permeability is 9 mD. Based on the average of two measurements, when moving perpendicular to the zone of deformation bands the permeability is 2 mD. These permeability measurements are consistent with measurements of previous authors working on cataclasis bands in the Entrada Sandstone, which range from 4 to 11 mD (Torabi et al., 2008).

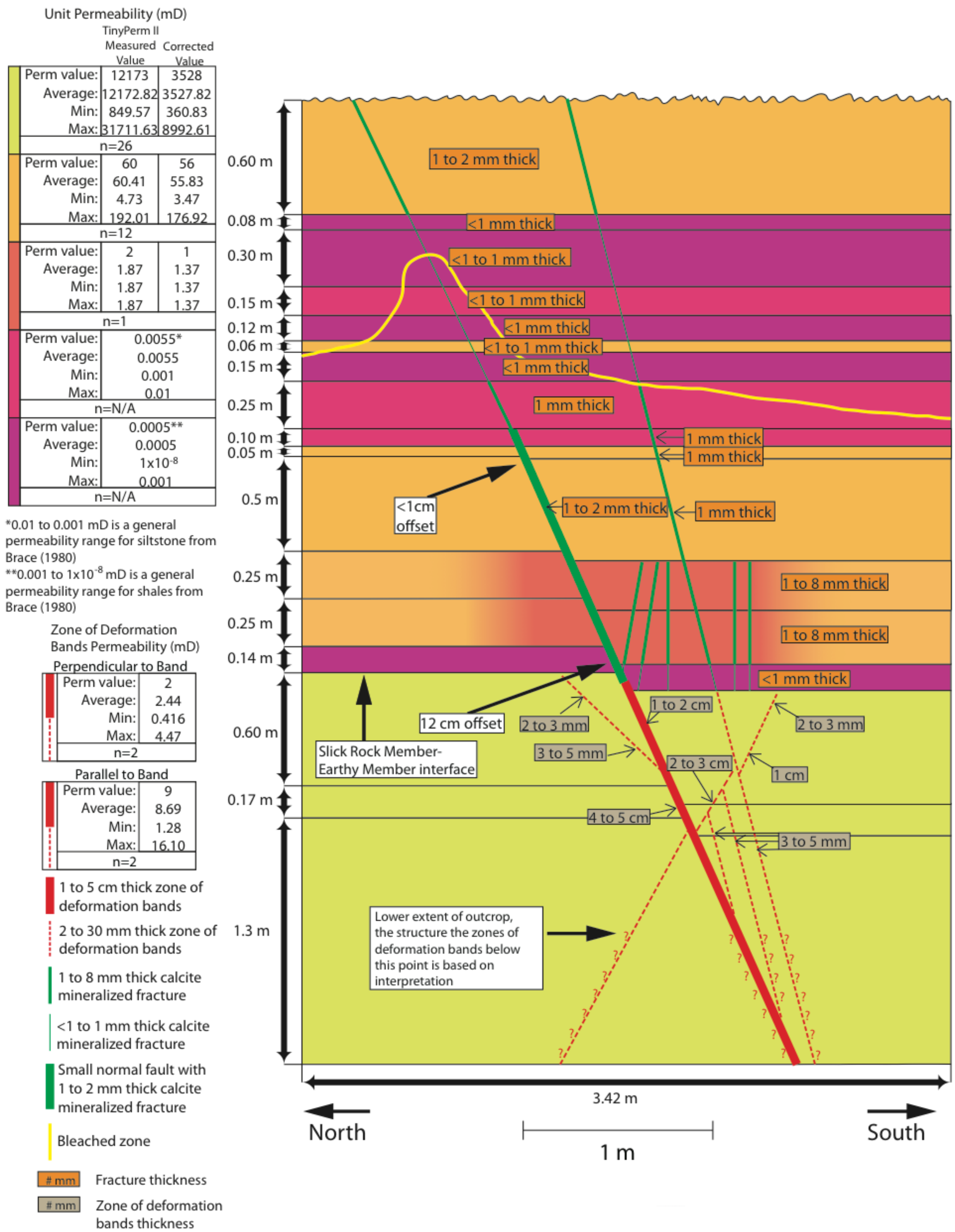

Figure 23. Permeability conceptual model of ISS-1. The color of each lithofacies corresponds to a different permeability, as noted in the legend. Permeability was determined using a combination of TinyPerm II measurements, laboratory permeability measurements, and laboratory permeability measurements from the literature.

Iron Wash Study Site #3 (ISS-3)

This site is roughly 400 m northwest of ISS-1 (12 S 0545682, 4288831, WGS 84 datum). The site has an excellent exposure of the interface between the Winsor Member of the Carmel Formation and the Slick Rock Member of the Entrada Sandstone (Fig. 24ab). It was chosen because it contains a normal fault that intersects a reservoir-caprock interface. Although the reservoir-caprock interface is reversed compared to the previous study sites, this study site can still be used as a natural analogue if it is turned upside down.

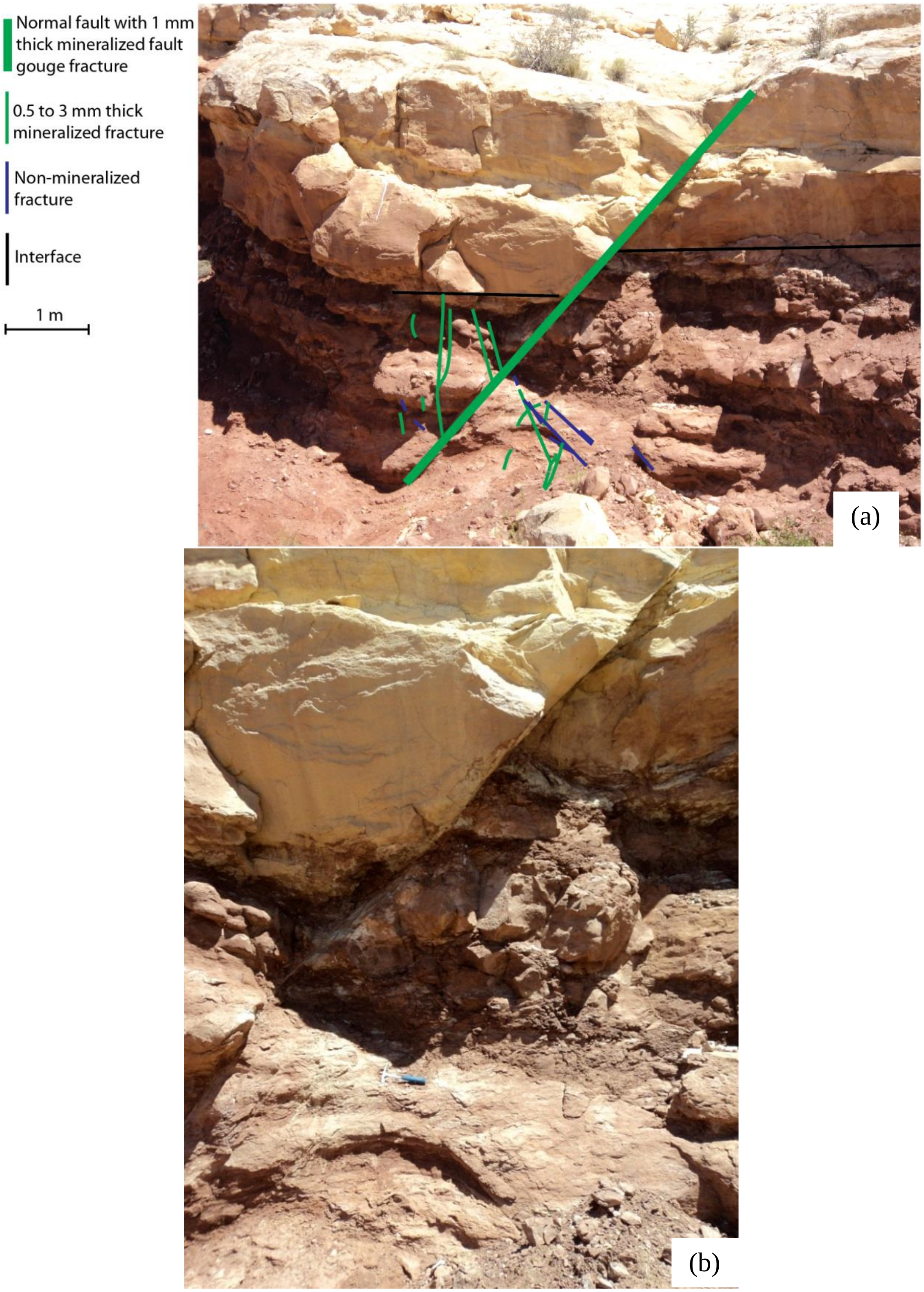

Figure 24. (a) Overview of ISS-3 with annotations, see image for scale. Above the black line labeled "interface" is the Entrada Sandstone, below this line is the Carmel Formation. (b) Enlarged view of ISS-3, hammer for scale. A normal fault cuts through the interface. Associated with the fault core and damage zone are opening-mode and sliding-mode fractures.

Interface Structural Features

Structural features of interest at ISS-3 are a set of fractures inside the damage zone and core of a normal fault cutting though the Carmel Formation and the Entrada Sandstone (Fig. 25). Displacement of the normal fault is roughly 1 m. The core of the normal fault is a 1 mm thick sliding-mode fracture. The fractures in the damage zone are opening-mode with a thickness ranging from 0.5 to 3 mm. Hazardous terrain made it difficult to determine if fractures are present in the fault damage zone inside the Slick Rock Member of the Entrada Sandstone. The Slick Rock Member of the Entrada Sandstone is bleached, as well as the margins of some of the fractures in the Carmel Formation close to the interface.

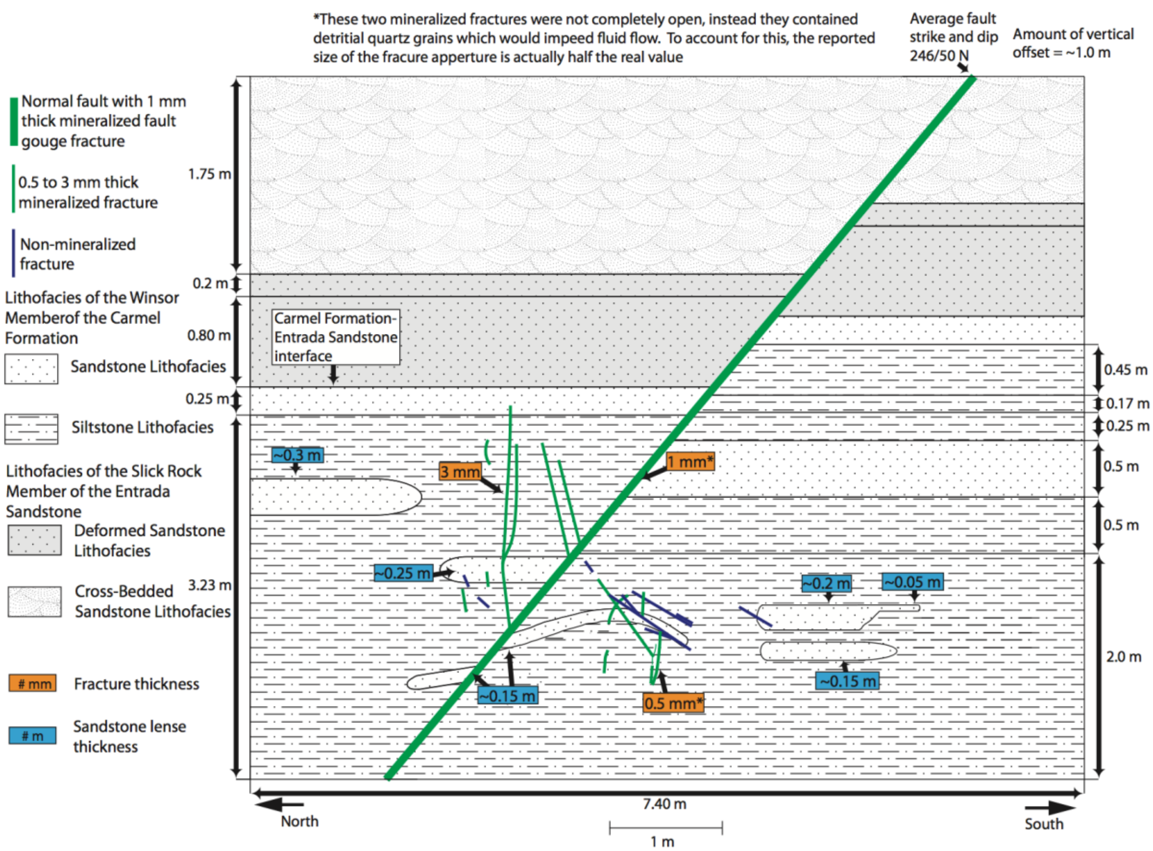

Figure 25. Geologic conceptual model of ISS-3. A normal fault cuts through the Carmel Formation and the Entrada Sandstone. A sliding-mode fracture is associated with the core of the normal fault. Several opening-mode fractures are associated with damage zone of the normal fault.

Permeability Variations

The permeability of the cross-bedded sandstone lithofacies and the deformed sandstone lithofacies of the Entrada Sandstone and the sandstone lithofacies of the Carmel Formation at ISS-3 were assigned values using corrected TinyPerm II field measurements. The permeability of the cross-bedded sandstone lithofacies, the average of two measurements taken at various locations within this lithofacies, is 443 mD (Fig. 26). The permeability of both the deformed sandstone lithofacies and the sandstone lithofacies, the average of nine measurements taken at various locations within these lithofacies, is 4 mD.

The permeability of the siltstone lithofacies of the Winsor Member is assigned the same value as the siltstone lithofacies at ISS-1.

Not all fractures in this model were completely open, as fault gouge is present locally in the fractures. To account for the effect of fault gouge in the permeability model, the fracture is reported as half its actual size (Figs. 25 and 26).

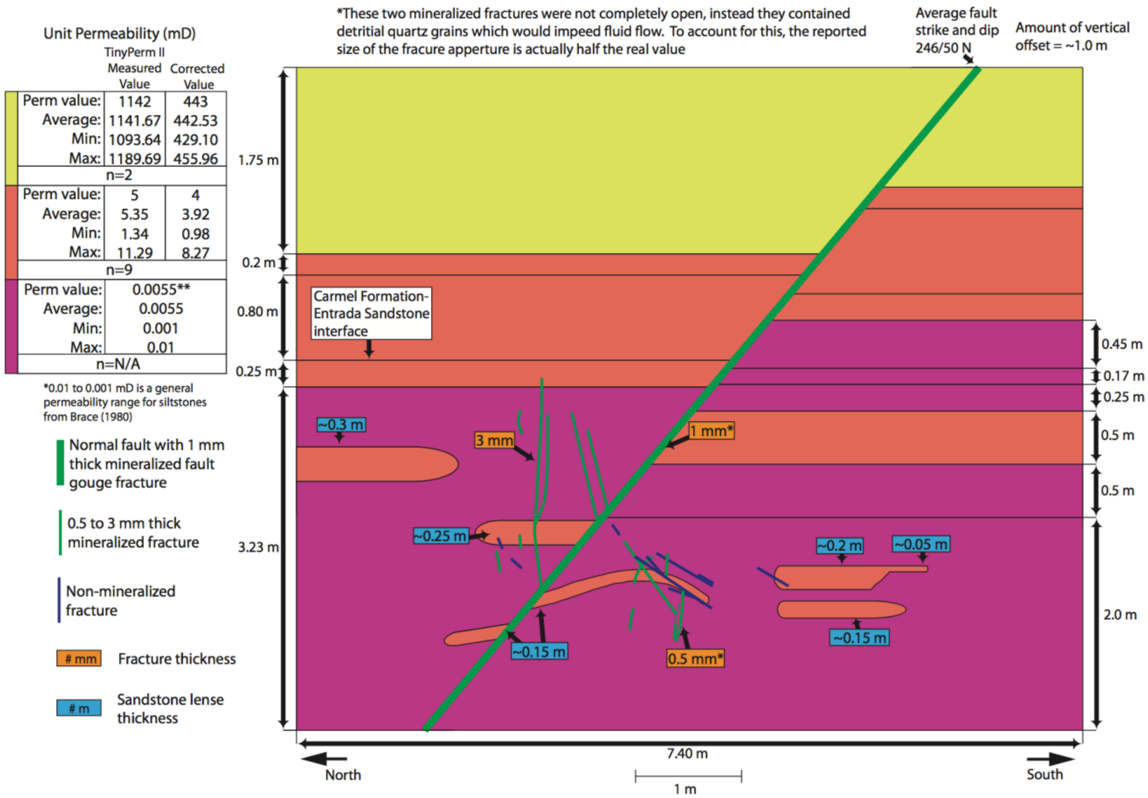

Figure 26. Permeability conceptual model of ISS-3. The color of each lithofacies corresponds to a different permeability, as listed above. Permeability was determined using a combination of TinyPerm II measurements and laboratory permeability measurements from existing authors.

Iron Wash Study Site #4 (ISS-4)

This site is roughly a 700 m northeast of ISS-1 (12 S 0546731, 4289063, WGS 84 datum). It has a great exposure of the interface between the cross-bedded sandstone lithofacies and the deformed sandstone lithofacies within the Slick Rock Member of the Entrada Sandstone (Fig. 27). This site was chosen because of the large difference in concentrations of zones of deformation bands associated with each lithofacies.

Field observations suggest that grain size and sorting of the different lithofacies at ISS-4 may have impacted the formation of structural features. The cross-bedded sandstone lithofacies has a grain size of fine upper to medium upper and is moderate to well sorted. The deformed sandstone lithofacies has a grain size of fine lower to fine upper and is moderately sorted.

Figure 27. Overview of ISS-4 with annotations, backpack for scale. This outcrop shows the interface between two different lithofacies within the Slick Rock Member of the Entrada Sandstone. Above the black line labeled "interface" is the cross-bedded sandstone lithofacies and below is the deformed sandstone lithofacies. Abundant zones of deformation bands are found in the cross-bedded sandstone lithofacies, whereas only one faulted zone of deformation bands is present in the deformed sandstone lithofacies.

Interface Structural Features

Structural features of interest at ISS-4 include a faulted zone of deformation bands (i.e. slip surface) in the deformed sandstone lithofacies and several zones of deformation bands in the cross-bedded sandstone lithofacies (Fig. 28). The faulted zone of deformation bands thickness inside the deformed sandstone lithofacies varies from 2 to 20 mm. The zones of deformation bands thickness inside the cross-bedded sandstone lithofacies also varies from 2 to 20 mm.

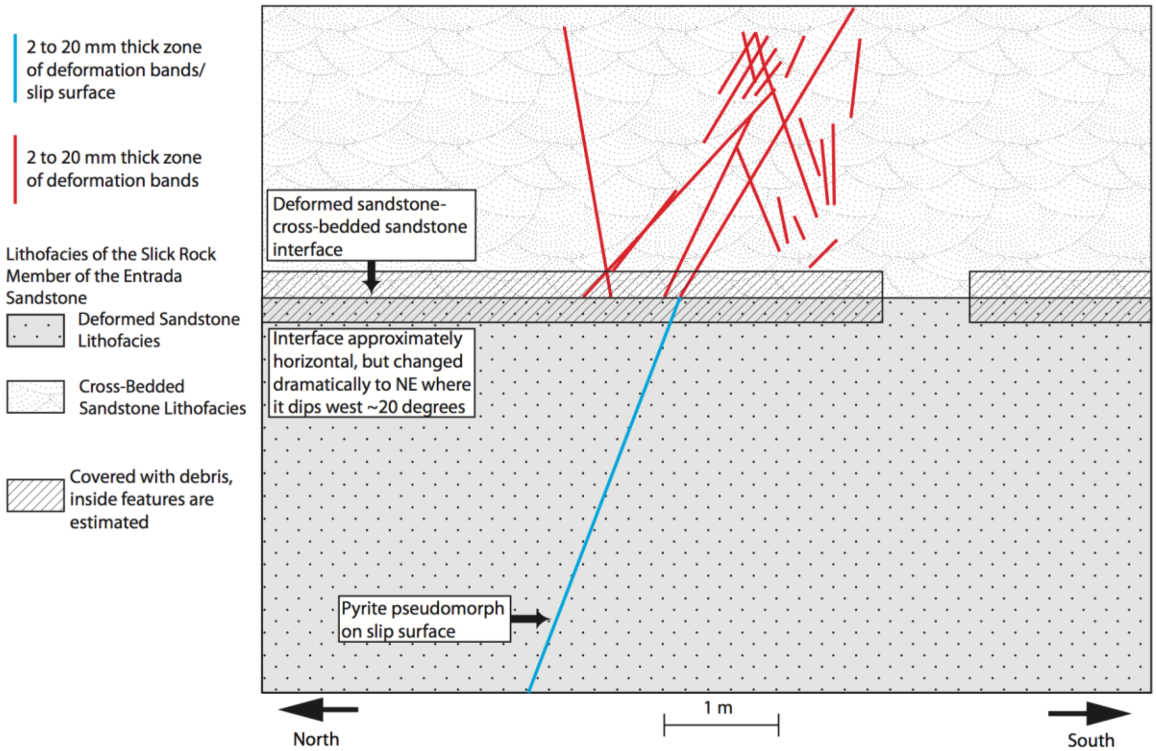

Figure 28. Geologic conceptual model of ISS-4. A faulted zone of deformation bands in the deformed sandstone lithofacies transitions into several zones of deformation bands in the cross-bedded sandstone lithofacies. Pyrite pseudomorphic iron oxide cement is found on the slip surface in the deformed sandstone lithofacies.

Permeability Variations

The permeability of the cross-bedded sandstone and deformed sandstone lithofacies at ISS-4 were assigned values using corrected TinyPerm II field measurements. The permeability of the cross-bedded sandstone lithofacies, the average of six measurements taken at various locations within this lithofacies, is 3,873 mD (Fig. 29). The permeability of the deformed sandstone lithofacies, the average of three measurements taken at various locations within this lithofacies, is 161 mD.

The permeability of the zones of deformation bands at ISS-4 are assigned the same value as those at ISS-1.

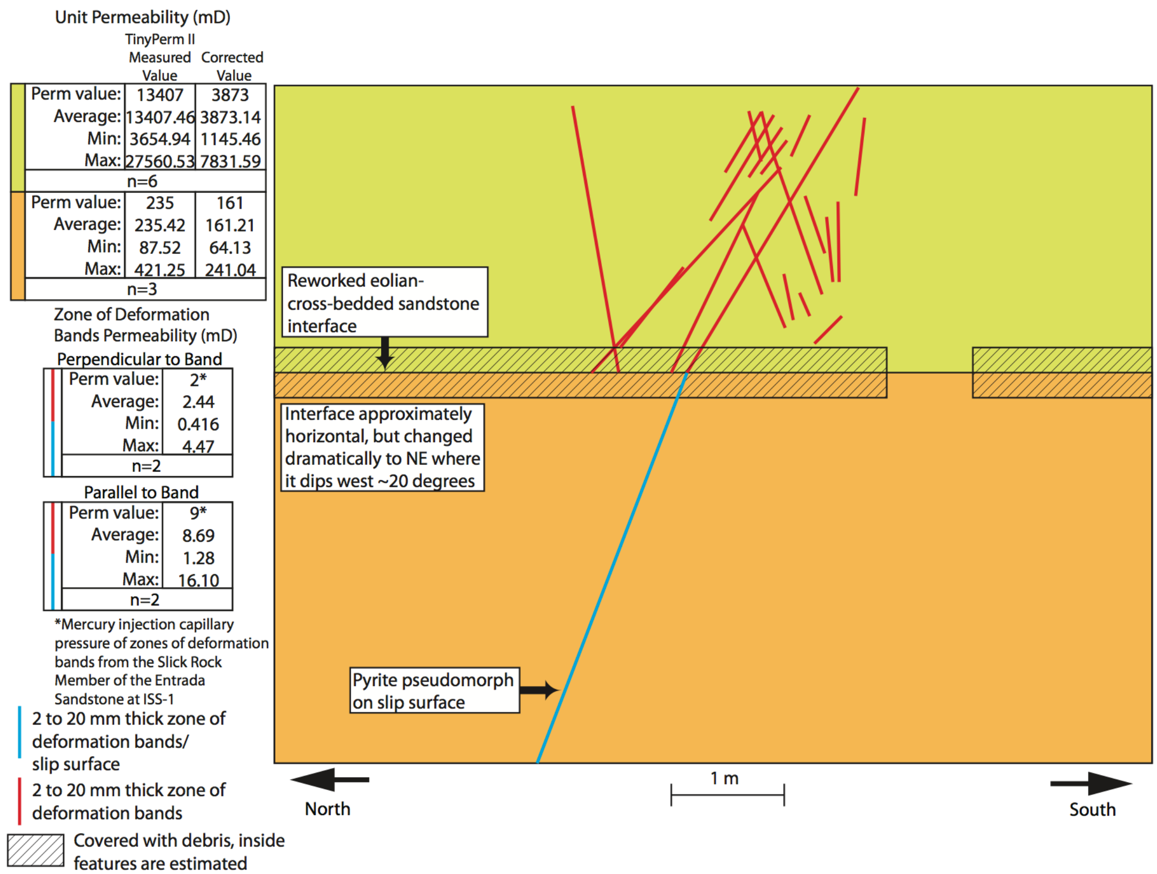

Figure 29. Permeability conceptual model of ISS-4. The color of each lithofacies corresponds to a different permeability, as listed above. Permeability was determined using a combination of TinyPerm II measurements and laboratory permeability measurements.

Iron Wash Study Site #5 (ISS-5)

This site is roughly a 250 m southwest of ISS-1 (12 S 0545868, 4288605, WGS 84 datum). It has includes an exposure of the interface between the Slick Rock Member and Earthy Member of the Entrada Sandstone (Fig. 30abc). This site was chosen because it contains a normal fault that intersects reservoir-caprock interface.

(a)

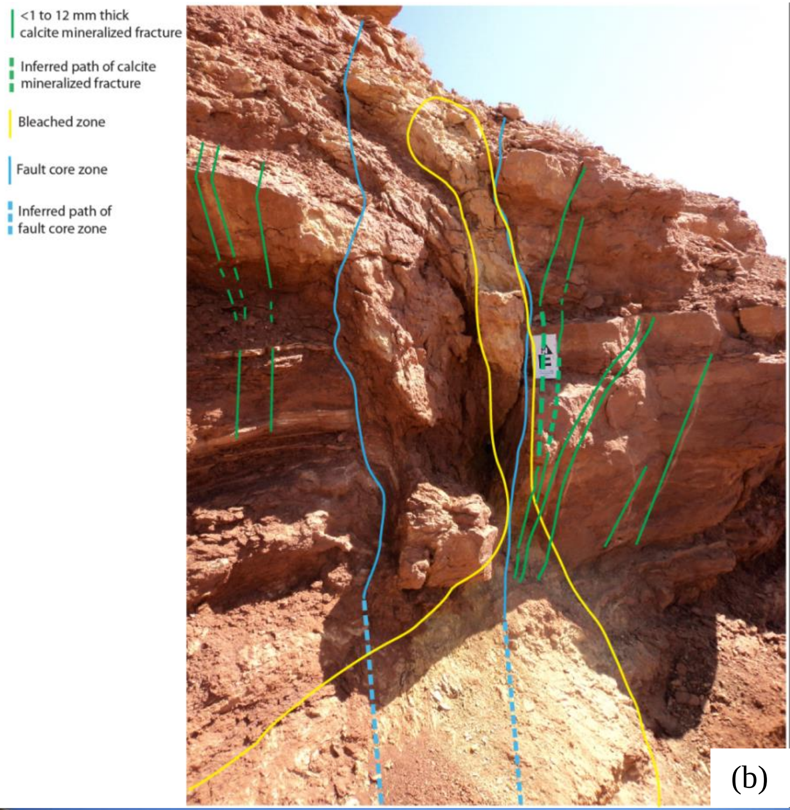

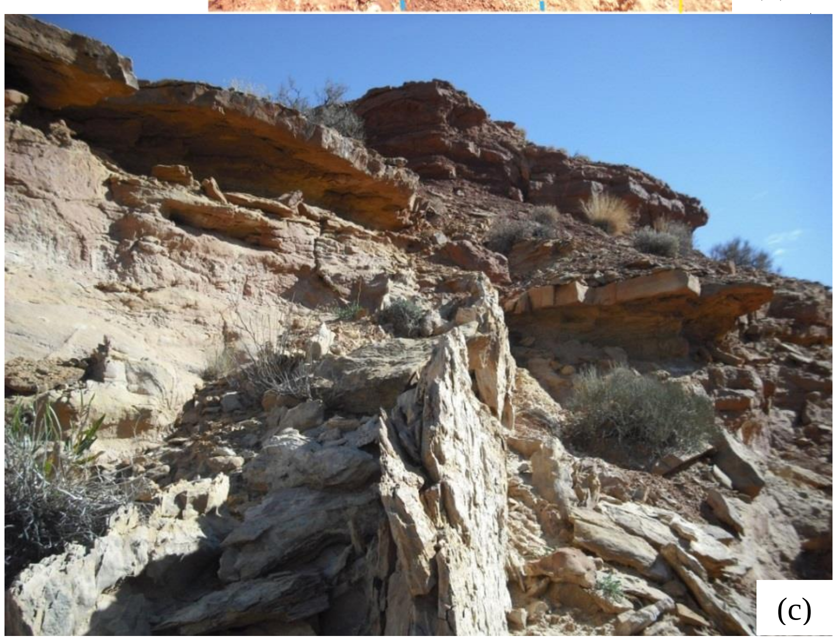

Figure 30. (a) Overview of ISS-5, 6 ft./1.83 m person for scale. The area slightly below the well cemented sandstone layer seen jutting out over the ledge represents reservoir-caprock interface. Below the interface is the Slick Rock Member whereas above is the Earthy Member. A faulted zone of deformation bands in the Slick Rock Member transitions into a set of fractures in the Earthy Member. The fracture network and the base of the Earthy Member are bleached. (b) Enlarged view of fracture network, bleached zone, and fault core zone with annotations, photo card for scale. (c) Enlarged view of the faulted zone of deformation bands.

Interface Structural Features

Structural features of interest at ISS-5 are a faulted zone of deformation bands in the Entrada Sandstone Slick Rock Member transitioning into a set of opening-mode fractures into the Entrada Sandstone Earthy Member (Fig. 31). The main zone of deformation bands is 14 cm thick. Smaller zones of deformation bands are also present at the interface ranging in thickness from 1 to 3 cm. The faulted zone of deformation bands has 1.4 m of offset.

The thickness of the Earthy Member fractures varies from <1 to 12 mm. The fracture network can be tracked for 5 m into the Earthy Member of the Entrada Sandstone before it can no longer be traced due to erosion and cover. The Slick Rock Member and the base of the Earthy Member of the Entrada Sandstone are bleached, with an increased concentration of bleaching in close proximately to the fault core zone. Bleaching is also associated with some of the fractures close to the interface.

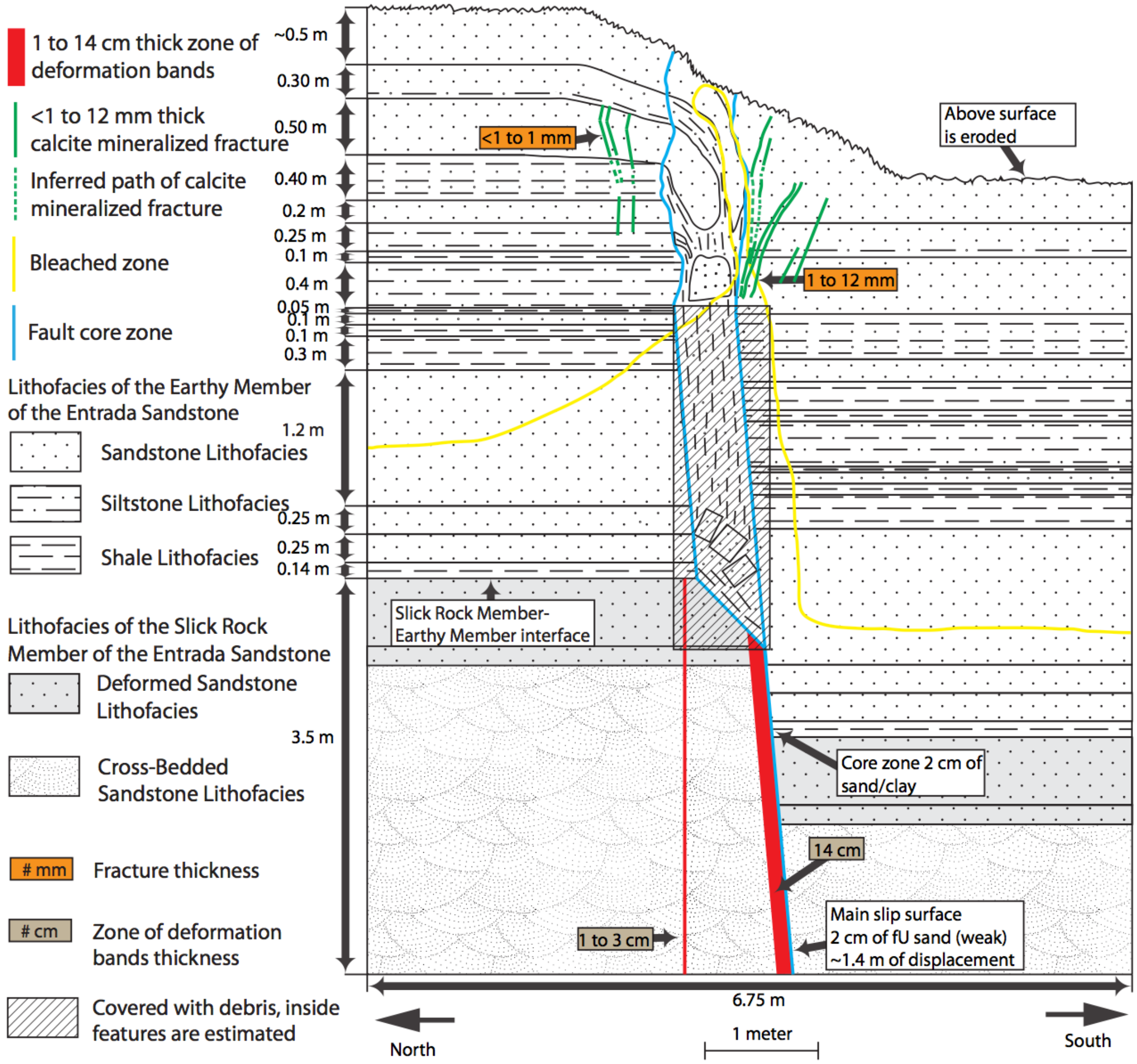

Figure 31. Geologic conceptual model of ISS-5. A faulted zone of deformation bands in the Slick Rock Member transition into a set of fractures in the Earthy Member. Bleaching fluids from the Slick Rock Member used the factures to penetrate into the caprock, bleaching the fracture margins in the process. Fractures penetrate the Earthy Member for 5 m until they can no longer be traced.

Permeability Variations

The permeability of the cross-bedded sandstone and deformed sandstone lithofacies of the Slick Rock Member and the sandstone lithofacies of the Earthy Member at ISS-5 were assigned values using corrected TinyPerm II field measurements. The permeability of the cross-bedded sandstone lithofacies, the average of four measurements taken at various locations within this lithofacies (plus one measurement from the sandstone lithofacies, the reasoning for which is explained below), is 5,231 mD (Fig. 32). The permeability of the deformed sandstone lithofacies, the average of two measurements taken at various locations within this lithofacies, is 1,005 mD. The permeability of the sandstone lithofacies was assigned two different values based on their position. Based on one measurement of the lowermost bed, this bed had a corrected permeability of 4,399 mD. This is several orders of magnitude larger than the other beds from the same lithofacies. In order to avoid misrepresenting the permeability of this bed by grouping it with the sandstone lithofacies, it was instead grouped with similar permeability measurements from the cross-bedded sandstone lithofacies. All other beds from the sandstone lithofacies were assigned the value of 33 mD, a value based on the average of seven measurements taken at various locations within this lithofacies.

The permeabilities of the siltstone and shale lithofacies are assigned the same value as the corresponding lithofacies at ISS-1. The permeability of the zones of deformation bands is also assigned the same value as the zones of deformation bands in ISS-1.

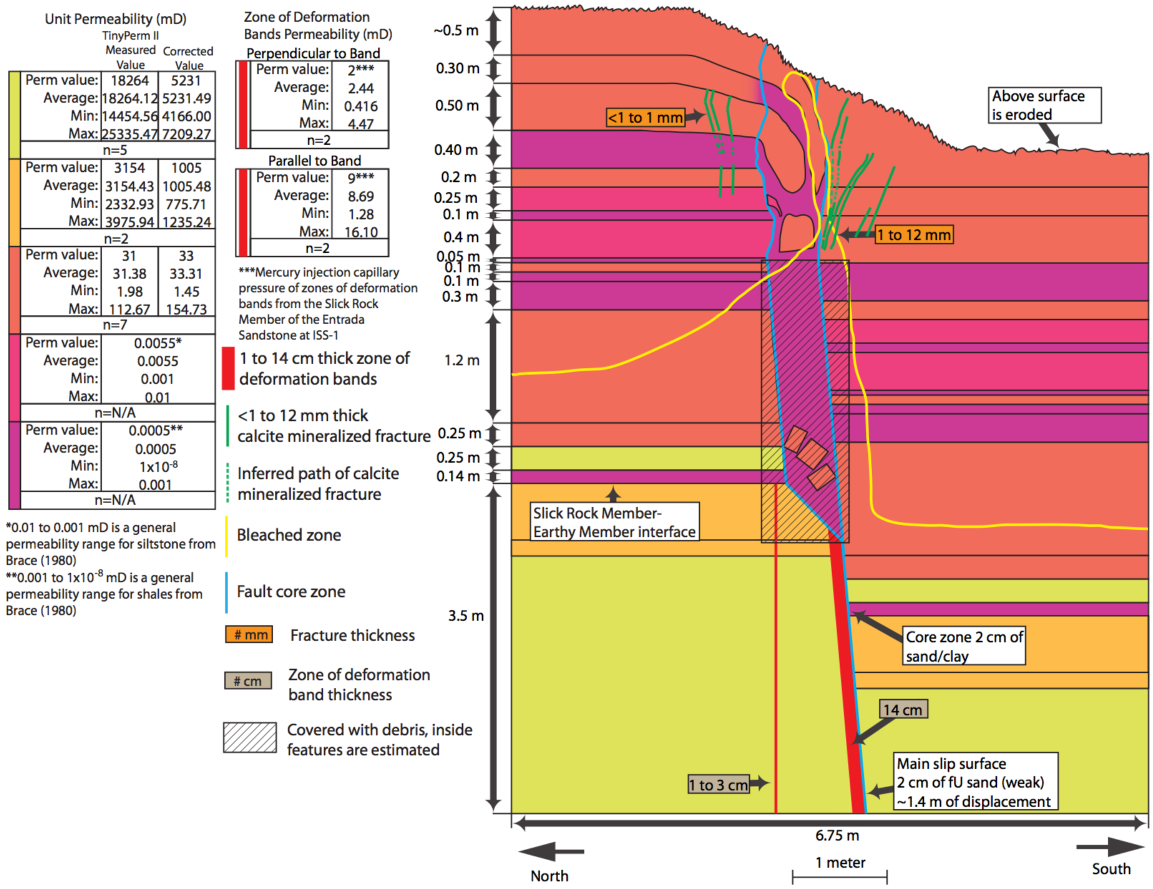

Figure 32. Permeability conceptual model of ISS-5. The color of each lithofacies corresponds to a different permeability, as listed above. Permeability was determined using a combination of TinyPerm II measurements, laboratory permeability measurements, and laboratory permeability measurements from existing authors.

Mineralogy and Texture

The mineralogy and texture of the reservoir and caprock lithologies and structural components were examined in order to: (1) understand controls on porosity and permeability, (2) constrain the hydrologic behavior of the sites when they were present in the subsurface (i.e., evidence of paleoflow), and (3) constrain the subsurface environment in which fluids circulated through open fractures. Only a basic description of the pore- and fracture-filling cements present in each unit is provided in this section, for a more detailed description of the cements see the diagenesis results section.

Navajo Sandstone

Thin sections of Navajo Sandstone displayed the characteristics typical of eolian derived sandstones. Six samples from the Navajo Sandstone were made into thin sections (see APPENDIX C for thin section inventory). Thin-section analysis shows that the framework grains are mainly monocrystalline quartz, with small amounts of polycrystalline quartz, feldspar, and chert (Table 1). The sandstones in this unit classify as either quartzarenite or subarkose (classification of Folk, 1968; Fig. 33a). The sandstones are mostly grain dominated, with lesser amounts of cement, matrix, and porosity (Fig. 33b). However, locally the Navajo Sandstone is heavily cemented with calcite, quartz, and/or iron oxide. An attempt was made to identify the iron oxide using X-ray diffraction (XRD) analysis, however this was not possible because the iron oxide was amorphous (See APPENDIX D for XRD analysis).

Porosity of the Navajo Sandstone is predominately non-fracture intergranular macroporosity (Table 2; Fig. 33c). Small amounts of intragranular macroporosity and microporosity are present in void-rich grains. Additionally, a minor amount of intergranular microporosity is present in cement.

Navajo Sandstone Deformation Bands and Mineralized Fractures

Deformation bands are abundant throughout the Navajo Sandstone. Four thin sections containing deformation bands were obtained from the Navajo Sandstone. All four samples were dominated by compactional shear/cataclastic bands.

The porosity inside the zone of deformation bands is roughly 3 times lower compared to the host rock (Table 1). The main type of porosity inside the deformation bands is non-fracture intergranular macroporosity (Table 2; Fig. 33c). The remaining portion of the porosity is present as intergranular microporosity within the cataclasite.

Mineralized fractures are present in Navajo Sandstone in areas that have undergone jointing. One of the Navajo Sandstone thin sections contains an opening-mode, mineralized fracture. The fracture is mineralized with calcite and iron oxide cement.

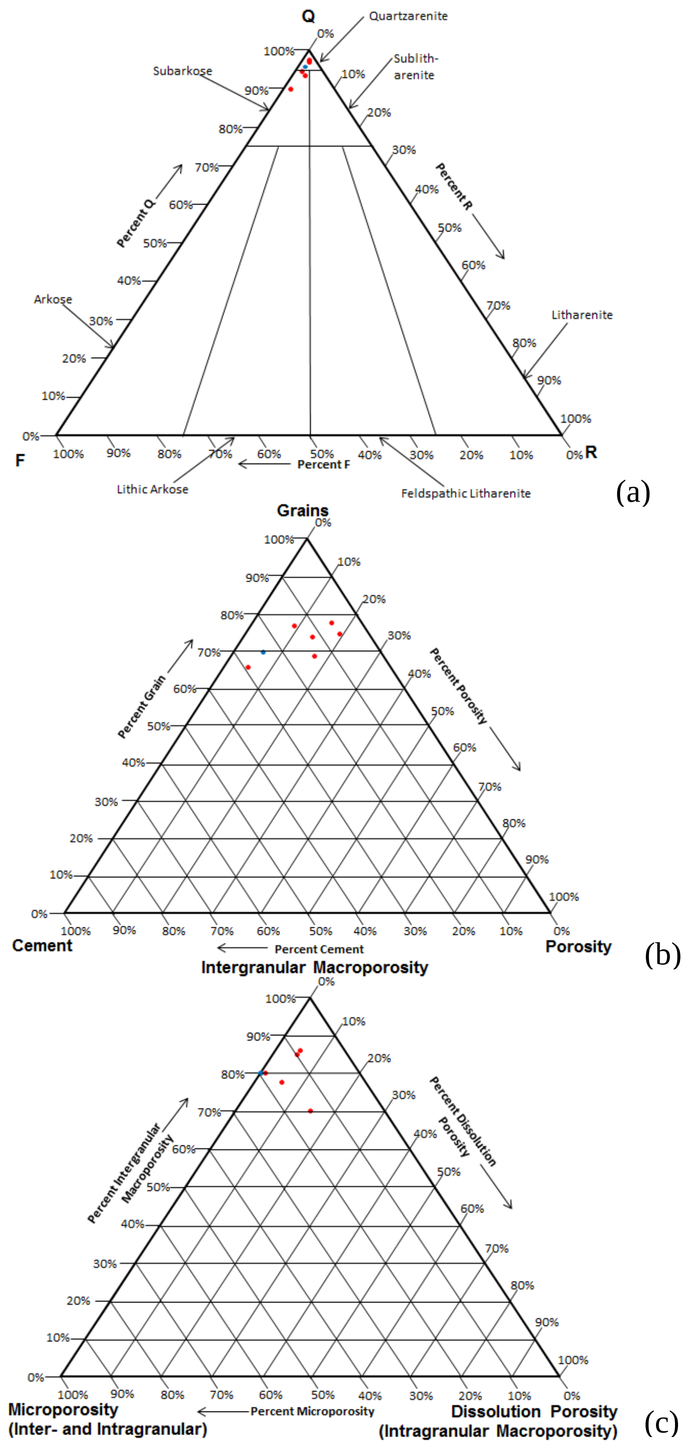

Figure 33. For all ternary diagrams red dots indicate the host rock while blue dots indicate a zone of deformation bands. (a) Diagram showing the quartz-feldspar-lithic fragment abundances of sandstones from the Navajo Sandstone (classification of Folk, 1968). (b) Diagram showing the grain-porosity-cement abundances of sandstones from the Navajo Sandstone. (c) Diagram showing the intergranular macroporosity-dissolution porosity-microporosity abundance of sandstones from the Navajo Sandstone (classification of Pittman, 1979). Fracture porosity is not included.

Table 1. Mineralogy of the Navajo Sandstone.

		Framework Grains					Cement				Porosity	Other		
Thin Section	Facies	Mono-Quartz	Poly-Quartz	Feldspar	Chert	Biotite	Calcite	Quartz	Iron Oxide	Kaol-inite	All Types	Unidentified Grains & Cement	Grain Size	Sort-ing
UM-102211-A	Def.	68%	1%	3%	1%	0%	1%	2%	3%	0%	19%	2%	vfU	m
UM-102211-B	Cross.	68%	3%	1%	1%	0%	3%	2%	7%	0%	14%	1%	vfU	m
UM-102211-C	Cross.	59%	4%	1%	1%	0%	13%	5%	11%	0%	5%	1%	fL	mw
UM-102211-D†	Def.	57%	4%	6%	1%	0%	0%	4%	10%	trace	17%	1%	mL/vfU	p
UM-102211-D† (DB*)	Def.	64%	2%	2%	1%	trace	0%	16%	8%	0%	6%	1%	mL/vfU	p
UM-31312-19†	Def.	63%	8%	3%	2%	0%	trace	3%	3%	trace	16%	2%	mL/vfU	m
UM-31312-20	Def.	70%	4%	2%	trace	0%	2%	4%	8%	0%	9%	1%	fL	m

*DB indicates the analysis is only performed on the zone of deformation bands portion of a sample
†Bimodal grain size distribution

trace indcates less than 0.5%

Def. = Deformed Sandstone Lithofacies
Cross. = Cross-bedded Sandstone Lithofacies

vp = very poorly sorted
vpp = very poorly to poorly sorted
p = poorly sorted
pm = poorly to moderately sorted
m = moderately sorted
mw = moderately to well sorted
w = well sorted
wvw = well to very well sorted
vw = very well sorted

vcU = very coarse upper
vcL = very coarse lower
cU = coarse upper
cL = coarse lower
mU = medium upper
mL = medium lower
fU = fine upper
fL = fine lower
vfU = very fine upper
vfL = very fine lower

Table 2. Porosity of the Navajo Sandstone.

			Porosity							
Thin Section	Facies	Esti-mate	Intergranular Macropropsity Non-fracture	Intergranular Macroporosity Fracture	Intragranular Macroporosity Non-fracture	Intragranular Macroporosity Fracture	Intergranular Microporosity	Intragranular Microporosity	Grain Size	Sort-ing
UM-102211-A	Def.		85%	0%	5%	0%	6%	4%	vfU	m
UM-102211-B	Cross.		80%	0%	1%	0%	16%	3%	vfU	m
UM-102211-C	Cross.	X	70%	10%	5%	0%	10%	5%	fL	mw
UM-102211-D†	Def.		83%	0%	0%	0%	17%	0%	mL/vfU	p
UM-102211-D† (DB*)	Def.	X	80%	0%	0%	0%	20%	0%	mL/vfU	p
UM-31312-19†	Def.		86%	0%	5%	0%	7%	2%	mL/vfU	m
UM-31312-20	Def.	X	70%	0%	15%	0%	10%	5%	fL	m

*DB indicates the analysis is only performed on the zone of deformation bands portion of a sample
†Bimodal grain size distribution

Def. = Deformed Sandstone Lithofacies
Cross. = Cross-bedded Sandstone Lithofacies

vp = very poorly sorted
vpp = very poorly to poorly sorted
p = poorly sorted
pm = poorly to moderately sorted
m = moderately sorted
mw = moderately to well sorted
w = well sorted
wvw = well to very well sorted
vw = very well sorted

vcU = very coarse upper
vcL = very coarse lower
cU = coarse upper
cL = coarse lower
mU = medium upper
mL = medium lower
fU = fine upper
fL = fine lower
vfU = very fine upper
vfL = very fine lower

Co-op Creek Member of the Carmel Formation

Thin sections of Co-op Creek Member varied significantly, with siliciclastic and carbonate lithologies both being present. Fifteen samples from the Co-op Creek Member of the Carmel Formation were made into thin sections. Two of the thin sections are of carbonate rocks, whereas the rest are siliciclastic. The principal framework grain in the clastic samples is monocrystalline quartz, with small amounts of polycrystalline quartz, feldspar, and chert (Table 3). The sandstones and sandy siltstones classify as quartzarenite, sublitharenite, or litharenite (classification of Folk, 1968; Fig. 34a). The sandstones and sandy siltstones are cement and matrix dominated, with small to moderate amounts of sand grains and minor amounts of porosity (Fig. 34b). The carbonate rocks classify as oolitic bivalve grainstones or micritic mudstones (classification of Dunham, 1962). The majority of the Co-op Creek Member samples contain large amounts of matrix and cement. Matrix is mainly found in the siliciclastic rocks of the Co-op Creek Member. The types of cement present include calcite, quartz, dolomite, and iron oxide. Iron oxide was identified as hematite using X-ray diffraction analysis.

Porosity of the siliciclastic rocks of the Co-op Creek Member is predominately intergranular microporosity (Table 4; Fig. 34c). Fracture induced macroporosity is locally important. Small to moderate amounts of intragranular macroporosity and microporosity are present in void-rich grains.

Porosity in the carbonate rocks of the Co-op Creek Member is either in fractures or intercrystalline (porosity classification of Choquette and Pray, 1970; Table 5).

Mineralized Fractures in the Co-op Creek Member

Mineralized fractures are common at the base of the Co-op Creek Member. Analysis of six thin sections of mineralized fractures from the Co-op Creek Member shows that both opening-mode and sliding-mode fractures are individually present. Fractures are filled only with calcite cement.

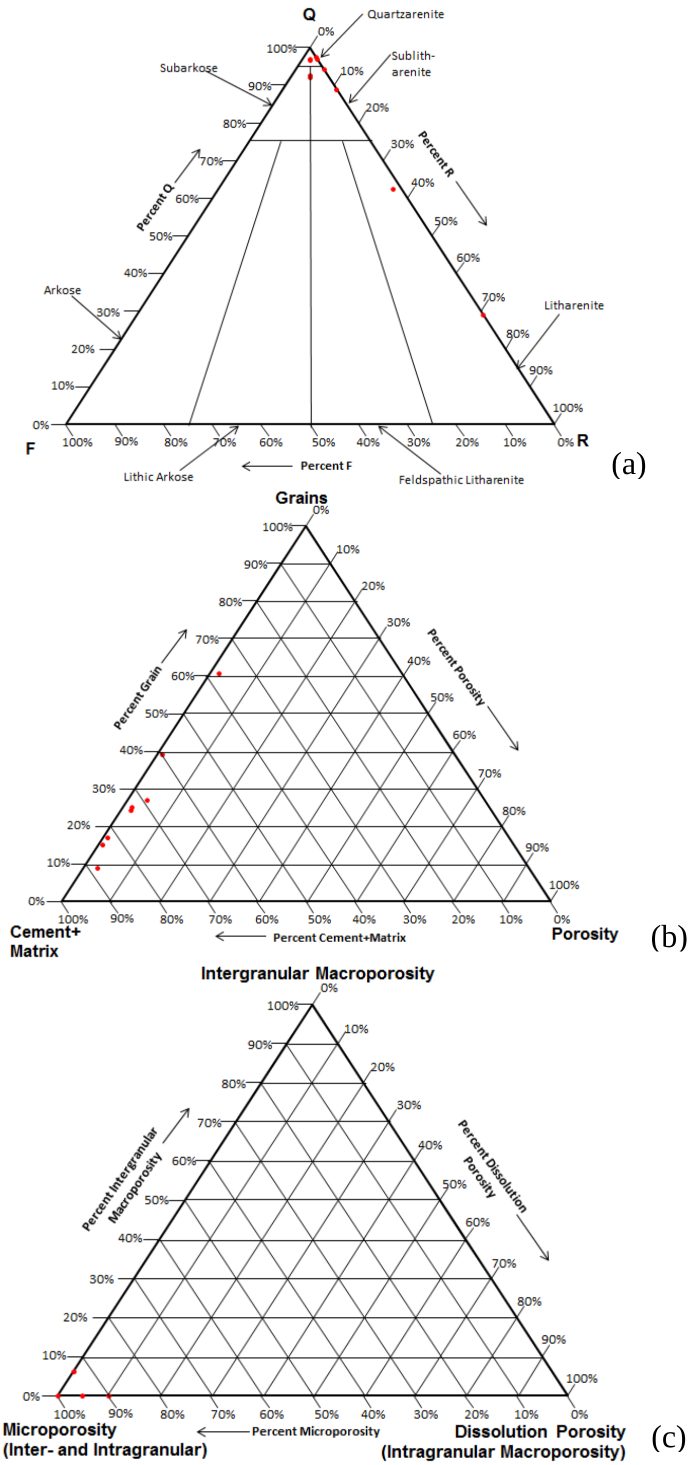

Figure 34. (a) Diagram showing the quartz-feldspar-lithic fragment abundances of sandstones and sandy siltstones from the Co-op Creek Member (classification of Folk, 1968). (b) Diagram showing the grain-porosity-cement abundances of sandstones sand sandy siltstones from the Co-op Creek Member. (c) Diagram showing the intergranular macroporosity-dissolution porosity-microporosity abundance of sandstones and sandy siltstones from the Co-op Creek Member (classification of Pittman, 1979). Fracture porosity is not included.

Table 3. Mineralogy of the Co-op Creek Member of the Carmel Formation.

		Framework Grains						Matrix	Cement				Porosity	Other		
Thin Section	Facies	Mono-Quartz	Poly-Quartz	Feldspar	Chert	Biotite	Shale Intraclast	Matrix*	Calcite	Quartz	Iron Oxide	Dolo-mite	All Types	Unidentified Grains & Cement	Grain Size	Sort-ing
UM-102211-E	Silt.	36%	1%	0%	1%	0%	0%	37%	11%	trace	10%	trace	1%	3%	silt	w
UM-102211-F	Sand.	33%	2%	1%	0%	trace	20%	10%	22%	2%	10%	trace	0%	trace	vfL	w
UM-102311-A	Sand.	23%	3%	1%	trace	0%	0%	14%	49%	2%	4%	3%	0%	1%	vfL	w
UM-102311-C	Sand.	59%	5%	1%	1%	0%	0%	0%	25%	6%	3%	0%	trace	trace	fL	w
UM-102311-D	Silt.	15%	1%	trace	1%	0%	0%	45%	24%	1%	11%	1%	1%	trace	silt	m
UM-102311-E	Silt.	10%	1%	trace	trace	0%	27%	47%	5%	0%	9%	1%	0%	0%	silt	p
UM-102311-F	Silt.	29%	1%	0%	1%	trace	0%	17%	35%	2%	4%	10%	0%	1%	silt	w
UM-102311-G	Oo.	N/A	N/A	N/A	N/A	N/A	N/A	N/A	N/A	N/A	N/A	N/A	N/A	N/A	N/A	N/A
UM-102311-H	Silt.	21%	2%	1%	1%	0%	0%	37%	31%	0%	1%	4%	2%	trace	silt	w
UM-102311-I	Silt.	22%	3%	1%	1%	0%	0%	11%	41%	2%	1%	14%	4%	0%	silt	w
UM-102311-J	Mic.	N/A	N/A	N/A	N/A	N/A	N/A	N/A	N/A	N/A	N/A	N/A	N/A	N/A	N/A	N/A
UM-102311-K	Silt.	13%	2%	trace	0%	0%	0%	41%	32%	1%	6%	4%	1%	trace	silt	m
UM-31312-16	Sand.	53%	5%	1%	1%	0%	0%	3%	19%	6%	9%	0%	2%	1%	fL	mw
UM-31312-17	Silt.	22%	2%	0%	0%	0%	0%	17%	16%	4%	3%	33%	2%	1%	silt	p
UM-31312-18	Silt.	7%	1%	trace	1%	0%	0%	34%	26%	1%	5%	22%	3%	trace	silt	p

*Likely once a clay matrix, it has now been replaced by a mixture of hematite and calcite cement

trace indcates less than 0.5%

Silt. = Siltstone Lithofacies
Sand. = Sandstone Lithofacies
Oo. = Oolitic Bivalve Grainstone Lithofacies
Mic. = Micritic Mudstone Lithofacies

vp = very poorly sorted
vpp = very poorly to poorly sorted
p = poorly sorted
pm = poorly to moderately sorted
m = moderately sorted
mw = moderately to well sorted
w = well sorted
wvw = well to very well sorted
vw = very well sorted

vcU = very coarse upper
vcL = very coarse lower
cU = coarse upper
cL = coarse lower
mU = medium upper
mL = medium lower
fU = fine upper
fL = fine lower
vfU = very fine upper
vfL = very fine lower

Table 4. Porosity of the siliciclastic rocks of the Co-op Creek Member of the Carmel Formation.

			Porosity							
Thin Section	Facies	Esti-mate	Intergranular Macropropsity Non-fracture	Intergranular Macroporosity Fracture	Intragranular Macroporosity Non-fracture	Intragranular Macroporosity Fracture	Intergranular Microporosity	Intragranular Microporosity	Grain Size	Sort-ing
UM-102211-E	Silt.	X	0%	0%	5%	0%	20%	75%	silt	w
UM-102211-F	Sand.	X	0%	55%	0%	35%	5%	5%	vfL	w
UM-102311-A	Sand.	X	0%	90%	0%	0%	5%	5%	vfL	w
UM-102311-C	Sand.	X	0%	0%	10%	0%	45%	45%	fL	w
UM-102311-D	Silt.	X	0%	95%	0%	0%	5%	0%	silt	m
UM-102311-E	Silt.	X	0%	0%	0%	0%	90%	10%	silt	p
UM-102311-F	Silt.	X	0%	0%	0%	0%	90%	10%	silt	w
UM-102311-H	Silt.	X	0%	20%	0%	0%	80%	0%	silt	w
UM-102311-I	Silt.	X	0%	15%	0%	0%	85%	0%	silt	w
UM-102311-K	Silt.	X	0%	70%	0%	0%	25%	5%	silt	m
UM-31312-16	Sand.	X	0%	30%	0%	0%	65%	5%	fL	mw
UM-31312-17	Silt.	X	5%	20%	0%	0%	75%	0%	silt	p
UM-31312-18	Silt.	X	0%	10%	0%	0%	90%	0%	silt	p

Silt. = Siltstone Lithofacies
Sand. = Sandstone Lithofacies

vp = very poorly sorted
vpp = very poorly to poorly sorted
p = poorly sorted
pm = poorly to moderately sorted
m = moderately sorted
mw = moderately to well sorted
w = well sorted
wvw = well to very well sorted
vw = very well sorted

vcU = very coarse upper
vcL = very coarse lower
cU = coarse upper
cL = coarse lower
mU = medium upper
mL = medium lower
fU = fine upper
fL = fine lower
vfU = very fine upper
vfL = very fine lower

Table 5. Porosity of the carbonate rocks of the Co-op Creek Member of the Carmel Formation.

			Porosity															
			Fabric Selective							Not Fabric Selective				Fabric Selective or Not				
Thin Section	Facies	Esti-mate	Inter-particle	Intra-particle	Inter-crystal	Moldic	Fene-stral	Shel-ter	Growth Framework	Frac-ture	Chan-nel	Vug	Cavern	Breccia	Boring	Burrow	Shrink-age
UM-102311-G	Oo.	X	0%	0%	0%	0%	0%	0%	0%	100%	0%	0%	0%	0%	0%	0%	0%
UM-102311-J	Mic.	X	0%	0%	90%	0%	0%	0%	0%	10%	0%	0%	0%	0%	0%	0%	0%

white background indicates a 100 porosity point count
gray background indicates a visual porosity estimation

Oo. = Oolitic Bivalve Grainstone Lithofacies
Mic. = Micritic Mudstone Lithofacies

Winsor Member of the Carmel Formation

Thin sections of the Winsor Member are sandstones with large amounts of matrix and cement. Ten samples from the Winsor Member of the Carmel Formation were made into thin sections. Framework grains mainly consist of monocrystalline quartz, with lesser amounts of polycrystalline quartz, feldspar, and chert (Table 6). Most of the sandstones are quartzarenite, with minor amounts of subarkose and sublitharenite (classification of Folk, 1968; Fig. 35a). Very little porosity is present in this unit, as sandstones are primarily made up of grains, cement, and matrix (Fig. 35b). The majority of the Winsor Member contains large amounts of matrix and cement. The types of cement present include calcite, quartz, dolomite, and iron oxide.

Porosity of the Winsor Member is predominately intergranular microporosity (Table 7; Fig. 35c). In some locations fracture macroporosity is present in large amounts. Small to moderate amounts of intragranular macroporosity and microporosity are present in void-filled grains.

Mineralized Fractures in the Winsor Member

Mineralized fractures are common in portions of the Winsor Member that have undergone faulting. Analysis of three thin sections of mineralized fractures from the

Winsor Member shows that both opening-mode and sliding-mode fractures are individually present. Fractures are filled with calcite, barite, iron oxide, and kaolinite.

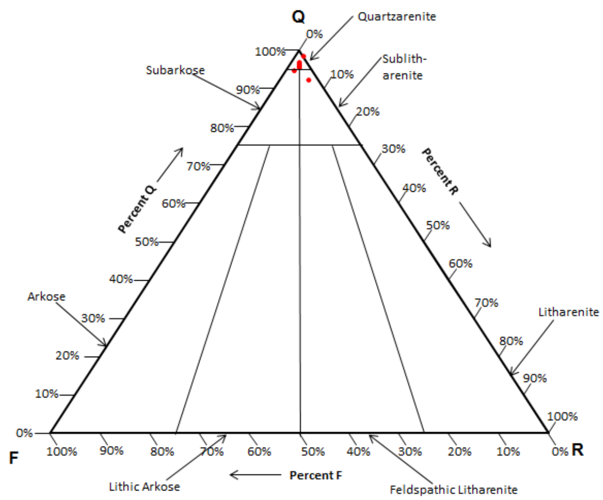

(a)

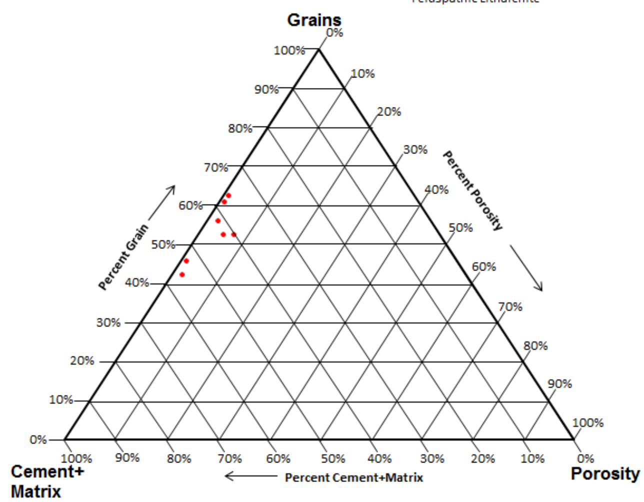

(b)

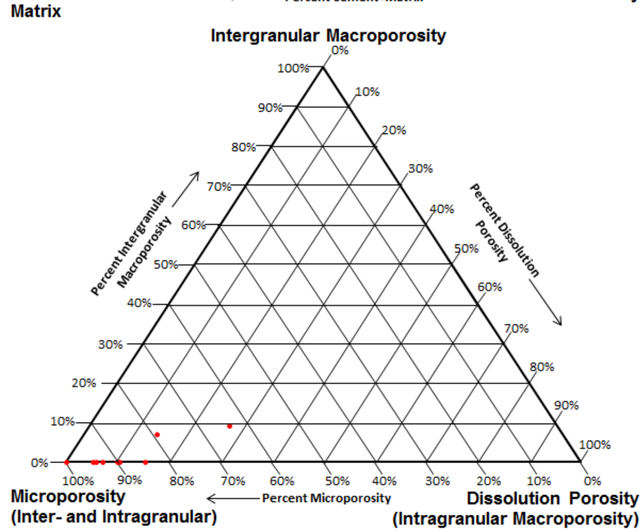

(c)

Figure 35. (a) Diagram showing the quartz-feldspar-lithic fragment abundances of sandstones from the Winsor Member (classification of Folk, 1968). (b) Diagram showing the grain-porosity-cement abundances of sandstones from the Winsor Member. (c) Diagram showing the intergranular macroporosity-dissolution porosity-microporosity abundance of sandstones from the Winsor Member (classification of Pittman, 1979). Fracture porosity is not included.

Table 6. Mineralogy of the Winsor Member of the Carmel Formation.

		Framework Grains						Matrix	Cement				Porosity	Other		
Thin Section	Facies	Mono-Quartz	Poly-Quartz	Feldspar	Chert	Biotite	Shale Intraclast	Matrix*	Calcite	Quartz	Iron Oxide	Dolo-mite	All Types	Unidentified Grains & Cement	Grain Size	Sort-ing
IW81111-3a	Sand.	40%	1%	1%	trace	0%	0%	33%	20%	2%	0%	0%	2%	1%	vfU	m
IW81111-4a	Sand.	48%	2%	1%	1%	0%	0%	0%	34%	1%	5%	0%	7%	1%	vfL	w
IW81111-5	Sand.	N/A	N/A	N/A	N/A	N/A	N/A	N/A	N/A	N/A	N/A	N/A	N/A	N/A	vfU	w
IW81111-6	Sand.	56%	2%	trace	1%	0%	0%	6%	30%	1%	0%	0%	1%	3%	vfU	w
IW81111-7	Sand.	46%	2%	1%	1%	trace	2%	14%	26%	2%	0%	0%	5%	1%	vfL	w
IW81111-11	Sand.	50%	2%	2%	1%	0%	trace	15%	17%	1%	8%	trace	2%	2%	vfL	w
IW81111-12	Sand.	43%	3%	1%	1%	0%	0%	16%	18%	1%	0%	0%	trace	17%	vfL	m
IW81111-13	Sand.	41%	1%	1%	1%	0%	0%	19%	26%	trace	6%	0%	1%	4%	vfL	w
IW81111-14	Sand.	58%	2%	1%	1%	0%	0%	4%	30%	2%	0%	0%	1%	1%	fL	P
IW81111-15	Sand.	41%	3%	1%	1%	0%	0%	15%	34%	1%	3%	0%	trace	1%	vfL	m

*Likely once a clay matrix, it has now been replaced by a mixture of hematite and calcite cement

trace indcates less than 0.5%

Sand. = Sandstone Lithofacies

vp = very poorly sorted
vpp = very poorly to poorly sorted
p = poorly sorted
pm = poorly to moderately sorted
m = moderately sorted
mw = moderately to well sorted
w = well sorted
wvw = well to very well sorted
vw = very well sorted

vcU = very coarse upper
vcL = very coarse lower
cU = coarse upper
cL = coarse lower
mU = medium upper
mL = medium lower
fU = fine upper
fL = fine lower
vfU = very fine upper
vfL = very fine lower

Table 7. Porosity of the Winsor Member of the Carmel Formation.

			Porosity							
Thin Section	Facies	Esti-mate	Intergranular Macropropsity Non-fracture	Intergranular Macroporosity Fracture	Intragranular Macroporosity Non-fracture	Intragranular Macroporosity Fracture	Intergranular Microporosity	Intragranular Microporosity	Grain Size	Sort-ing
IW81111-3a	Sand.	X	0%	30%	5%	0%	55%	10%	vfU	m
IW81111-4a	Sand.	X	0%	15%	0%	0%	80%	5%	vfL	w
IW81111-5	Sand.	X	0%	0%	0%	80%	20%	0%	vfU	w
IW81111-6	Sand.	X	5%	45%	15%	0%	20%	15%	vfU	w
IW81111-7	Sand.	X	0%	25%	10%	10%	40%	15%	vfL	w
IW81111-11	Sand.	X	5%	30%	10%	0%	35%	20%	vfL	w
IW81111-12	Sand.	X	0%	5%	10%	0%	50%	35%	vfL	m
IW81111-13	Sand.	X	0%	0%	10%	0%	40%	50%	vfL	w
IW81111-14	Sand.	X	0%	10%	5%	5%	60%	20%	fL	P
IW81111-15	Sand.	X	0%	5%	5%	0%	70%	20%	vfL	m

Sand. = Sandstone Lithofacies

vp = very poorly sorted
vpp = very poorly to poorly sorted
p = poorly sorted
pm = poorly to moderately sorted
m = moderately sorted
mw = moderately to well sorted
w = well sorted
wvw = well to very well sorted
vw = very well sorted

vcU = very coarse upper
vcL = very coarse lower
cU = coarse upper
cL = coarse lower
mU = medium upper
mL = medium lower
fU = fine upper
fL = fine lower
vfU = very fine upper
vfL = very fine lower

Slick Rock Member of the Entrada Sandstone

Thin sections of the Slick Rock Member display characteristics typical of eolian derived sandstones. Thirty-one samples from the Slick Rock Member of the Entrada Sandstone were made into thin sections. Thin section analysis shows that the framework grains are mainly monocrystalline quartz, with small amounts of polycrystalline quartz, feldspar, and chert (Table 8). The sandstones in this unit are mainly quartzarenite, although subarkose and sublitharentite sandstones are also present (classification of Folk, 1968; Fig. 36a). The sandstones are mostly grain dominated, with lesser amounts of cement, matrix, and porosity (Fig. 36b). However, locally the Slick Rock Member is heavily cemented with calcite, quartz, goethite, kaolinite, and/or dolomite. Goethite was identified using X-ray diffraction analysis.

Porosity of the Slick Rock Member is predominately non-fracture intergranular macroporosity (Table 9; Fig, 36c). Small amounts of intragranular macroporosity and microporosity are present in void-rich grains. Additionally, minor to moderate amounts intergranular microporosity is present in cement.

Slick Rock Member Deformation Bands and Mineralized Fractures

Deformation bands are abundant throughout the Slick Rock Member. Fourteen thin sections containing deformation bands were obtained from the Slick Rock Member. All fourteen samples were dominated by compactional shear/cataclastic bands.

The porosity inside the deformation bands is 4-5 times lower compared to the host rock (Table 8). The main type of porosity inside the zones of deformation bands is non-fracture intergranular macroporosity (Table 9; Fig. 36c). The remaining portion of the porosity is present as fracture intergranular macroporosity and intergranular microporosity. The microporosity is found within the cataclasite.

Mineralized fractures are present throughout Slick Rock Member. Three of the Slick Rock Member thin sections contain opening-mode mineralized fractures. The fractures are mineralized with pyrite and goethite cement. The goethite was identified using X-ray diffraction analysis.

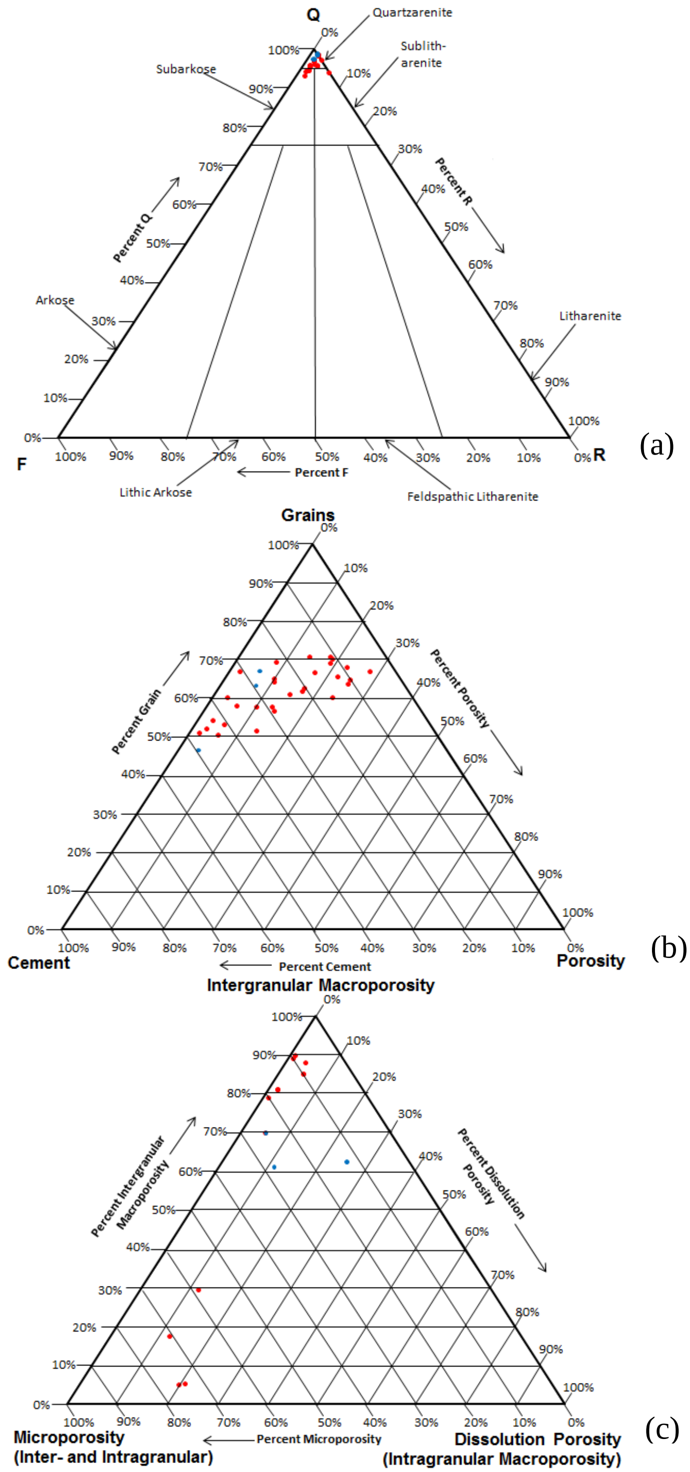

Figure 36. For all ternary diagrams red dots indicate the host rock while blue dots indicate a zone of deformation bands. (a) Diagram showing the quartz-feldspar-lithic fragment abundances of sandstones from the Slick Rock Member (classification of Folk, 1968). (b) Diagram showing the grain-porosity-cement abundances of sandstones from the Slick Rock Member. (c) Diagram showing the intergranular macroporosity-dissolution porosity-microporosity abundance of sandstones from the Slick Rock Member (classification of Pittman, 1979). Fracture porosity is not included.

Table 8. Mineralogy of the Slick Rock Member of the Entrada Sandstone.

		Framework Grains					Cement					Porosity	Other		
Thin Section	Facies	Mono-Quartz	Poly-Quartz	Feldspar	Chert	Biotite	Calcite	Quartz	Iron Oxide	Kaol-inite	Dolo-mite	All Types	Unidentified Grains & Cement	Grain Size	Sort-ing
IW80811-1psm	N/A	57%	3%	1%	0%	0%	0%	4%	17%	0%	0%	17%	1%	mL	w
IW8911-1	Cross.	62%	4%	1%	2%	0%	3%	1%	6%	1%	1%	19%	trace	fL	w
IW8911-3	Cross.	59%	3%	1%	1%	0%	1%	6%	2%	1%	0%	25%	1%	fL	w
IW8911-3 (DB*)	Cross.	43%	2%	1%	trace	0%	1%	43%	5%	0%	0%	4%	1%	fL	w
IW8911-5	Def.	59%	2%	1%	1%	0%	4%	3%	4%	0%	trace	25%	1%	fU	w
IW8911-6	Def.	62%	4%	1%	trace	0%	2%	trace	2%	1%	0%	28%	trace	mL	mw
IW81011-3	N/A	54%	2%	1%	trace	0%	0%	3%	26%	0%	0%	13%	1%	fL	w
IW81011-4	N/A	59%	4%	1%	1%	0%	0%	4%	21%	0%	0%	10%	trace	mL	w
IW81011-5	N/A	61%	1%	trace	4%	0%	1%	4%	11%	0%	0%	17%	1%	mU	mw
IW81011-6	Cross.	57%	3%	trace	1%	0%	0%	1%	23%	trace	0%	15%	trace	mL	m
IW81111-1 (DB)	N/A	59%	2%	1%	trace	0%	1%	28%	trace	0%	0%	7%	2%	fL	mw
IW81111-2	N/A	47%	2%	1%	1%	0%	0%	trace	47%	0%	0%	2%	trace	fU	w
IW81111-3b	Cross.	64%	2%	trace	2%	0%	5%	1%	3%	0%	0%	23%	trace	fU	m
IW81111-4b†	Cross.	62%	5%	2%	1%	0%	7%	3%	1%	0%	0%	18%	1%	mL/vfL	m
IW81111-8	Def.	49%	1%	2%	1%	0%	29%	3%	7%	0%	3%	3%	2%	vfL	w
IW81111-9	Def.	56%	2%	1%	trace	0%	19%	7%	9%	0%	1%	3%	2%	vfL	w
IW81111-10	Cross.	62%	5%	2%	1%	0%	7%	2%	5%	1%	0%	14%	1%	vfU	w
IW81211-1	Def.	62%	2%	3%	1%	0%	12%	5%	5%	0%	trace	8%	2%	fL	mw
IW81211-2	Cross.	60%	4%	1%	2%	0%	27%	2%	trace	0%	2%	2%	trace	fU	vw
IW81211-3	Def.	57%	2%	3%	trace	0%	14%	3%	1%	2%	0%	17%	1%	vfU	w
IW81211-4	Cross.	63%	3%	3%	1%	0%	7%	2%	1%	1%	0%	19%	trace	fU	m
IW81311-1	Cross.	N/A	N/A	N/A	N/A	0%	N/A	N/A	N/A	N/A	N/A	N/A	N/A	fU	w
IW81311-2	Def.	58%	2%	2%	1%	0%	18%	2%	4%	1%	0%	10%	2%	fL	m
IW81311-3	Cross.	55%	4%	trace	1%	0%	1%	1%	14%	0%	trace	24%	0%	fU	w
IW81311-3 (DB)	Cross.	64%	1%	1%	1%	0%	1%	26%	trace	0%	0%	6%	trace	fU	w
IW81311-4	Def.	50%	3%	3%	1%	trace	19%	4%	5%	4%	trace	10%	1%	vfU	pm
IW-Float	N/A	50%	3%	2%	1%	0%	0%	trace	29%	0%	0%	14%	1%	mL	w
SPR-1	N/A	49%	1%	1%	0%	0%	0%	14%	21%	0%	0%	13%	1%	fL	mw
SPR-2	N/A	59%	5%	1%	trace	0%	2%	6%	4%	0%	0%	22%	1%	fU	vw
SPR-3a	N/A	54%	3%	0%	1%	0%	0%	0%	36%	0%	0%	6%	0%	mL	w
SPR-3b	N/A	50%	2%	trace	1%	0%	0%	1%	40%	0%	0%	6%	trace	mL	w
WP52 float	N/A	48%	1%	1%	trace	0%	0%	11%	32%	0%	0%	6%	1%	mL	m
WP55 float	N/A	50%	1%	1%	0%	0%	1%	4%	40%	0%	0%	3%	trace	fU	w

*DB indicates the analysis is only performed on the zone of deformation bands portion of a sample

†Bimodal grain size distribution

trace indcates less than 0.5%

Def. = Deformed Sandstone Lithofacies

Cross. = Cross-bedded Sandstone Lithofacies

vp = very poorly sorted
vpp = very poorly to poorly sorted
p = poorly sorted
pm = poorly to moderately sorted
m = moderately sorted
mw = moderately to well sorted
w = well sorted
wvw = well to very well sorted
vw = very well sorted

vcU = very coarse upper
vcL = very coarse lower
cU = coarse upper
cL = coarse lower
mU = medium upper
mL = medium lower
fU = fine upper
fL = fine lower
vfU = very fine upper
vfL = very fine lower

Table 9. Porosity of the Slick Rock Member of the Entrada Sandstone.

			Porosity							
Thin Section	Facies	Esti-mate	Intergranular Macropropsity Non-fracture	Intergranular Macroporosity Fracture	Intragranular Macroporosity Non-fracture	Intragranular Macroporosity Fracture	Intergranular Microporosity	Intragranular Microporosity	Grain Size	Sort-ing
IW80811-1psm	N/A		90%	0%	1%	0%	9%	0%	mL	w
IW8911-1	Cross.		81%	0%	2%	0%	12%	5%	fL	w
IW8911-3	Cross.		89%	0%	1%	0%	7%	3%	fL	w
IW8911-3 (DB*)	Cross.	X	70%	0%	5%	0%	20%	5%	fL	w
IW8911-5	Def.		86%	0%	0%	0%	11%	3%	fU	w
IW8911-6	Def.		81%	0%	2%	0%	15%	2%	mL	mw
IW81011-3	N/A		80%	0%	0%	0%	17%	3%	fL	w
IW81011-4	N/A		80%	2%	0%	0%	14%	4%	mL	w
IW81011-5	N/A		92%	0%	0%	0%	7%	1%	mU	mw
IW81011-6	Cross.		81%	0%	2%	0%	15%	2%	mL	m
IW81111-1 (DB)	N/A	X	50%	20%	20%	0%	5%	5%	fL	mw
IW81111-2	N/A	X	80%	5%	0%	0%	10%	5%	fU	w
IW81111-3b	Cross.		88%	0%	4%	0%	6%	2%	fU	m
IW81111-4b†	Cross.		90%	0%	0%	0%	9%	1%	mL/vfL	m
IW81111-8	Def.	X	5%	5%	20%	0%	55%	15%	vfL	w
IW81111-9	Def.	X	5%	0%	20%	0%	60%	15%	vfL	w
IW81111-10	Cross.		79%	0%	1%	0%	15%	5%	vfU	w
IW81211-1	Def.	X	70%	0%	5%	0%	20%	5%	fL	mw
IW81211-2	Cross.	X	85%	0%	5%	0%	5%	5%	fU	vw
IW81211-3	Def.		82%	0%	0%	0%	14%	4%	vfU	w
IW81211-4	Cross.		90%	0%	0%	0%	7%	3%	fU	m
IW81311-1	Cross.	X	85%	0%	5%	0%	5%	5%	fU	w
IW81311-2	Def.	X	25%	15%	10%	0%	40%	10%	fL	m
IW81311-3	Cross.		88%	0%	0%	0%	11%	1%	fU	w
IW81311-3 (DB)	Cross.	X	55%	5%	10%	5%	15%	10%	fU	w
IW81311-4	Def.	X	15%	15%	10%	0%	50%	10%	vfU	pm
IW-Float	N/A		90%	0%	0%	0%	9%	1%	mL	w
SPR-1	N/A		59%	11%	0%	0%	25%	5%	fL	mw
SPR-2	N/A		95%	0%	0%	0%	4%	1%	fU	vw
SPR-3a	N/A	X	90%	0%	0%	0%	10%	0%	mL	w
SPR-3b	N/A	X	90%	0%	0%	0%	10%	0%	mL	w
WP52 float	N/A	X	45%	40%	0%	0%	15%	0%	mL	m
WP55 float	N/A	X	50%	40%	0%	0%	10%	0%	fU	w

*DB indicates the analysis is only performed on the zone of deformation bands portion of a sample
†Bimodal grain size distribution

Def. = Deformed Sandstone Lithofacies
Cross. = Cross-bedded Sandstone Lithofacies

vp = very poorly sorted
vpp = very poorly to poorly sorted
p = poorly sorted
pm = poorly to moderately sorted
m = moderately sorted
mw = moderately to well sorted
w = well sorted
wvw = well to very well sorted
vw = very well sorted

vcU = very coarse upper
vcL = very coarse lower
cU = coarse upper
cL = coarse lower
mU = medium upper
mL = medium lower
fU = fine upper
fL = fine lower
vfU = very fine upper
vfL = very fine lower

Earthy Member of the Entrada Sandstone

Thin sections of the Earthy Member are all of siliciclastic lithology, have a variable grain size, and contain large amounts of matrix and cement. Eleven samples from the Earthy Member were made into thin sections. Thin-section analysis shows that the framework grains are mainly monocrystalline quartz, with small amounts of polycrystalline quartz, feldspar, and chert (Table 10). Some samples contained moderate to major amounts of shale intra-clasts. The classification of sandstones and sandy siltstones vary considerably in this unit, with quartzarenite, subarkose, sublitharenite, and litharenite lithologies all being present (classification of Folk, 1968; Fig. 37a). The sandstones and sandstone siltstones are primarily made up of grains, cement, matrix, and contain minor amounts of porosity (Fig. 37b). Pore-filling cements making up the Earthy Member include calcite, quartz, iron oxide, kaolinite, and dolomite.

Porosity of the Earthy Member is predominately intergranular microporosity (Table 11; Fig. 37c). Microporosity is present in the matrix and partially cemented areas. In some locations fracture and non-fracture intergranular macroporosity is present. Small to moderate amounts of intragranular macro and microporosity are present in void-rich grains.

Earthy Member Mineralized Fractures

Mineralized fractures are common at the base of the Earthy Member. Three of the Earthy Member thin sections contain opening-mode mineralized fractures. Fractures are mineralized with gypsum, pyrite, iron oxide, calcite, barite, and kaolinite cement.

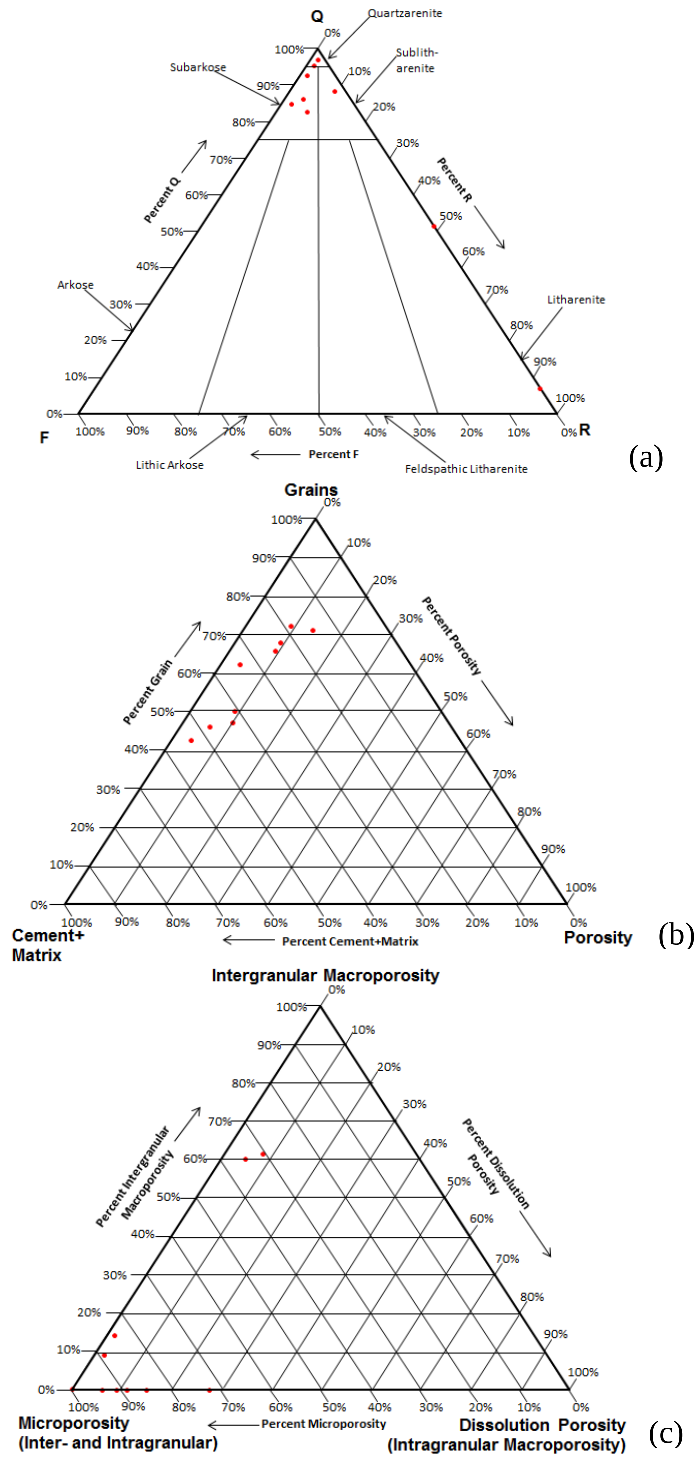

Figure 37. (a) Diagram showing the quartz-feldspar-lithic fragment abundances of sandstones from the Earthy Member (classification of Folk, 1968). (b) Diagram showing the grain-porosity-cement abundances of sandstones from the Earthy Member. (c) Diagram showing the intergranular macroporosity-dissolution porosity-microporosity abundance of sandstones from the Earthy Member (classification of Pittman, 1979). Fracture porosity is not included.

Table 10. Mineralogy of the Earthy Member of the Entrada Sandstone.

		Framework grains						Matrix	Cement						Porosity	Other		
Thin Section	Facies	Mono-Quartz	Poly-Quartz	Feld-spar	Chert	Shale Intraclast	Bio-tite	Matrix*	Calcite	Quartz	Iron Oxide	Gyp-sum	Kaol-inite	Dolo-mite	All Types	Unidentified Grains & Cement	Grain Size	Sort-ing
IW8911-9a	Shale	trace	0%	0%	0%	0%	0%	96%	0%	0%	0%	2%	0%	0%	2%	0%	clay	w
IW8911-9b	Sand.	4%	1%	0%	trace	66%	0%	15%	0%	0%	0%	0%	0%	0%	14%	0%	cL	vp
IW8911-10	Sand.	57%	6%	1%	1%	0%	0%	5%	12%	5%	3%	0%	0%	trace	9%	1%	fU	w
IW8911-11	Sand.	57%	5%	4%	1%	0%	0%	6%	13%	1%	3%	0%	0%	0%	9%	1%	fU	w
IW8911-12	Sand.	34%	3%	trace	2%	33%	0%	14%	2%	0%	3%	0%	0%	0%	9%	0%	vfU	m
IW8911-13	Sand.	38%	1%	6%	1%	trace	0%	42%	4%	1%	1%	0%	0%	0%	6%	trace	vfL	w
IW8911-14	Shale	N/A	N/A	N/A	N/A	N/A	N/A	N/A	N/A	N/A	N/A	N/A	N/A	N/A	N/A	N/A	clay	w
IW8911-15	Sand.	37%	1%	5%	2%	1%	1%	34%	5%	1%	3%	0%	0%	0%	10%	trace	vfU	w
IW8911-16	Sand.	41%	2%	5%	1%	1%	trace	13%	21%	1%	6%	0%	0%	0%	9%	trace	vfU	m
IW-31112-1	Silt.	34%	3%	1%	3%	1%	0%	28%	20%	1%	4%	0%	0%	0%	4%	1%	silt	m
IW-31112-2A	Sand.	55%	4%	2%	1%	0%	0%	0%	18%	3%	13%	0%	0%	0%	4%	trace	fU	w

*Likely once a clay matrix, it has now been replaced by a mixture of hematite and calcite cement

trace indcates less than 0.5%

Shale = Shale Lithofacies
Silt. = Siltstone Lithofacies
Sand. = Sandstone Lithofacies

vp = very poorly sorted
vpp = very poorly to poorly sorted
p = poorly sorted
pm = poorly to moderately sorted
m = moderately sorted
mw = moderately to well sorted
w = well sorted
wvw = well to very well sorted
vw = very well sorted

vcU = very coarse upper
vcL = very coarse lower
cU = coarse upper
cL = coarse lower
mU = medium upper
mL = medium lower
fU = fine upper
fL = fine lower
vfU = very fine upper
vfL = very fine lower

Table 11. Porosity of the Earthy Member of the Entrada Sandstone.

			Porosity							
Thin Section	Facies	Esti-mate	Intergranular Macropropsity Non-fracture	Intergranular Macroporosity Fracture	Intragranular Macroporosity Non-fracture	Intragranular Macroporosity Fracture	Intergranular Microporosity	Intragranular Microporosity	Grain Size	Sort-ing
IW8911-9a	Shale	X	0%	0%	25%	10%	0%	65%	clay	w
IW8911-9b	Sand.		9%	18%	1%	18%	29%	25%	cL	vp
IW8911-10	Sand.		9%	0%	2%	0%	72%	17%	fU	w
IW8911-11	Sand.	X	60%	0%	5%	0%	30%	5%	fU	w
IW8911-12	Sand.	X	0%	25%	5%	20%	25%	25%	vfU	m
IW8911-13	Sand.	X	0%	0%	15%	0%	70%	15%	vfL	w
IW8911-14	Shale		N/A	N/A	N/A	N/A	N/A	N/A	clay	w
IW8911-15	Sand.	X	0%	20%	5%	0%	60%	15%	vfU	w
IW8911-16	Sand.	X	0%	10%	10%	0%	75%	5%	vfU	m
IW-31112-1	Silt.	X	0%	0%	0%	0%	100%	0%	silt	m
IW-31112-2A	Sand.	X	40%	35%	5%	0%	15%	5%	fU	w

Shale = Shale Lithofacies
Silt. = Siltstone Lithofacies
Sand. = Sandstone Lithofacies

vp = very poorly sorted
vpp = very poorly to poorly sorted
p = poorly sorted
pm = poorly to moderately sorted
m = moderately sorted
mw = moderately to well sorted
w = well sorted
wvw = well to very well sorted
vw = very well sorted

vcU = very coarse upper
vcL = very coarse lower
cU = coarse upper
cL = coarse lower
mU = medium upper
mL = medium lower
fU = fine upper
fL = fine lower
vfU = very fine upper
vfL = very fine lower

Diagenesis

The diagenetic histories of the study units were investigated in order to constrain the nature of pore fluids that moved through the sediments and structural features in the past, and to determine how diagenetic alterations have impacted porosity and permeability. Because the Navajo Sandstone, Carmel Formation, and Entrada Sandstone have broadly similar diagenetic histories, they are discussed together, with key differences noted where appropriate.

Compaction

Significant compaction has occurred in the study units, as evidenced by deformation of relatively weak constituents such as skeletal chert and feldspar grains, and void-filling dolomite rhombs. However, these weak grains and rhombs appear to only have undergone minor amounts of deformation, suggesting compaction occurred prior to dissolution (Figs. 38 and 39). Some highly cemented areas also contain evidence of compaction, suggesting compaction occurred prior to complete cementation (Fig. 40). Large amounts of original intergranular volume were likely lost due to compaction (see Discussion section for details).

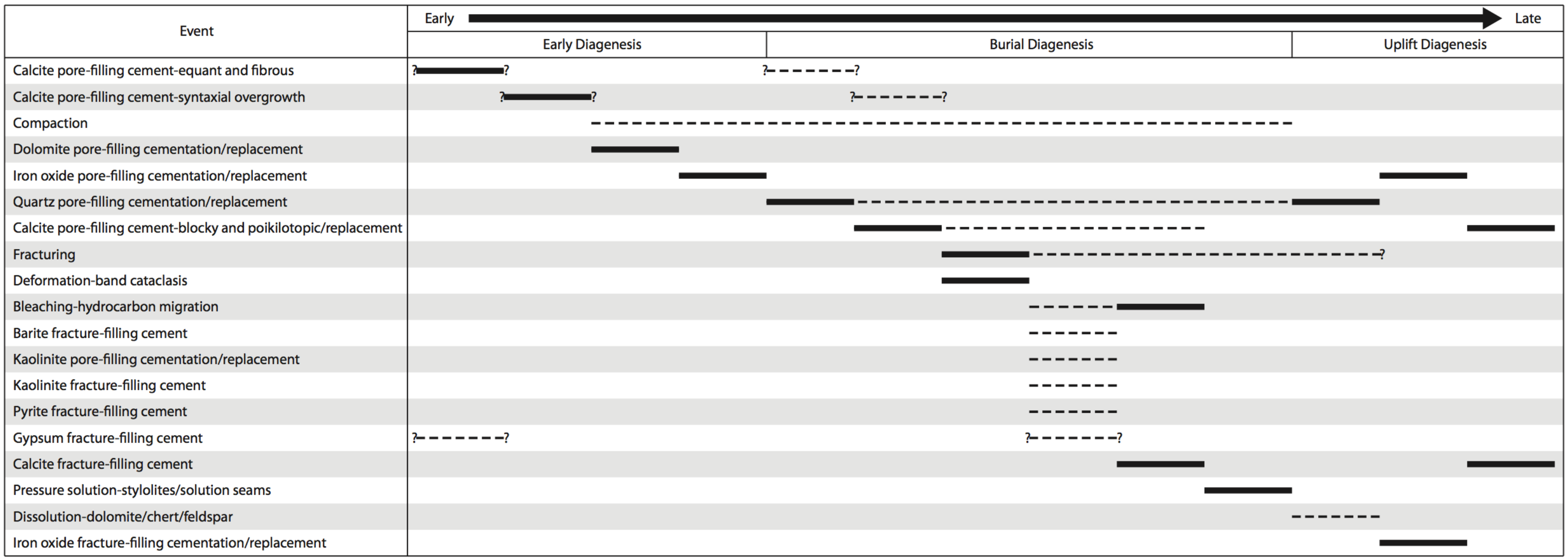

Figure 38. Summary of the relative timing of diagenetic alterations influencing the Navajo Sandstone, Carmel Formation, and Entrada Sandstone. Solid lines indicate the period during which an event occurred, dashed indicate a range of time over which the event may have occurred. Relatively early events are plotted towards the left, late towards the right. Question marks indicate uncertainty. Possible diagenetic environments are shown (see discussion section for justification).

Figure 39. Thin-section photomicrograph showing iron oxide cement inside a skeletal (dissolved) feldspar grain. This indicates that iron oxide probably precipitated after feldspar dissolution. Because the delicate skeletal feldspar grain is still intact, feldspar dissolution likely occurred after significant compaction. IW8911-10, Entrada Sandstone Earthy Member, plane polarized light.

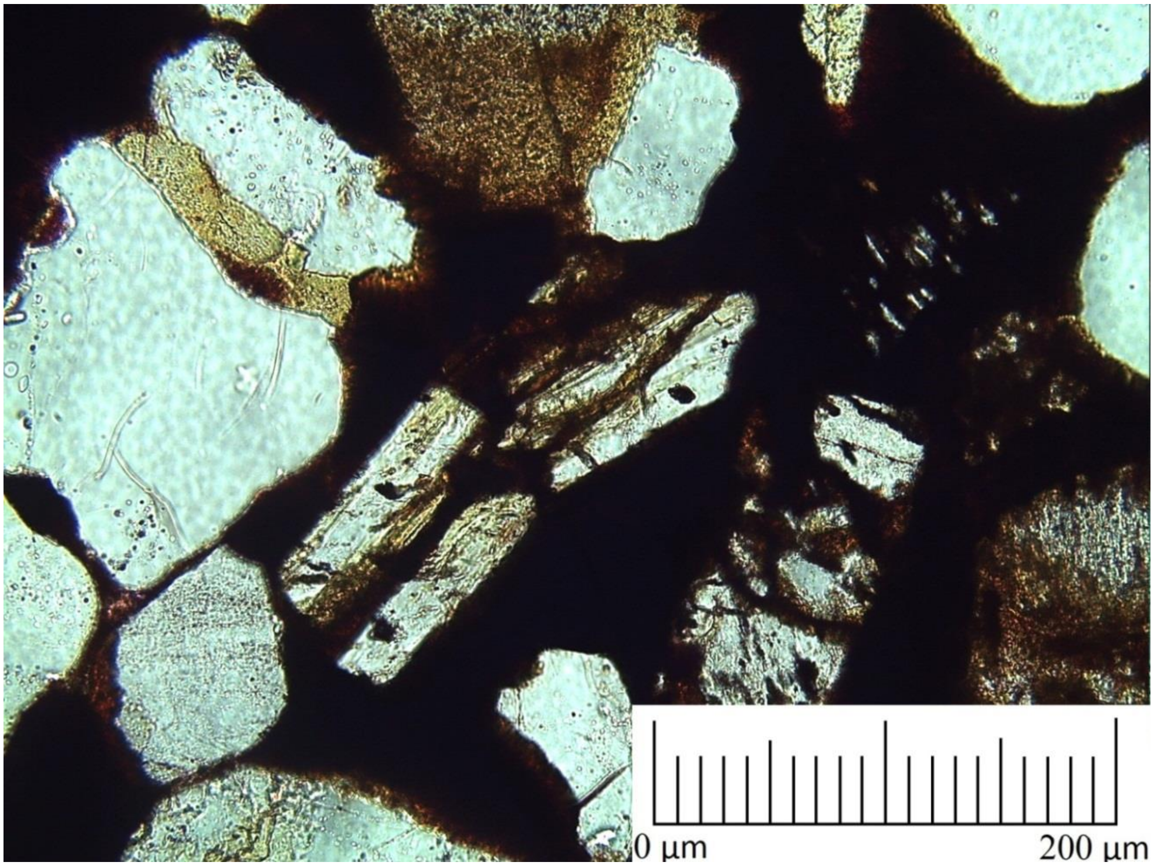

Figure 40. Thin-section photomicrograph showing a fractured grain that is cemented by goethite. This suggests that compaction occurred prior to goethite cementation. IW81111-2, Entrada Sandstone Slick Rock Member, plane polarized light.

Dolomite Cementation

Rhombs of dolomite are present as a pore-filling cement in the Entrada Sandstone and Carmel Formation. Several of the rhombs contain voids and are filled with iron oxide and calcite(?) cement, indicating the rhombs have either undergone dissolution and/or replacement (Fig. 41). Dolomite rhombs are also present in the matrix of sandstones from the Carmel Formation, suggesting dolomite replacement of the matrix.

Precipitation of dolomite rhombs appears to be one of earliest events in the paragenetic sequence. Dolomite rhombs are encased in authigenic quartz, suggesting that dolomite precipitation occurred prior to quartz (Fig. 42). Dolomite rhombs are also coated by iron oxide, suggesting that iron oxide cement formed after dolomitization (Fig.

42). The iron oxide coated dolomite rhombs are also encased in blocky calcite cement, suggesting that both dolomite and iron oxide cementation occurred prior to blocky calcite cementation (Fig. 42). Iron oxide and non-optically continuous calcite(?) cement are present inside of some dissolved dolomite rhombs, suggesting these phases formed after dolomite dissolution (Fig. 41). Parry et al. (2009) reported similar dolomite rhombs in the Navajo Sandstone in central Utah, and concluded the dolomite formed early in the paragenesis from the replacement of calcite cement. Evidence of this is present in the Carmel Formation and Entrada Sandstone, but not the Navajo Sandstone.

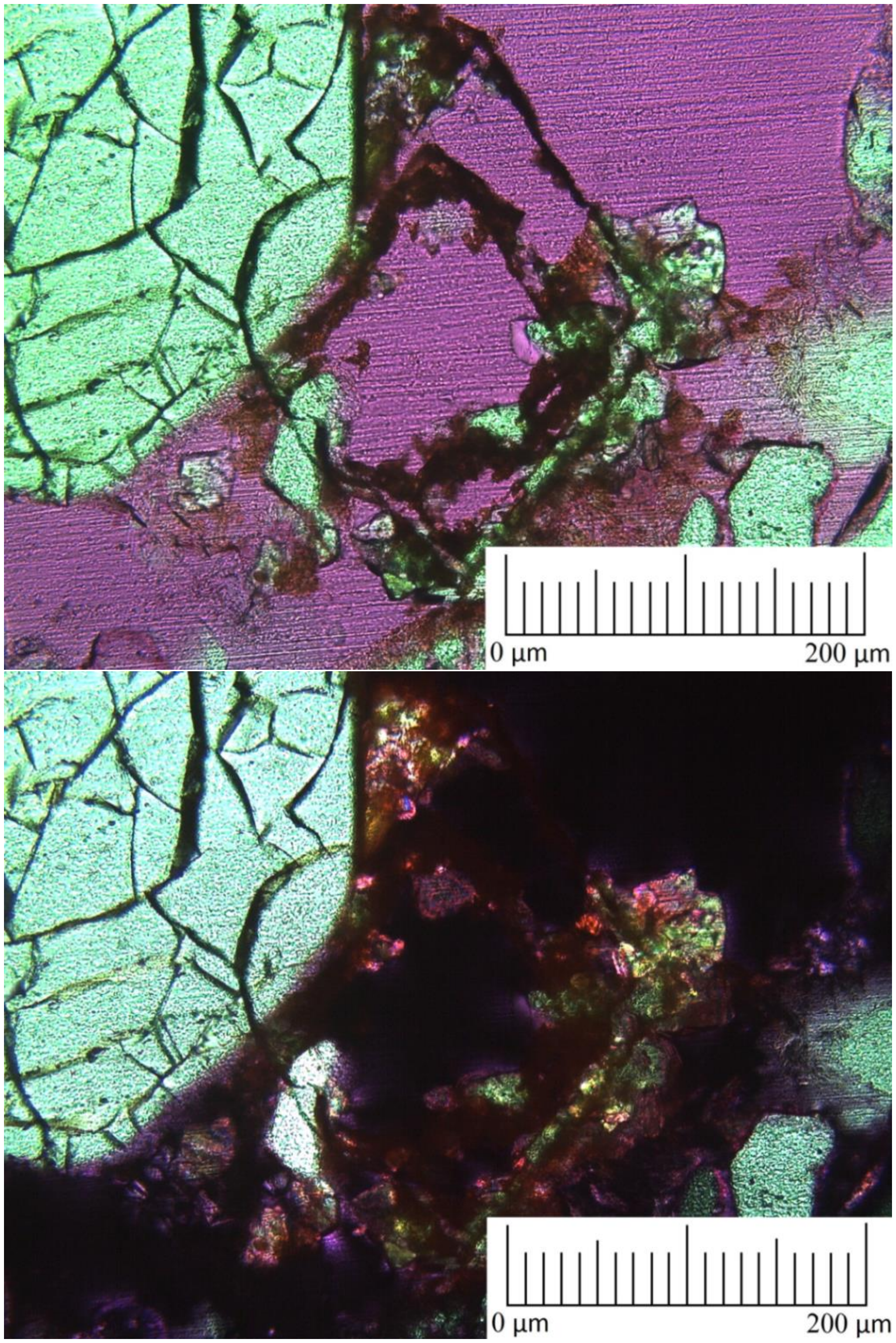

Figure 41. Thin-section photomicrograph showing the outline of a dolomite rhomb that was removed by dissolution (outlined by iron oxide cement). The minor amounts of deformation of this delicate structure indicate that the carbonate dissolution postdates significant compaction. Iron oxide cement is found both on the interior and exterior of the rhomb, suggesting iron oxide cementation occurred both before and after dolomite dissolution. Alternatively, there may have been partial dissolution of the rhomb, followed by iron oxide cementation, then more dissolution. Also present inside of the dissolved rhomb is non-optically continuous calcite(?) cement, possibly suggesting that calcite cementation post-dated dolomite dissolution. IW8911-6, Entrada Sandstone Slick Rock Member, plane polarized light.

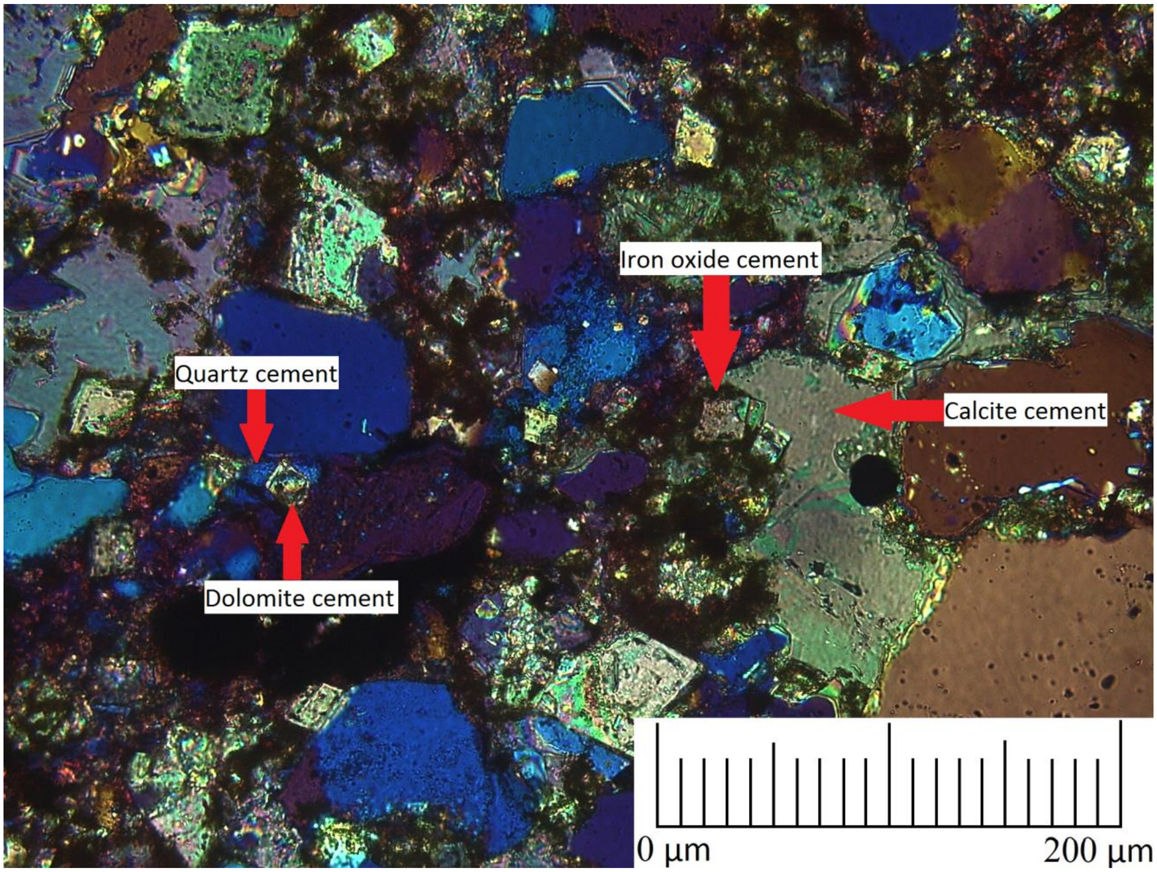

Figure 42. Thin-section photomicrograph showing a dolomite rhomb encased in quartz cement, suggesting that dolomite formed prior to quartz. Also shown is an iron oxide coated dolomite rhomb encased in calcite cement, suggesting that dolomite cementation occurred before iron oxide and calcite. UM-31312-17, Carmel Formation Co-op Creek Member, cross polarized light with gypsum plate.

Iron Oxide Cementation/Replacement

Iron oxide is present as pore- and fracture-filling cement. Pore-filling iron oxide cement is present rimming grains, at contacts between grains, and locally completely filling pores in all of the units. The texture of the fracture-filling iron oxide cement in the Navajo Sandstone and Carmel Formation is wall-rimming. Fracture-filling iron oxide “shrubs” are also seen within the Navajo Sandstone (Fig. 43). In the Entrada Sandstone fracture-filling iron oxide is present as euhedral hexagonal crystals, pseudomorphing cubic crystals, and locally completely filling fractures. Throughout all of the units there are grains and matrix that consist of iron oxide, demonstrating iron oxide replacement has occurred. However, it is also possible that the iron oxide grains are detrital in origin and were not replaced.

Multiple stages of iron oxide cementation occurred. Locally quartz cement appears to have precipitated in areas not completely covered by iron oxide cement (Fig. 44), whereas in other locations quartz cement is coated by iron oxide cement (Fig. 45). This suggests two stages of pore-filling iron oxide cement, one prior to significant quartz overgrowth formation and the other after quartz overgrowth formation. Fracture-filling iron oxide is encased in calcite cement, suggesting that the iron oxide cement occurred prior to the calcite cement (Fig. 43). Cubic outlines found inside of fracture-filling iron oxide cement indicates that it formed by pseudomorphic replacement of pyrite crystals and thus occurred after pyrite precipitation (Fig. 46). This pseudomorphic iron oxide is encased in calcite cement, suggesting that if formed prior to the fracture-filling calcite (Fig. 46).

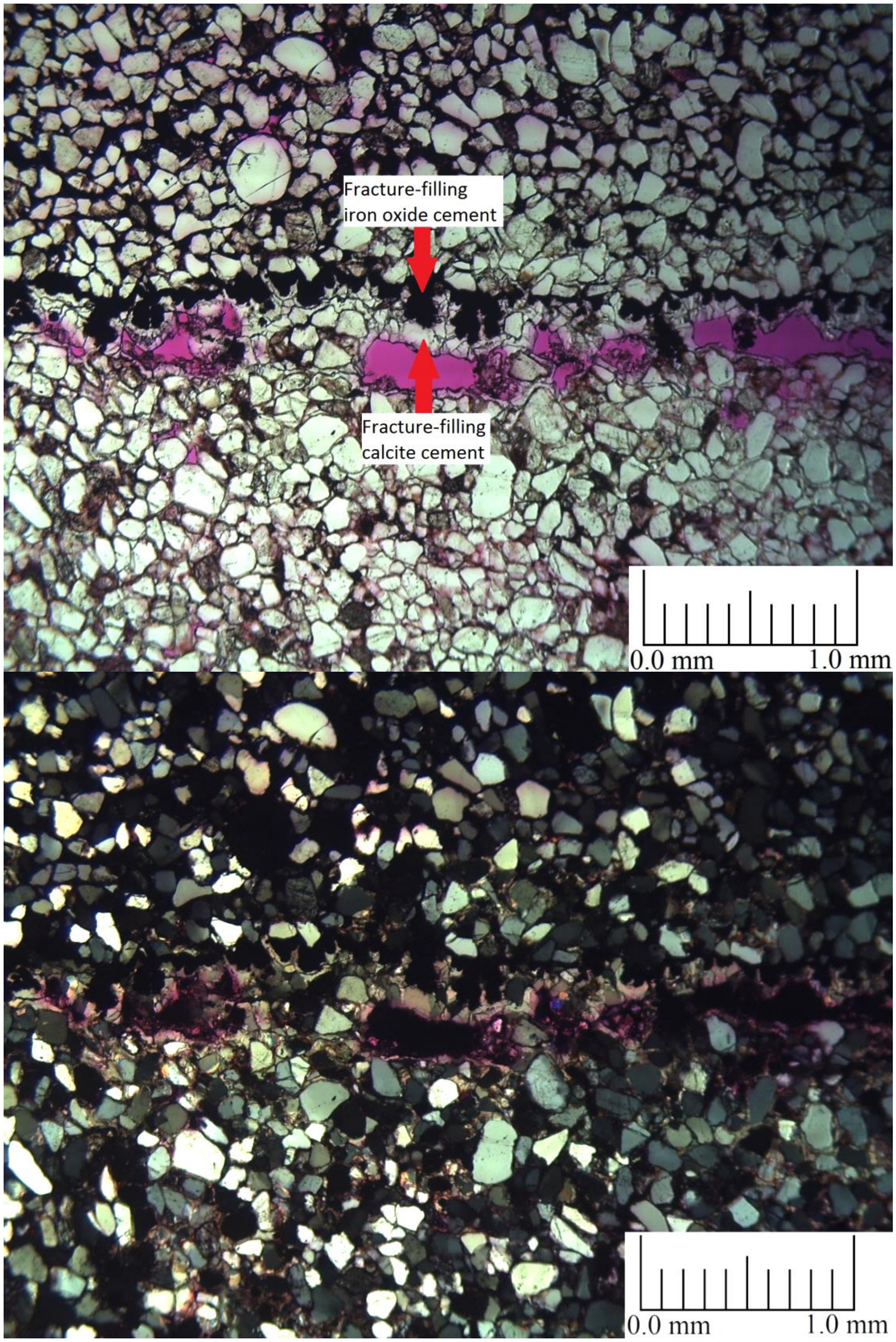

Figure 43. Thin-section photomicrograph of an opening-mode fracture showing fracture-filling iron oxide “shrubs” encased in calcite. This suggests that the iron oxide formed prior to the calcite. UM-102211-C, Navajo Sandstone, plane polarized light above and cross polarized light below.

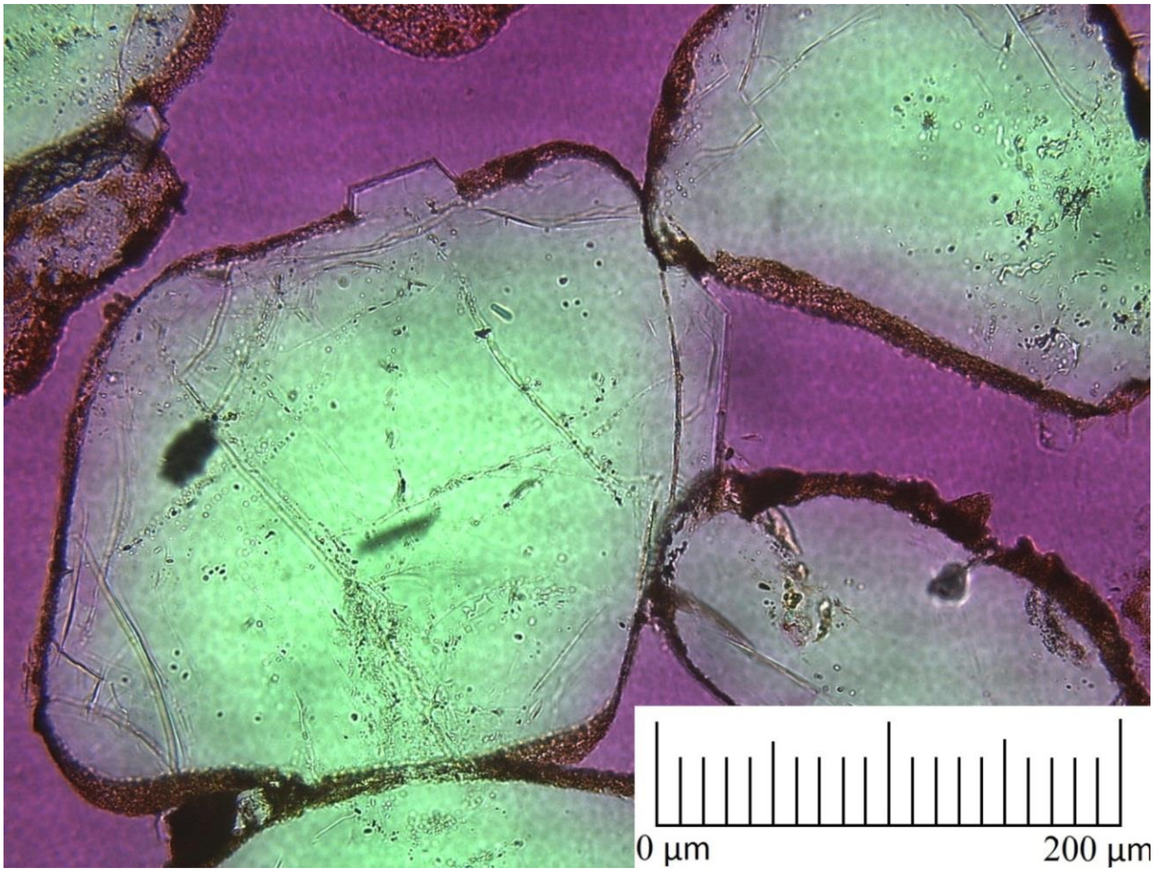

Figure 44. Thin-section photomicrograph showing an iron oxide cemented quartz grain that also contains quartz overgrowths. The quartz overgrowths are not covered by iron oxide, indicating that they formed after the iron oxide in areas of the quartz grain that were not completely covered by iron oxide. IW80811-1psm, Entrada Sandstone Slick Rock Member, plane polarized light.

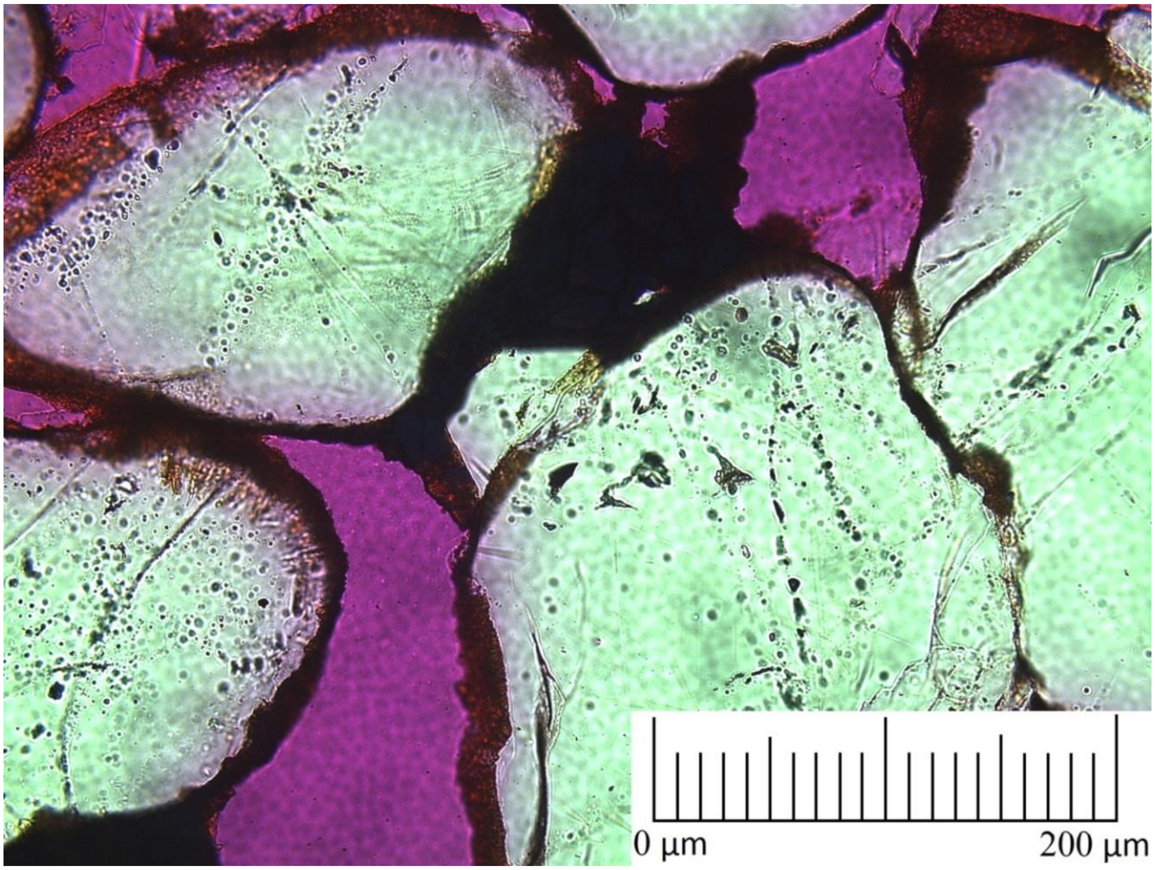

Figure 45. Thin-section photomicrograph showing a quartz overgrowth surrounded by iron oxide cement, suggesting that iron oxide precipitated after the quartz. IW81011-4, Entrada Sandstone Slick Rock Member, plane polarized light.

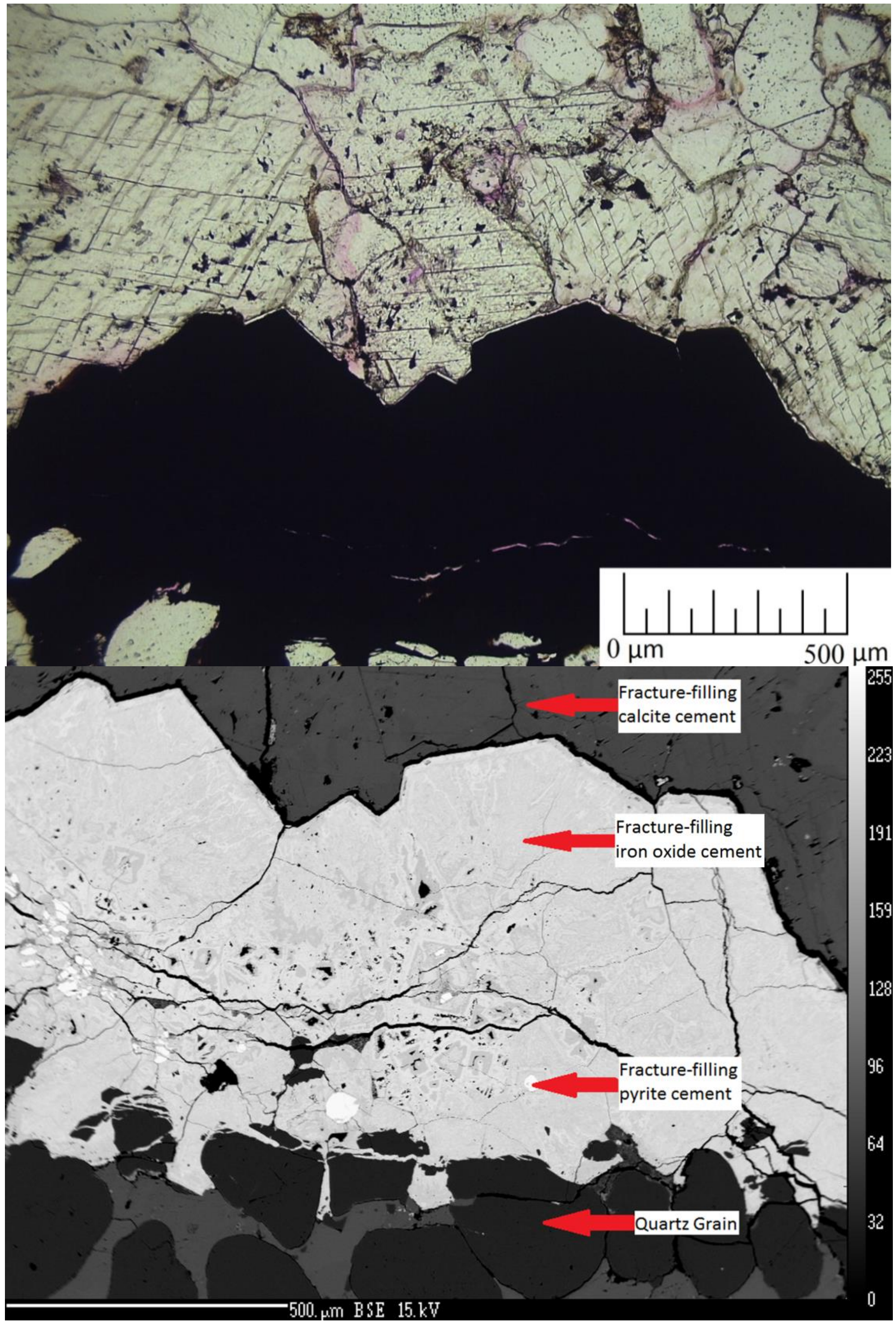

Figure 46. Thin-section photomicrograph (top) and back-scattered electron image (bottom) showing an opening-mode fracture filled by pyrite that was replaced by iron oxide. Calcite cement encases the iron oxide/pyrite, suggesting that calcite cement formed after both. Small relics of non-replaced pyrite are present inside the iron oxide. IW-31112-2A, Entrada Sandstone Earthy Member, plane polarized light above and backscattered electron image below.

Quartz Cement

Quartz cement occurs as overgrowths around detrital quartz grains throughout all of the units. In the Navajo Sandstone and the Slick Rock Member of the Entrada Sandstone quartz cement also formed around grains that were fractured due to deformation-band cataclasis.

Quartz cementation occurred after deformation-band cataclasis, as demonstrated by the high degree of quartz cementation of the cataclasite (Fig. 47). Quartz grains with quartz overgrowths are found within the cataclasite. The quartz overgrowth inside the deformation band is rounded, likely a result of cataclasis, suggesting that the quartz overgrowth formed prior to deformation-band cataclasis (Fig. 47). An alternative hypothesis is that the quartz grain has a recycled quartz overgrowth. However, this is unlikely as there is no evidence of grains with recycled quartz overgrowth found outside the deformation bands. This is in agreement with Davatzes et al. (2003) who also found preexisting quartz overgrowths in deformation bands from the Navajo Sandstone in the San Rafael Swell.

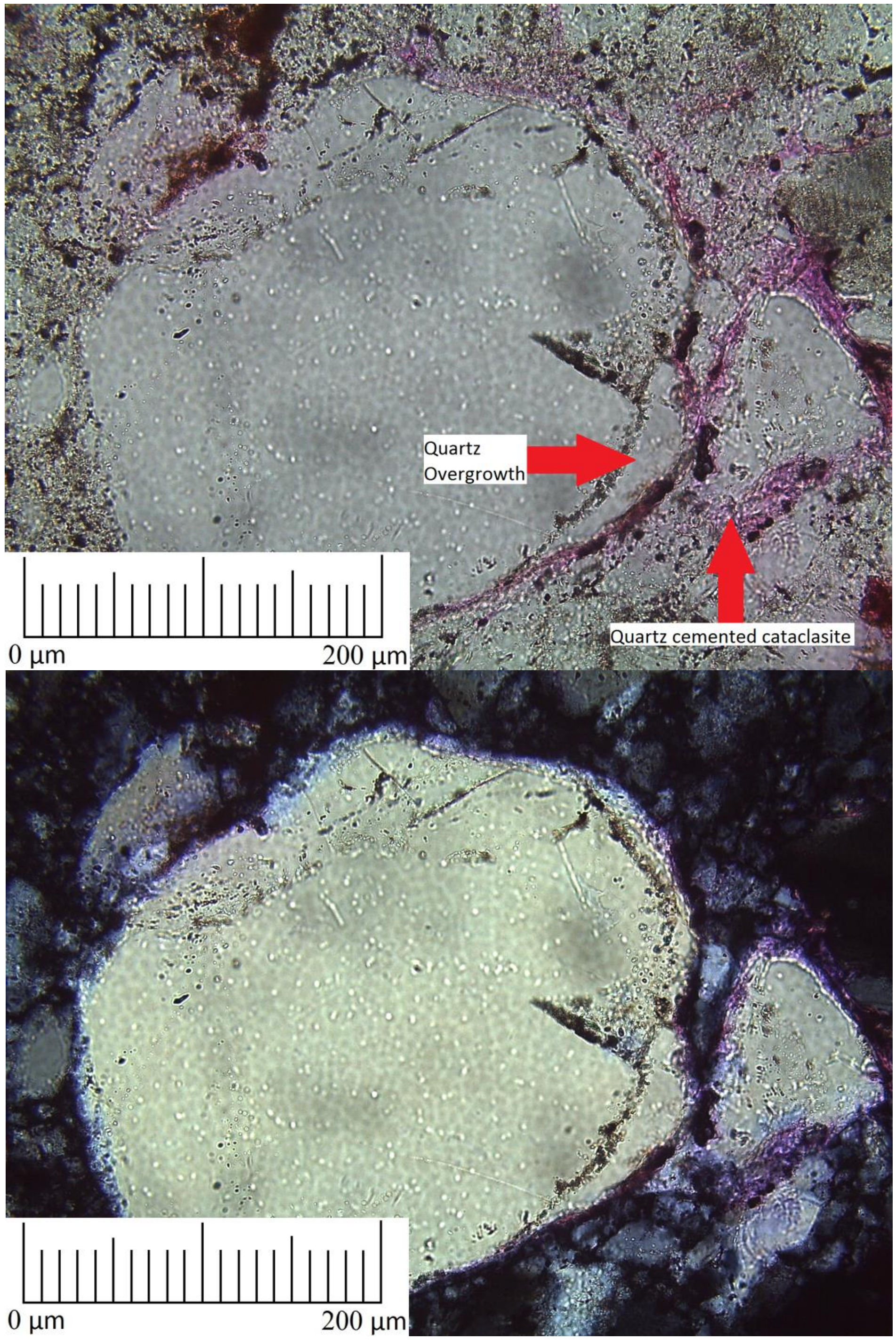

Figure 47. Thin-section photomicrograph showing a quartz grain with a rounded quartz overgrowth encased in quartz cement resulting from deformation-band cataclasis. The quartz overgrowth may have been rounded during cataclasis. Alternatively, it may be a recycled overgrowth, though this is unlikely (see text for discussion). IW8911-3, Entrada Sandstone Slick Rock Member, plane polarized light above and cross polarized light below.

Deformation-Band Cataclasis

Deformation bands are present in the Navajo Sandstone and the Slick Rock Member of the Entrada Sandstone. Deformation bands exhibit extensive cataclasis, which was followed by quartz cementation (on the newly created grain fracture surfaces; Fig. 48). Deformation bands within the Jurassic units are mainly cataclastic/ compactional shear bands (deformation mechanism and kinematic classification, respectively, from Fossen et al., 2007).

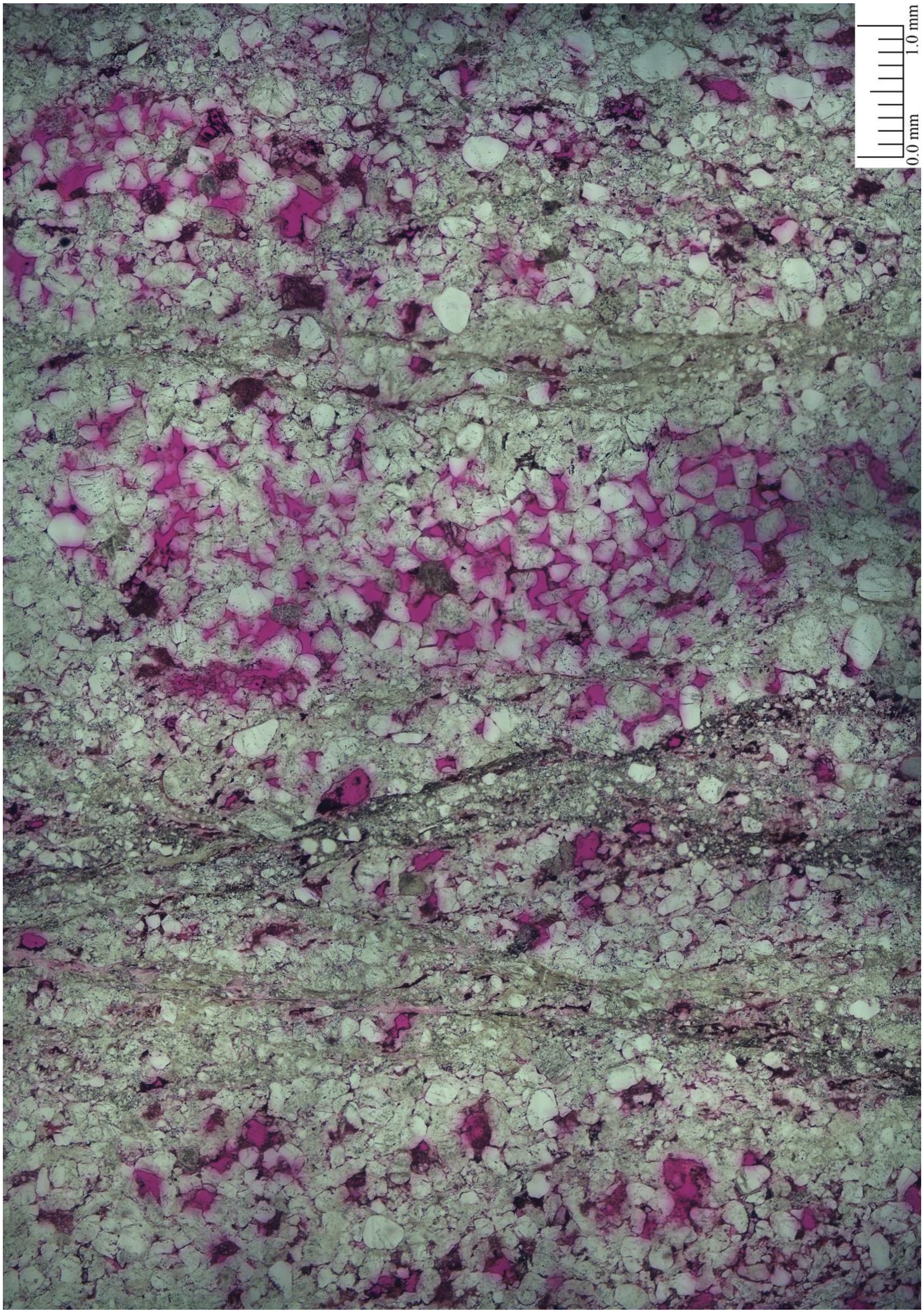

Figure 48. Thin-section photomicrograph mosaic showing a zone of deformation bands. Within the zone is a large portion of relatively undeformed host rock. IW8911-3, Entrada Sandstone Slick Rock Member, plane polarized light.

Fracturing

Fracturing has occurred in all of the units. The majority of the fractures are completely cemented and in the caprock units contain bleached margins. Fracture cements include calcite, iron oxide, pyrite, kaolinite, and barite. The majority of the fractures are opening-mode, with minor amounts of sliding-mode fractures within the Carmel Formation.

Fracturing occurred throughout a large span of the paragenetic sequence. A zone of deformation bands in the Slick Rock Member transitions into a set of fractures in the Earthy Member, indicating that fractures occurred simultaneously with deformation-band cataclasis. Fractures in the Navajo Sandstone and Slick Rock Member of the Entrada Sandstone formed in highly cemented areas, such as near zones of deformation bands (Fig. 49) or where grains were likely previously cemented (Fig. 50). These fractures were later filled with pyrite, iron oxide, and calcite cement. Some fractures in the Co-op Creek Member occurred after pore-filling calcite cement, as demonstrated by fracture truncation of the blocky and equant pore-filling calcite textures (Fig. 51). Calcite filled fractures in the Co-op Creek Member also contain different textures that crosscut one another, demonstrating that multiple fracture and mineralization events have occurred (Fig. 52).

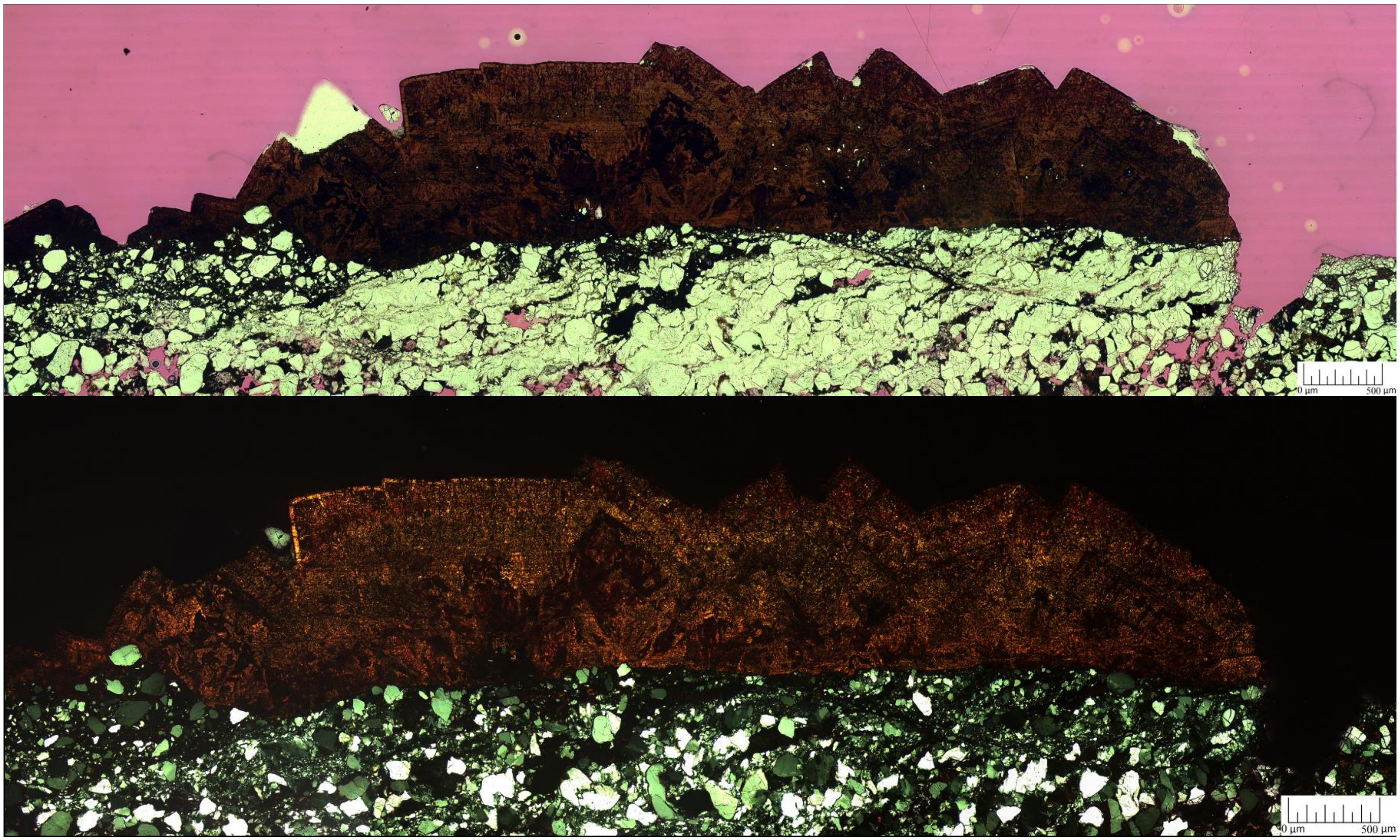

Figure 49. Thin-section photomicrograph mosaic showing half of a highly mineralized opening-mode fracture. The fracture formed alongside a cemented deformation band. The fracture was filled with euhedral pyrite cement, which was later replaced by goethite. SPR-1, Entrada Sandstone Slick Rock Member, plane polarized light above and cross polarized light below.

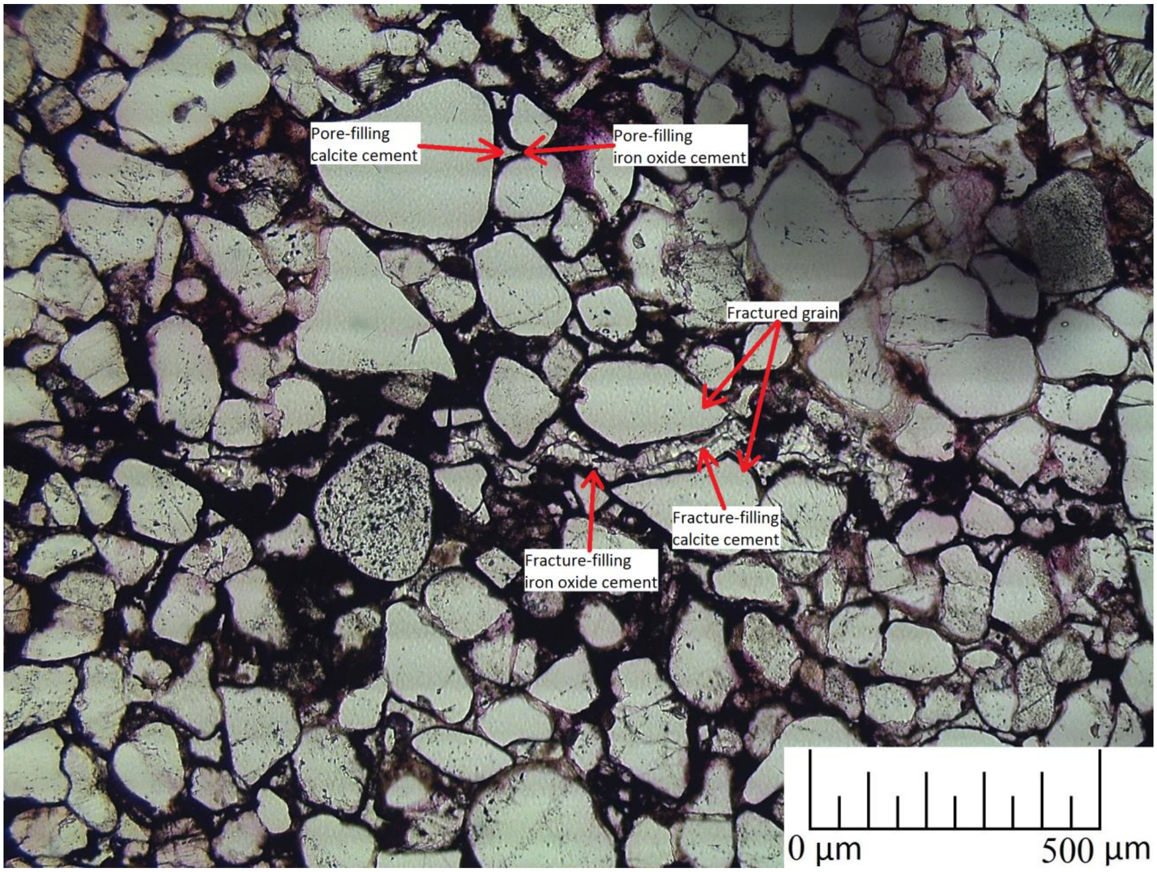

Figure 50. Thin-section photomicrograph showing an opening-mode mineralized fracture. The fracture cuts through both the outsides of grains and the grains themselves, suggesting that pore-filling iron oxide cement bound the grains together prior to fracturing. It is unclear if the pore-filling calcite cement occurred prior to the fracture. The fracture was later filled by iron oxide and calcite cements. UM-102211-C, Navajo Sandstone, plane polarized light.

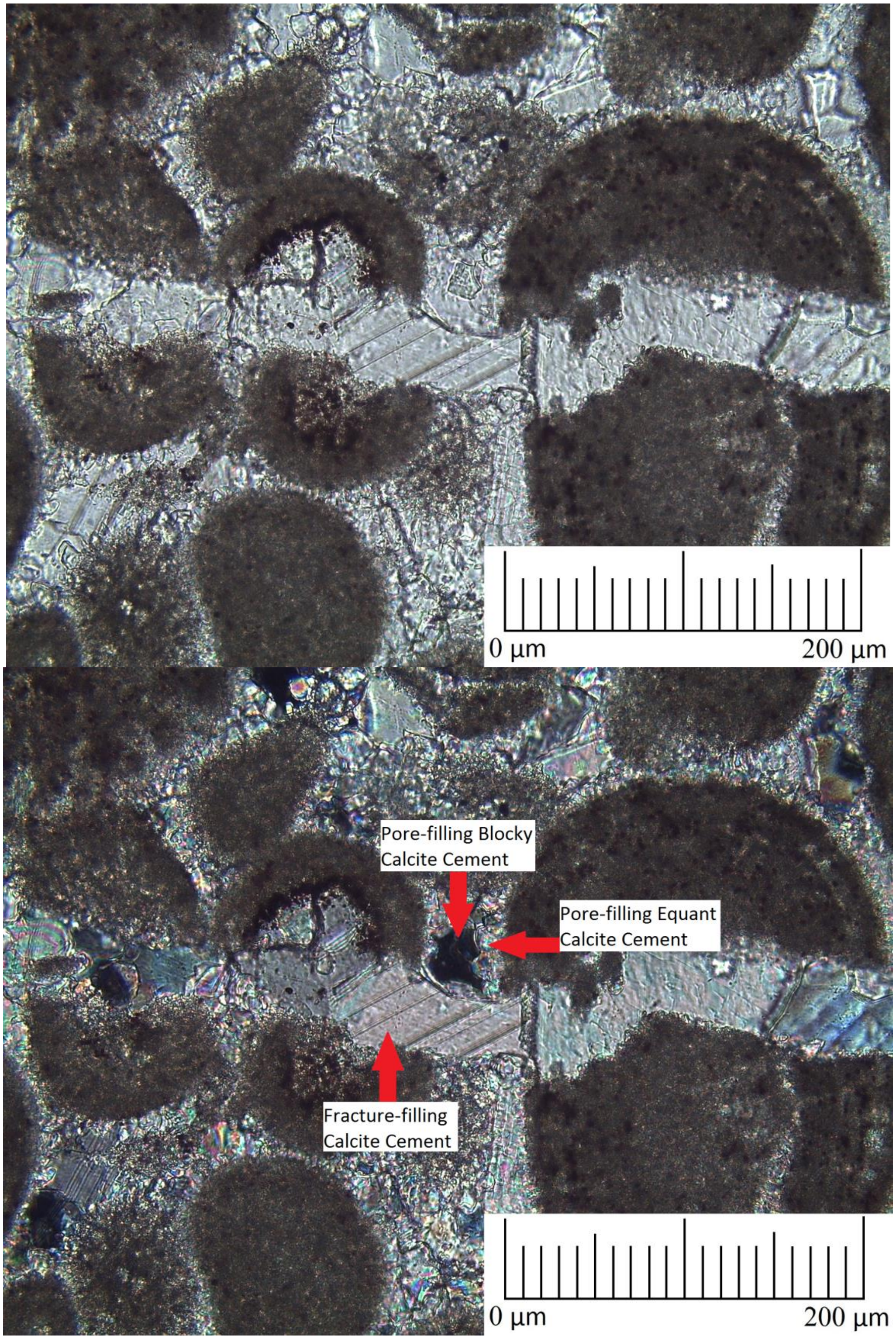

Figure 51. Thin-section photomicrograph showing a mineralized fracture cutting through equant and blocky pore-filling calcite cement, suggesting pore-filling cementation occurred prior to fracturing. UM-102211-G, Carmel Formation Co-op Creek Member, plane polarized light above and cross polarized light below.

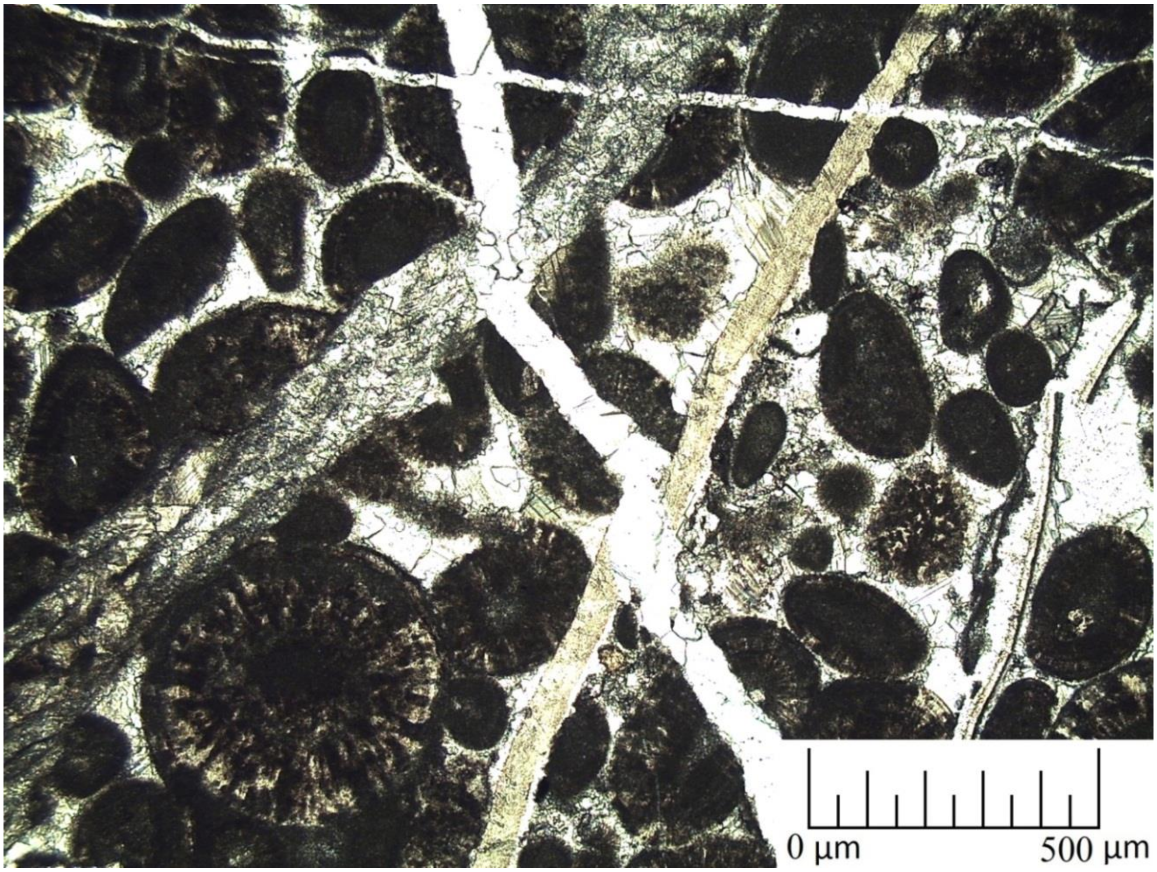

Figure 52. Thin-section photomicrograph showing multiple generations of opening-mode fractures and calcite mineralization. Crosscutting textures suggest that each fracture formed at a different time. Note, the yellow feature is actually a bivalve shell, not a fracture. UM-102211-G, Carmel Formation Co-op Creek Member, plane polarized light.

Bleaching

The reservoir units are whitish-tan in color and are overlain by the red colored caprocks. Portions of the red colored caprocks are bleached to a whitish-tan color near the reservoir-caprock interface. This suggests that bleaching is also responsible for the whitish-tan color of the reservoir units. The host rock surrounding mineralized fractures inside of the caprocks also shows evidence of bleaching. Because the host rock surrounding fractures is bleached, bleaching must post date the fractures.

Bleaching is diagnostic of a reducing environment. Reducing conditions may have been due to microbial decomposition of organic matter. Abundant shale units are found in the Carmel Formation and Entrada Sandstone. If these shales contained organic matter, microbial decomposition of this organic matter may have produced the reducing conditions necessary for bleaching. Some of the other most common geologic reducing environments are related to hydrocarbons, organic acids, methane, and hydrogen sulfide (Garden et al., 1997; Chan et al., 2000). Parry et al. (2009) attributed hydrocarbons to be the cause of bleaching in the Navajo Sandstone in the nearby Covenant oil field. Given the presence of the hydrocarbon source rocks in the underlying Paradox Formation, and the fact these source rocks likely underwent thermal maturity (Nuccio and Condon, 1996), hydrocarbons were likely at least in part the cause of the reducing environment necessary for bleaching.

Further evidence for hydrocarbon-bleaching is supported by the presence of hydrocarbon-filled fluid inclusions within calcite fracture-fill (Figs. 53 and 54). The fluid inclusions are proven to be hydrocarbons because they are fluorescent (Fig. 54). Water-filled fluid inclusions would not fluoresce in this manner. The existence of a fluid inclusion-rich zone within calcite mineralized fractures suggests fracture-filling calcite cement may have precipitated simultaneously with hydrocarbon-related bleaching.

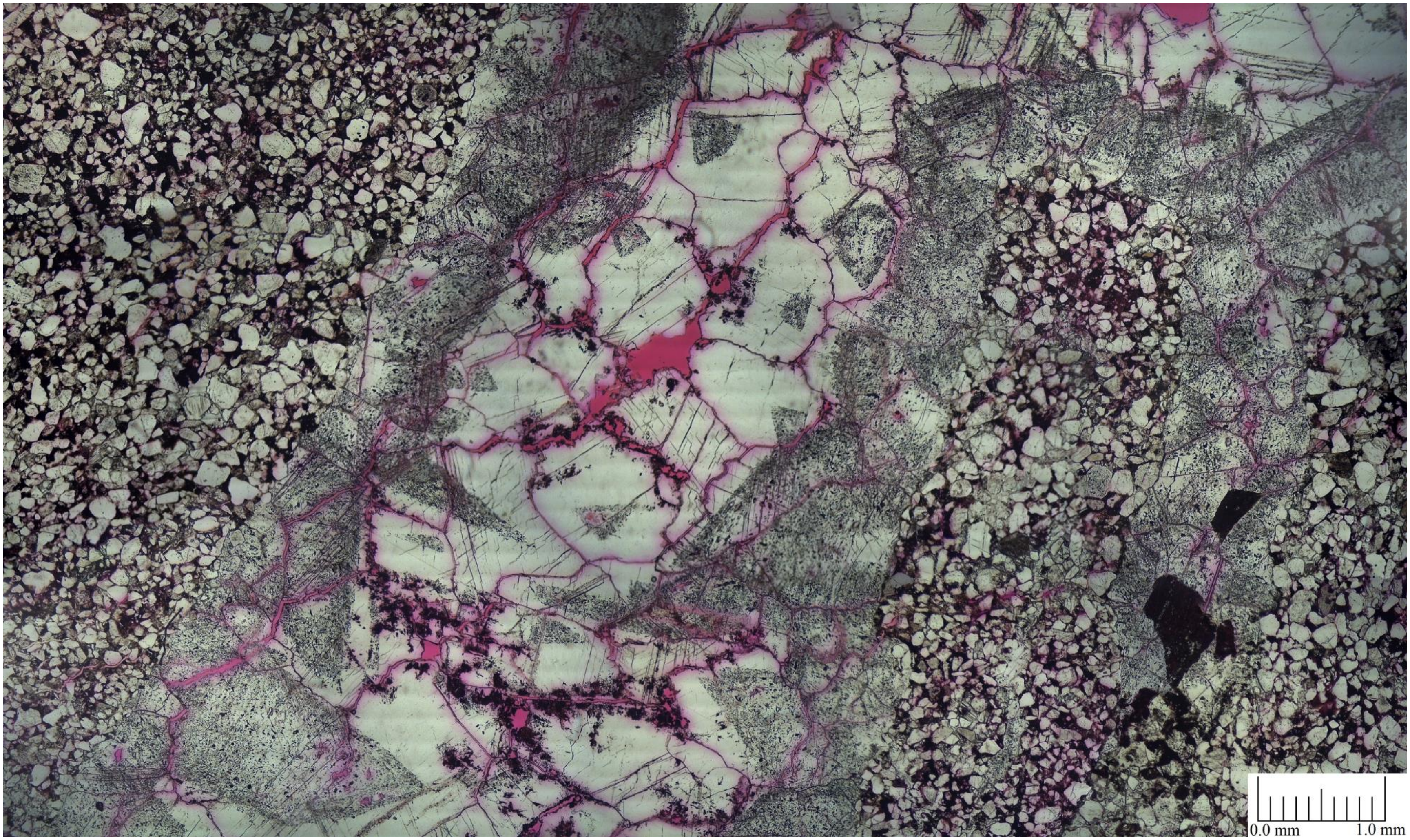

Figure 53. Thin-section photomicrograph mosaic showing a fluid inclusion rich zone inside a calcite-filled fracture. UM-31312-17, Carmel Formation Co-op Creek Member, plane polarized light.

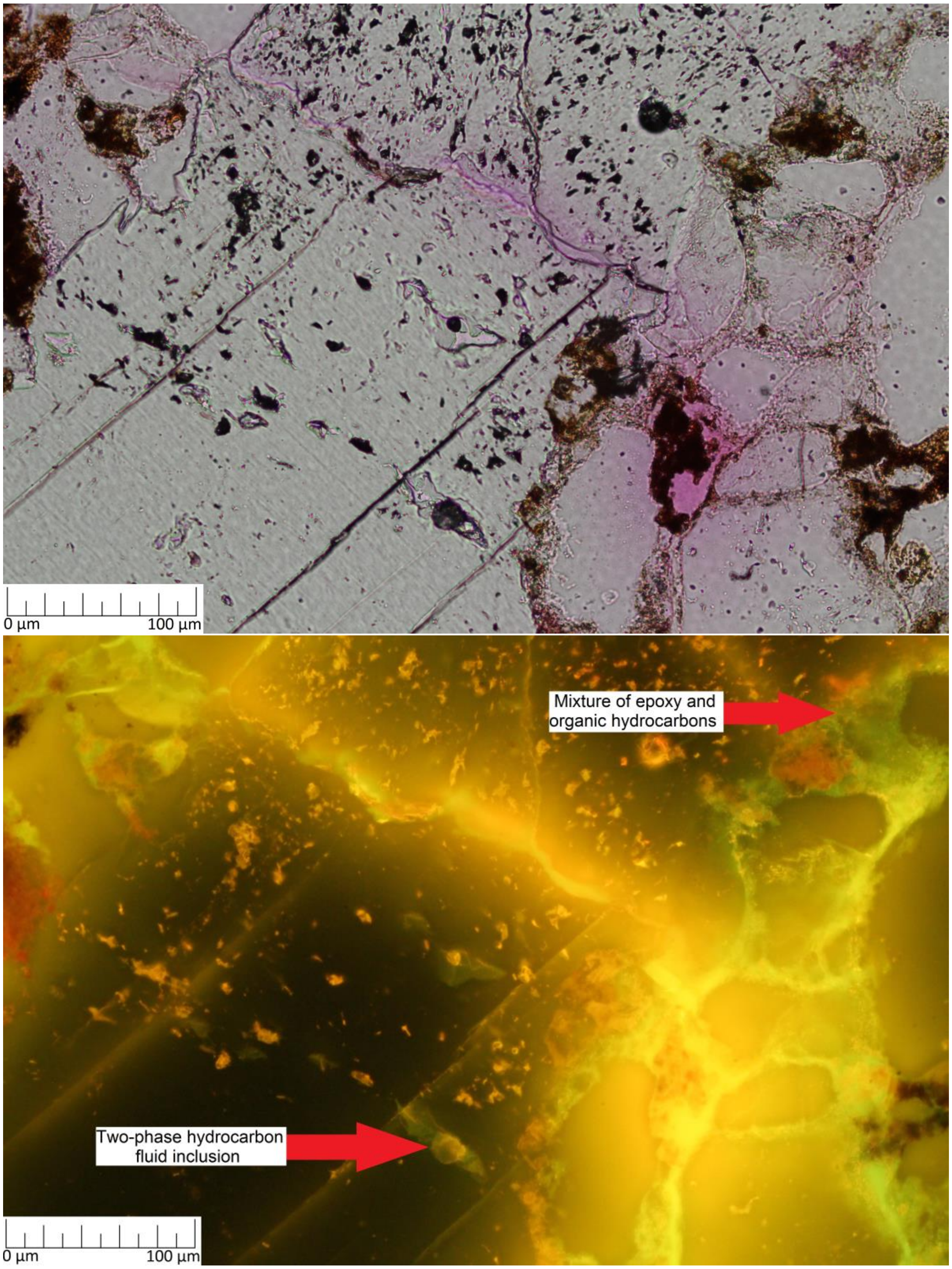

Figure 54. Thin-section photomicrograph showing two-phase hydrocarbon fluid inclusions inside calcite fracture-fill. The green inclusions are higher grade than the orange. This thin section is impregnated with fluorescent epoxy. The epoxy shows up red in plane polarized light and bright yellow in fluorescent light. Some of the fluorescence within the cracks between calcite fracture-filling cement is due to a mixture of organic hydrocarbons (green fluorescence) and epoxy (yellow fluorescence). UM-31312-16, Carmel Formation Co-op Creek Member, conoscopic plane polarized light above and fluorescent light below.

Dissolution

Skeletal chert and feldspar grains, and void-filled dolomite rhombs are found throughout the study units demonstrating that grain and cement dissolution has occurred (Figs. 39, 41, and 55). Voids within skeletal (dissolved) grains and rhombs are filled with iron oxide cement, indicating that dissolution occurred prior to iron oxide cementation (Figs. 39, 41, and 55). An alternative hypothesis is that grains and rhombs were first replaced by iron oxide, then underwent dissolution, though it seems unlikely that replacing fluids interacted with the interior of feldspar grains. The delicate skeletal grains and rhombs remain fairly intact, suggesting that they were dissolved subsequent to significant compaction (Figs. 39, 41, and 55).

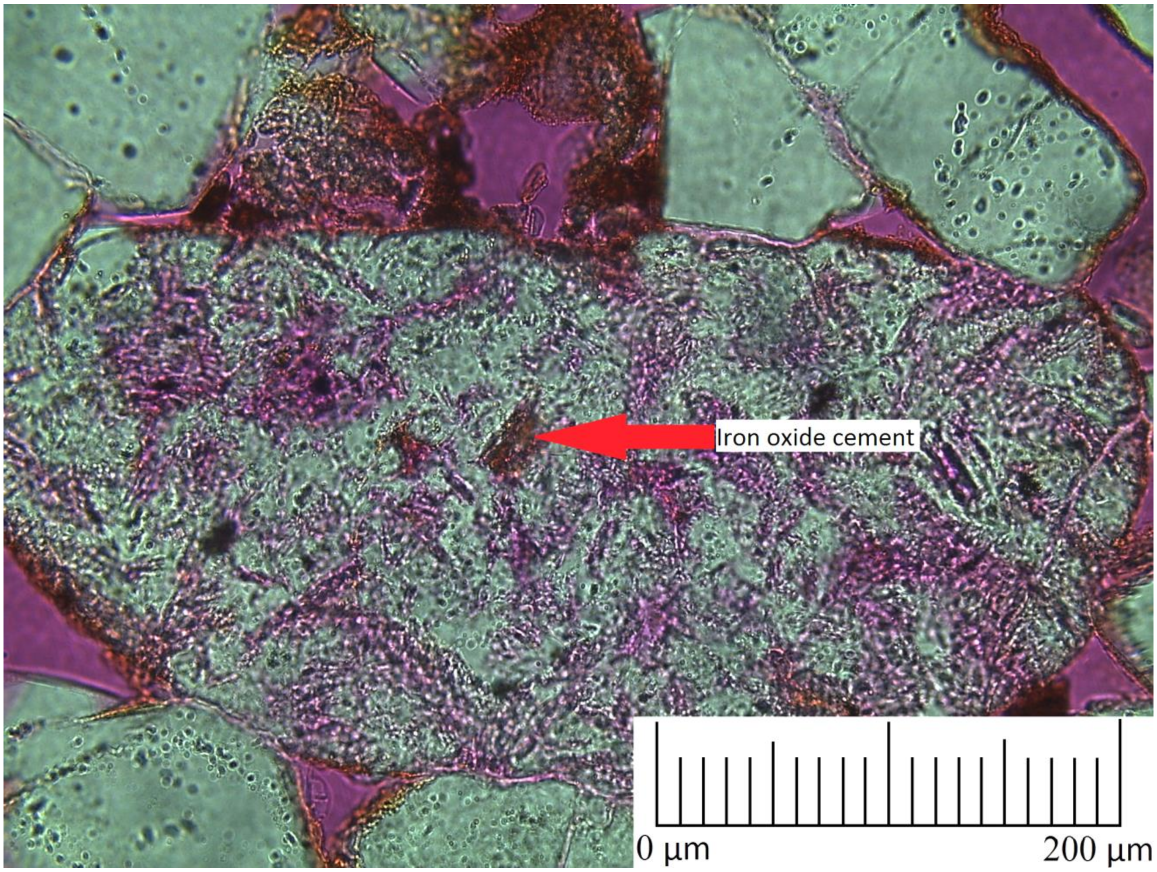

Figure 55. Thin-section photomicrograph showing iron oxide cement inside of a chert grain. This indicates that chert dissolution occurred prior to iron oxide cementation. The delicate void-rich chert grain is still intact, suggesting that chert dissolution occurred after significant compaction. UM-31312-19, Navajo Sandstone, plane polarized light.

Kaolinite Cementation/Replacement

Minor amounts of kaolinite are present as pore- and fracture-filling cement in all of the units. The kaolinite occurs as small to large books (Figs. 56 and 57), and as grain-sized clusters, which suggest that kaolinite replaced unstable grains (Fig. 58).

Several relationships were found between kaolinite cementation and other diagenetic events. Pore-filling kaolinite surrounds authigenic quartz, suggesting that kaolinite formed after the onset of quartz precipitation (Fig. 59). Kaolinite is locally coated with iron oxide cement, suggesting that kaolinite formed prior to iron oxide (Figs. 56 and 57). Fracture-filling kaolinite is surrounded by fracture-filling calcite, suggesting that the kaolinite formed prior to calcite fracture-fill (Fig. 60). An alternative hypothesis is that kaolinite replaced the calcite, although it seems unlikely that replacing fluids could have penetrated the interior of the calcite cement. The relationship between kaolinite fracture-fill and iron oxide fracture-fill is difficult to determine. However, if pore-filling kaolinite formed prior to pore-filling iron oxide, the same is likely true for fracture-filling kaolinite. Some of the kaolinite replaced grains contain a speckled, micaceous texture suggesting they formed by replacement of sericitized feldspar (Fig. 58). Kaolinite replaced grains are coated with iron oxide cement, suggesting that the kaolinite replacement occurred prior to iron oxide cementation (Fig. 58).

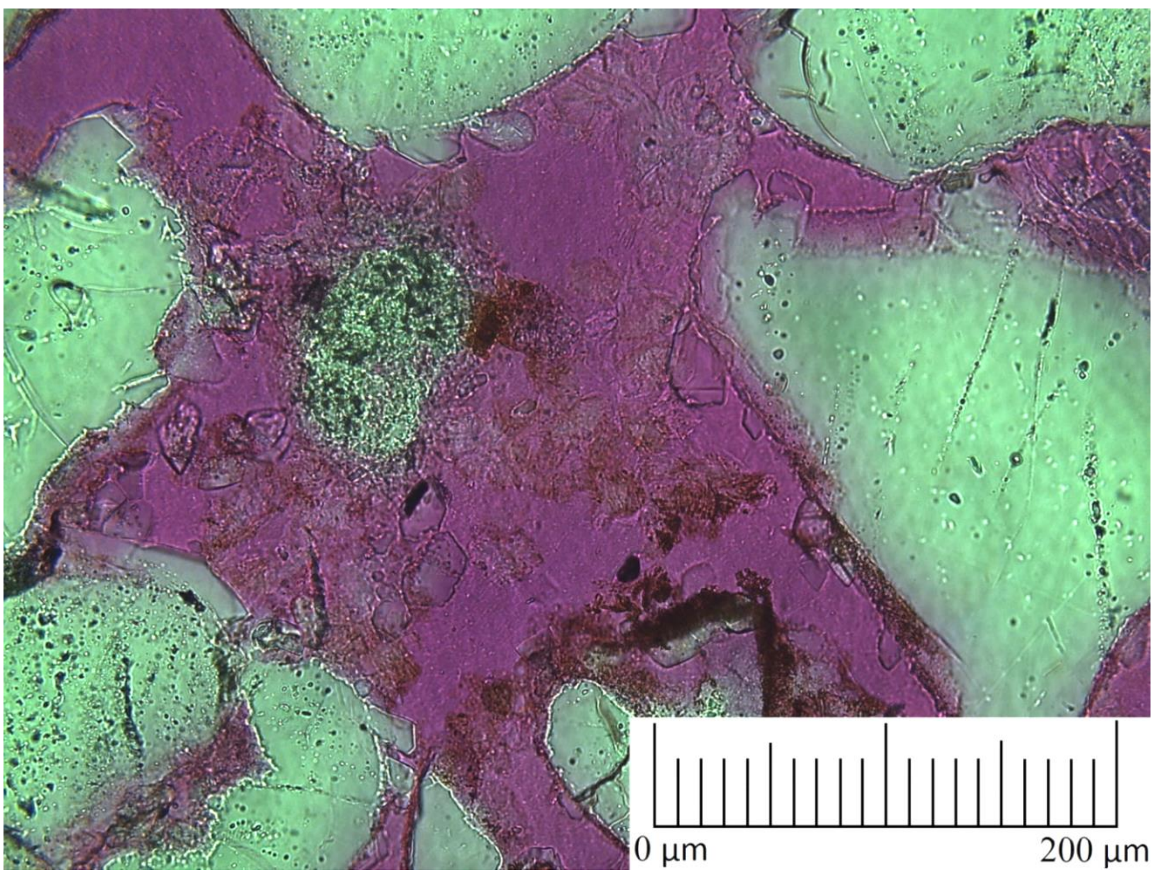

Figure 56. Thin-section photomicrograph showing small books of authigenic kaolinite coated by iron oxide. This suggests that kaolinite formed prior to iron oxide. IW8911-5, Entrada Sandstone Slick Rock Member, plane polarized light.

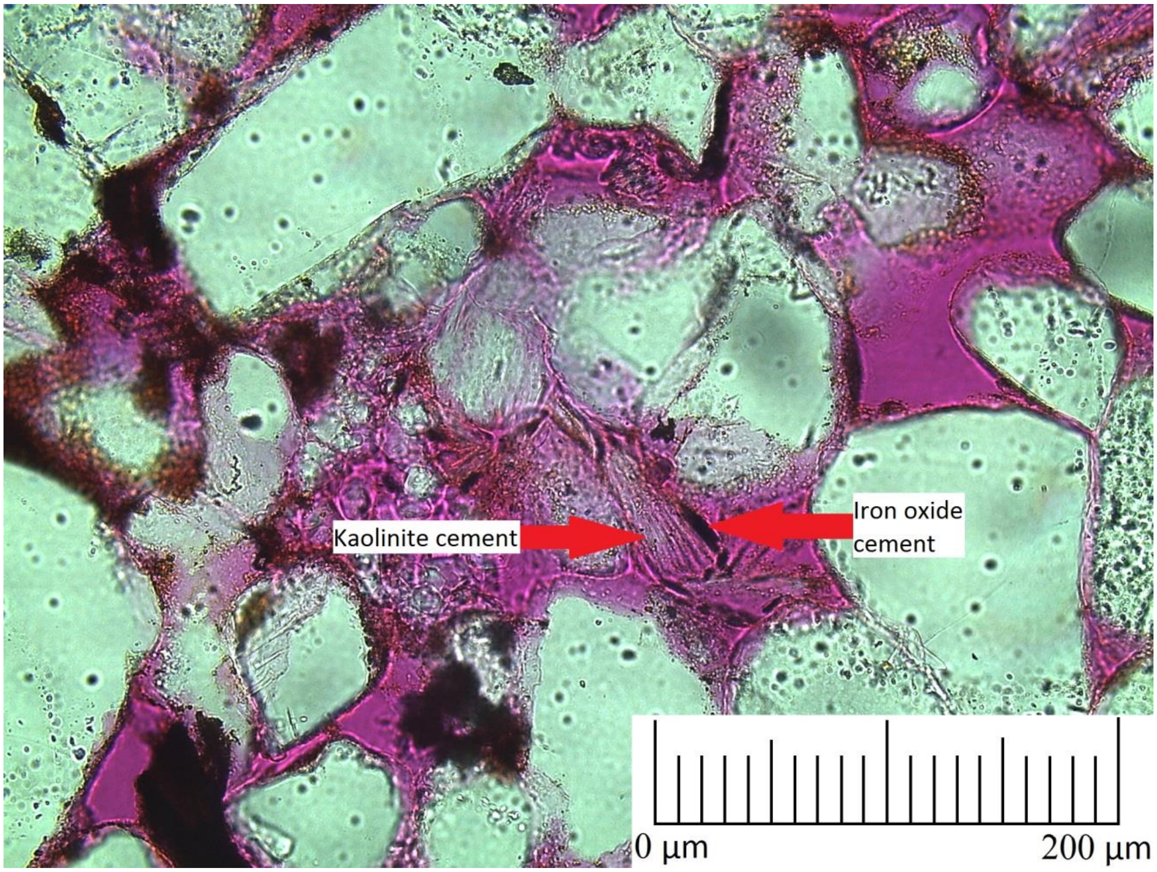

Figure 57. Thin-section photomicrograph showing authigenic kaolinite coated by iron oxide, suggesting that kaolinite precipitated prior to iron oxide. The texture of kaolinite cement is large books. UM-31312-19, Navajo Sandstone, plane polarized light.

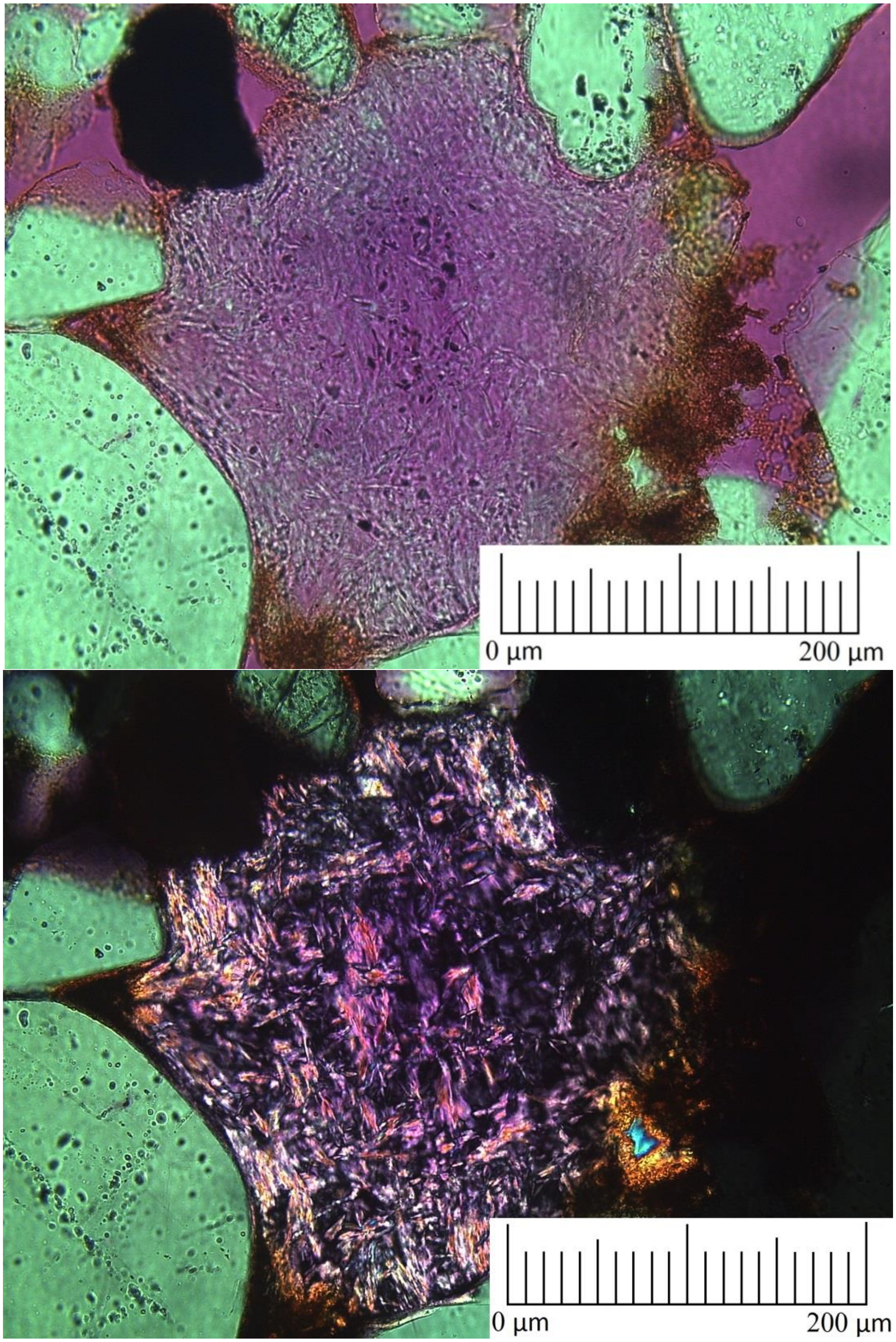

Figure 58. Thin-section photomicrograph showing a kaolinite replaced sericitized feldspar grain coated with iron oxide cement. This relationship suggests that kaolinite formed prior to iron oxide. UM-31312-19, Navajo Sandstone, plane polarized light above and cross polarized light below.

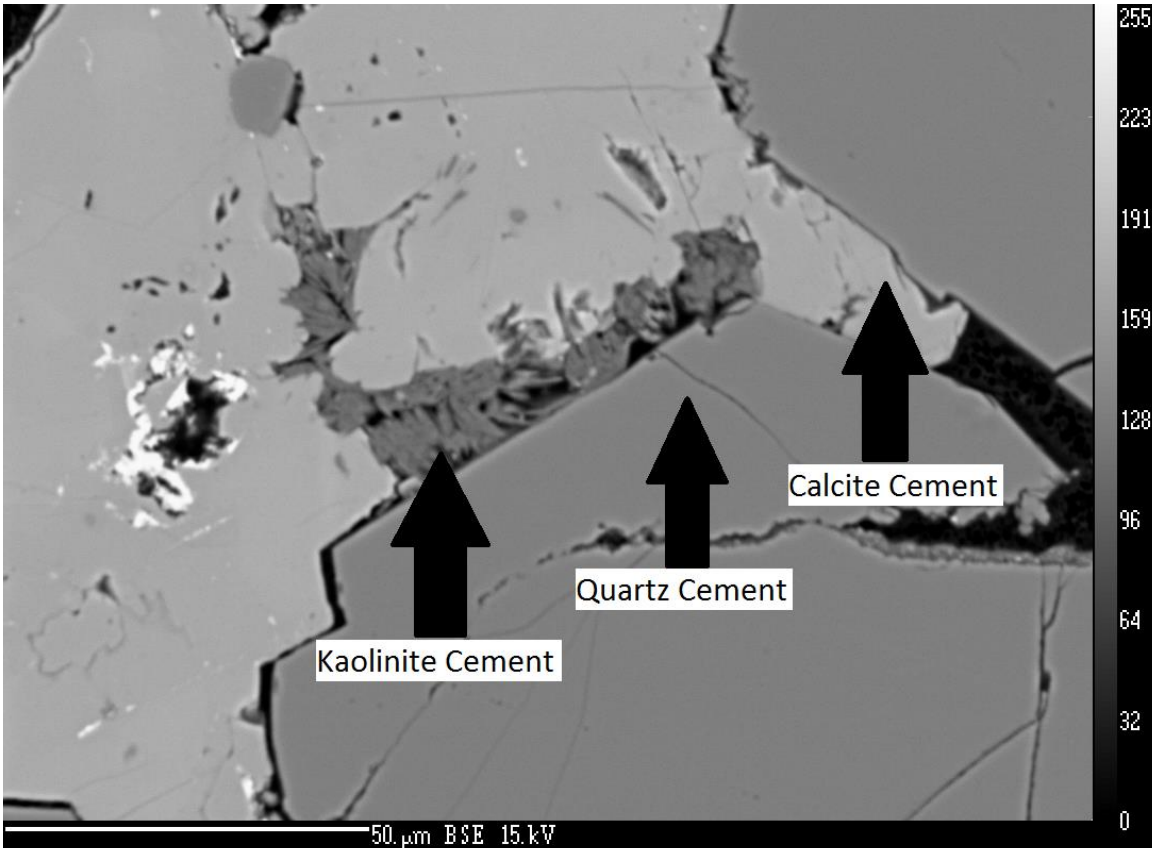

Figure 59. Back-scattered electron image showing pore-filling kaolinite that precipitated outside of a quartz overgrowth. This suggests that kaolinite formed after quartz. The kaolinite cement is surrounded by calcite, suggesting that the kaolinite formed prior to calcite cement. IW-31112-2A, Entrada Sandstone Earthy Member, backscattered electron image.

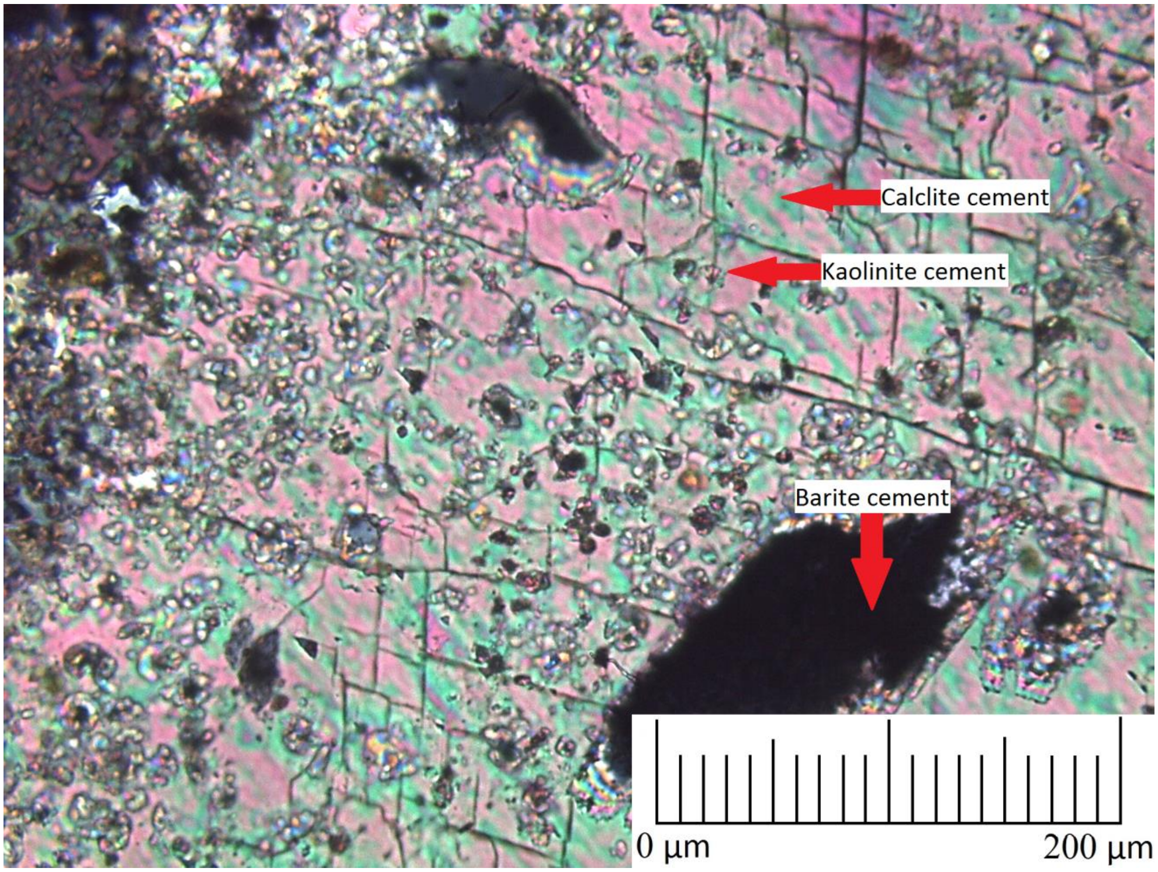

Figure 60. Thin-section photomicrograph showing a fracture that has been mineralized with barite, kaolinite, and calcite cements. Because the kaolinite and barite are encased in calcite, the calcite probably formed after the barite and kaolinite. IW-31112-1, Entrada Sandstone Earthy Member, crossed polarized light.

Pressure Solution

Pressure solution is present in the Carmel Formation and the Entrada Sandstone. Stylolites in the Co-op Creek Member are present both parallel and perpendicular to bedding, suggesting a combination of burial and tectonic influence. Stylolites cut through fracture-filling calcite, demonstrating that pressure solution occurred after the calcite fracture-fill (Fig. 61). However, some fractures cut through stylolites, indicating that a stage of fracturing and calcite mineralization occurred after the formation of stylolites (Fig. 62). Solution seams are present in the Earthy Member of the Entrada

Sandstone within matrix-rich areas, but their exact timing is difficult to determine (Fig. 63).

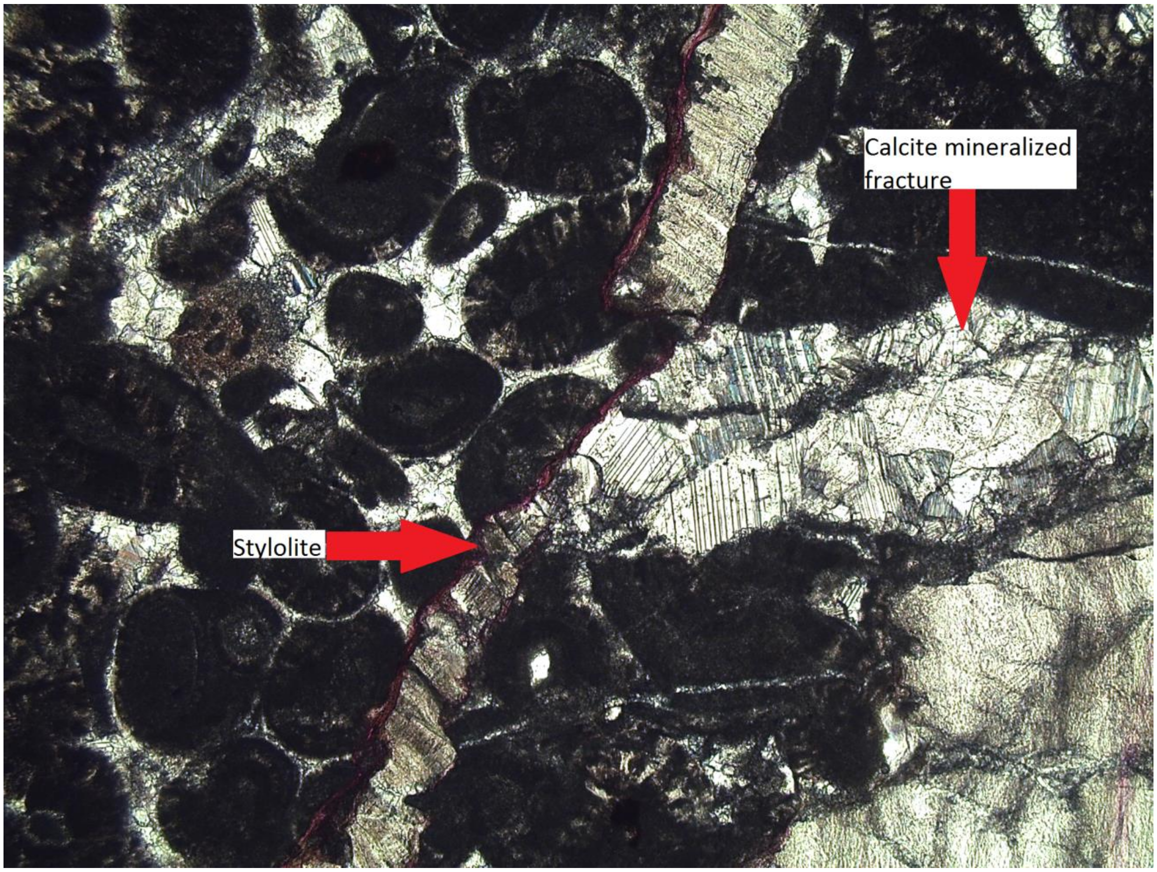

Figure 61. Thin-section photomicrograph showing a calcite-filled fracture (not to be confused with the similar looking bivalve shell fragment in the lower right corner) being crosscut by a stylolite, demonstrating that stylolite pressure solution occurred after calcite fracture-fill cementation. UM-102211-G, Carmel Formation Co-op Creek Member, plane polarized light.

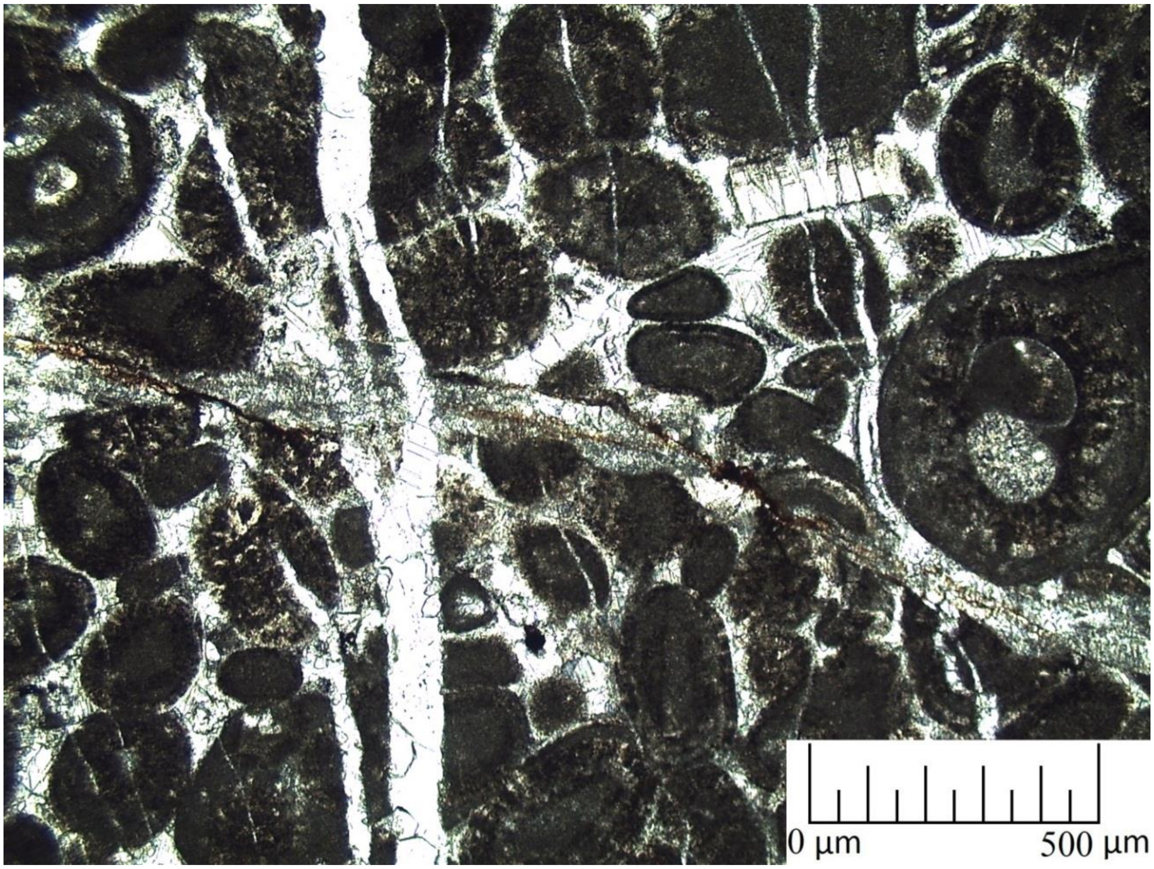

Figure 62. Thin-section photomicrograph showing a calcite-filled opening-mode fracture crosscutting a stylolite, indicating that the fracture formed after the stylolite. UM-102211-G, Carmel Formation Co-op Creek Member, plane polarized light.

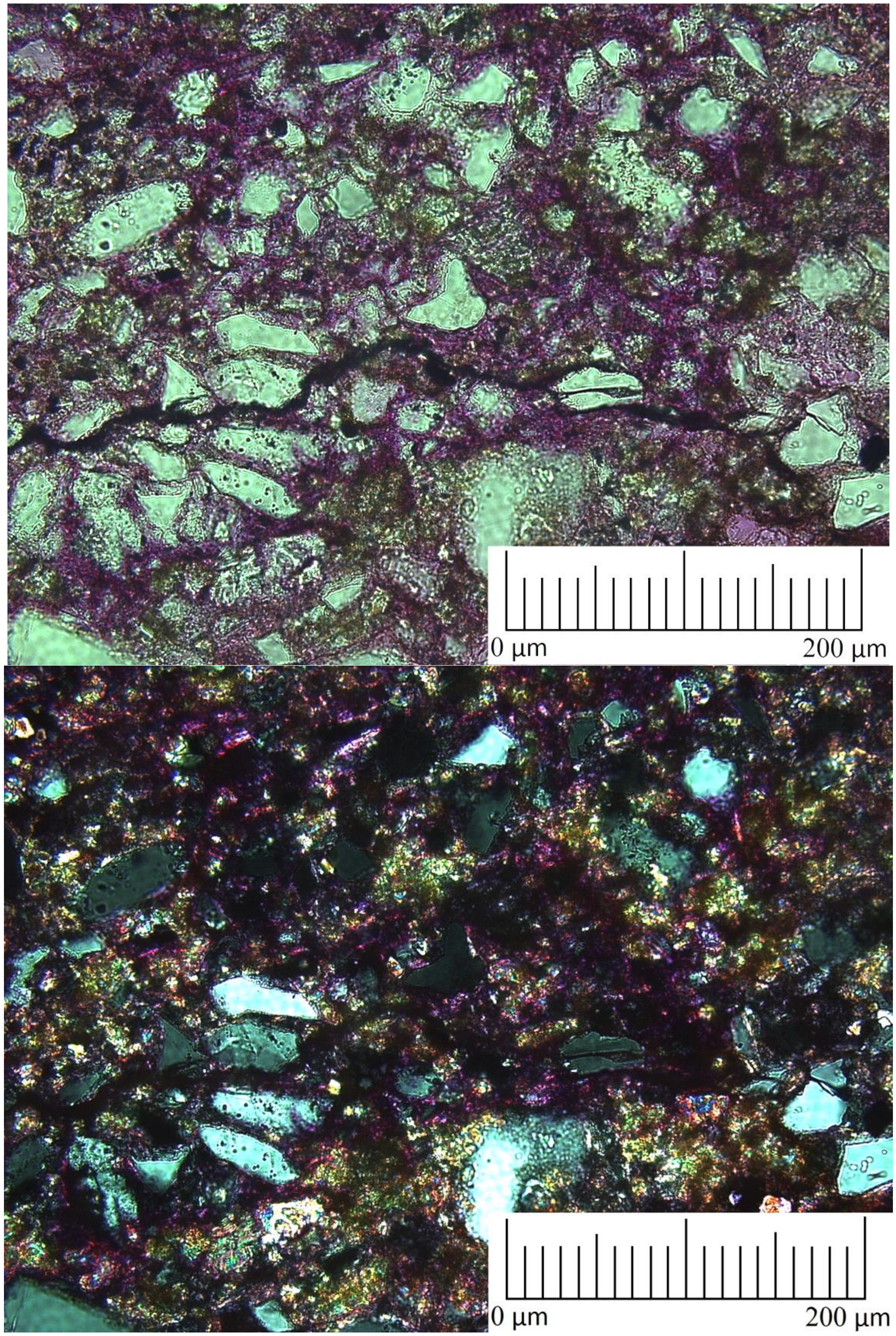

Figure 63. Thin-section photomicrograph depicting a solution seam cutting through the matrix-rich Earthy Member. The seam cuts through the iron oxide and calcite-rich matrix. IW8911-16, Entrada Sandstone Earthy Member, plane polarized light above and cross polarized light below.

Pyrite Cementation/Replacement

Iron oxide fracture-filling cement is present in both the Slick Rock and Earthy Members. The cubic nature of this iron oxide suggests that it was originally pyrite that was subsequently psuedomorphically replaced by iron oxide. This is confirmed by microprobe analysis, which detected small amounts of pyrite in the cores of iron oxide (Fig. 46). Pyrite is also present as a replacement of clay-rich grains within the Earthy and Slick Rock Members (Fig. 64).

The iron oxide pseudomorphs of pyrite are encased in calcite cement, suggesting that iron oxide replacement of pyrite occurred prior to calcite fracture-fill (Fig. 46).

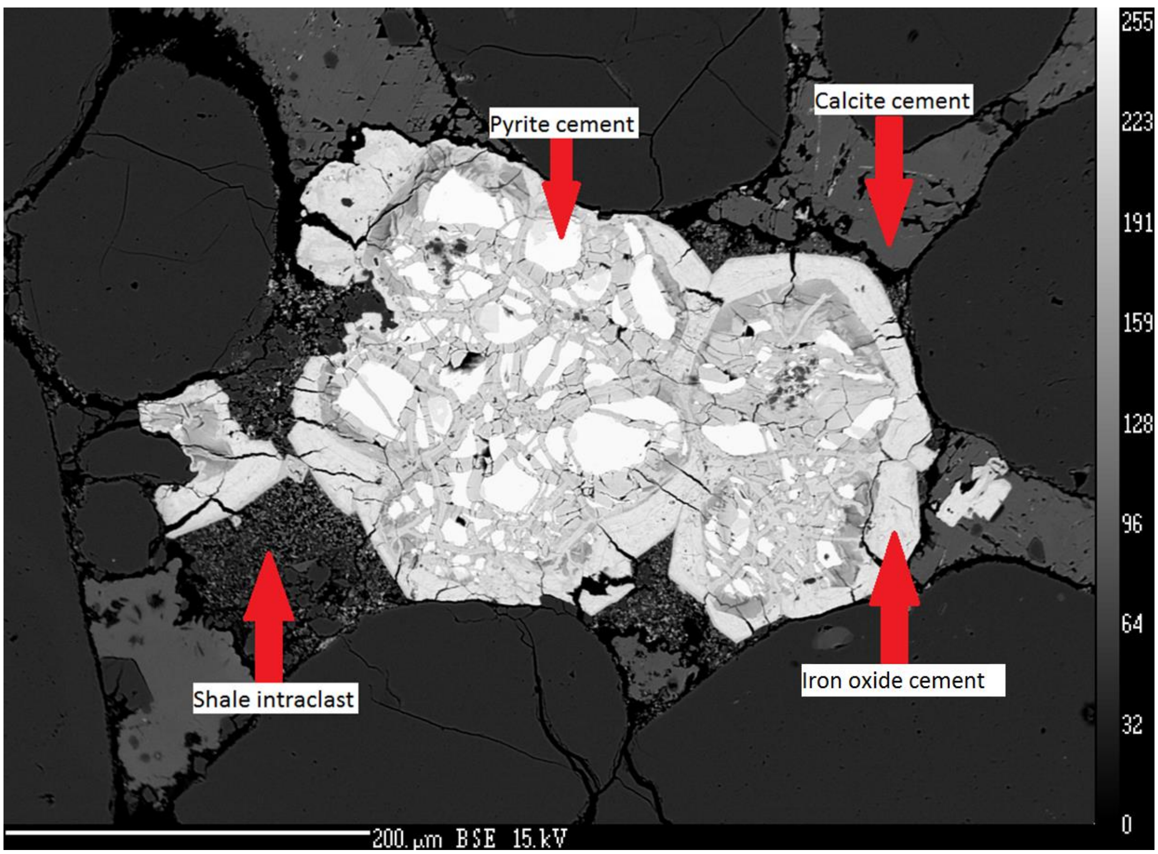

Figure 64. Photomicrograph showing a shale intraclast that was replaced by pyrite, which was later replaced by iron oxide. Pore-filling calcite cement encases the replaced grains, suggesting that calcite cement occurred after replacement. IW-31112-2A, Entrada Sandstone Earthy Member, backscattered electron image.

Barite Cement

Plumose barite is present as fracture-filling cement in the Earthy Member of the Entrada Sandstone and the Winsor Member of the Carmel Formation (Fig. 65). The barite is encased in calcite cement, suggesting that barite formed before calcite (Fig. 65). An alternative hypothesis to this is that barite replaced the calcite cement, although it is unlikely for replacing fluids to interact with the interior of calcite cement. The relationship between barite and iron oxide fracture-fills is difficult to determine optically. Garden et al. (2001) concluded that barite cementation in the Entrada Sandstone halted around the same time that kaolinite cementation ended, which was just prior to the end of reducing conditions. If this is the case, then barite cementation likely halted prior to the oxidizing conditions required for iron oxide cementation. Breit et al. (1990) indicated that the source of barium for the barite in the overlying Jurassic Morrison Formation in the northern Colorado Plateau was evaporites in the underlying Hermosa Formation. If evaporites provided the necessary ions for barite in the overlying Morison Formation, it seems logical that evaporites were also the source for barite in the Carmel Formation and Entrada Sandstone. Alternatively, evaporites in the Carmel Formation may have contributed as well.

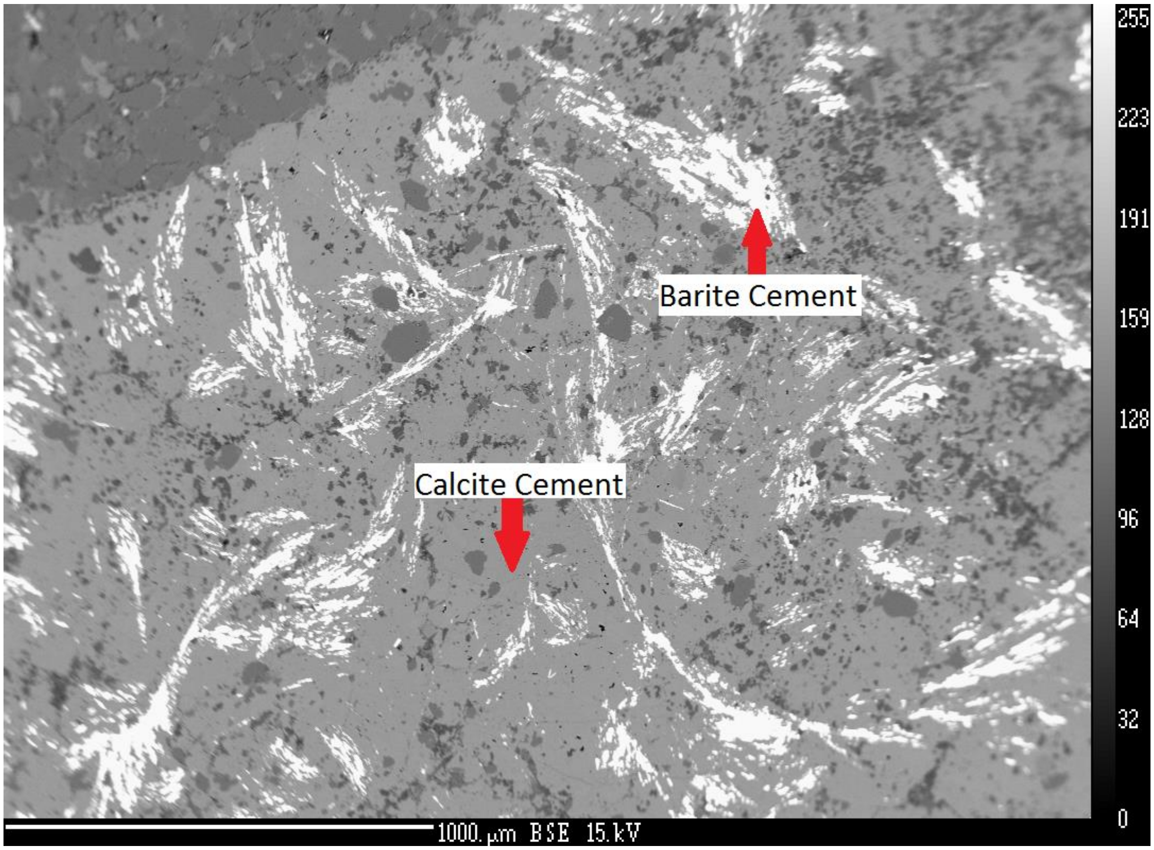

Figure 65. Back-scattered electron image of a fracture filled by authigenic barite and calcite. Because barite is encased in calcite the calcite probably formed after the barite. IW-81111-4A, Carmel Formation Winsor Member, backscattered electron image.

Gypsum Cement

Fibrous gypsum is present as a fracture-fill in the shale layers of the Earthy Member of the Entrada Sandstone. The fracture-filling gypsum is exclusive to the shale layers and is difficult to relate to other fracture-filling cements (Fig. 66).

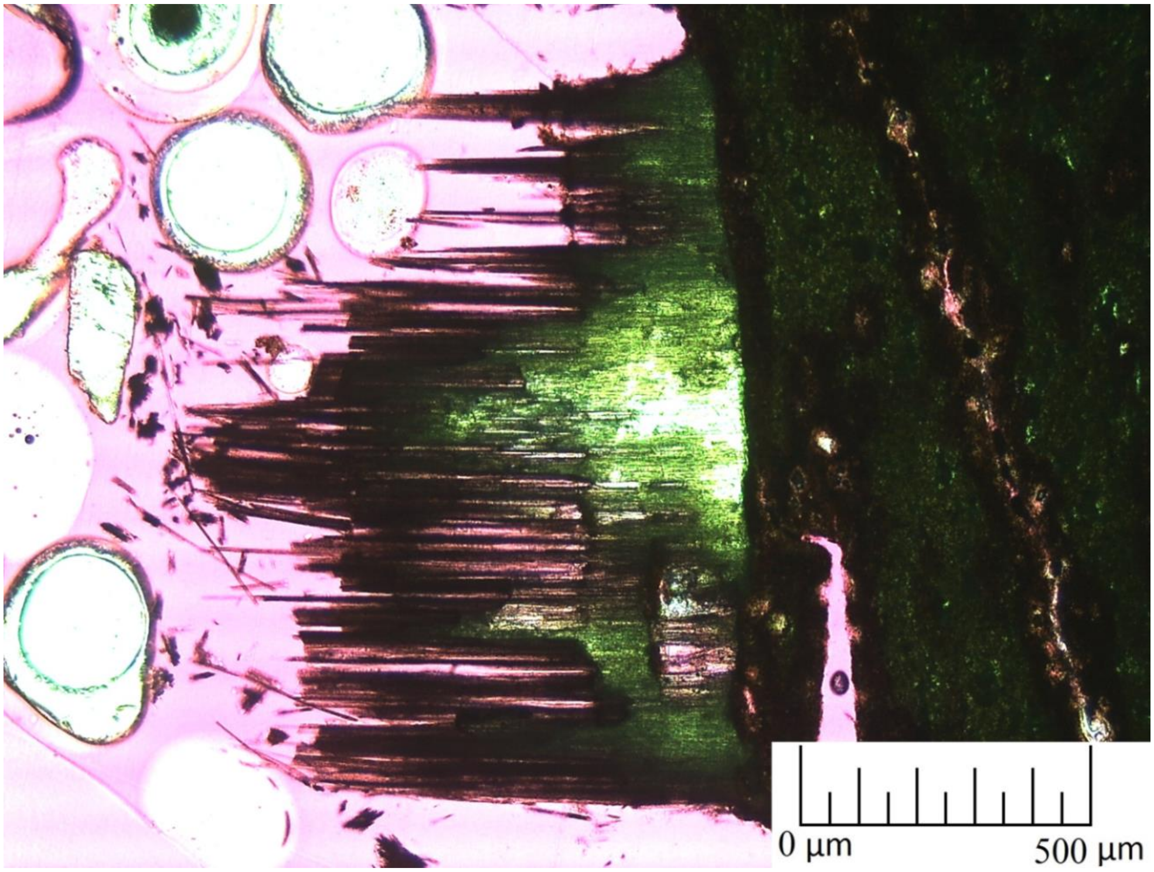

Figure 66. Thin-section photomicrograph showing fracture-filling gypsum within a shale. IW8911-9a, Entrada Sandstone Earthy Member, plane polarized light.

Calcite Cementation/Replacement

Calcite is present as pore- and fracture-filling cement throughout all of the units. The texture of the pore-filling calcite in the Carmel Formation varies, with equant, fibrous, blocky, and poikilotopic varieties present locally. Syntaxial overgrowths occur around echinoderms. Pore-filling cement in the Navajo and Entrada sandstone varies from poikilotopic, rimming grains, and at contacts between grains. The texture of the fracture-filling calcite is blocky. Within the Carmel Formation and Entrada Sandstone the matrix consists of calcite, demonstrating calcite replacement has occurred. However, also possible is the calcite matrix was depositional in origin.

Multiple calcite cementation events occurred during the diagenetic history. The equant textured calcite cement is encased in the blocky calcite cement, suggesting the equant cement formed first (Fig. 67). Likewise, fibrous textured calcite cement is encased by syntaxial overgrowths, suggesting the fibrous cement formed earlier (Fig. 68). Pore-filling iron oxide cement is covered by pore-filling calcite, indicating that iron oxide cementation occurred prior to the calcite precipitation (Fig. 69). Finally, fracture-filling iron oxide cement is covered by fracture-filling calcite, indicating that the iron oxide cement occurred prior to fracture-filling calcite (Fig. 46).

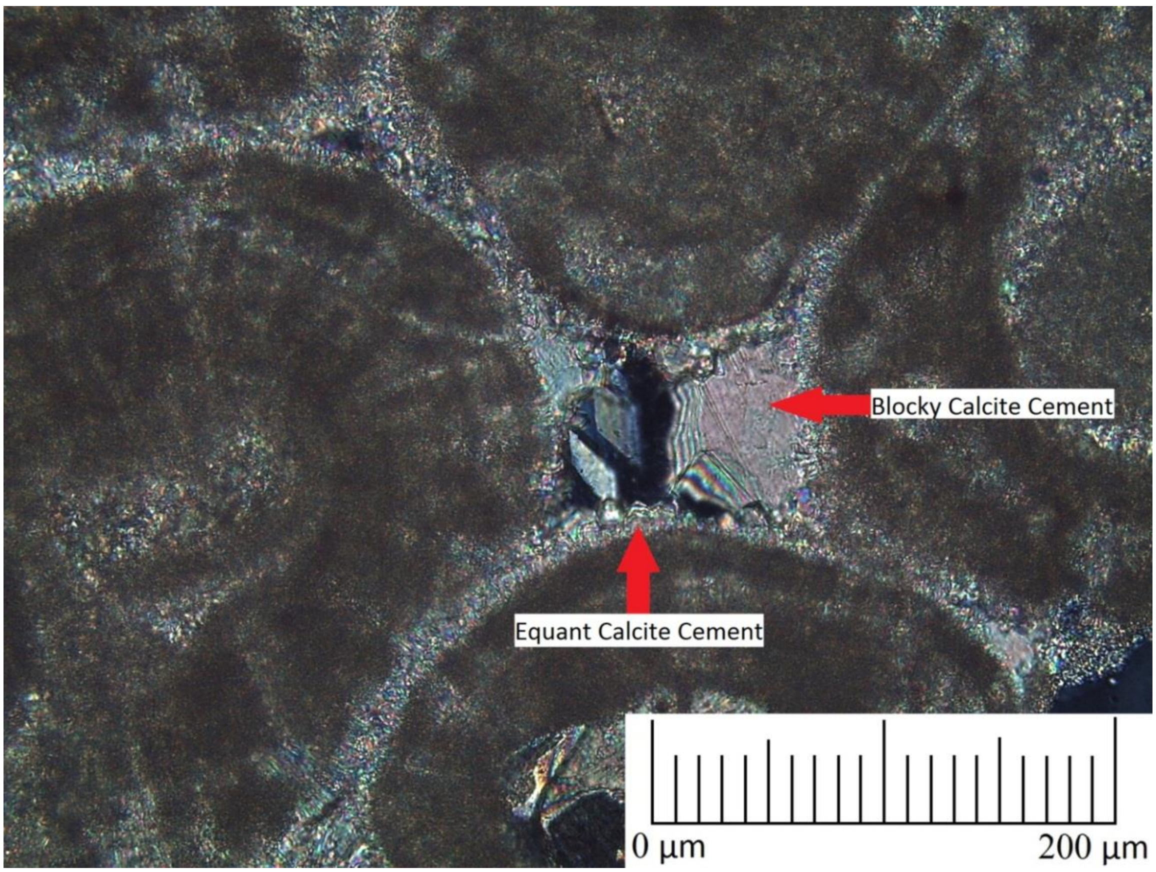

Figure 67. Thin-section photomicrograph showing equant calcite cement encased in blocky calcite cement, suggesting that the equant calcite formed first. UM-102311-G, Carmel Formation Co-op Creek Member, cross polarized light.

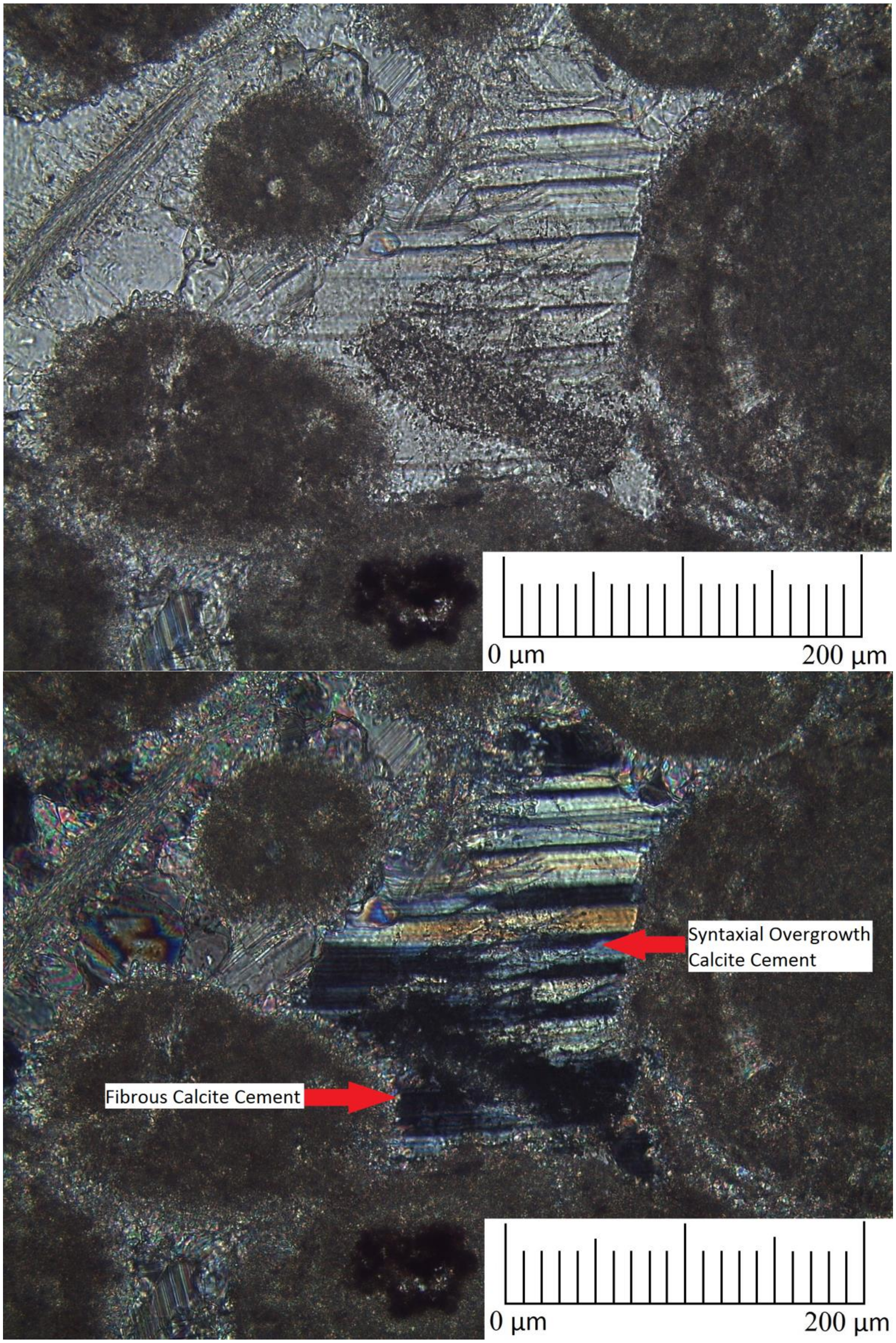

Figure 68. Thin-section photomicrograph showing fibrous calcite cement encased in syntaxial calcite cement, suggesting that the fibrous calcite formed first. UM-102311-G, Carmel Formation Co-op Creek, plane polarized light above and cross polarized light below.

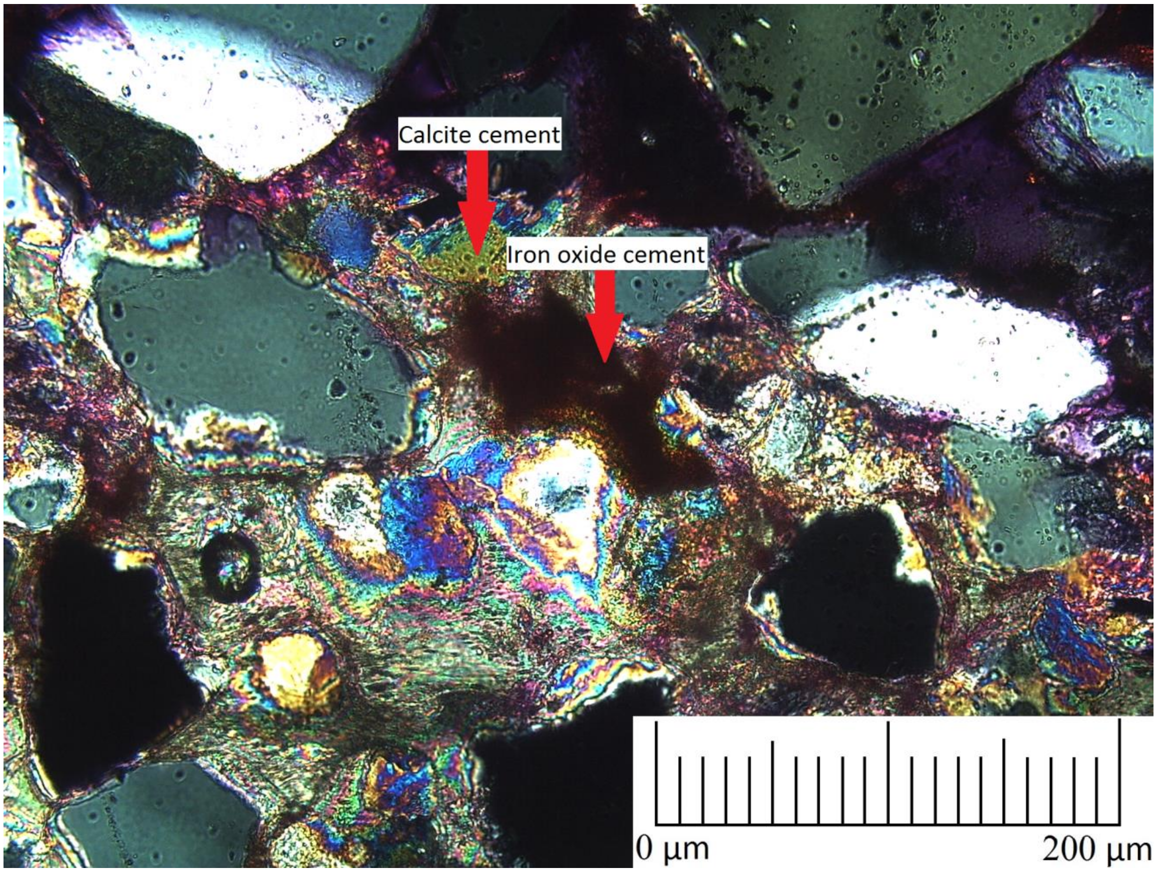

Figure 69. Thin-section photomicrograph showing pore-filling iron oxide cement encased in pore-filling calcite. This suggests that iron oxide cement formed prior to calcite. UM-102211-B, Navajo Sandstone, cross polarized light.

Quantitative Microprobe Analysis

Four thin sections were examined using quantitative microprobe analysis. Two of the thin sections contain mineralized fractures from the Carmel Formation. UM-31312-17 is a thin section from the Co-op Member of the Carmel Formation directly above the Navajo Sandstone interface at UMS-3. IW81111-4a is a thin section from the Winsor Member of the Carmel Formation directly below the Entrada Sandstone interface at ISS-3. The remaining two thin sections contain mineralized fractures from the Earthy Member of the Entrada Sandstone directly above the Slick Rock Member of the Entrada Sandstone interface at ISS-1.

Carmel Formation

Microprobe results show the pore-filling carbonate cement is slightly Ca-enriched dolomite, whereas the fracture-filling carbonate is calcite (Table 12, Fig. 70a). The calcite has two distinct chemical trends, a Ca-Mg trend and a Ca-Fe+Mn trend (Fig. 70b). Although there is no consistent relationship between elemental composition and position in the vein, there is a relationship with vein size. Small calcite veins (<50 μm) have a more Mg and less Fe and Mn compared to the larger calcite veins (>50 μm; Fig. 71).

Table 12. Elemental composition of carbonate cement from the Carmel Formation. Values are in mol% normalized to 100% and were computed from Wt% oxide recalculated as carbonate.

Sample	Sample description	SiO2	SO2	MgCO3	CaCO3	MnCO3	FeCO3	SrCO3	BaCO3	Na2O
mgco3-01	dolomite standard	0.06%	0.00%	49.26%	50.54%	0.04%	0.09%	0.01%	0.00%	0.00%
mgco3-02	dolomite standard	0.00%	0.02%	49.48%	50.21%	0.02%	0.17%	0.02%	0.04%	0.03%
caco3-01	calcite standard	0.06%	0.04%	0.06%	99.61%	0.19%	0.00%	0.00%	0.03%	0.02%
caco3-02	calcite standard	0.09%	0.00%	0.00%	99.71%	0.14%	0.00%	0.00%	0.04%	0.02%
IW-81111-4a-01	large calcite vein	0.00%	0.02%	0.43%	99.01%	0.11%	0.37%	0.06%	0.00%	0.00%
IW-81111-4a-02	large calcite vein	0.01%	0.02%	0.32%	99.31%	0.02%	0.27%	0.02%	0.00%	0.02%
IW-81111-4a-03	small calcite vein	0.24%	0.23%	3.30%	95.76%	0.15%	0.15%	0.10%	0.05%	0.02%
IW-81111-4a-04	dolomite pore-filling cement	0.71%	0.13%	45.08%	53.38%	0.20%	0.39%	0.04%	0.04%	0.02%
IW-81111-4a-05	small calcite vein	1.96%	0.16%	3.67%	93.53%	0.15%	0.43%	0.07%	0.02%	0.00%
IW-81111-4a-06	dolomite pore-filling cement	1.42%	0.11%	44.61%	51.31%	0.28%	2.18%	0.05%	0.00%	0.04%
IW-81111-4a-09	dolomite pore-filling cement	1.52%	0.16%	42.68%	52.40%	0.31%	2.58%	0.03%	0.00%	0.32%
IW-81111-4a-10	large calcite vein	0.64%	0.10%	0.74%	96.96%	0.07%	1.45%	0.00%	0.01%	0.04%
IW-81111-4a-11	large calcite vein	0.33%	0.10%	0.80%	97.11%	0.10%	1.54%	0.02%	0.00%	0.00%
IW-81111-4a-14	small calcite vein w/ mg	4.12%	0.25%	3.04%	92.13%	0.09%	0.20%	0.04%	0.07%	0.05%
IW-81111-4a-15	small calcite vein w/ mg	10.93%	0.26%	3.68%	84.49%	0.10%	0.47%	0.00%	0.05%	0.01%
UM-31312-17-01	large calcite vein inside dogtooth	0.01%	0.06%	1.54%	96.70%	0.68%	0.90%	0.00%	0.06%	0.05%
UM-31312-17-02	large calcite vein inside dogtooth	0.01%	0.05%	1.68%	96.40%	0.96%	0.86%	0.00%	0.00%	0.04%
UM-31312-17-03	large calcite vein outside dogtooth	0.05%	0.03%	0.92%	96.43%	0.94%	1.52%	0.02%	0.08%	0.01%
UM-31312-17-04	large calcite vein outside dogtooth	0.00%	0.02%	0.58%	97.38%	0.65%	1.36%	0.00%	0.00%	0.00%
UM-31312-17-05	small calcite vein	0.04%	0.00%	2.94%	96.64%	0.31%	0.04%	0.00%	0.03%	0.00%
UM-31312-17-06	small calcite vein	0.00%	0.10%	1.09%	95.63%	2.17%	0.94%	0.00%	0.03%	0.03%
UM-31312-17-07	dolomite pore-filling cement	2.34%	0.12%	46.25%	50.40%	0.19%	0.61%	0.00%	0.03%	0.06%
UM-31312-17-08	dolomite pore-filling cement	0.43%	0.11%	46.25%	52.68%	0.12%	0.30%	0.06%	0.00%	0.04%
UM-31312-17-09	dolomite pore-filling cement	0.89%	0.13%	46.46%	51.42%	0.31%	0.70%	0.02%	0.00%	0.07%
UM-31312-17-010	dolomite pore-filling cement	1.91%	0.08%	46.42%	50.65%	0.21%	0.61%	0.06%	0.00%	0.06%
UM-31312-17-011	small calcite vein	0.00%	0.26%	1.61%	95.53%	1.22%	1.20%	0.00%	0.09%	0.10%
UM-31312-17-012	small calcite vein	0.04%	0.39%	1.57%	95.45%	1.26%	1.21%	0.00%	0.04%	0.05%
mgco3-03	dolomite standard	0.02%	0.00%	49.41%	50.35%	0.01%	0.14%	0.03%	0.04%	0.00%
mgco3-04	dolomite standard	0.00%	0.03%	49.51%	50.31%	0.03%	0.08%	0.05%	0.00%	0.00%
caco3-03	calcite standard	0.02%	0.00%	0.00%	99.77%	0.14%	0.05%	0.01%	0.00%	0.00%
caco3-04	calcite standard	0.05%	0.03%	0.00%	99.72%	0.12%	0.06%	0.02%	0.00%	0.00%

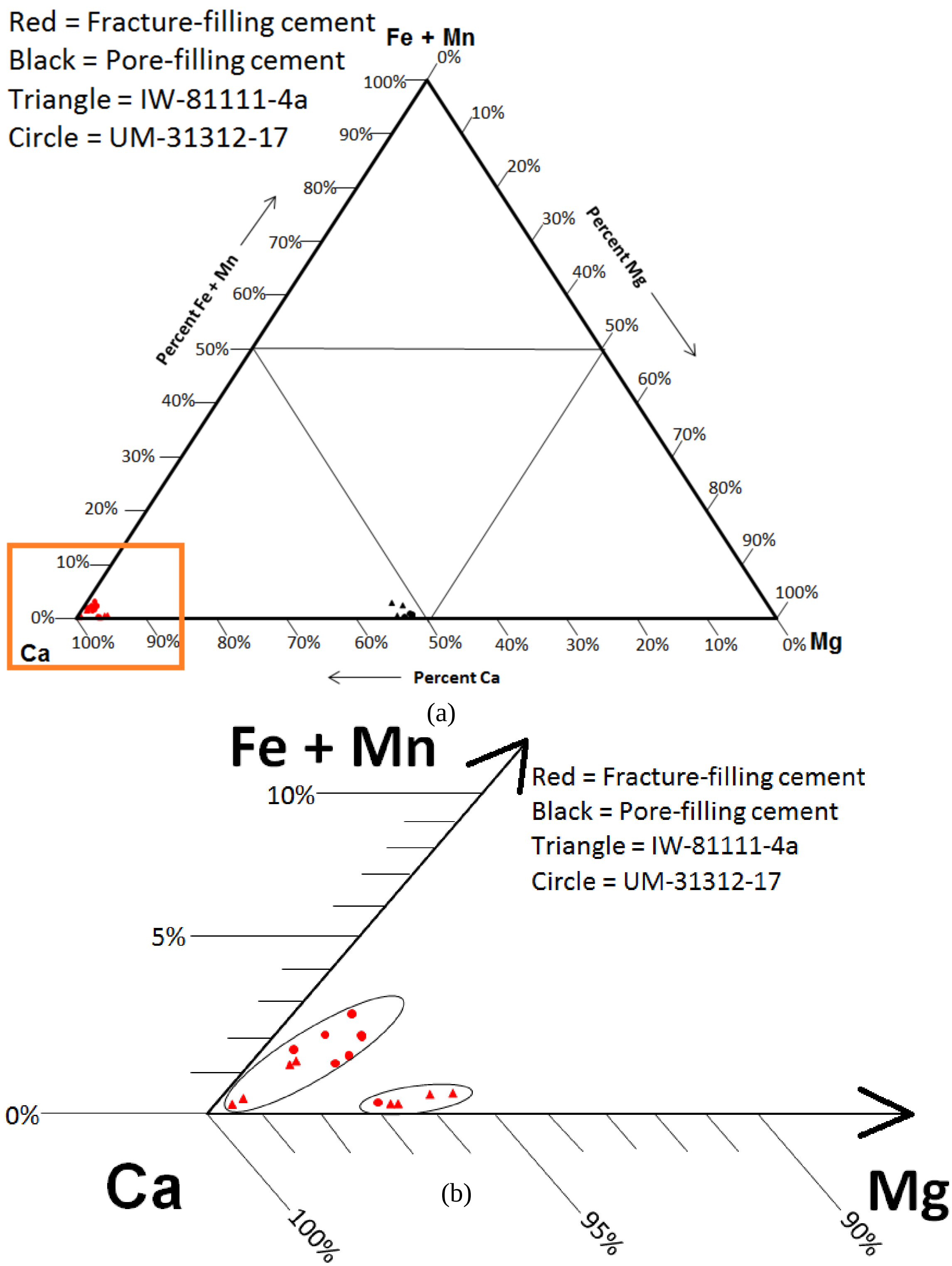

Figure 70. (a) Ternary diagram showing the elemental composition of authigenic calcite and dolomite in the Carmel Formation. (b) An enlarged version of the highlighted region from Fig. 70a. Note the existence of two distinct chemical trends in the calcite.

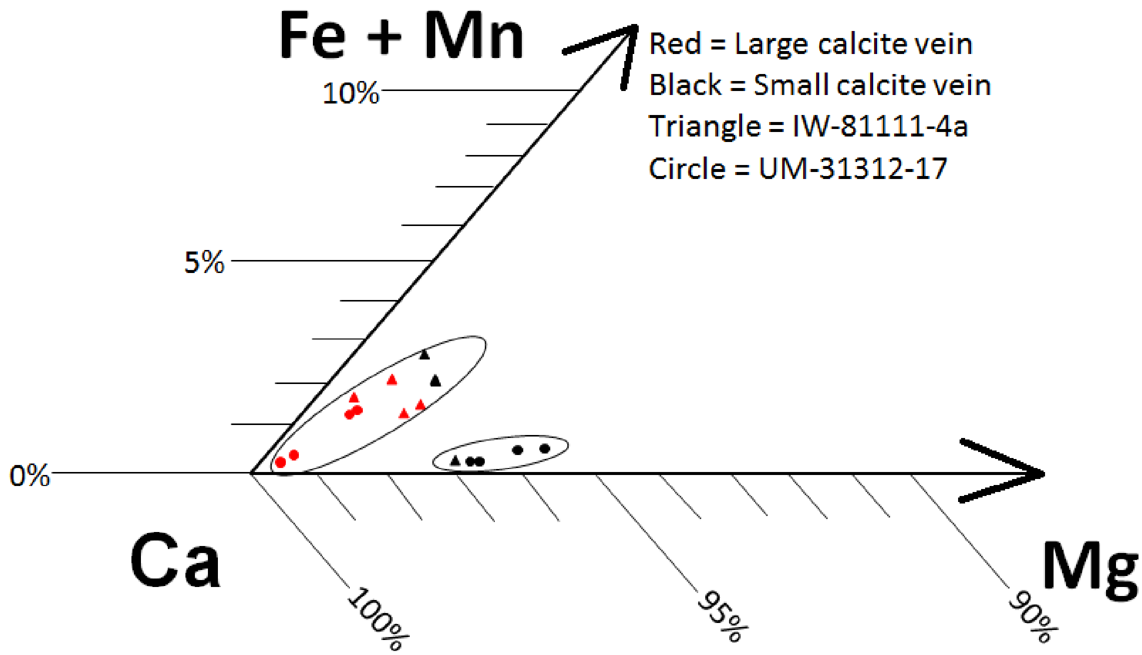

Figure 71. Ternary diagram showing relationship between calcite composition and vein size in mineralized fractures from the Carmel Formation. Small calcite veins are <50 µm and large calcite veins are >50 µm.

<u>Entrada Sandstone</u>

The pore-filling and fracture filling carbonate in the Entrada Sandstone is near end-member calcite, showing a trend of enrichment in Fe and Mn (Table 13, Fig. 72). No distinct chemical difference exists between the pore-filling and fracture-filling calcite cement. Veins of different sizes also did not contain a distinct chemical difference. Likewise, no strong chemical relationship could be found between the interior and exterior of calcite-filled fractures.

Table 13. Quantitative microprobe analysis of carbonate cement from the Entrada Sandstone Formation. Values are in mol% normalized to 100% and were computed from Wt% oxide recalculated as carbonate.

Sample	Sample description	SiO2	SO2	MgCO3	CaCO3	MnCO3	FeCO3	SrCO3	BaCO3	Na2O
mgco3-01	dolomite standard	0.07%	0.00%	49.98%	49.74%	0.01%	0.12%	0.07%	0.00%	0.01%
mgco3-02	dolomite standard	0.01%	0.01%	50.34%	49.46%	0.03%	0.11%	0.01%	0.03%	0.00%
caco3-01	calcite standard	0.06%	0.04%	0.00%	99.78%	0.10%	0.00%	0.03%	0.00%	0.00%
caco3-02	calcite standard	0.04%	0.00%	0.02%	99.82%	0.07%	0.00%	0.03%	0.02%	0.00%
IW-31112-2A-019	pore-filling calcite	0.11%	0.00%	0.53%	99.08%	0.04%	0.20%	0.04%	0.00%	0.00%
IW-31112-2A-020	pore-filling calcite	0.21%	0.07%	0.86%	98.13%	0.18%	0.55%	0.00%	0.00%	0.00%
IW-31112-2A-021	pore-filling calcite	0.29%	0.02%	0.80%	98.05%	0.24%	0.57%	0.00%	0.03%	0.00%
IW-31112-2A-022	pore-filling calcite	0.00%	0.02%	0.76%	98.88%	0.21%	0.05%	0.00%	0.04%	0.03%
IW-31112-2A-023	large calcite vein	0.00%	0.02%	0.38%	99.11%	0.01%	0.44%	0.03%	0.02%	0.00%
IW-31112-2A-024	large calcite vein	0.02%	0.01%	0.29%	99.24%	0.05%	0.35%	0.05%	0.00%	0.00%
IW-31112-2A-025	large calcite vein	0.02%	0.00%	1.12%	98.37%	0.36%	0.05%	0.04%	0.03%	0.01%
IW-31112-2A-026	large calcite vein	0.00%	0.05%	0.78%	98.42%	0.26%	0.37%	0.00%	0.07%	0.06%
IW-31112-2A-027	pore-filling calcite	0.23%	0.03%	0.90%	97.47%	0.14%	1.18%	0.04%	0.00%	0.00%
IW-31112-2A-028	pore-filling calcite	0.40%	0.04%	0.61%	98.80%	0.03%	0.06%	0.00%	0.06%	0.00%
IW-31112-2A-029	pore-filling calcite	0.10%	0.00%	0.99%	97.96%	0.16%	0.73%	0.05%	0.00%	0.00%
IW-31112-2A-030	pore-filling calcite	0.13%	0.03%	1.14%	98.14%	0.37%	0.13%	0.06%	0.00%	0.01%
IW-31112-1-01	large calcite vein	0.06%	0.02%	1.23%	97.01%	0.30%	1.33%	0.04%	0.00%	0.00%
IW-31112-1-02	large calcite vein	0.00%	0.00%	1.15%	97.49%	0.36%	1.01%	0.00%	0.00%	0.00%
IW-31112-1-03	large calcite vein	0.01%	0.05%	0.99%	97.38%	0.20%	1.26%	0.04%	0.08%	0.00%
IW-31112-1-04	large calcite vein	0.05%	0.00%	0.89%	97.78%	0.25%	0.94%	0.00%	0.08%	0.00%
IW-31112-1-05	large calcite vein	0.04%	0.04%	0.98%	97.70%	0.21%	1.01%	0.02%	0.02%	0.00%
IW-31112-1-06	large calcite vein	0.08%	0.02%	1.02%	97.41%	0.21%	1.15%	0.05%	0.06%	0.00%
IW-31112-1-07	pore-filling calcite	0.07%	0.01%	0.49%	99.03%	0.10%	0.11%	0.17%	0.02%	0.00%
IW-31112-1-08	pore-filling calcite	0.53%	0.06%	0.93%	97.96%	0.39%	0.10%	0.01%	0.00%	0.02%
IW-31112-1-09	pore-filling calcite	0.86%	0.37%	0.64%	97.84%	0.00%	0.26%	0.02%	0.00%	0.03%
IW-31112-1-011	pore-filling calcite	1.90%	0.12%	0.80%	94.15%	0.15%	2.86%	0.01%	0.00%	0.01%
IW-31112-1-012	pore-filling calcite	0.50%	0.24%	0.45%	98.55%	0.08%	0.19%	0.00%	0.00%	0.00%
IW-31112-1-013	pore-filling calcite	0.21%	0.08%	1.00%	98.38%	0.00%	0.08%	0.21%	0.00%	0.04%
IW-31112-1-014	pore-filling calcite	2.84%	0.52%	0.98%	95.30%	0.02%	0.23%	0.03%	0.07%	0.00%
mgco3-03	dolomite standard	0.07%	0.00%	50.26%	49.50%	0.05%	0.09%	0.00%	0.00%	0.02%
mgco3-04	dolomite standard	0.01%	0.01%	50.33%	49.41%	0.03%	0.21%	0.00%	0.00%	0.00%
caco3-03	calcite standard	0.02%	0.00%	0.00%	99.74%	0.13%	0.00%	0.00%	0.06%	0.06%
caco3-04	calcite standard	0.04%	0.05%	0.02%	99.68%	0.15%	0.03%	0.03%	0.00%	0.00%

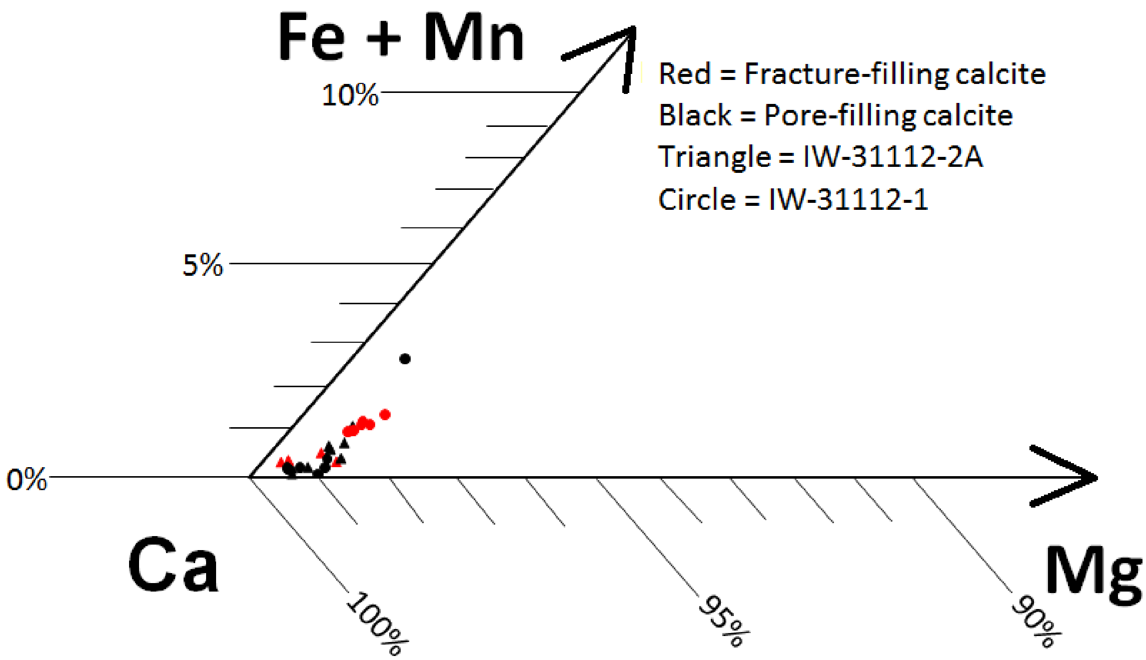

Figure 72. Ternary diagram showing the elemental composition of calcite cement in the Entrada Sandstone. The calcite is near end-member in composition, with a trend line defined by minor variation in Fe and Mn content.

Stable Isotopes

Stable isotope analysis was performed on calcite veins to help determine precipitation conditions (Table 14, Fig. 73). $\delta^{13}C$ and $\delta^{18}O$ were analyzed for five veins from the Co-op Member of the Carmel Formation directly above the Navajo Sandstone interface at UMS-1 and UMS-3. Two veins were analyzed from the Winsor Member of the Carmel Formation directly below the Entrada Sandstone interface at ISS-3, although only one vein produced reliable results. Five veins were analyzed from the Earthy Member of the Entrada Sandstone directly above the Slick Rock Member of the Entrada Sandstone interface at ISS-1.

Table 14. Corrected $\delta^{13}C$ and $\delta^{18}O$ of calcite-filled fractures. Samples EE-3-1 and EE-3-2 are from the same vein but come from different locations, as with EE-4-1 and EE-4-2.

Sample	Member/Formation	Study Area	$\delta^{13}C$ PDB	$\delta^{18}O$ PDB	$\delta^{18}O$ SMOW
CC-1	Co-op Creek/Carmel	UMS-1	-0.39	-14.26	16.16
CC-2	Co-op Creek/Carmel	UMS-1	-1.22	-15.02	15.38
CC-3	Co-op Creek/Carmel	UMS-3	-2.37	-15.92	14.45
CC-4	Co-op Creek/Carmel	UMS-1	1.66	-16.01	14.35
CC-5	Co-op Creek/Carmel	UMS-1	-0.45	-12.99	17.47
CW-1	Winsor/Carmel	ISS-3	-5.98	-14.78	15.63
EE-1	Earthy/Entrada	ISS-1	-5.52	-14.71	15.69
EE-2	Earthy/Entrada	ISS-1	-3.59	-16.02	14.35
EE-3-1	Earthy/Entrada	ISS-1	-6.61	-15.30	15.08
EE-3-2	Earthy/Entrada	ISS-1	-5.13	-14.79	15.62
EE-4-1	Earthy/Entrada	ISS-1	-3.84	-15.01	15.39
EE-4-2	Earthy/Entrada	ISS-1	-4.15	-15.44	14.94
EE-5	Earthy/Entrada	ISS-1	-4.25	-13.58	16.86

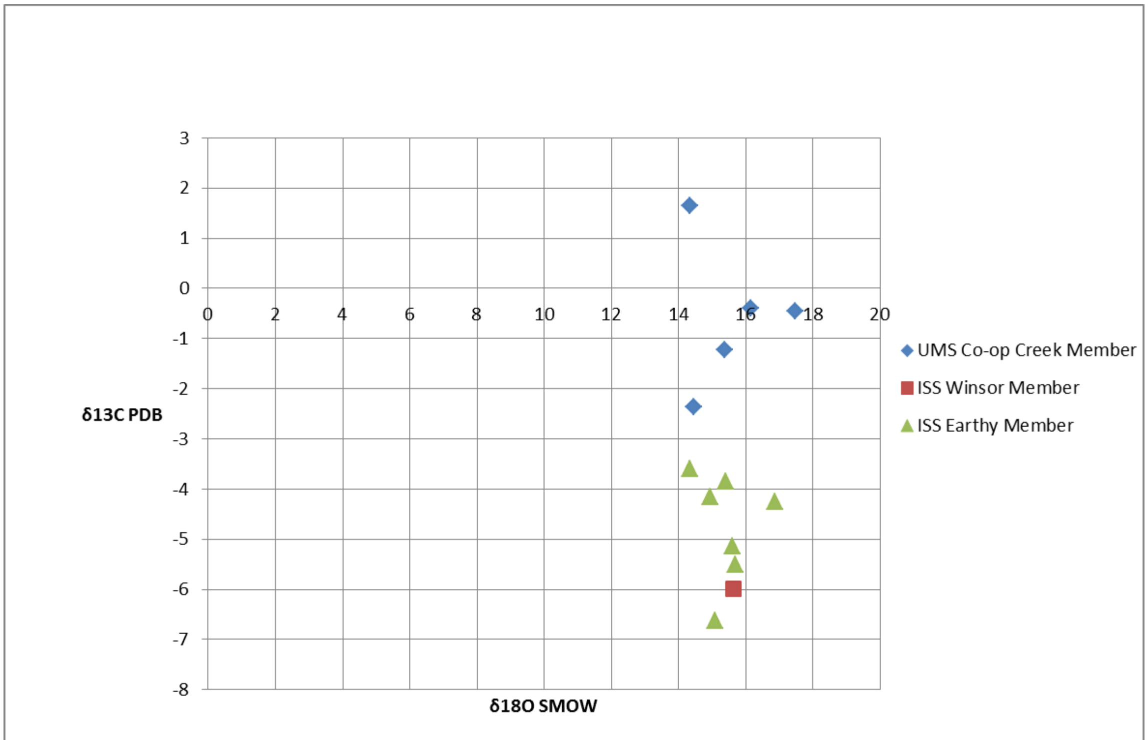

Figure 73. Corrected $\delta^{13}C$ and $\delta^{18}O$ of calcite fractures in the Carmel Formation and Earthy Member of the Entrada Sandstone.

$\delta^{18}O_{SMOW}$ of the calcite fractures in both the Carmel Formation and the Earthy Member of the Entrada Sandstone range from 14.35 to 17.47‰. The $\delta^{13}C_{PDB}$ of the fracture-filling calcite in the Co-op Creek Member of the Carmel Formation ranges from -2.37 to 1.66‰, and in the Winsor Member of the Carmel Formation and the Earthy

Member of the Entrada Sandstone ranges from -6.61 to -3.59‰. The $\delta^{18}O$ appears to be relatively consistent between the Carmel Formation and Entrada Sandstone, however, the $\delta^{13}C$ varies considerable. The consistent $\delta^{18}O$ among the calcite veins of the Carmel Formation and Entrada Sandstone suggests the veins precipitated from fluids with similar $\delta^{18}O$ signatures and temperatures. The large spread in $\delta^{13}C$ values between the Earthy Member of the Entrada Sandstone and the Co-op Creek Member of the Carmel Formation suggests the calcite veins of each unit precipitated from fluids of different $\delta^{13}C$ signatures.

The $\delta^{18}O$ of calcite cement alone does not indicate the exact conditions at which the calcite formed, however the value can be used to show the possible range of conditions from which it may have formed. This can be represented graphically by using the $\delta^{18}O$ value from the calcite cement to plot the isotopic water composition the calcite precipitated from as a function of temperature (Fig. 74). This is performed using the fractionation relationship:

$$1000 \ln \alpha_{\text{calcite-water}} = (2.78 \text{ X } 10^6 / T^2) - 2.89$$

This is a slightly modified version of the original equation from O'Neil et al. (1969); the last coefficient has been changed from 3.39×10^{-3} to 2.89×10^{-3} based on improved data (O'Neil et al. 1975).

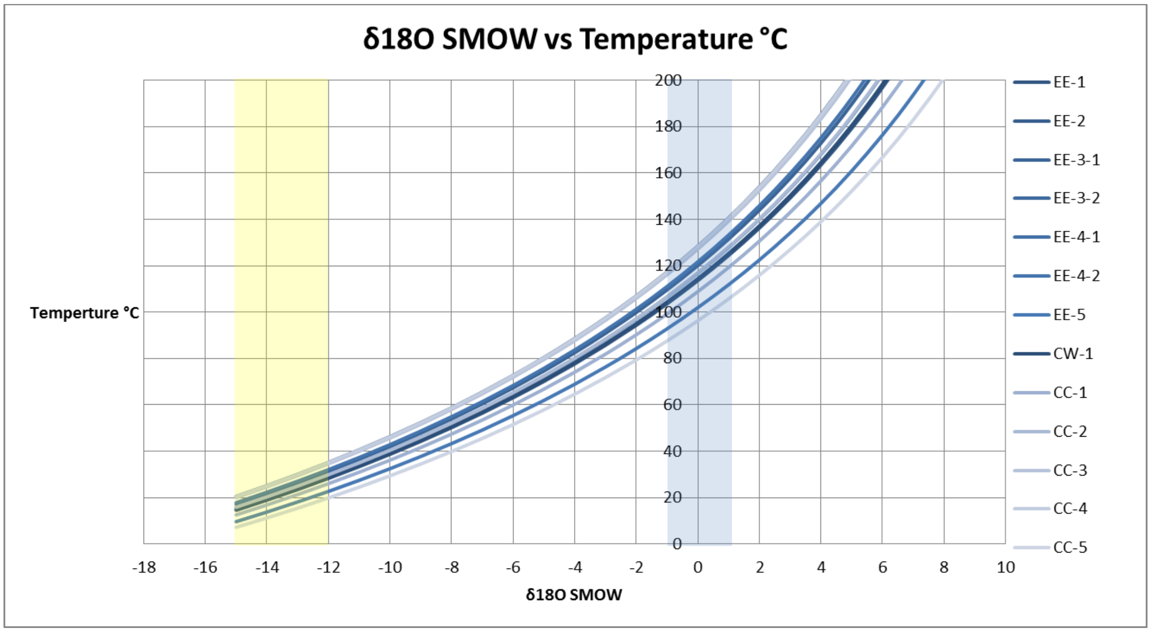

Figure 74. Possible combinations of water composition and temperature for precipitation of calcite in fractures above the reservoir-caprock interfaces. The blue box represents the $\delta^{18}O$ composition of present day seawater from Criss (1999). This range is interpreted to be similar to Jurassic seawater (see text). The yellow box is the $\delta^{18}O$ composition of meteoric water of southeast Utah from Spangler et al. (1996).

Because the Carmel Seaway existed during the deposition of the Carmel Formation and the Entrada Sandstone it is possible that the pore-water involved in calcite precipitation was seawater, or slightly modified seawater. Although ocean chemistry has shifted over geologic time, $\delta^{18}O$ carbonate shells of middle Jurassic marine organisms indicate that the $\delta^{18}O$ of seawater during the middle Jurassic was likely fairly similar to that of today's oceans (Fig. 75). Thus, if seawater was the source, the calcite would have precipitated at relatively high temperatures, between 90°C and 140°C (Fig. 74). This demonstrates that if the calcite did form from seawater, it would have had to occur at considerable depths. If the calcite veins formed from seawater, the $\delta^{13}C$ would be enriched (Veizer et al., 1999). The $\delta^{13}C$-enriched veins support the theory that the seawater is the source fluid, however seawater alone does not explain the $\delta^{13}C$-depleted veins.

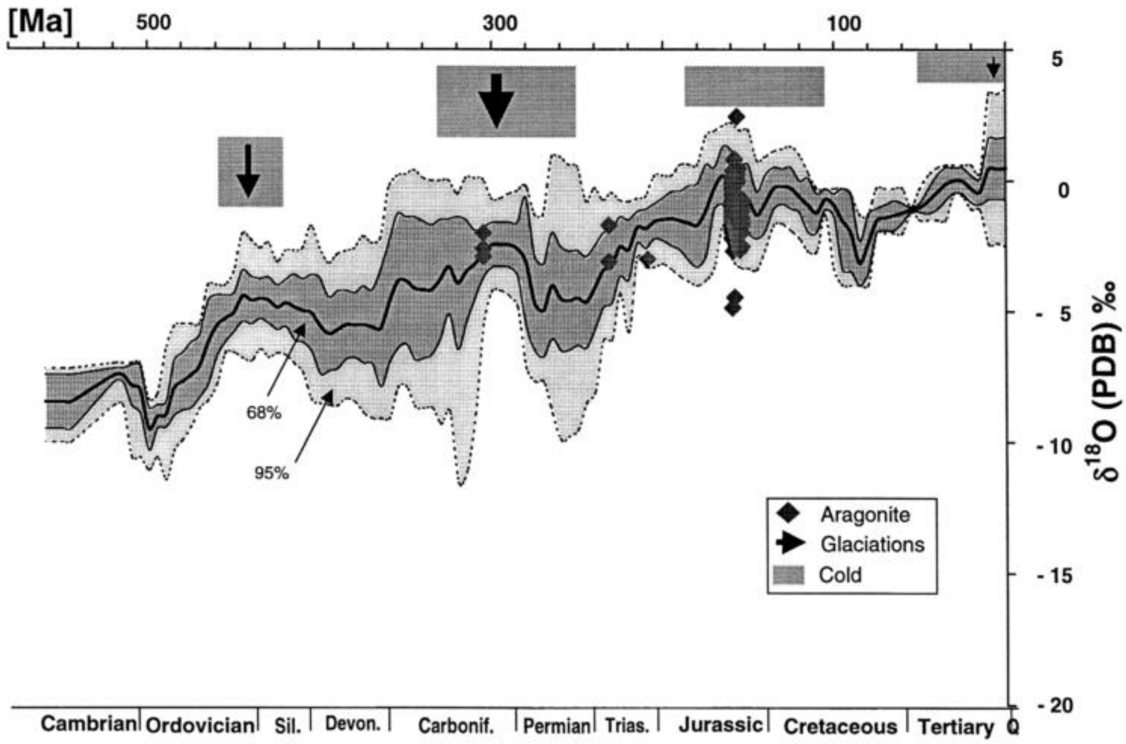

Figure 75. Graph showing the $\delta^{18}O$ of carbonate shells over geologic time. The $\delta^{18}O$ of shells during the middle Jurassic are similar to those of today, suggesting the possibility that the $\delta^{18}O$ of ocean water is similar as well. The $\delta^{18}O_{SMOW}$ of shells during the middle Jurassic are around 30‰, possibly having an enrichment effect on the calcite-filled factures. From Veizer et al. (1999).

Davatzes et al. (2003) concluded the middle Jurassic units in the Chimney Rock area (also located on the eastern San Rafael Swell, ~40 km north of the Uneva Mine Canyon study area) were once buried to a depth of 3 to 4 km (Fig. 76). Using a typical geothermal gradient of 30 °C per km of depth, the maximum burial temperature would have been between 90 and 120 °C. This is consistent with Nuccio and Condon (1996) whom concluded that that the middle Jurassic units in the Green River area (~25 km east of the Uneva Mine Canyon study site) were once buried to a depth of ~2.9 km, achieving a maximum burial temperature of close to 120°C (Fig. 77). This indicates that proper conditions existed for calcite to precipitate from seawater at high temperatures.

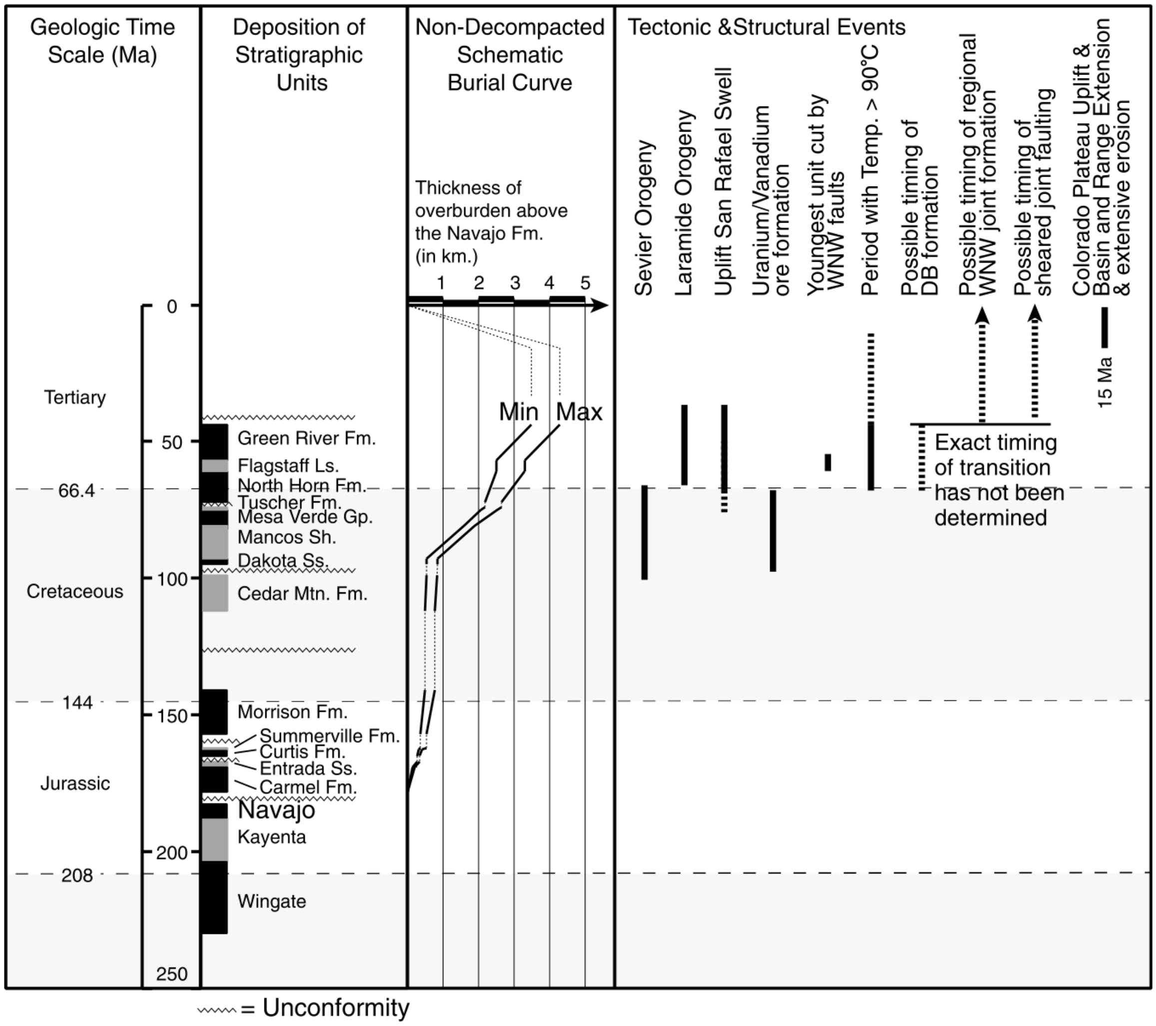

Figure 76. Burial history of the geologic units in the Chimney Rock area. The two curves represent the minimum and maximum burial extent of the top of the Navajo Sandstone. From Davatzes et al. (2003).

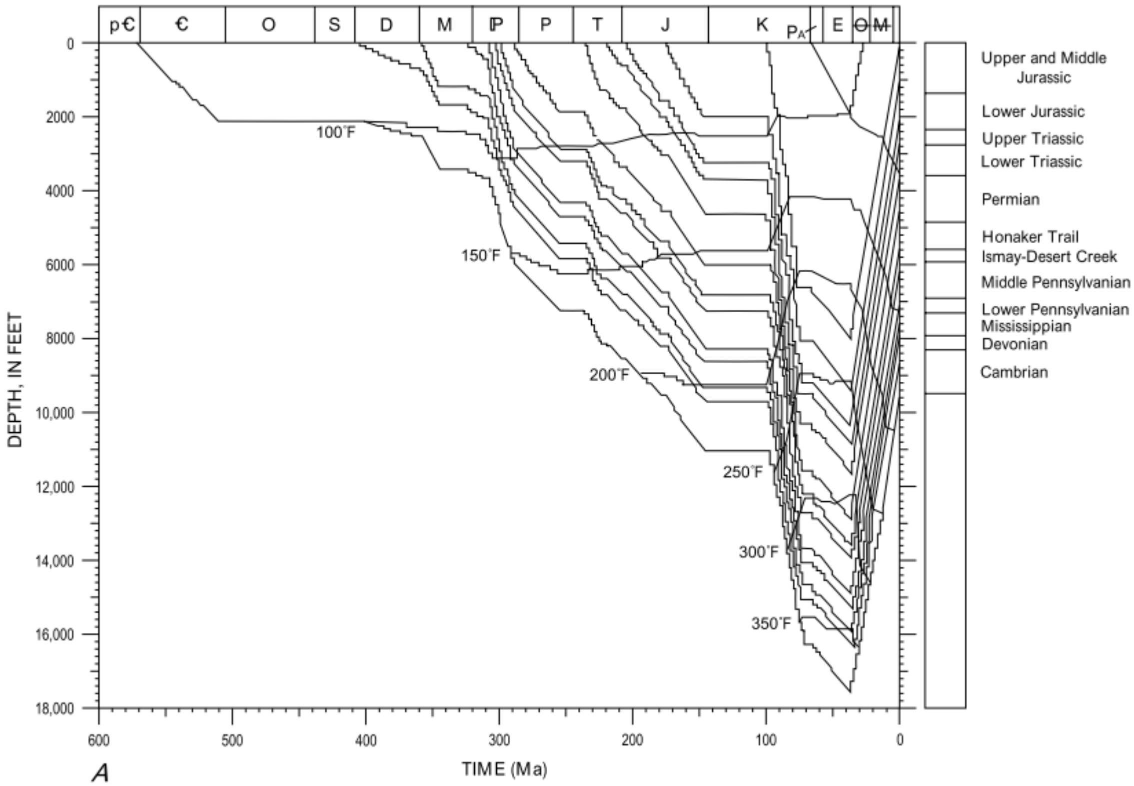

Figure 77. Burial and temperature history of geologic units in the area of Green River, Utah. From Nuccio and Condon (1996).

The source of the δ^{13}C-enriched carbon and δ^{18}O-enriched oxygen found in mineralized fractures may possibly have been calcite that was dissolved and re-precipitated from the surrounding limestone beds. Evidence for dissolution of limestone in the Co-op Creek Member is present in the form of stylolites (see Diagenesis section). Typical $\delta^{13}C_{PDB}$ and $\delta^{18}O_{SMOW}$ values for middle Jurassic carbonate shells are roughly 1.5‰ and 30‰, respectively (Figs. 75 and 78). This reasoning explains the δ^{13}C enriched calcite-filled fractures in the Co-op Member, but does not explain the δ^{13}C depleted calcite-filled fractures. However, this effect may explain why calcite-filled factures in the Carmel Formation are more δ^{13}C enriched than fractures in the Entrada Sandstone.

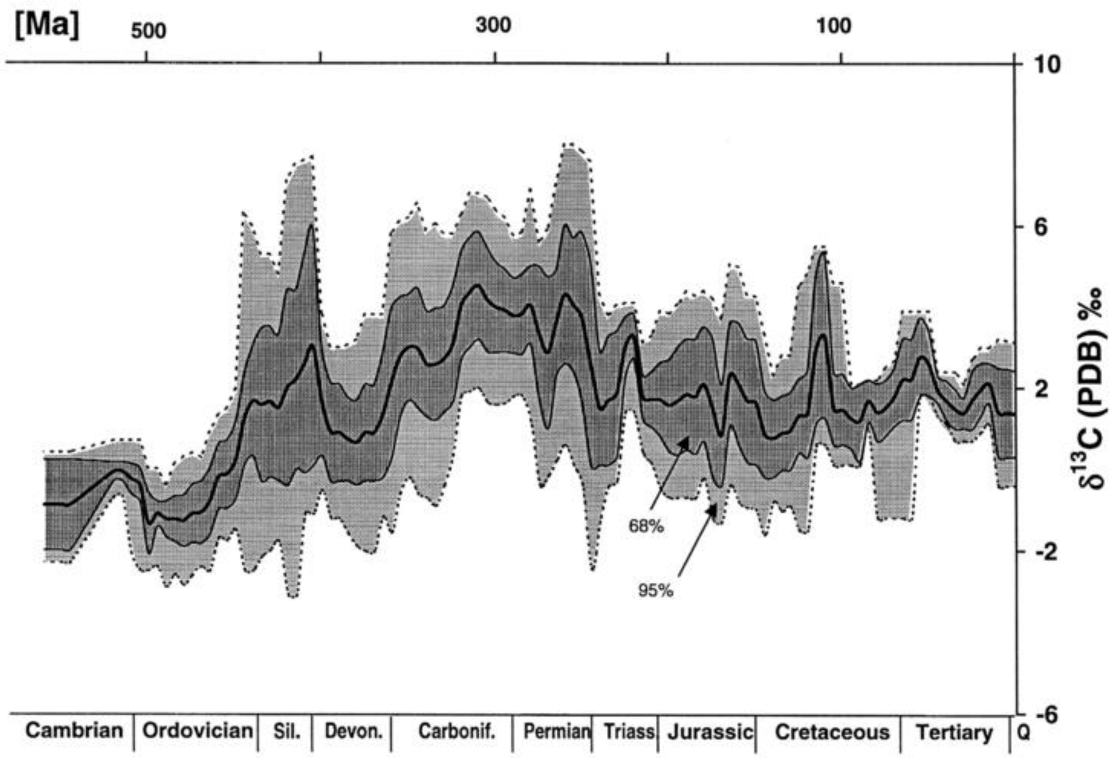

Figure 78. Graph showing the $\delta^{13}C$ of carbonate shells over geologic time. The $\delta^{13}C$ of shells during the middle Jurassic are around 1 to 2‰, possibly having an enrichment effect on the calcite-filled factures. From Veizer et al. (1999).

It is also possible that the pore waters were meteoric in origin. Spangler et al. (1996) reports that $\delta^{18}O_{SMOW}$ of the meteoric water from southeast Utah ranges from -17 to -12‰. Analysis of water in the nearby Crystal Geyser suggests that water currently inside the Jurassic units is meteoric. Crystal Geyser is a CO_2 charged geyser with water sourced from 300 to 500 m depth from the Wingate and Navajo Sandstone (Shipton et al., 2005). Mayo et al. (1991) found the $\delta^{18}O$ of water from the Crystal Geyser is -14.3‰, similar to local meteoric water. If meteoric water was the parent water, the calcite may have precipitated at temperatures between 10°C and 40°C (Fig. 74). The middle Jurassic units likely experienced this temperature range when undergoing uplift. The $\delta^{13}C$ values of water in the Crystal Geyser also suggest meteoric water may have been the source fluid for the fracture-filling calcite. The $\delta^{13}C$ of total dissolved carbon from Crystal

Geyser and the surrounding springs ranges from -1.8 to 1.2‰ (Shipton et al., 2005; Assayag et al. 2009). Some of calcite mineralized fractures $\delta^{13}C$ values of this study are consistent with meteoric water as the carbon source. However, the more depleted $\delta^{13}C$ values of this study indicate input of $\delta^{13}C$ depleted carbon.

The depleted source of $\delta^{13}C$ may have been from microbial decay of organic matter or interaction with hydrocarbons. Abundant shale beds are found within the Carmel Formation and Entrada Sandstone. If the shale beds contained organic matter microbial decay of this organic matter may have contributed to the $\delta^{13}C$-depleated calcite veins. Hydrocarbon-filled fractures and fluid inclusions (Fig. 54) provide evidence that hydrocarbons likely affected the units being studied. The $\delta^{13}C$ values of most petroleum deposits are between -32 to -21‰ (Sharp, 2007), a range consistent with influencing the most depleted calcite veins of this study.

CHAPTER 5. DISCUSSION

This section addresses the following topics: (1) the influence of diagenesis and deformation on porosity and permeability, (2) timing of the major diagenetic events, and (3) the implications of structural features of the reservoir-caprock interface for potential seal bypass at carbon capture, utilization, and storage (CCUS) sites.

The Influence of Diagenesis and Deformation on Porosity and Permeability

Cementation, compaction, cataclasis of the reservoir sandstones, and fracturing of caprock greatly influenced the porosity and permeability of the units being studied.

Effect of Cementation and Compaction

A large portion of the original porosity of the eolian sandstones was destroyed by cementation and compaction. Following the approach of Houseknecht (1987), one is able to visually see how the cementation and compaction affected the intergranular volume of the eolian sandstones. This is done by plotting cement and porosity abundances obtained from point-count data. The intergranular volume of a sample (which is the total intergranular porosity plus all cements that occupy intergranular space) is plotted on the vertical axis. An assumed value for the original porosity is assigned the maximum value for this axis. By doing this it is possible to quantify the percentage of the original porosity that was destroyed due to compaction. The total amount of cement is plotted on the horizontal axis. This axis also contains the original porosity as the maximum value. This makes it possible to quantify the percentage of the original porosity that was destroyed due to cementation. Lines of intergranular porosity are plotted as straight diagonals on the graph, allowing for easy comparison of the current intergranular porosity of a sample with the original intergranular porosity. The dashed line on the Houseknecht diagram divides samples which have lost more intergranular porosity due to compaction (lower left) from samples which have lost more intergranular porosity due to cementation (upper right). Assuming an original porosity of 48% (average for freshly deposited high energy sandstones; North, 1985) cementation and compaction in the Slick Rock Member of the Entrada Sandstone destroyed on average (n = 29) 52% and 23% of the original porosity, respectively (Fig. 79); whereas in the Navajo Sandstone cementation and compaction destroyed on average (n = 6) 29% and 46% of the original porosity, respectively (Fig. 80).

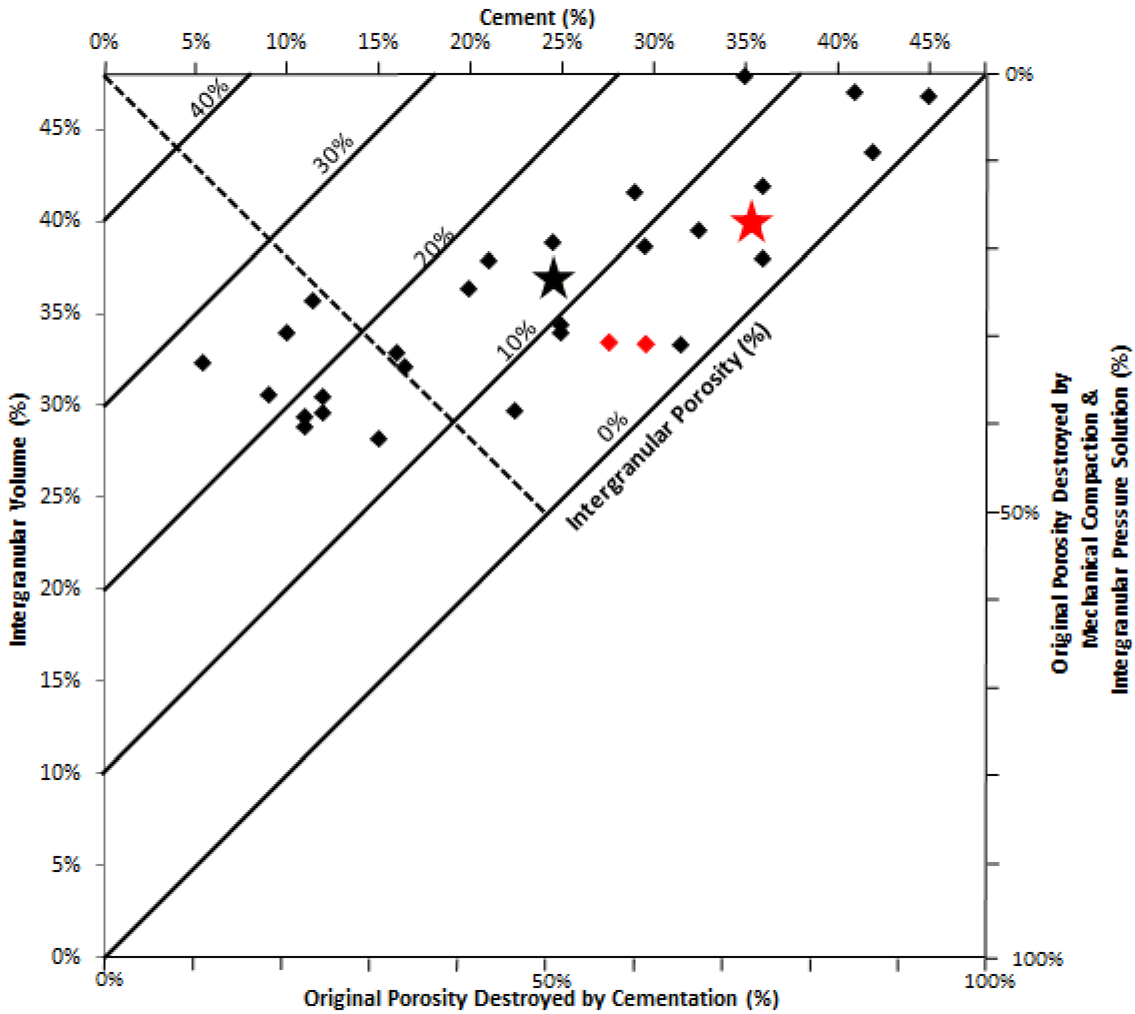

Figure 79. Intergranular volume vs. cement for the Slick Rock Member of the Entrada Sandstone. Black dots represent sandstone samples (n = 29), red dots represent zone of deformation bands samples (n = 3). The star represents the average of the each group, with the color of the star corresponding to the color of each group.

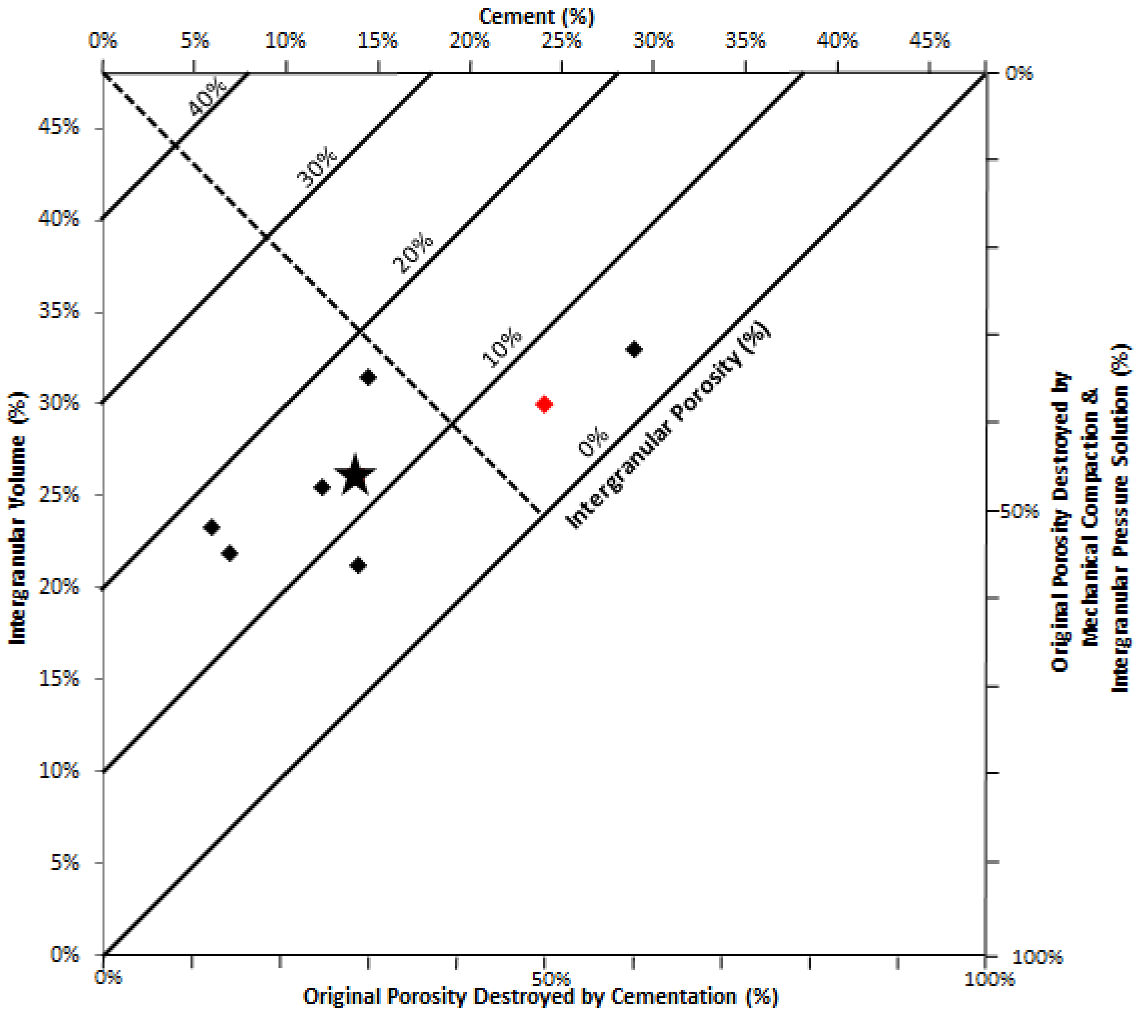

Figure 80. Intergranular volume vs. cement for the Navajo Sandstone. Black dots represent sandstone samples (n = 6), red dots represent zone of deformation bands samples (n = 1). The star represents the average of the each group, with the color of the star corresponding to the color of each group.

Cementation and compaction also affected the intergranular volume of the tidal flat sandstones and sandy siltstones of the Earthy Member of the Entrada Sandstone, the Co-op Creek Member of the Carmel Formation, and the Winsor Member of the Carmel Formation. Assuming an original porosity of 45% (average for tidal flat sandstones; Pryor, 1973) cementation and compaction in the Earthy of the Entrada Sandstone destroyed on average (n = 9) 36% and 53% of the original porosity, respectively (Fig. 81); in the Co-op Creek Member of the Carmel Formation Sandstone cementation and compaction destroyed on average (n = 8) 71% and 29% of the original porosity, respectively (Fig. 82); and in the Winsor Member of the Carmel Formation Sandstone cementation and compaction destroyed on average (n = 8) 64% and 36% of the original porosity, respectively (Fig. 83).

The intergranular volume of some tidal flat samples is inaccurate due to inadvertent inclusion of cement that formed from replacement of grains. This produced overestimates for the intergranular volume that are up to 17% higher than would be possible using an original porosity of 45%. Samples with intergranular volumes greater than 45% plot outside the graph. These samples are not included in the total average for each member.

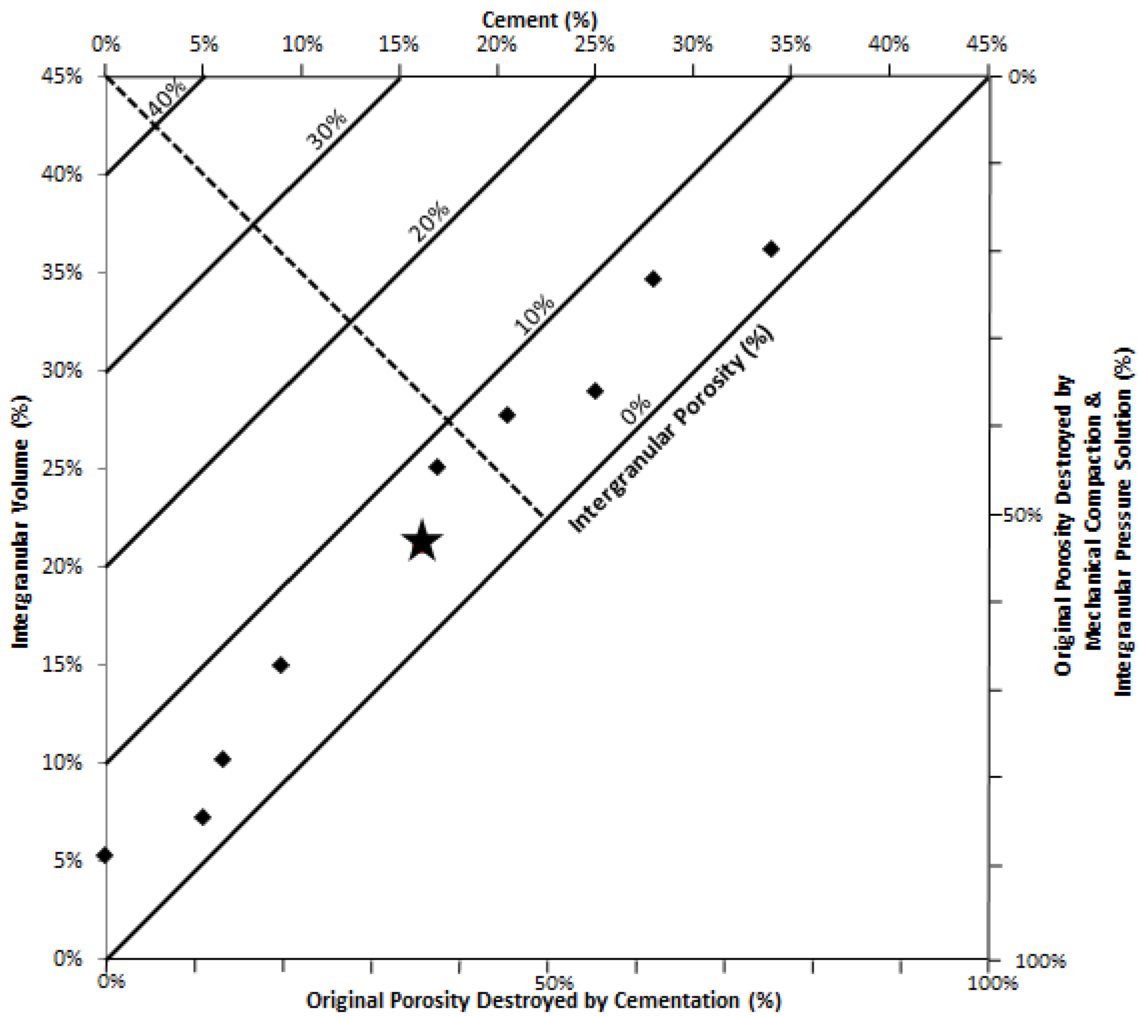

Figure 81. Intergranular volume vs. cement for the Earthy Member of the Entrada Sandstone. The star represents the average (n = 9) of the sandstone and sandy siltstone samples.

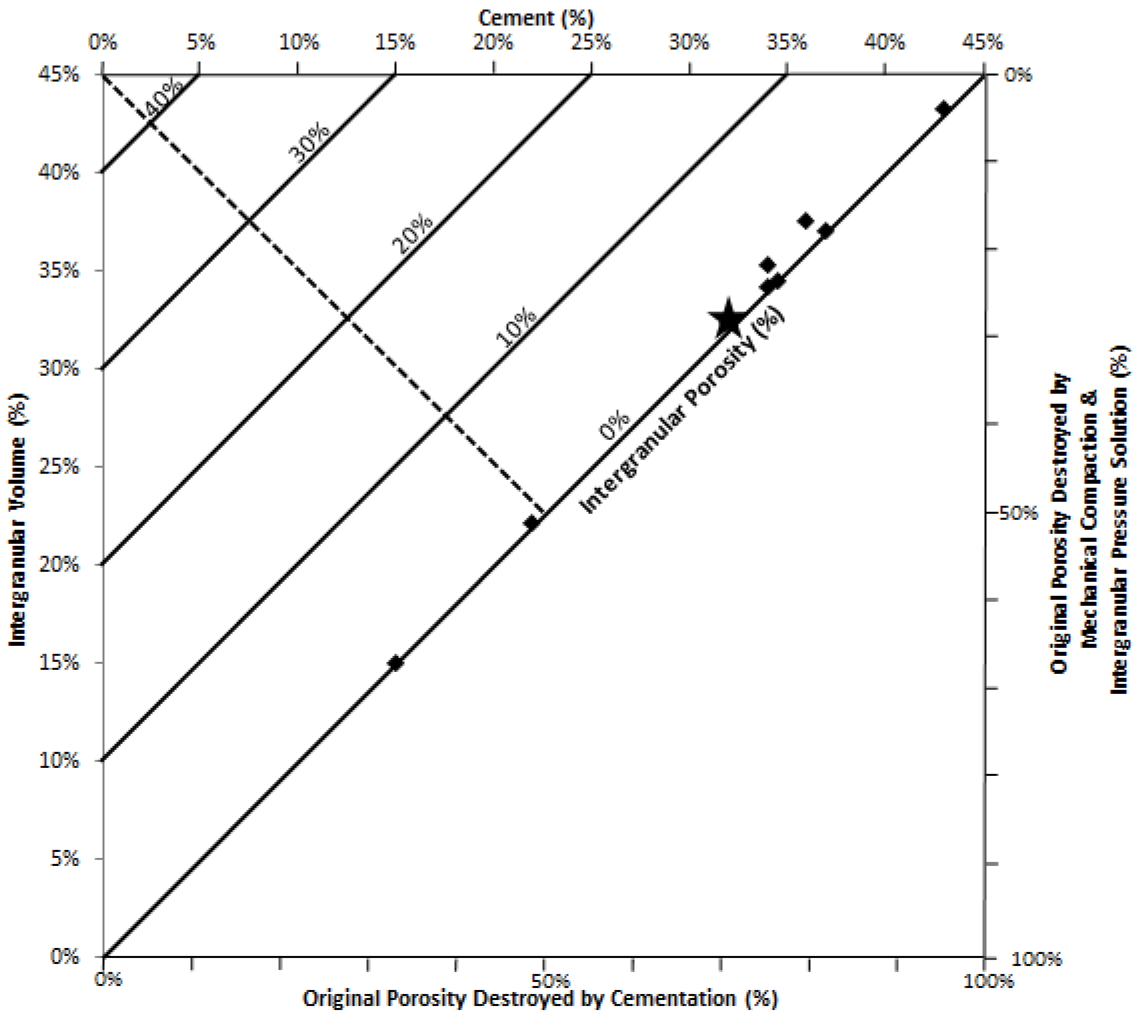

Figure 82. Intergranular volume vs. cement for the Co-op Creek Member of the Carmel Formation. The star represents the average (n = 8) of the sandstone and sandy siltstone samples.

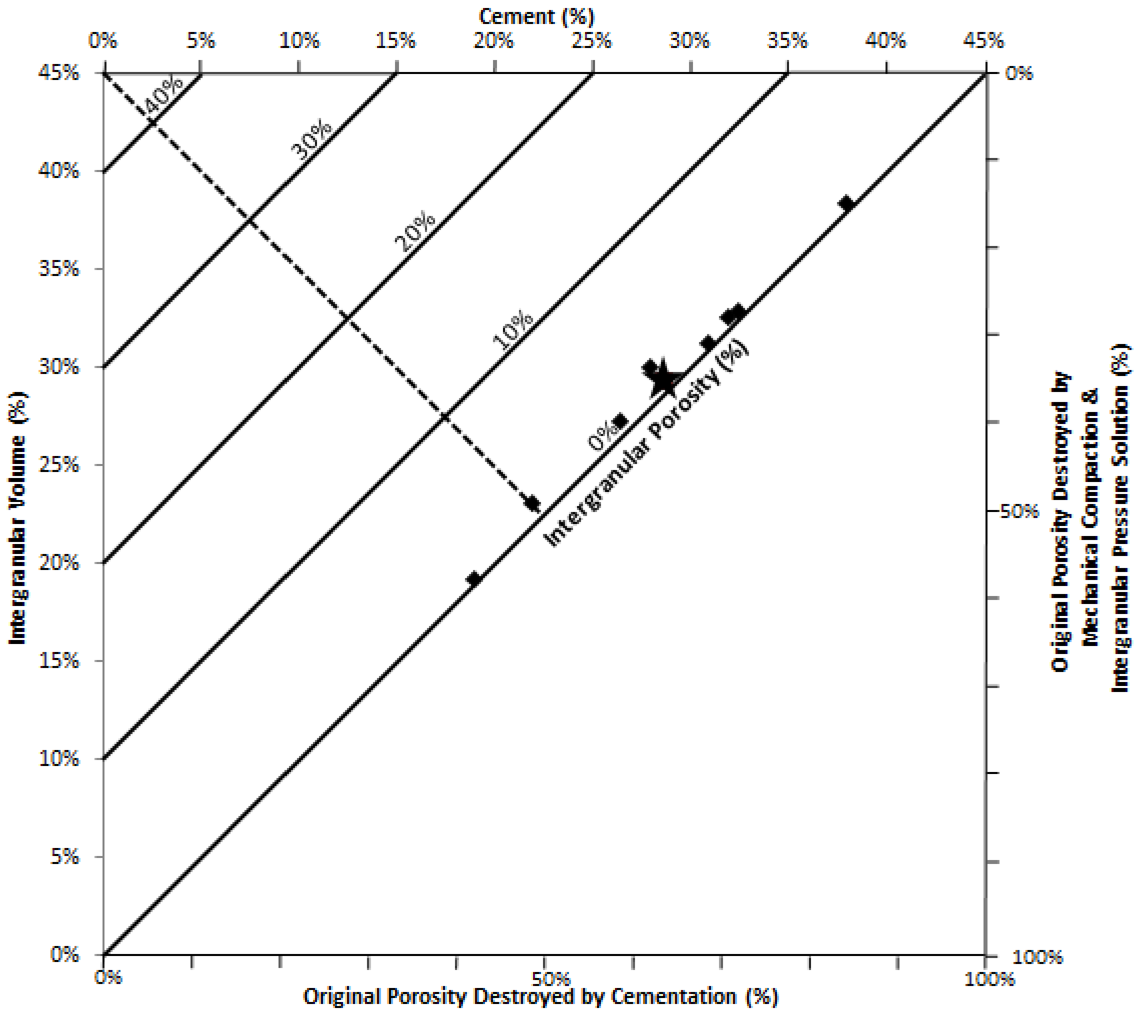

Figure 83. Intergranular volume vs. cement for the Winsor Member of the Carmel Formation. The star represents the average (n = 8) of the sandstone and sandy siltstone samples.

The permeability of all of the units studied decreased due to the effects of cementation and compaction. Freshly deposited eolian dune sand typically has original permeabilities of 5.40 to 104.82 darcys (Pryor, 1973). Permeabilities for the eolian sandstones of this study range from 0.192 to 8.992 darcys, indicating a decrease in permeability of perhaps several orders of magnitude. Freshly deposited tidal flat sands typically have permeabilities that range from 3.62 to 10.06 darcys (Pryor, 1973). The tidal flat derived sandstones of this study have permeabilities that range from 0.98 to 154.73 mD, also indicating a large decrease in permeability.

Effects of Deformation Bands

Deformation bands locally reduced porosity in the eolian sandstones. Using the same methods as above, cementation and compaction (deformation induced) inside zones of deformation bands in the Slick Rock Member destroyed on average (n = 3) 73% and 17% of the original porosity, respectively (Fig. 79); and in the Navajo Sandstone (n = 1) 50% and 38% of the original porosity, respectively (Fig. 80). One zone of deformation bands plots outside the graph. This is likely due to difficulties in differentiating between grains and cement inside of the cataclasite.

Deformation bands also decreased the permeability of the Navajo Sandstone and Slick Rock Member of the Entrada Sandstone. Zones of deformation bands at ISS-1 exhibit a decrease in permeability by two to four orders of magnitude compared to the host rock (Fig. 84). This is consistent with the conclusions of Fossen and Bale (2007) who showed zones of deformation bands from multiple units have a 1 to 5 order of magnitude decrease in permeability compared to the host rock.

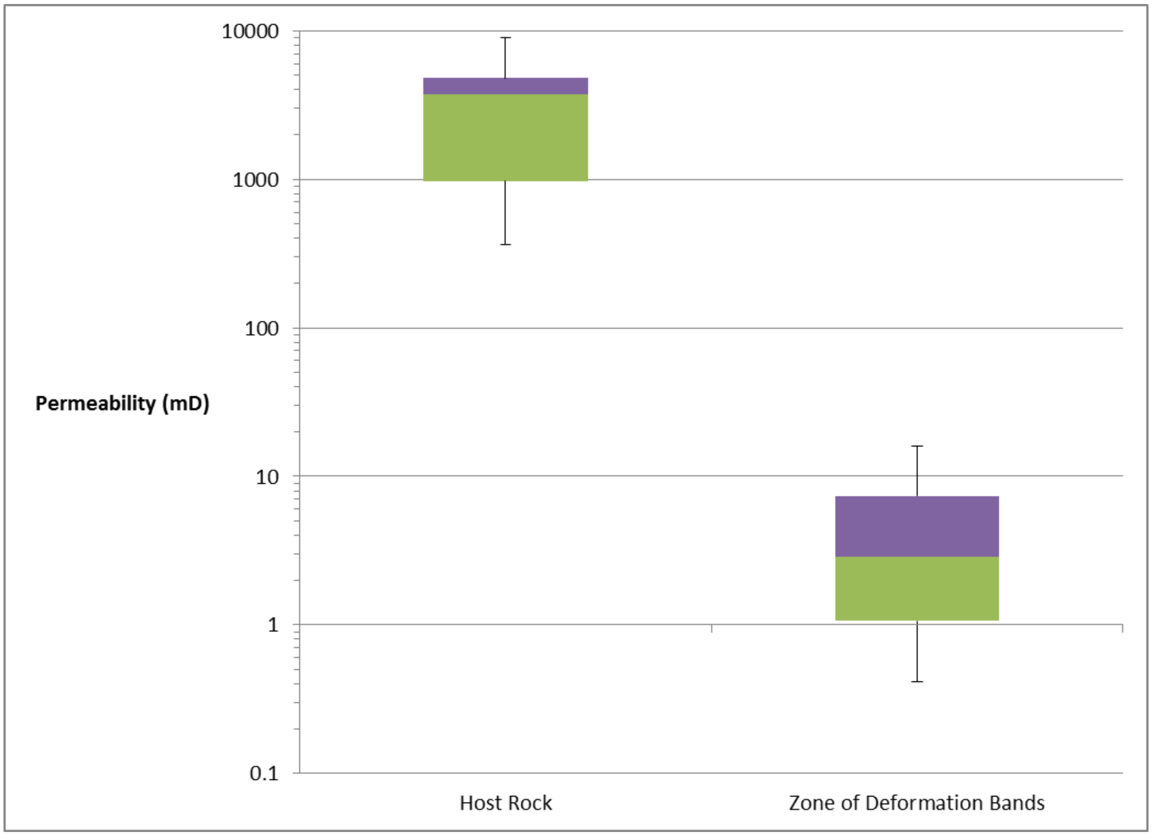

Figure 84. Box plot showing the difference in permeability between the host rock and a zone of deformation bands at ISS-1. The host rock data are for 26 corrected TinyPerm II measurements, whereas the zone of deformation bands data are 4 measurements calculated from mercury injection capillary pressure analysis. The upper and lower black lines represent the maximum and minimum values of the data range. The green and purple boxes represent data within the 25th to the 75th percentile, with the contact between the green and purple boxes representing the median value.

Timing of the Major Diagenetic Events

The diagenetic events of the lower and middle Jurassic units are divided into three main groups: early, burial, and uplift diagenesis (Fig. 85). Early diagenesis includes events that occurred shortly after deposition at shallow burial depths, burial diagenesis occurred after significant burial up to the point of maximum burial, and uplift diagenesis occurred after the onset of exhumation.

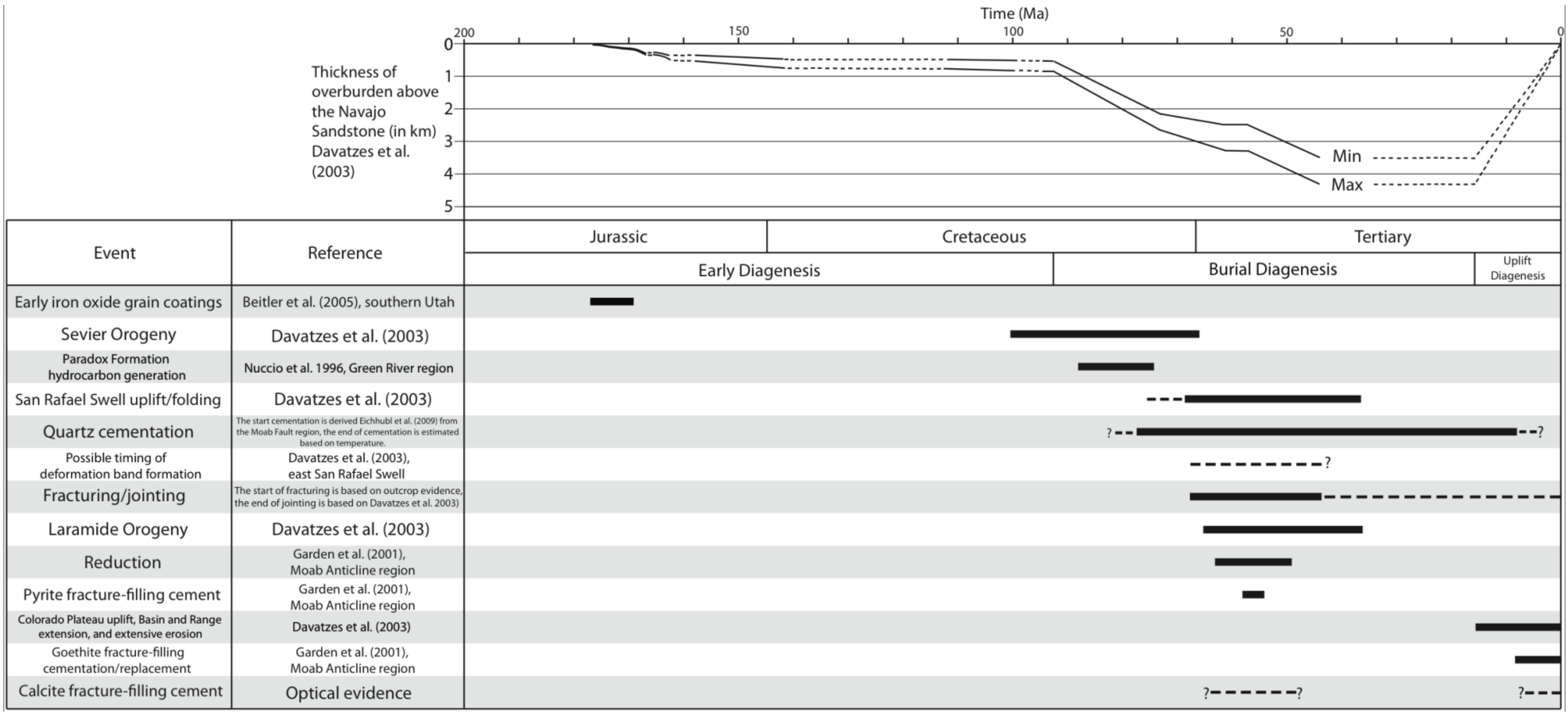

Figure 85. Summary of the major diagenetic alterations influencing the lower and middle Jurassic units. Solid lines indicate the period during which an event occurred, dashed indicate a range of time over which the event may have occurred. Corresponding diagenetic environments are shown. A burial history curve from Davatzes et al. (2003) corresponding to the top of the Navajo Sandstone is shown above. Min and Max correspond to the possible range in overburden above the Navajo Sandstone.

One of the first major diagenetic events to affect the units was precipitation pore-filling iron oxide cement. Foxford et al. (1996), Beitler et al. (2005), and Chan et al. (2000) concluded that this event occurred shortly after deposition of the Jurassic units.

The units were then buried by a large amount of overburden, beginning the stage of burial diagenesis. The increase in pressure and temperatures from overburden lead to the formation of quartz overgrowths. Based upon existing literature, the timing of quartz overgrowth formation is uncertain. From work done on the Moab Fault Eichhubl et al. (2009) concluded that fluid inclusions along the dust rims of quartz overgrowths formed at temperatures lower than 60°C. Using a 30°C per km geothermal gradient, this would mean the quartz overgrowths started forming above 2 km depth. However, the elevated pressures from burial below 2.5 km and temperatures above 90 °C are more typically associated with the conditions best suited for quartz cementation (Bjørlykke and Egeberg, 1993). Davatzes et al. (2003) conducted a detailed analysis of deformation bands in the Navajo Sandstone of the San Rafael Swell and concluded that they formed during the Laramide Orogeny. As demonstrated by outcrop evidence, deformation bands in the reservoir sandstones occurred simultaneously with the fractures in the overlying caprocks. The elevated pressures and temperatures also matured the underlying organic rich Paradox Formation, leading to the release and migration of hydrocarbons (Nuccio and Condon, 1996). The hydrocarbons and hydrocarbon altered fluids, which existed under reducing conditions, migrated upwards into the lower and middle Jurassic units. These reducing fluids were likely responsible for the bleaching of iron oxide rimmed grains in the lower and middle Jurassic units. As these fluids migrated upwards through the reservoirs units they eventually came in contact with the overlying caprocks. Some of these fluids entered the fractures found at the reservoir-caprock interface, partially (or perhaps completely) penetrating the caprock. While under these reducing conditions the fractures were partially cemented by pyrite. Based on the presence of hydrocarbon-filled fluid inclusions within calcite filled fractures (Figs. 53 and 54), the calcite fracture-fill formed during hydrocarbon migration. Timing for reduction (63 to 49 Ma) and pyrite cementation (59 to 55 Ma) is based on paleomagnetic results from Garden et al. (2001) performed on Jurassic units at the Moab Anticline. Because the conditions that formed the Moab Anticline are different from the conditions along the San Rafael Swell, the exact timing used may be slightly inaccurate for this field area.

Eventually the Colorado Plateau began to undergo uplift, producing the last stage of diagenesis. As the Jurassic units were uplifted quartz cementation likely slowed as conditions became less ideal for precipitation. I am in agreement with Davatzes et al. (2003) that the deformation mechanisms in the reservoir units transitioned from deformation banding to fracturing. Two factors likely caused this transition; a change in rheology and/or a change in the deformation environment (Davatzes et al., 2003). Over time the pore space in the high porosity sandstones decreased due to cementation, promoting fracturing instead of cataclasis. Also over time there may have been a change in the state of stress or pore fluid pressure that promoted fracturing over cataclasis (Davatzes et al., 2003). This change may have been brought about by the transition from burial to uplift diagenesis. The hydrocarbon altered pore waters eventually moved out of the lower and middle Jurassic units, likely being replaced by uplift related meteoric water. This caused chemical conditions to transition from reducing to oxidizing. Oxidizing cement such as goethite replaced the majority of the pyrite cement inside of the factures. Timing for goethite fracture-fill (~8 Ma to present) is an estimate based on field and petrographic relationships from Garden et al. (2001). Afterwards the fractures were completely cemented by calcite.

Implications for Carbon Capture, Utilization, and Storage (CCUS)

The results of this study are relevant to reservoir characterization and caprock analysis for potential subsurface sequestration sites. In particular, my findings have implications for the evaluation of potential seal bypass and reservoir compartmentalization.

The Potential of Seal Bypass Due to Fractures in Caprock

Mineralization and bleaching patterns associated with fractures in the seal lithologies demonstrates that at least partial bypass occurred when these rocks were present in the subsurface. Bleaching has occurred at the bottom of both caprocks studied, indicating that reservoirs fluids are capable of penetrating both caprocks by up to one meter without the aid of fractures. However, fracture bleaching patterns and mineralized fracture networks demonstrate that reservoir fluids penetrated at least 17.7 m into the caprock. This demonstrates partial seal bypass, but thus far I have not been able to trace these features all the way through the sealing lithologies. It is possible that the fracture networks of this study do not completely traverse the caprock units.

Based upon mass-balance considerations, significant volumes of fluid must have passed through the fractures for them to be completely mineralized. However, whether the fluid used the fractures to completely traverse the caprock or the fluid just used the fractures to flow into permeable beds within the caprock is difficult to say. It is also possible fluids traversed multiple fracture networks within the caprock which were connected by permeable beds.

Mesoscale features at the caprock interface may prove problematic for CCUS. Although the fracture networks described in this study are small, they could potentially contribute to leakage of CO_2 from a target reservoir. The leakage flux would likely be small, but overtime significant amounts of CO_2 could bypass the seal. To further complicate matters for CCUS, mesoscale interface features are too small to be detected with standard geophysical techniques.

Fracture networks may be self-healing due to mineral trapping, possibly decreasing the leakage rates over time. CO_2 which is in solution with brines may precipitate to form carbonate minerals (IPCC, 2005). Mineral precipitation in potential leakage prone caprock fracture networks will decrease the leakage rates of the fractures. Ideally, the fracture networks would be completely cemented shut, halting leakage altogether. Unfortunately, mineral precipitation does not always occur rapidly, as it may take a thousand years or longer before it occurs in significant amounts (Fig. 86). Mesoscale features may not be that much of a concern to CCUS if fracture cementation has already occurred. If all of the fracture pathways inside of the caprock were already closed, as was the case for the majority of the fractures seen in outcrop, the threat of CO_2 leakage is reduced. However, even if the fractures were completely cemented during burial diagenesis the cemented fracture pathway may still be a potential leakage point. Fracture planes are weak points in a caprock and could potentially be reactivated due to increased pressure from CO_2 injection.

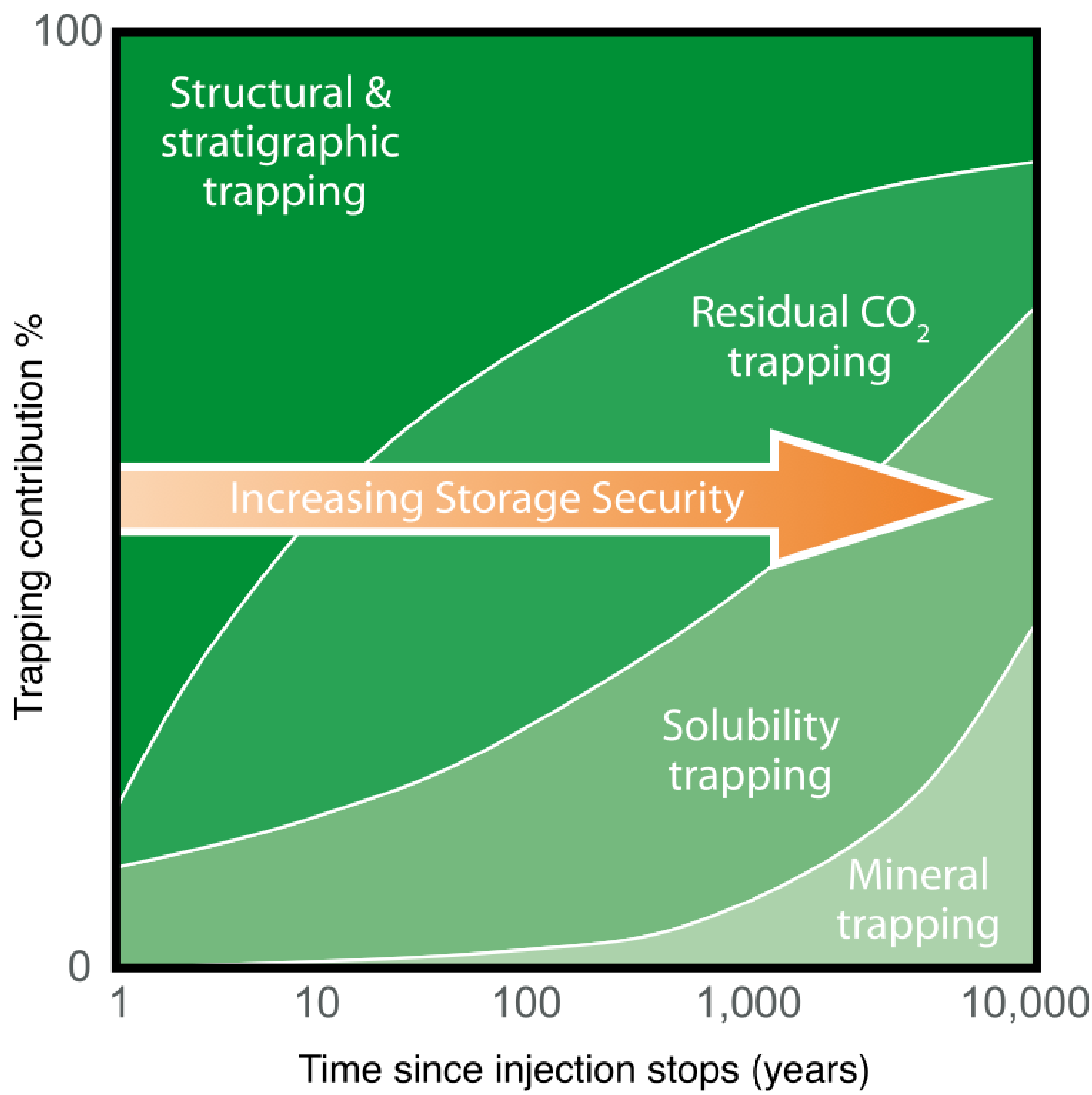

Figure 86. The total trapping contribution of different types of CO_2 trapping mechanisms over time. Mineral trapping has the potential to trap large amounts of CO_2 although it takes significant amounts of time for this to occur. Taken from IPCC (2005).

<u>Reservoir Compartmentalization Due to Zones of Deformation Bands</u>

MICP data demonstrates that zones of deformation bands can act as barriers to flow. The MICP data can be used to determine the amount of supercritical CO_2, natural gas, or oil that can be trapped by zones of deformation bands. This is done by using the breakthrough (aka displacement or threshold) pressure of each sample. The breakthrough pressure is the pressure at which the non-wetting phase (mercury, CO_2, oil, or gas) forms a continuous filament across the sample (Dewhurst et al., 2002; Daniel and Kaldi, 2008). The breakthrough pressure can be determined by reading the injection pressure at the point on the injection curve where it has its maximum inflection upwards (Dewhurst et al., 2002; Daniel and Kaldi, 2008). The injection curves and the corresponding breakthrough pressures for each sample are reported in APPENDIX E. Using the following equations from Daniel and Kaldi (2008) and Schowalter (1979) it is possible to determine the column height of CO_2 or hydrocarbons that can be trapped by zones of deformation bands.

$$Ps_{b/j} = \frac{Ps_{a/m}\,(\sigma_{b/j}\cos\theta_{b/j})}{(\sigma_{a/m}\cos\theta_{a/m})} \tag{1}$$

$$Pr_{b/j} = \frac{2\,\sigma_{b/j}\cos\theta_{b/j}\,(0.145)}{R} \tag{2}$$

$$h_j = \frac{Ps_{b/j} - Pr_{b/j}}{(\rho_b - \rho_j)0.433} \tag{3}$$

$j = CO_2$*, oil, or gas*

$Ps_{b/j}$ and $Ps_{a/m}$ are the breakthrough (aka displacement or threshold) pressure of the seal in the brine-CO_2/oil/gas and air-mercury systems, respectively (psi), $\sigma_{b/j}$ and $\sigma_{a/m}$ are the interfacial tension of the brine-CO_2/oil/gas and air-mercury systems, respectively (dyne/cm); $\theta_{b/j}$ and $\theta_{a/m}$ are the contact angles for the brine-CO_2/oil/gas-rock and air-mercury-rock systems, respectively (degrees); $Pr_{b/j}$ is the breakthrough pressure of the reservoir in the brine-CO_2/oil/gas system (psi); R is the radius of the largest connected pore throats (µm); 0.145 is the constant to convert to psi (psi/(dyne/cm^2)); h_j is the column height of CO_2/oil/gas (ft); ρ_b and ρ_j are the density of the brine and CO_2/oil/gas, respectively (g/cm^3); and 0.433 is pressure gradient of water due to gravity (psi/ft). Table 15 gives the values for the variable of equations used in this study. No mercury experiments were used to determine breakthrough pressure of the reservoir rock, so equation (2) is used to determine this value.

Contact angles for the brine-CO_2/oil/gas-rock system can have a large impact on calculations of the column height a zone of deformation bands can contain. Several authors have assumed a contact angle of 0° when performing column height calculations for CO_2, oil, and gas (Schowalter, 1979). However, more recent work has shown that contact angles can vary significantly based on the mineralogy, pressure, and salinity (Daniel and Kaldi, 2008). Using the approach of Daniel and Kaldi (2008), a range of contact angles from 0 to 60° were used to take into account the effect contact angles have on the column height of supercritical CO_2. Chiquet and Broseta (2005) have shown experimentally that the contact angle can be as high as 55° in a quartz-brine-CO_2 system, thus I use a range from 0 to 60° in these calculations. The contact angle for hydrocarbons can also vary significantly. Silicate reservoirs similar to the Navajo and Entrada Sandstone can have significantly variable contact angles, with reservoirs being water-wet, oil-wet, or in the intermediate range (Treiber et al. 1972). To account for this large amount of variation, a range of 0 to 90° was used in calculating the column heights of oil. Li and Firoozabadi (2000) concluded that the contact angle may not be zero in gas-liquid systems, instead it is several degrees or more but not intermediately gas-wetting. This is supported by experimental work from Okasha and Al-Shiwaish (2010) that shows the contact angle can be as high as 68° in a gas-brine-rock system. To account for the large discrepancy between assumed and measured contact angles, a range of 0 to 70° was used.

Table 15. Values used to determine the supercritical CO_2, oil, and gas column heights.

Variable	Value Used	Source
$\sigma_{b/CO2}$	24 dynes/cm	Daniel and Kaldi (2008) Average of the typical range of 21 to 27 dynes/cm
$\sigma_{b/oil}$	20 dynes/cm	Schowalter (1979) Average of the typical range of 5 to 35 dynes/cm
$\sigma_{b/gas}$	50 dynes/cm	Schowalter (1979) Average of the typical range of 30 to 70 dynes/cm
$\sigma_{a/m}$	481 dynes/cm	Daniel and Kaldi (2008) Typical value
$\theta_{b/CO2}$	0 - 60°	Daniel and Kaldi (2008) Possible range of values
$\theta_{b/oil}$	0 - 90°	Treiber et al. (1972) Possible range of values
$\theta_{b/gas}$	0 - 70°	Li and Firoozabadi (2000) Possible range of values
$\theta_{a/m}$	140°	Daniel and Kaldi (2008) Typical value
ρ_b	1.1 g/cm^3	Schowalter (1979) Average of the typical range of 1.0 to 1.2 g/cm^3
ρ_{CO2}	0.7 g/cm^3	Parry et al. (2007) Average of the estimated range if injected in to Navajo Sandstone, ranging from 0.6 to 0.8 g/cm^3
ρ_{oil}	0.75 g/cm^3	Schowalter (1979) Average of the typical range of 0.5 to 1.0 g/cm^3
ρ_{gas}	0.25 g/cm^3	Vavra et al. (1992) Average of the typical range of 0.00073 to 0.5 g/cm^3
R	10 μm	Wardlaw and Cassan (1979) Pore throat radius at breakthrough pressure of a 300 μm sandstone, the average grain size of the Slick Rock Member of the Entrada Sandstone

Based on the above equations the maximum amount of supercritical CO_2 that can be trapped by the zone of deformation bands at ISS-1 is 11 feet (3 m; Fig. 87a). However, the equation used to calculate these values does not take into account the seal thickness, lateral continuity, and ductility. These play a large role in determining how effective a seal will be (Downey, 1984). Additionally, this equation only works if the zone of deformation bands is an overlying seal. The contact angle used in this equation has a large impact on the column height. Using the equations listed above, a 75% reduction in column height exists when comparing the use of a 0° contact angle with a 60° contact angle (Fig. 87a).

Using the above equations the maximum column height of oil and gas a zone of deformation bands can contain is 11 feet (3 m; Fig. 87bc). These calculations appear to be in line with the lower range from Antonellini and Aydin (1994) that deformation bands can contain a 2.3 to 150 m column of hydrocarbons. The height of the hydrocarbon column varies considerably based on the value of the contact angle. The closer the contact angle is to 90°, the smaller the total hydrocarbon column will be (Fig. 87bc).

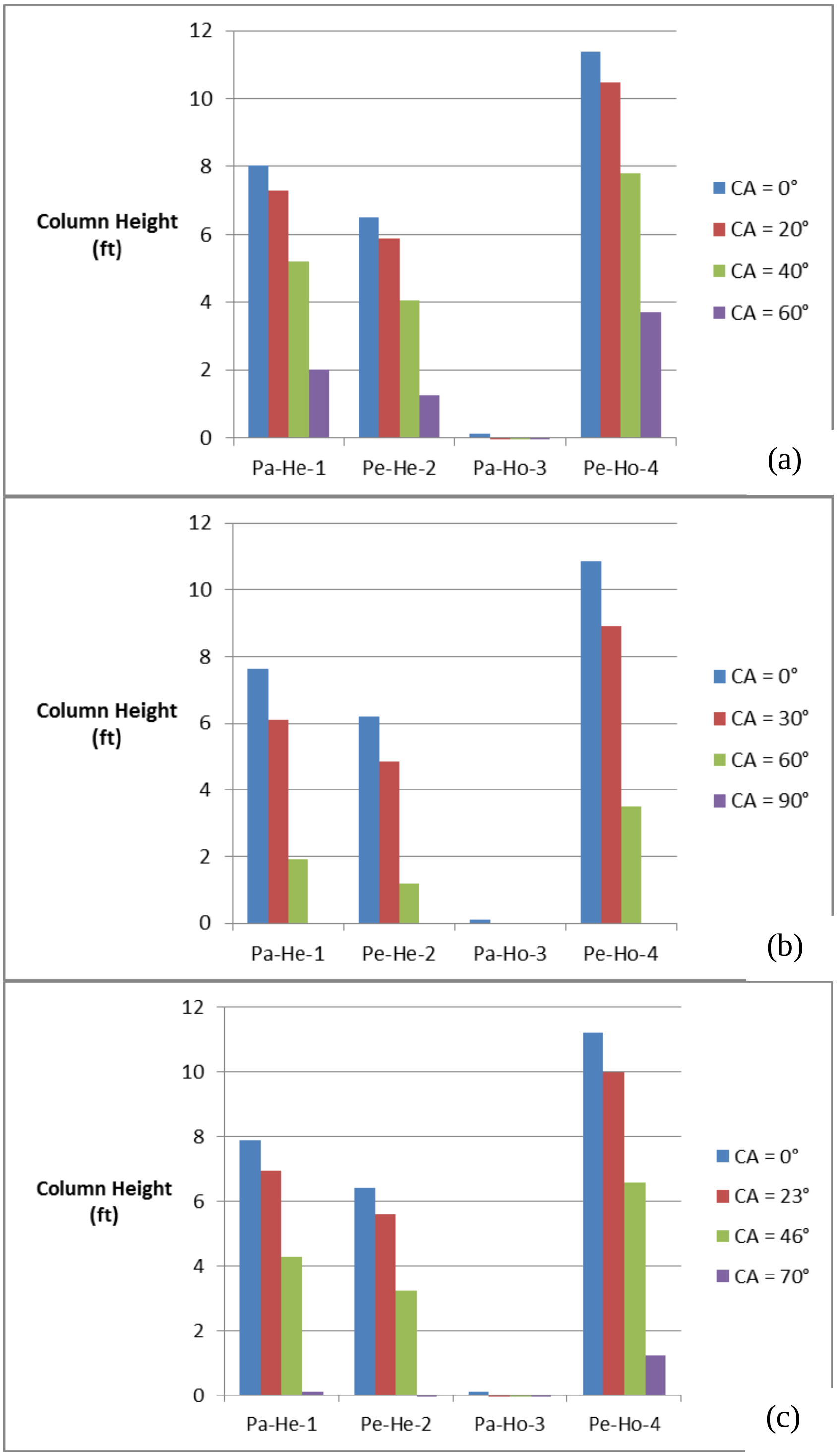

Figure 87. The highest and lowest possible column heights for a zone of deformation bands at ISS-1 for (a) supercritical CO_2, (b) oil, and (c) gas. The color of each bar corresponds to the contact angle used to calculate the column height, as listed above. Samples with “Pe” and “Pa” denote perpendicular and parallel to the zone of deformation bands, respectively. Samples with “He” and “Ho” denote heterogeneous and homogeneous zone of deformation bands samples, respectively.

The MICP data demonstrates that a zone of deformation bands which intersect with the caprock can compartmentalize a reservoir being injected with supercritical CO_2. When a CO_2 plume comes in contact with a low-permeability caprock it normally disperses outwards across the caprock to areas of lower pressure. However, as modeled by Pasala et al. (2013), when a CO_2 plume comes in contact with a caprock intersected by a zone of deformation bands the low permeability deformation bands will restrict lateral migration of the CO_2, leading to compartmentalization. This can be avoided by injecting CO_2 from a horizontal well (Pasala et al., 2013).

CCUS Projects that may have Mesoscale Features at the Reservoir-Caprock Interface

Many CCUS projects across the United States and abroad may have mesoscale features that could potentially increase the risk of leaking CO_2. This study investigated target reservoirs and caprocks for the proposed Gordon Creek injection site in Utah (Southwestern Partnership for Carbon Sequestration, 2010). The Navajo and Entrada Sandstones are the target reservoirs for this site, so my results directly demonstrate the potential for seal bypass and reservoir compartmentalization associated with interface features. Another example is the ADM/ISGS project in Decatur, IL, a Phase-3 injection site, where deformation bands have been reported in the Mt. Simon Sandstone in core from the injection site (Chentnik, 2012). Thus, zones of deformation bands in the Mt. Simon Sandstone may transition into fracture networks in the overlying Eau Clair Formation. As most basins chosen for CCUS have undergone some degree tectonism, the possibility that sandstone reservoirs contain zones of deformation bands is quite high.

CHAPTER 6. CONCLUSIONS

(1) Zones of deformation bands in reservoir rock commonly transition to opening-mode fracture networks in the caprock.

(2) Petrographic evidence indicates that multiple fracture-forming and fracture-filling events occurred during the diagenetic history.

(3) The presence of pyrite in the mineralized fractures inside the Earthy Member of the Entrada Sandstone demonstrates some degree of mineralization by strongly reducing fluids.

(4) The presence of hydrocarbon-filled fractures and fluid inclusions in the Carmel Formation suggests that bleaching was likely at least in part caused by hydrocarbons.

(5) Patterns of bleaching and mineralization in caprock fractures provide evidence for at least partial seal bypass when the units were in the subsurface. I do not know the full extent of the bypass because I was only able to trace the fracture networks a portion of the way through the caprock units due to outcrop limitations.

(6) MICP results show that a zone of deformation bands intersecting the interface can trap a 3 m column of supercritical CO_2, oil, or gas. The calculated column height varies considerably depending on the value of contact angle used.

SUGGESTIONS FOR FUTURE WORK

The conceptual models provided in this thesis should be analyzed quantitatively by numerical hydrologic modeling. This will allow for a better understanding of how mesoscale features at the reservoir-caprock interface can impact multiphase (water and CO_2) fluid flow into and through the caprock. David Butler, an MS student in the hydrology program at New Mexico Tech, is currently undertaking such work

Fluid inclusion paleothermometry should be attempted to better constrain the interpretation of the stable isotope data. By knowing the temperature at which the calcite formed it would be possible to determine if the calcite-filled fractures formed during deep burial conditions or later during uplift. However, obtaining accurate data for inclusions in such samples is notoriously difficult.

Additional field work should be performed to determine the frequency of which mesoscale interface features occur in a given area. This information will be useful when performing regional modeling. Santiago Flores, an MS student in the geology program at Utah State University, is conducting this work.

REFERENCES

Antonellini, M., & Aydin, A. (1994). Effect of faulting on fluid flow in porous sandstones: petrophysical properties. *AAPG bulletin*, *78*(3), 355–377.

Assayag, N., Bickle, M., Kampman, N., & Becker, J. (2009). Carbon isotopic constraints on CO2 degassing in cold-water Geysers, Green River, Utah. *Energy Procedia*, *1*(1), 2361–2366.

Aydin, A, & Johnson, A. (1978). Development of faults as zones of deformation bands and as slip surfaces in sandstone. *Pure and Applied Geophysics*, *116*(4-5), 931–942.

Aydin, Atilla. (1978). Small faults formed as deformation bands in sandstone. *Pure and Applied Geophysics*, *116*.

Aydin, Atilla, Borja, R. I., & Eichhubl, P. (2006). Geological and mathematical framework for failure modes in granular rock. *Journal of Structural Geology*, *28*(1), 83–98.

Baker, A. A. (1935). Geologic Structure of Southeast Utah. *Bulletin of the American Association of Petroleum Geologists*, *19*(10), 1472–1507.

Baker, A. A. (1946). *Geology of the Green River Desert-Cataract Canyon Region, Emery, Wayne, and Garfield Counties, Utah - Geological Survey Bulletin 951* (p. 122). Washington D.C.: U.S. Government Printing Office.

Beitler, B., Parry, W. T., & Chan, M. A. (2005). Fingerprints of Fluid Flow: Chemical Diagenetic History of the Jurassic Navajo Sandstone, Southern Utah, U.S.A. *Journal of Sedimentary Research*, *75*(4), 547–561.

Bjørlykke, K., & Egeberg, P. (1993). Quartz cementation in sedimentary basins. *AAPG Bulletin*, *77*(9), 1538–1548.

Blakey, R C, & Ranney, W. (2008). *Ancient landscapes of the Colorado plateau* (p. 176). Grand Canyon, Arizona: Grand Canyon Association.

Blakey, Ronald C, Peterson, F., Caputo, M. V, Geesaman, R. C., & Voorhees, B. J. (1983). Paleogeography of Middle Jurassic continental, shoreline, and shallow marine sedimentation, southern Utah. *Mesozoic Paleogeography of west central United States, Rocky Mountain Section of Society of Economic Paleontologists and Mineralogists (Symposium)* (pp. 77–100).

Brace, W. F. (1980). Permeability of crystalline and argillaceous rocks. *International Journal of Rock Mechanics and Mining Sciences & Geomechanics Abstracts*, *17*(5), 241–251.

Breit, G. N., Goldhaber, M. B., Shawe, D. R., & Simmons, E. C. (1990). Authigenic barite as an indicator of fluid movement through sandstones within the Colorado Plateau. *Journal of Sedimentary Petrology*, *60*(6), 884–896.

Cartwright, J., Huuse, M., & Aplin, A. (2007). Seal bypass systems. *AAPG Bulletin*, *91*(8), 1141–1166.

Cashion, W. B. (1967). *Carmel formation of the Zion Park region, southwestern Utah: A review (Geological Survey bulletin 1244-J)*. Washington: U.S. Government Printing Office.

Chan, M. A., Parry, W. T., & Bowman, J. R. (2000). Diagenetic hematite and manganese oxides and fault-related fluid flow in Jurassic sandstones, southeastern Utah. *AAPG bulletin*, *84*(9), 1281–1310.

Chentnik, B. (2012). Characterizing Fractures and Deformation Bands: Implications for Long-Term CO2 Storage within the Cambrian Mount Simon Sandstone. *The Journal of Purdue Undergraduate Research*, *2*(3), 8–15.

Chiquet, P. & Broseta, D. (2005) Capillary alteration of shaly caprocks by carbon dioxide. *Society of Petroleum Engineers.* No. 102918, 10 p.

Choquette, P. W., & Pray, L. C. (1970). Geologic nomenclature and classification of porosity in sedimentary carbonates. *AAPG Bulletin*, *54*(2), 207–250.

Criss, R. E. (1999). *Principles of Stable Isotope Distribution* (p. 264). New York, NY: Oxford University Press.

Dalrymple, A., & Morris, T. (2007). Facies analysis and reservoir characterization of outcrop analogs to the Navajo Sandstone in the central Utah thrust belt exploration play. In G. C. Willis, M. D. Hylland, D. L. Clark, & J. Chidsey, T.C. (Eds.), *Utah Geological Association Publication 36* (pp. 311–322).

Daniel, R. F., & Kaldi, J. G. (2008). Evaluating seal capacity of caprocks and intraformational barriers for the geosequestration of CO_2. *PESA Eastern Australasian Basins Symposium EABS III*.

Davatzes, N. C., Aydin, A., & Eichhubl, P. (2003). Overprinting faulting mechanisms during the development of multiple fault sets in sandstone, Chimney Rock fault array, Utah, USA. *Tectonophysics*, *363*(1-2), 1–18.

Dewhurst, D. N., Jones, R. M., & Raven, M. D. (2002). Microstructural and petrophysical characterization of Muderong Shale: application to top seal risking. *Petroleum Geoscience*, *8*(4), 371–383.

Doelling, H. H. (2002). Interim Geologic Map of the San Rafael Desert 30’ x 60' Quadrangle, Emery and Grand Counties , Utah by. *Open-File Report 404 Utah Geological Survey*.

Doelling, H. H., & Kuehne, P. A. (2008). Interim Geologic Map of the Temple Mountain Quadrangle , Emery County , Utah. *Open-File Report 541 Utah Geological Survey*.

Downey, M. W. (1984). Evaluating seals for hydrocarbon accumulations. *AAPG Bulletin*, *68*(11), 1752–1763.

Dunham, R. J. (1962). Classification of carbonate rocks according to depositional texture. In W. E. Ham (Ed.), *Classification of carbonate rocks* (pp. 108–121). American Association of Petroleum Geologists Memoir.

Eichhubl, P., Davatzes, N. C., & Becker, S. P. (2009). Structural and diagenetic control of fluid migration and cementation along the Moab fault, Utah. *AAPG Bulletin*, *93*(5), 653–681.

Eschner, T., & Kocurek, G. (1986). Marine destruction of eolian sand seas: origin of mass flows. *Journal of Sedimentary Petrology*, *56*(3), 401–411.

Fischer, M. P., & Christensen, R. D. (2004). Insights into the growth of basement uplifts deduced from a study of fracture systems in the San Rafael monocline, east central Utah. *Tectonics*, *23*(1), 1–14.

Folk, R. L. (1977). Stratigraphic Analysis of the Navajo Sandstone: DISCUSSION. *Journal of Sedimentary Research*, *47*(1), 483–484.

Folk, Robert L. (1968). *The Petrology of Sedimentary Rocks* (p. 170). Austin, Texas: Hemphill’s Book Store.

Fossen, H., & Bale, A. (2007). Deformation bands and their influence on fluid flow. *AAPG Bulletin*, *91*(12), 1685–1700.

Fossen, H., Schultz, R. A., Shipton, Z. K., & Mair, K. (2007). Deformation bands in sandstone: a review. *Journal of the Geological Society of London*, *164*, 1–15.

Fossen, H., Schultz, R. A., & Torabi, A. (2011). Conditions and implications for compaction band formation in the Navajo Sandstone, Utah. *Journal of Structural Geology*, *33*(10), 1477–1490.

Foxford, K., Garden, I., & Guscott, S. (1996). The field geology of the Moab Fault. In A. C. Huffman, W. R. Lund, & L. H. Godwin (Eds.), *Geology and Resources of the Paradox Basin: Utah Geological Association Guidebook 25* (pp. 265–283).

Freeman, W. E., & Visher, G. S. (1975). Stratigraphic Analysis of the Navajo Sandstone. *Journal of Sedimentary Research*, *45*(3), 651–668.

Garden, I. R., Guscott, S.C., Foxford, K.A., Burley, S.D., Walsh, J.J., & Watterson, J. (1997). An exhumed fill and spill hydrocarbon fairway in the Entrada sandstone of the Moab anticline, Utah, in J. Hendry, P. Carey, J. Parnell, A. Ruffell, and R. Worden, eds., *Migration and interaction in sedimentary basins and orogenic belts: Second International Conference on Fluid evolution*, Belfast, Northern Ireland, p. 287–290.

Garden, I. R., Guscott, S. C., Burley, S. D., Foxford, K. A., Walsh, J. J., & Marshall, J. (2001). An exhumed palaeo-hydrocarbon migration fairway in a faulted carrier system, Entrada Sandstone of SE Utah, USA. *Geofluids*, *1*(3), 195–213.

Gauthier, B., & Lake, S. (1993). Probabilistic Modeling of Faults Below the Limit of Seismic Resolution in Pelican Field, North Sea, Offshore United Kingdom. *AAPG Bulletin*, *77*(5), 761–777.

Gibson, R. (1998). Physical character and fluid-flow properties of sandstone-derived fault zones (in Structural geology in reservoir characterization). *Geological Society, London, Special Publications*, *127,* 83–97.

Grover, B. (1955). Simplified air permeameters for soil in place. *Soil Science Society of America Journal*, *19*(4), 414–418.

Houseknecht, D. (1987). Assessing the relative importance of compaction processes and cementation to reduction of porosity in sandstones. *AAPG bulletin*, *71*(6), 633–642.

IPCC, 2005: IPCC Special Report on Carbon Dioxide Capture and Storage. Prepared by Working Group III of the Intergovernmental Panel on Climate Change [Metz, B., O. Davidson, H. C. de Coninck, M. Loos, and L. A. Meyer (eds.)]. Cambridge University Press, Cambridge, United Kingdom and New York, NY, USA, 442 pp.

Kanninen, M., & Popelar, C. (1985). *Advanced Fracture Mechanics* (p. 563). New York, NY: Oxford University Press.

Li, K. & Firoozabadi, A. (2000). Experimental study of wettability alteration to preferential gas-wetting in porous media and its effects. *Society of Petroleum Engineers.* No. 62515-Pa. 139-149.

Liang, P., Bowers, C., & Bowen, H. (1995). Finite element model to determine the shape factor for soil air permeability measurements. *Transactions of the ASAE*, *38*(4), 997–1003.

Marino, J. (1992). Erg Margin and Marginal Marine Facies Analysis of the Entrada Sandstone, San Rafael Swell, Utah: Implications to Hydrocarbon Entrapment. *BYU Master's Thesis*.

Mayo, A. L., Shrum, D. B., & Chidsey, T. C. J. (1991). Factors contributing to exsolving carbon dioxide in ground water systems in the Colorado Plateau, Utah. *Utah Geological Association Publication*, *19*, 335–342.

North, F. K. (1985). *Petroleum Geology* (p. 607). Winchester, Massachusetts: Allen & Unwin Inc.

Nuccio, V. F., & Condon, S. M. (1996). *Burial and thermal history of the Paradox Basin, Utah and Colorado, and petroleum potential of the middle Pennsylvanian Paradox Formation-U.S. Geological Survey Bulletin 2000-O* (pp. O1–O41). Washington D.C.: United States Government Printing Office.

Okasha, T.M., & Al-Shiwaish, A.A. (2010). Effect of temperature and pressure on interfacial tension and contact angle of Khuff gas reservoir, Saudi Arabia. *Society of Petroleum Engineers.* No. 136934-Ms. 11 p.

O'Neil, J., Adami, L., & Epstein, S. (1975). Revised value for the O18 fractionation between CO2 and H2O at 25°C. *Journal of Research of the U.S. Geological Survey*, *3*(5), 623–524.

O'Neil, J. R., Clayton, R. N., & Mayeda, T. K. (1969). Oxygen Isotope Fractionation in Divalent Metal Carbonates. *The Journal of Chemical Physics*, *51*(12), 5547–5558.

O'Sullivan, R. B. (1981). The Middle Jurassic San Rafael Group and related rocks in east-central Utah. *New Mexico Geological Society Guidebook. 32 Field Conference, Western Slope Colorado*, 89–96.

Parry, W. T., Chan, M. A., & Nash, B. P. (2009). Diagenetic characteristics of the Jurassic Navajo Sandstone in the Covenant oil field, central Utah thrust belt. *AAPG Bulletin*, *93*(8), 1039–1061.

Parry, W. T., Forster, C. B., Evans, J. P., Bowen, B. B., & Chan, M. A. (2007). Geochemistry of CO2 sequestration in the Jurassic Navajo Sandstone, Colorado Plateau, Utah. *Environmental Geosciences*, *14*(2), 91–109.

Pasala, S. M., Forster, C. B., Deo, M., & Evans, J. P. (2013). Simulation of the impact of faults on CO 2 injection into sandstone reservoirs. *Geofluids*.

Payne, W. G. (2011). Controls on Porosity and Permeability in the Carmel Formation: Implications for Carbon Sequestration at Gordon Creek, Utah. *NMT Master's Thesis*, 155.

Picard, M. D. (1977). Stratigraphic Analysis of the Navajo Sandstone: DISCUSSION. *Journal of Sedimentary Research*, *47*(1), 475–483.

Pipiringos, G. N., & O'Sullivan, R. B. (1978). Principal unconformities in Triassic and Jurassic rocks, western interior United States: a preliminary survey. *Geological Survey Professional Paper 1035-A*, A1–A29.

Pittman, E. (1979). Porosity diagenesis and productive capability of sandstone reservoirs. *Special Publications of Society of Economic Paleontologists and Mineralogists*, *26*, 159–173.

Pryor, W. A. (1973). Permeability-Porosity Patterns and Variations in Some Holocene Sand Bodies. *AAPG Bulletin*, *57*(1), 162–189.

Ruzyla, K. (1977). Stratigraphic Analysis of the Navajo Sandstone: DISCUSSION. *Journal of Sedimentary Research*, *47*(1), 489–491.

Schowalter, T. T. (1979). Mechanics of secondary hydrocarbon migration and entrapment. *The American Association of Petroleum Geologist Bulletin*, *63*(5), 723–760.

Sharp, Z. (2007). *Principles of stable isotope geochemistry* (p. 344). Upper Saddle River, New Jersey: Pearson Prentice Hall.

Shipton, Z., & Cowie, P. (2001). Damage zone and slip-surface evolution over Î¼m to km scales in high-porosity Navajo sandstone, Utah. *Journal of Structural Geology*, *23*(12), 1825–1844.

Shipton, Z. K. (1999). Fault displacement profiles and damage zone geometry; interpreting the record of fault growth in the Navajo Sandstone. *University of Edinburgh PhD Thesis*.

Shipton, Z. K., Evans, J. P., Dockrill, B., Heath, J. E., Williams, A., Kirchner, D., & Kolesar, P. T. (2005). Natural Leaking CO2-Charged Systems as Analogs for Failed Geologic Storage Reservoirs. *In: Thomas D. and Benson S.M (Eds). Carbon Dioxide Capture for Storage in Deep Geologic Formations; Results from the CO2 Capture Project*, *Volume 2.* (pp. 699–712). Elsevier Science.

Southwestern Partnership for Carbon Sequestration. (2010). *The 2010 Carbon sequestration atlas of the United States and Canada*, 96–107.

Spangler, L. E., Naftz, D. L., Peterman, Z. E., United States Environmental Protection Agency., & United States Geological Survey (1996). *Hydrology, chemical quality, and characterization of salinity in the Navajo aquifer in and near the Greater Aneth Oil Field, San Juan County, Utah.* Salt Lake City, Utah : Denver, Colo.: U.S. Dept. of the Interior, U.S. Geological Survey.

Steidtmann, J. R. (1977). Stratigraphic Analysis of the Navajo Sandstone: DISCUSSION. *Journal of Sedimentary Research*, *47*(1), 484–489.

TinyPerm II Portable Air Permeameter User's Manual. New England Research, Inc. Vindum Engineering, Inc.

Torabi, A., & Fossen, H. (2009). Spatial variation of microstructure and petrophysical properties along deformation bands in reservoir sandstones. *AAPG Bulletin*, *93*(7), 919–938. doi:10.1306/03270908161

Torabi, A., Fossen, H., & Alaei, B. (2008). Application of spatial correlation functions in permeability estimation of deformation bands in porous rocks. *Journal of Geophysical Research*, *113*(B8), 1–10.

Treiber, L.E., Archer, D.L., & Owens, W.W. (1972) A laboratory evaluation of the wettability of fifty oil-producing reservoirs. *Society of Petroleum Engineers.* No. 3526-Pa. 531-540.

Vavra, C.L., Kaldi, J.G., & Sneider, R.M. (1992) *AAPG Buletin.* 76(6), 840-850

Veizer, J., Ala, D., Azmy, K., Bruckschen, P., Buhl, D., Bruhn, F., Carden, G.A.F., Diener, A., Ebneth, S., Godderis, Y., Jasper, T., Korte, C., Pawellek, F., Podlaha, O.G., Strauss, H. (1999). 87Sr/86Sr, δ13C and δ18O evolution of Phanerozoic seawater. *Chemical Geology*, *161*(1–3), 59–88.

Wardlaw, N., & Cassan, J. (1979). Oil recovery efficiency and the rock-pore properties of some sandstone reservoirs. *Bulletin of Canadian Petroleum Geology*, *27*(2), 117–138.

APPENDICES

LIST OF APPENDIX FIGURES

LIST OF APPENDIX TABLES

APPENDIX A. STRATIGRAPHIC COLUMNS

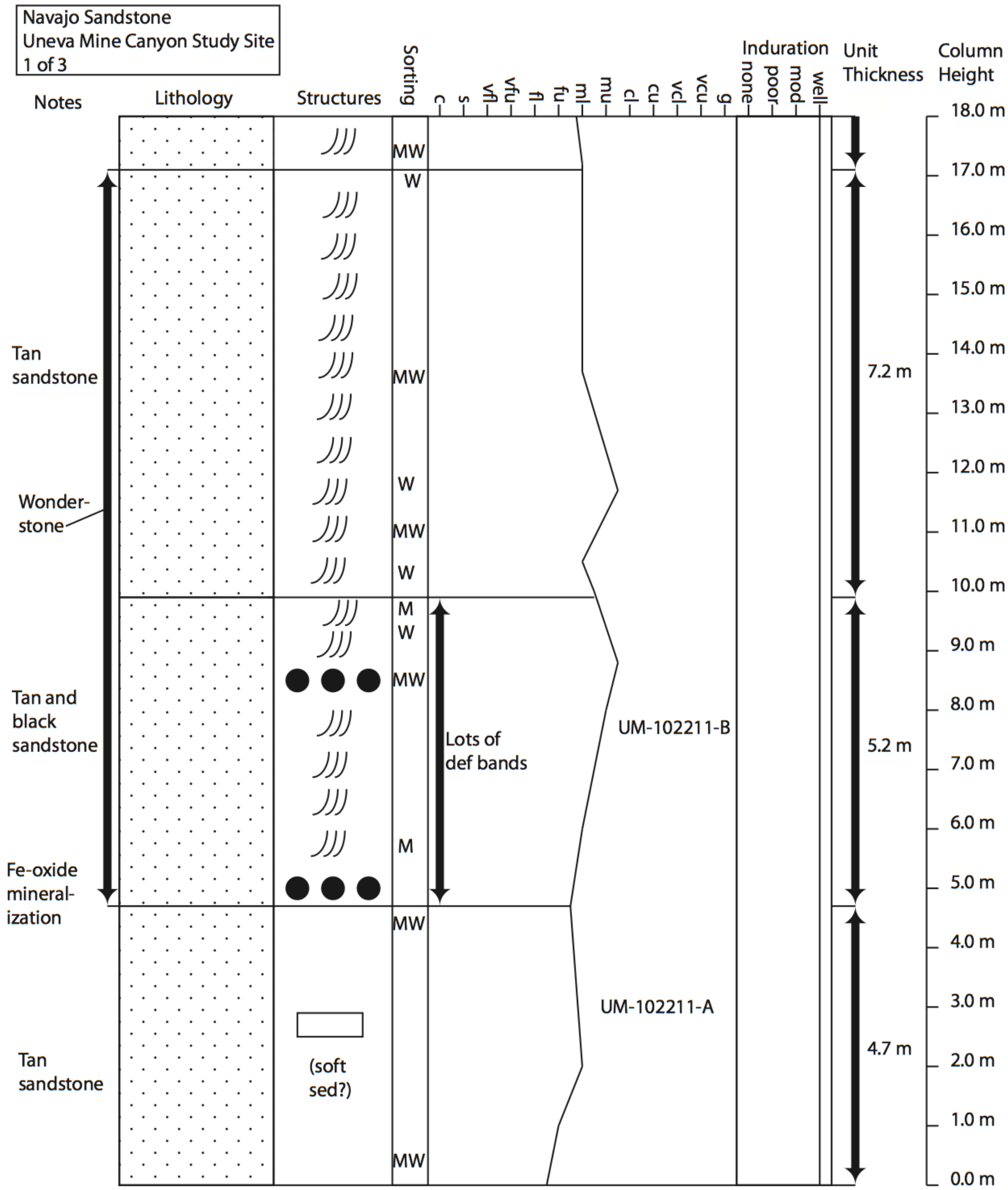

Figure A1. Stratigraphic column of the Navajo Sandstone at the Uneva Mine Canyon study site.

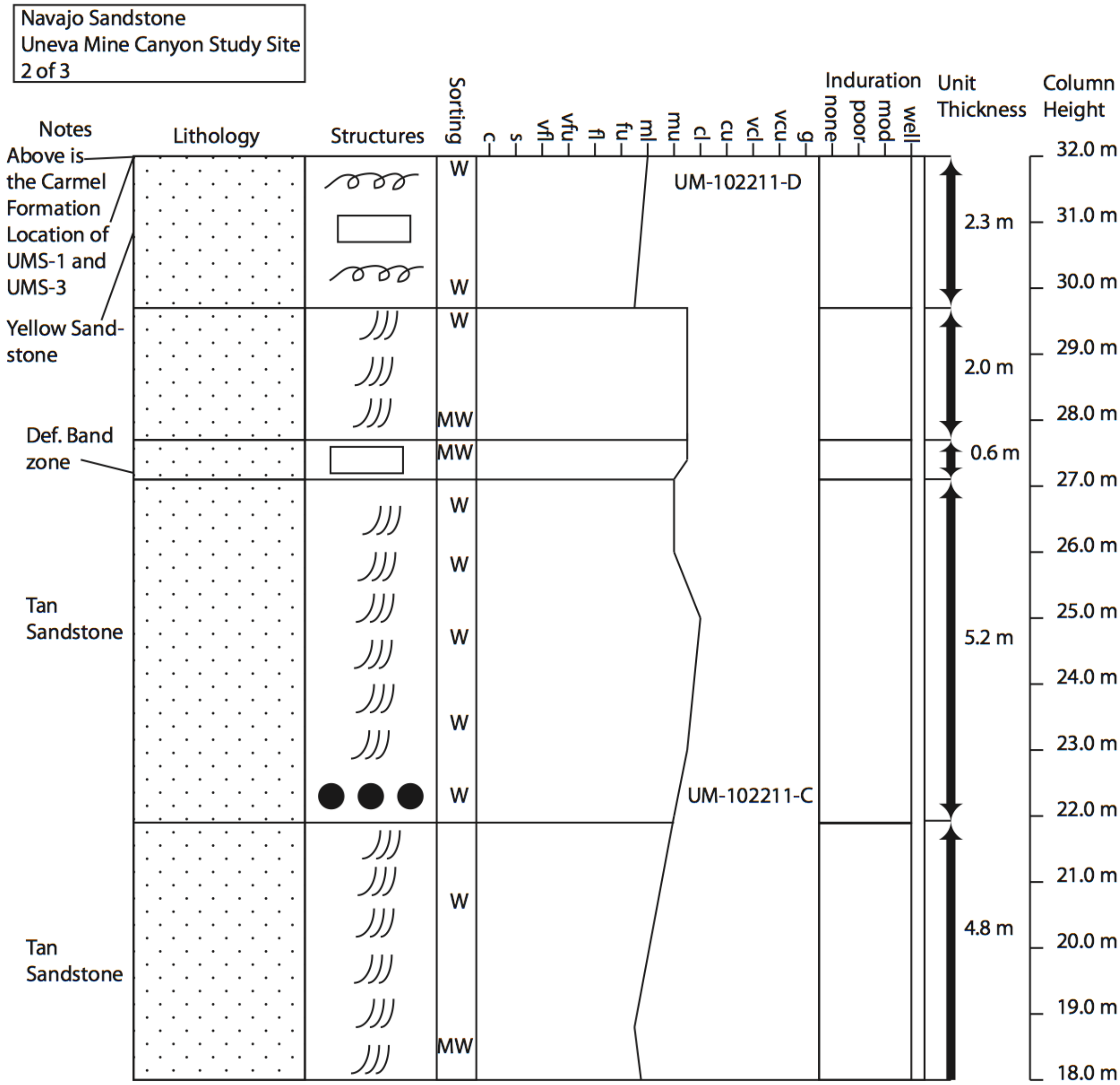

Figure A1. Stratigraphic column of the Navajo Sandstone at the Uneva Mine Canyon study site continued...

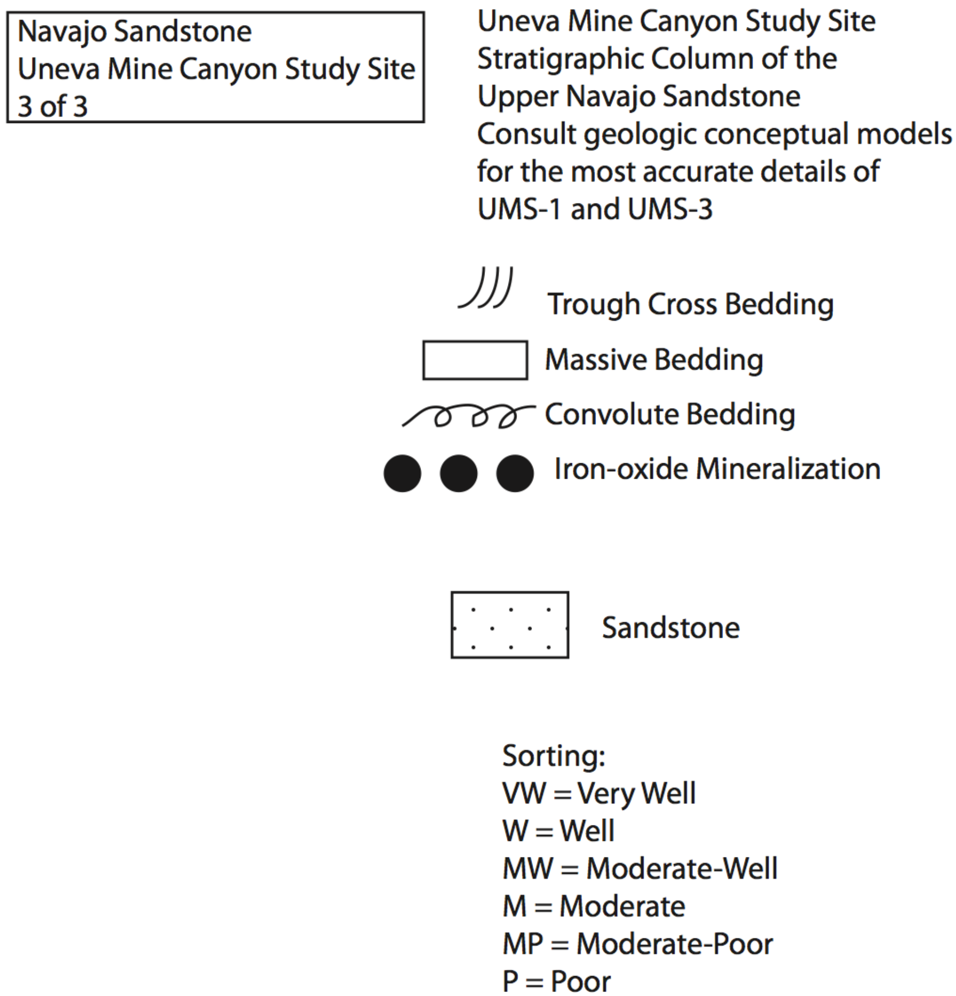

Figure A1. Stratigraphic column of the Navajo Sandstone at the Uneva Mine Canyon study site continued...

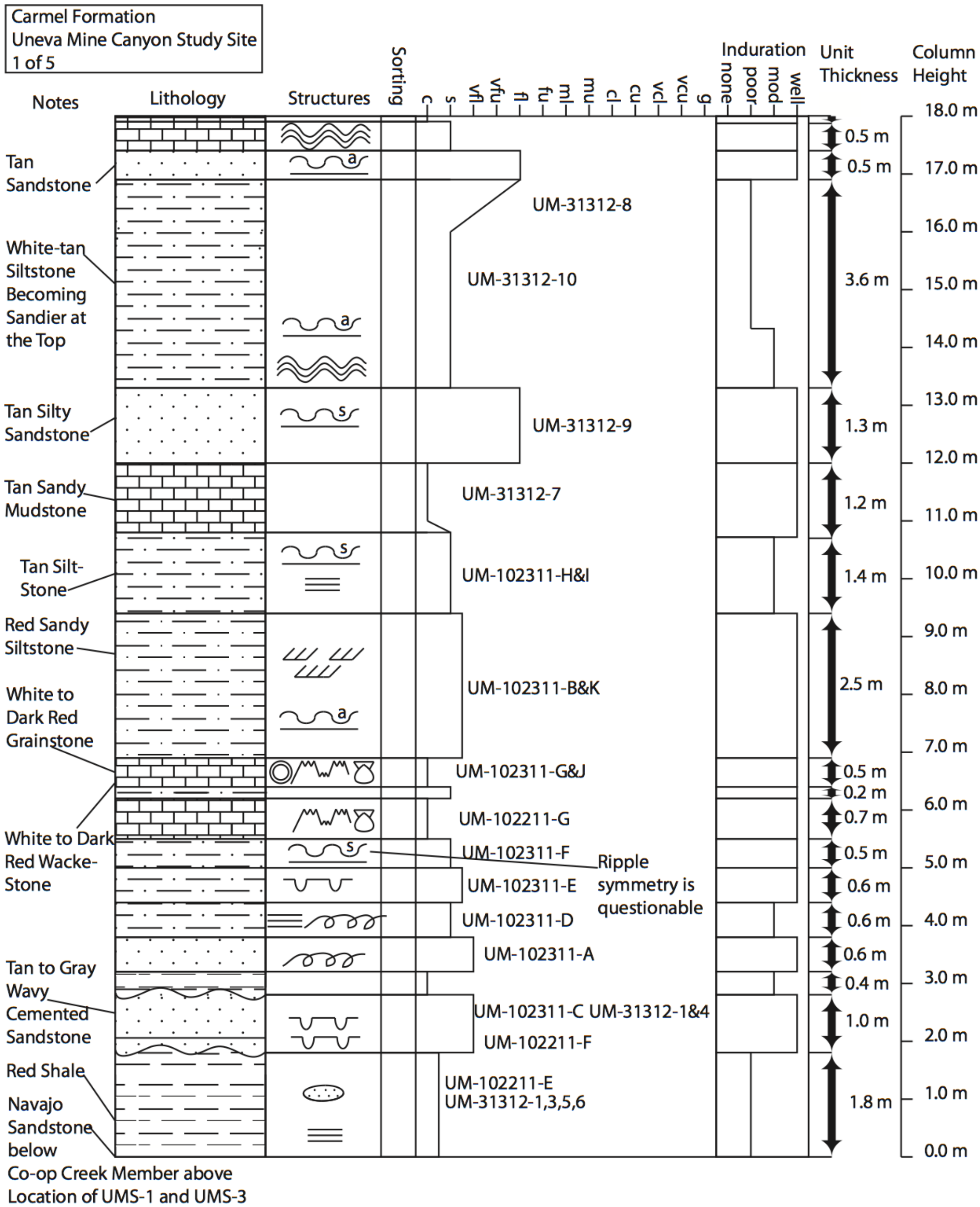

Figure A2. Stratigraphic column of the Carmel Formation at the Uneva Mine Canyon study site.

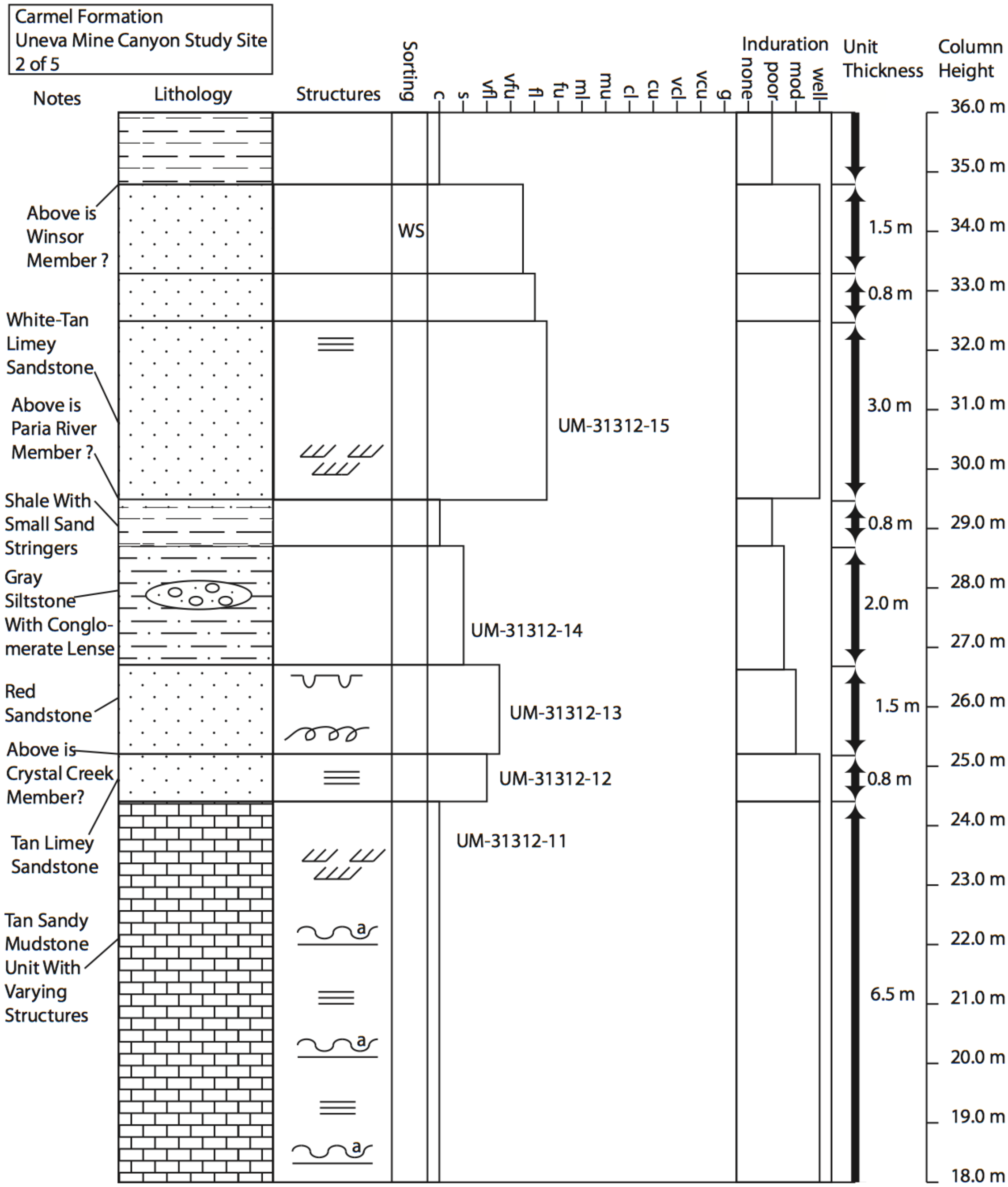

Figure A2. Stratigraphic column of the Carmel Formation at the Uneva Mine Canyon study site continued...

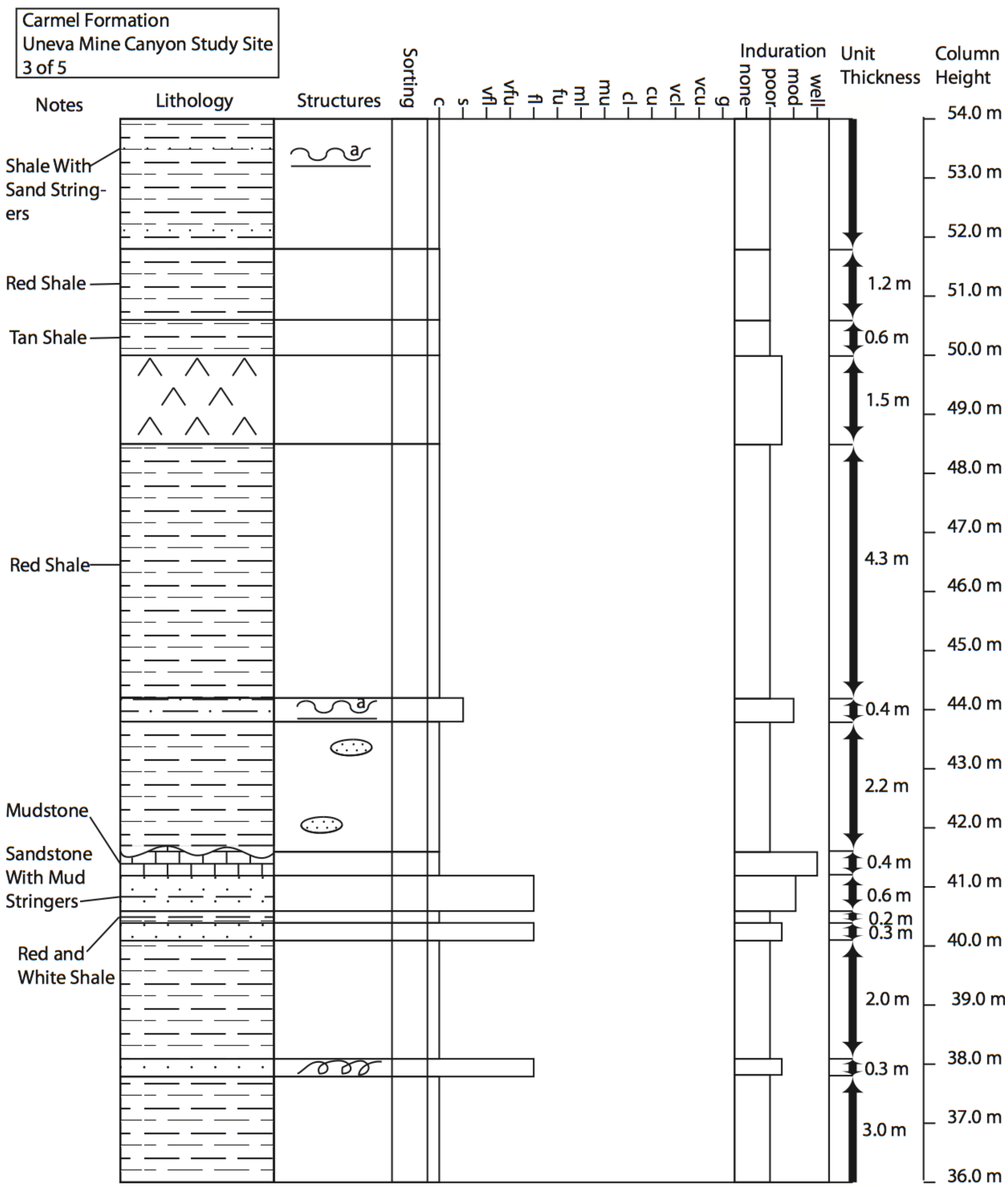

Figure A2. Stratigraphic column of the Carmel Formation at the Uneva Mine Canyon study site continued...

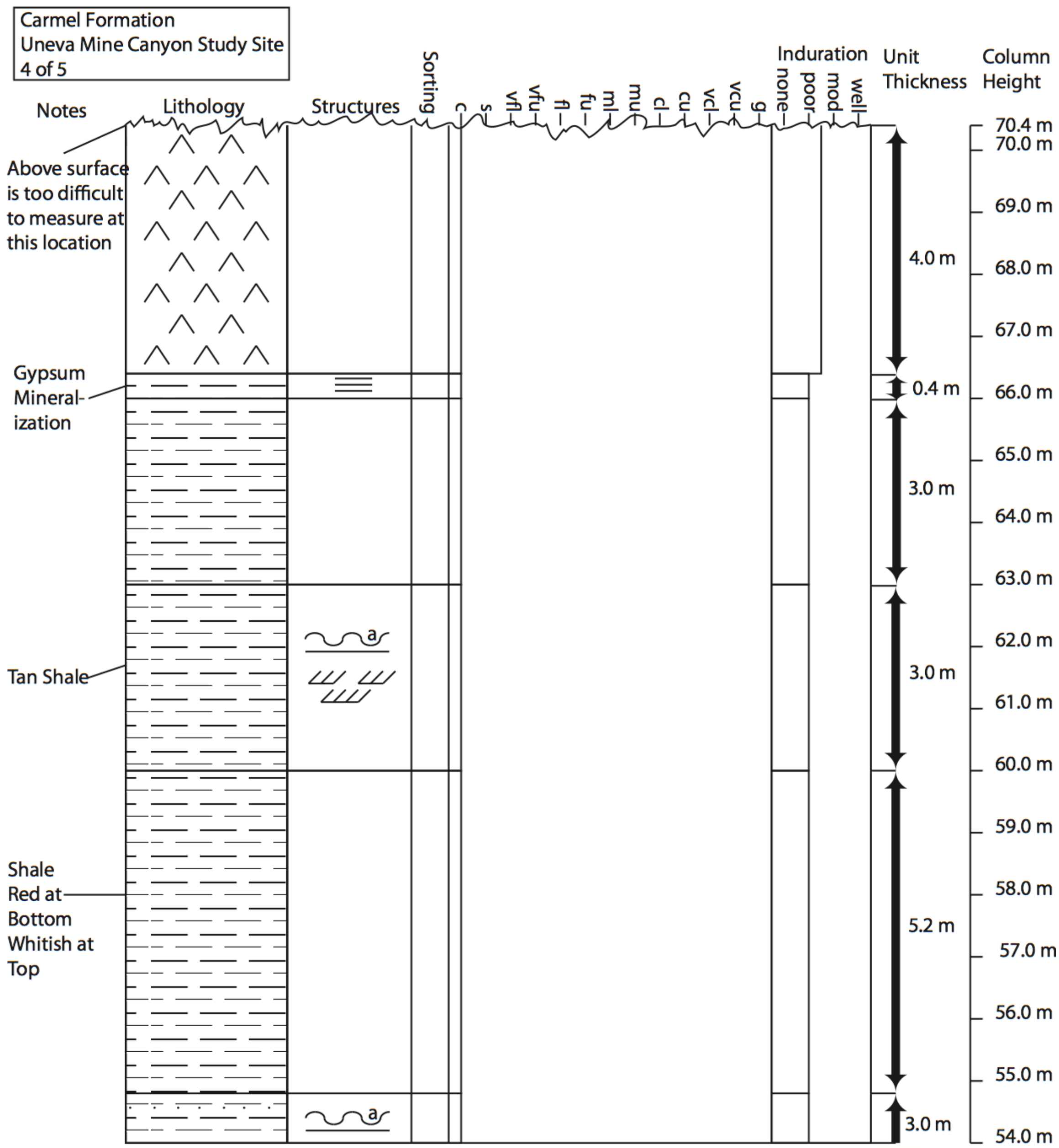

Figure A2. Stratigraphic column of the Carmel Formation at the Uneva Mine Canyon study site continued...

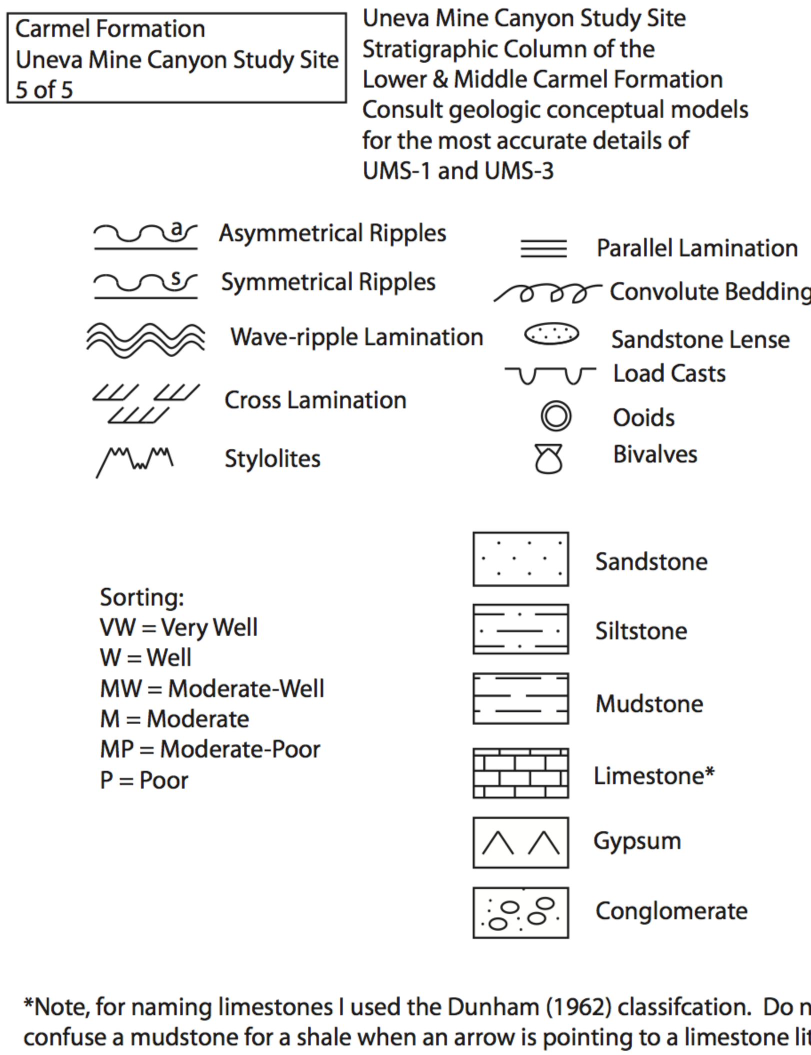

Figure A2. Stratigraphic column of the Carmel Formation at the Uneva Mine Canyon study site continued...

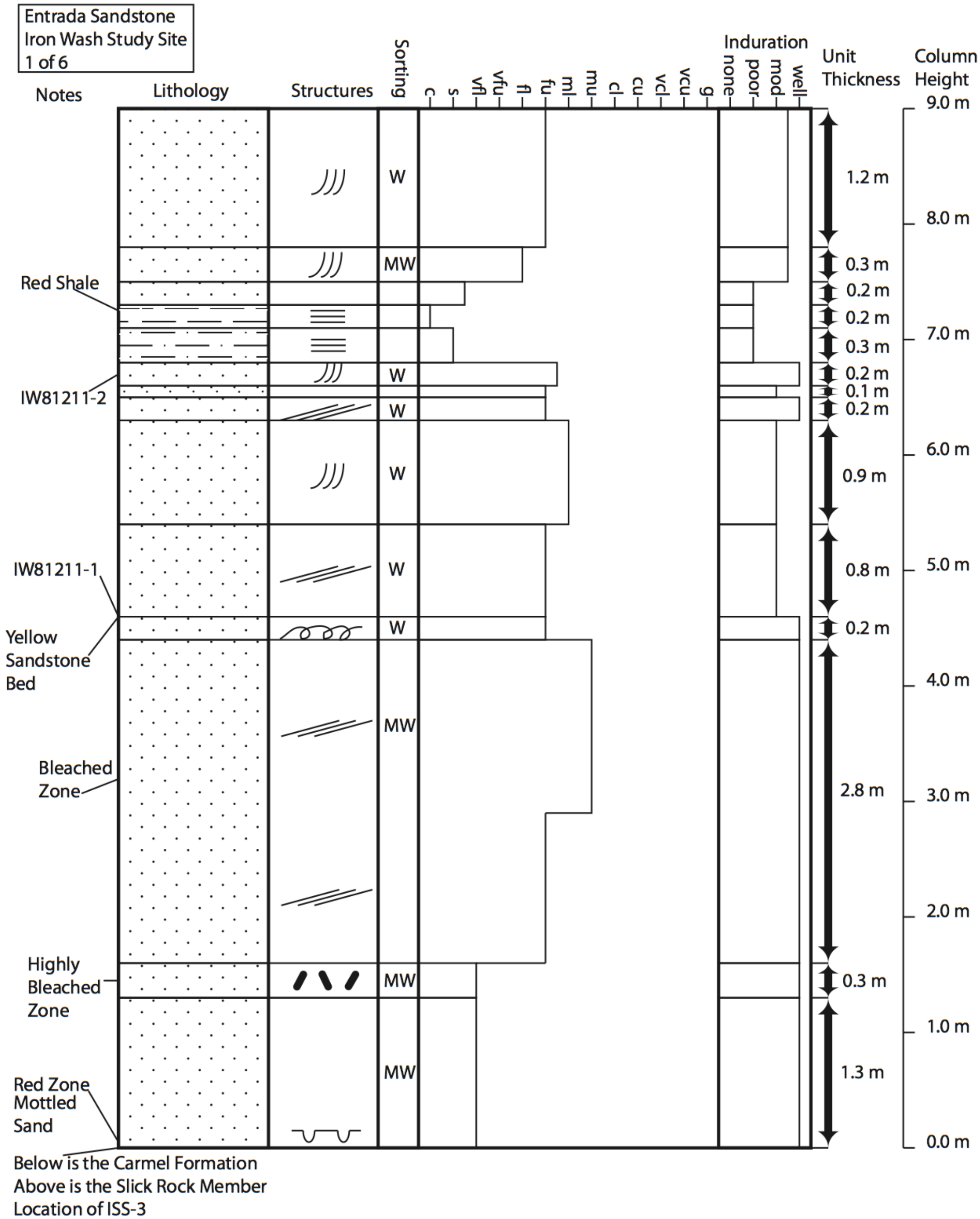

Figure A3. Stratigraphic column of the Entrada Sandstone at the Iron Wash study site.

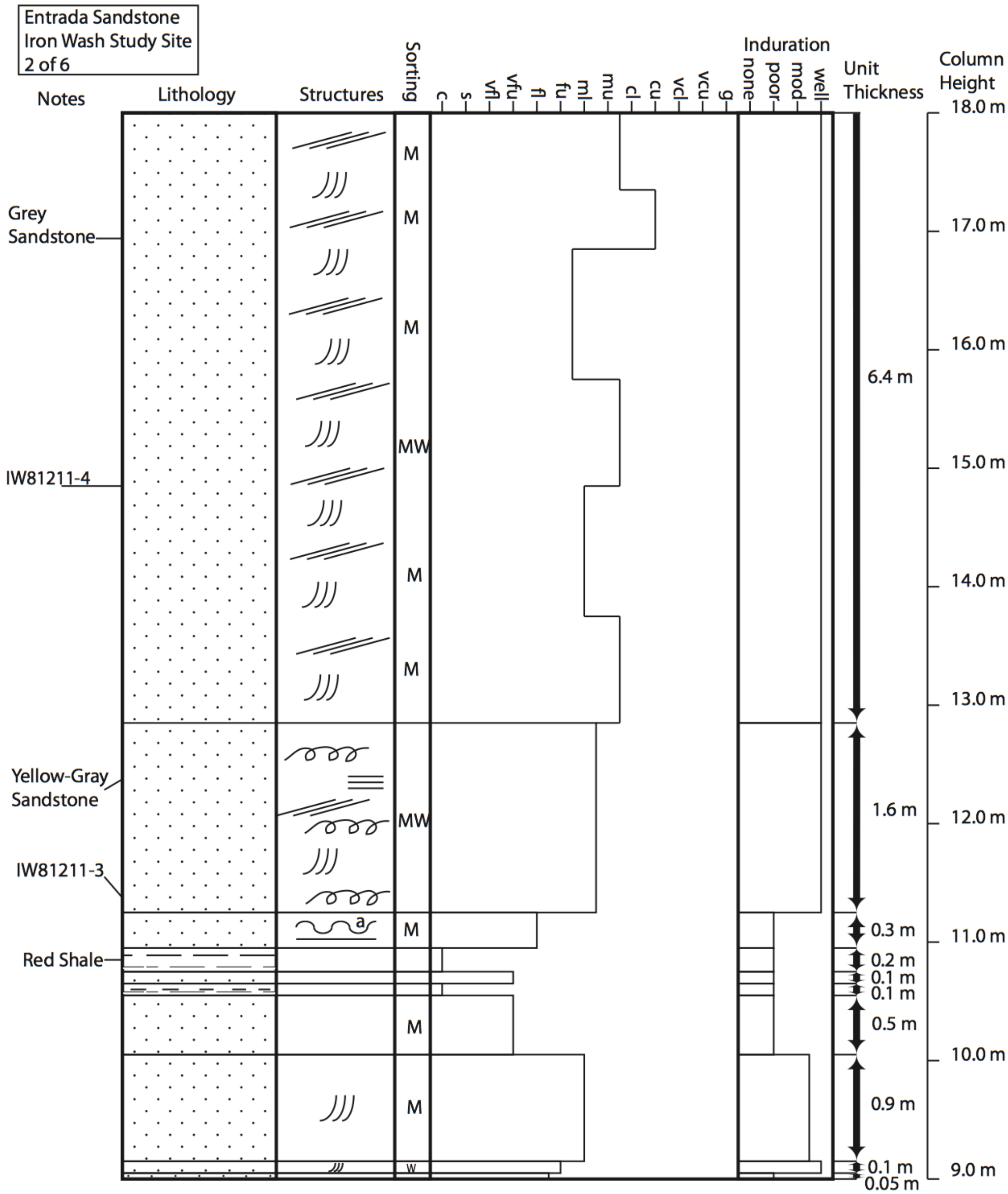

Figure A3. Stratigraphic column of the Entrada Sandstone at the Iron Wash study site continued...

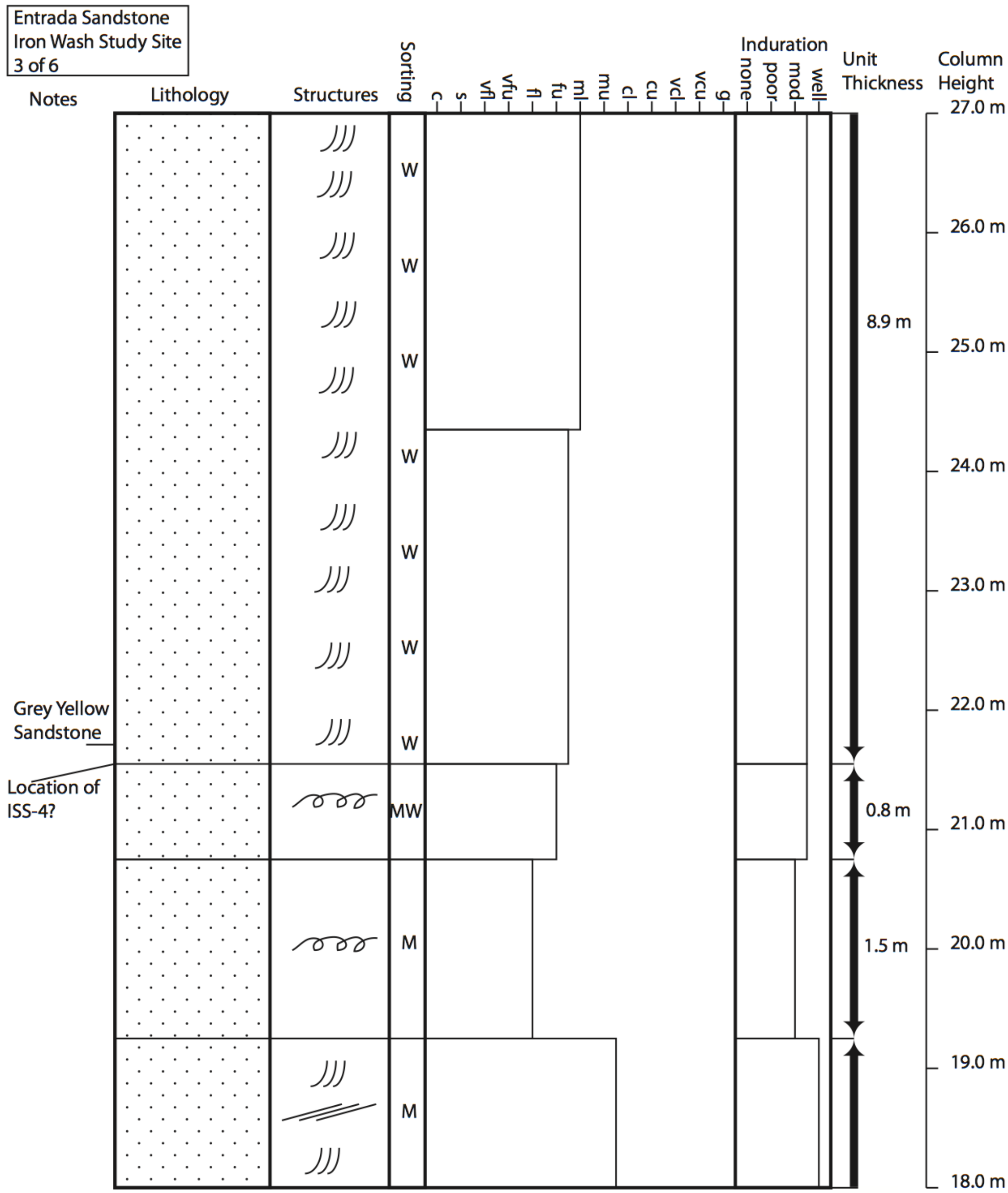

Figure A3. Stratigraphic column of the Entrada Sandstone at the Iron Wash study site continued...

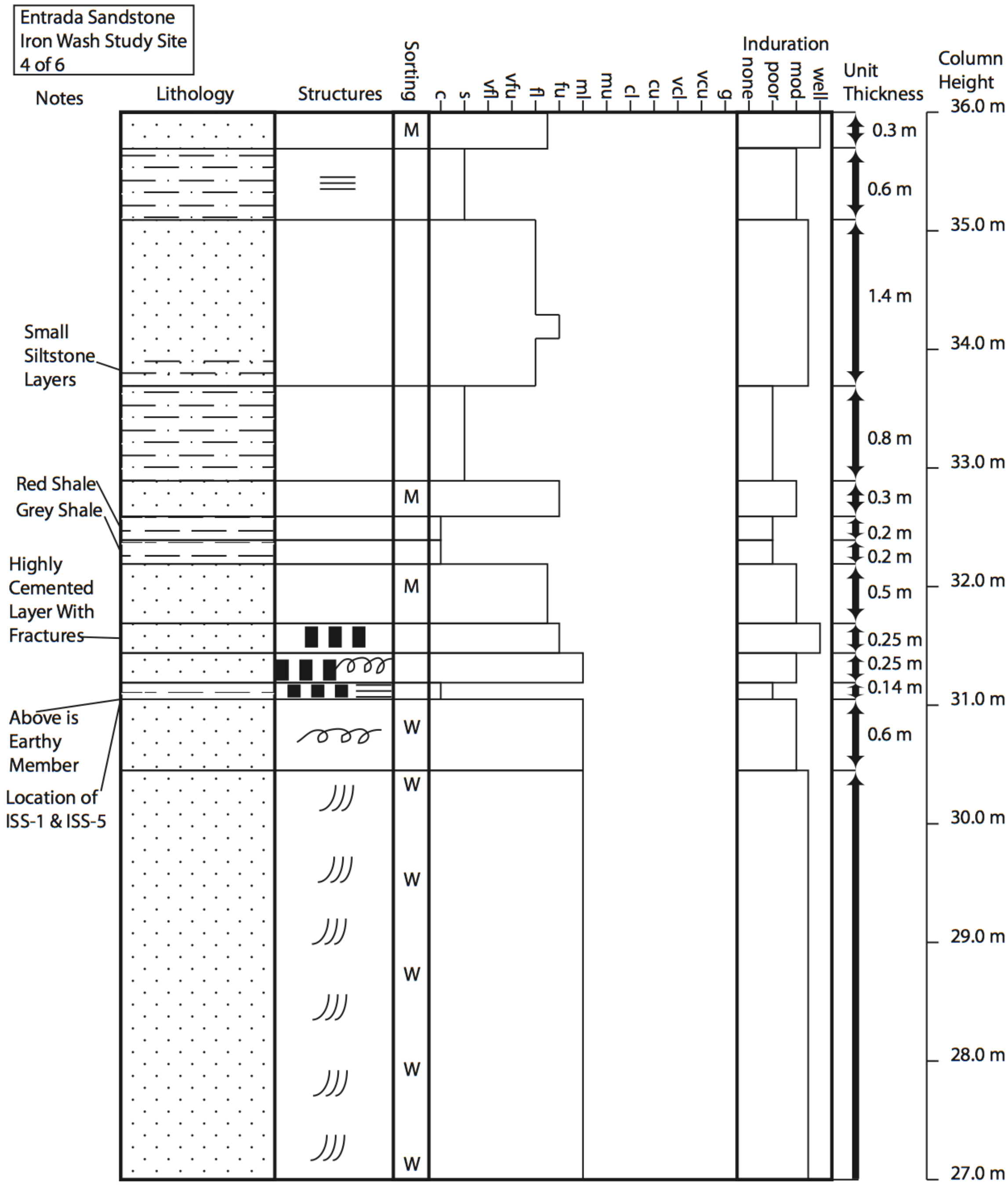

Figure A3. Stratigraphic column of the Entrada Sandstone at the Iron Wash study site continued...

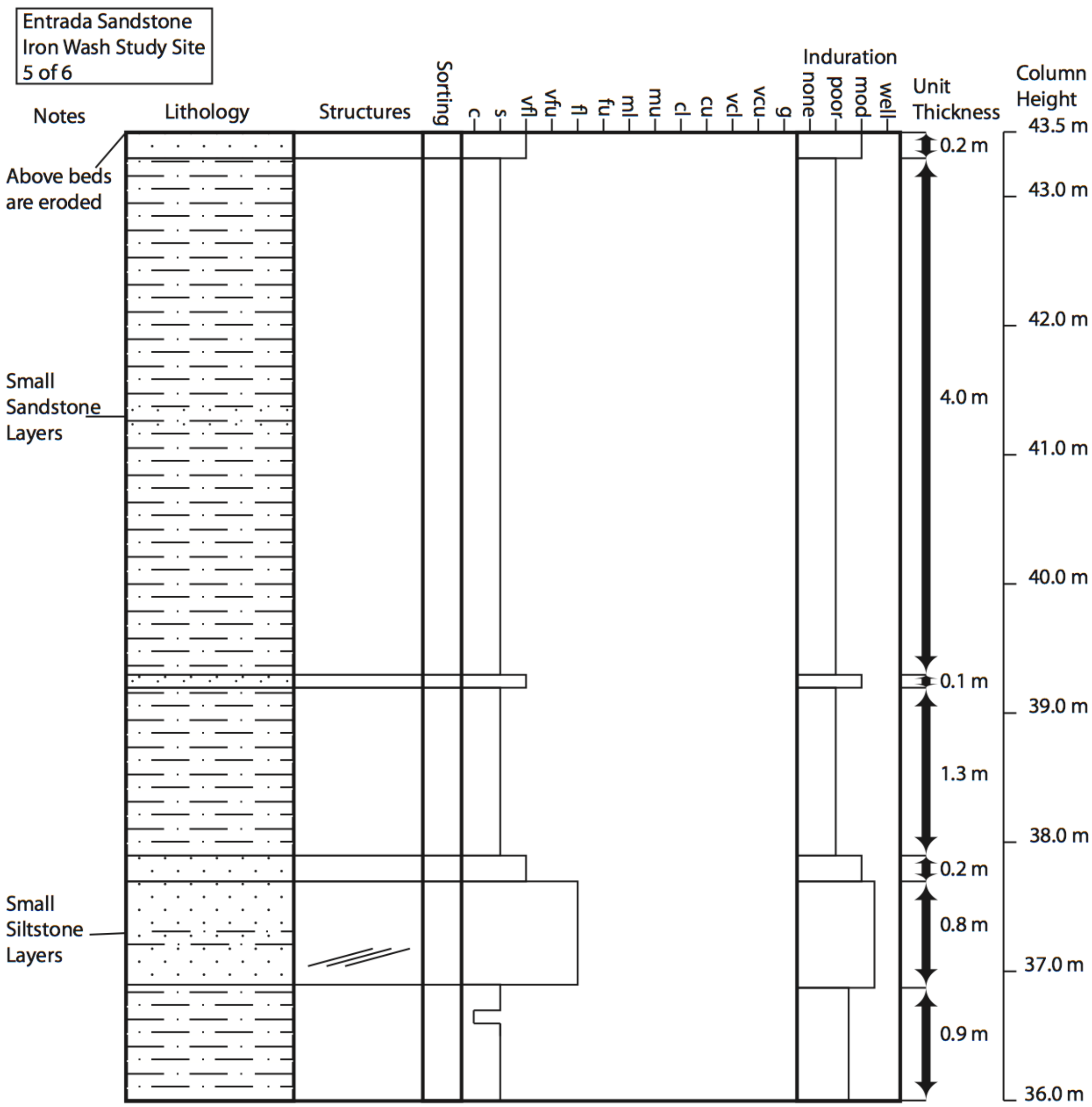

Figure A3. Stratigraphic column of the Entrada Sandstone at the Iron Wash study site continued...

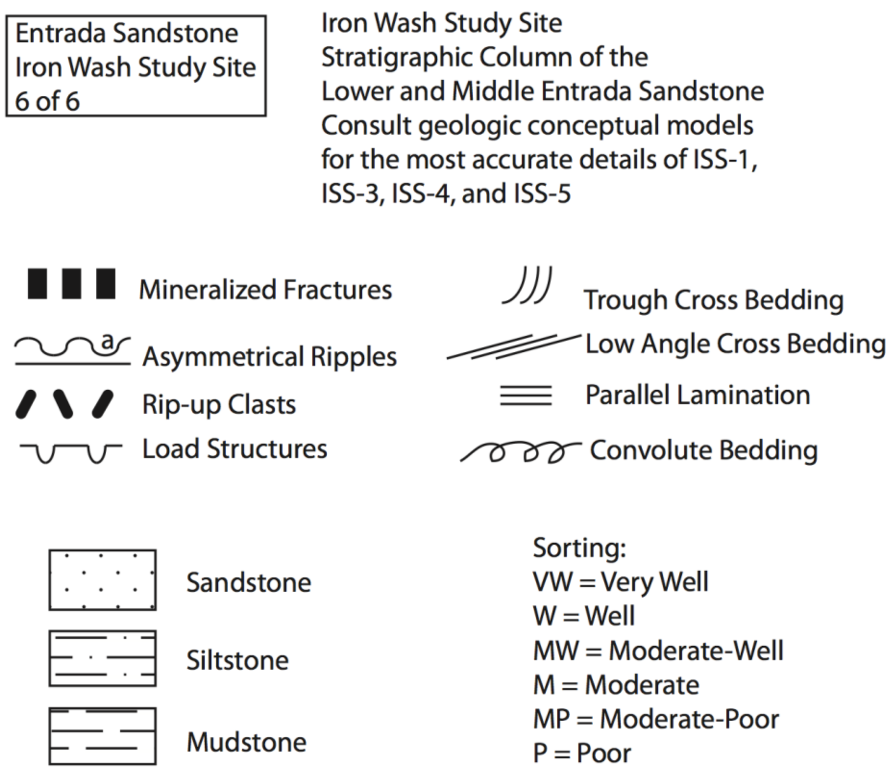

Figure A3. Stratigraphic column of the Entrada Sandstone at the Iron Wash study site continued...

APPENDIX B. TINYPERM II DATA

Figure B1. UMS-1 TinyPerm II measurement locations in the Navajo Sandstone.

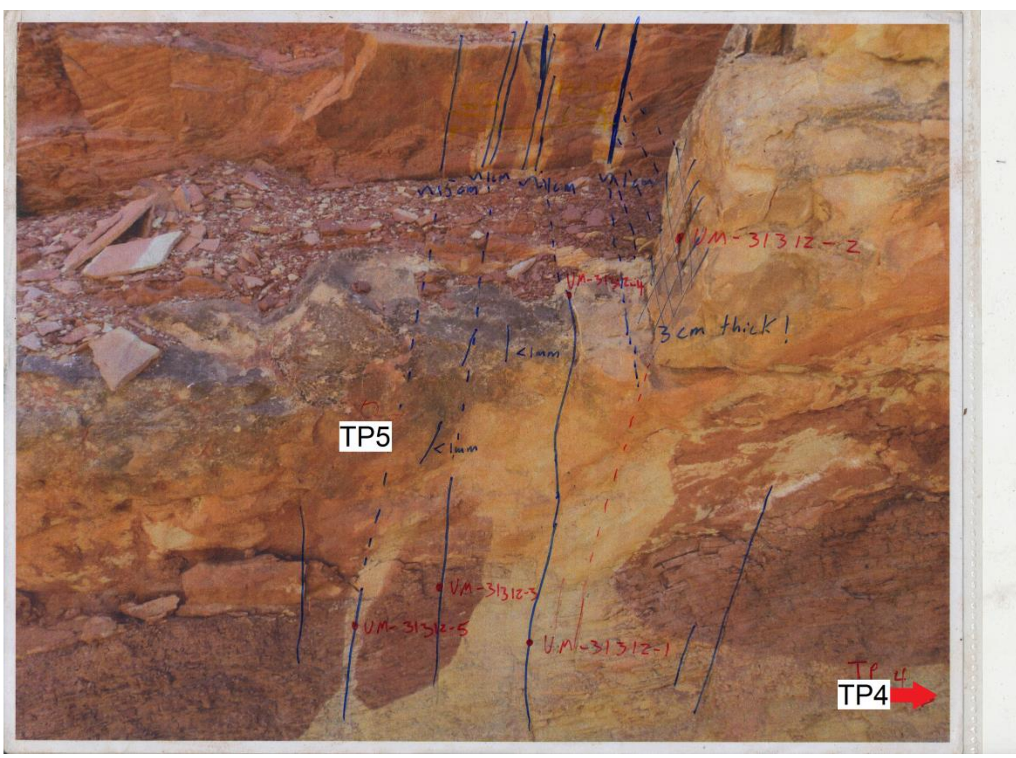

Figure B2. UMS-1 TinyPerm II measurement locations in the Carmel Formation.

Table B1. UMS-1 TinyPerm II data.

Location	Raw TinyPerm II Data			Converted TinyPerm II Data (mD)			Corrected TinyPerm II Data (mD)			Litho-
	Trial 1	Trial 2	Trial 3	Trial 1	Trial 2	Trial 3	Trial 1	Trial 2	Trial 3	facies
TP1	10.73	10.77	10.68	409.60	366.11	471.29	237.78	225.61	255.03	Def.
TP2	10.89	10.71	10.91	261.44	433.24	247.18	196.34	244.39	192.35	Def.
TP3	10.55	10.59	10.59	678.75	606.69	606.69	313.06	292.90	292.90	Def.
TP4										Shale.
TP5	11.52	12.07	11.81	44.63	9.54	19.78	32.70	6.99	14.49	Sand.

Raw Data = (-0.8206)*log(Converted TinyPerm II Value in mD) + 12.8737
Samples >100 mD: Converted TinyPerm II Value in mD = 3.5754*(Corrected TinyPerm II value in mD) - 440.55 mD
Samples <100 mD: Converted TinyPerm II Value in mD = 1.3647*(Corrected TinyPerm II value in mD)

Def. = Deformed Sandstone Lithofacies
Shale. = Shale Lithoface
Sand. = Sandstone Lithofacie

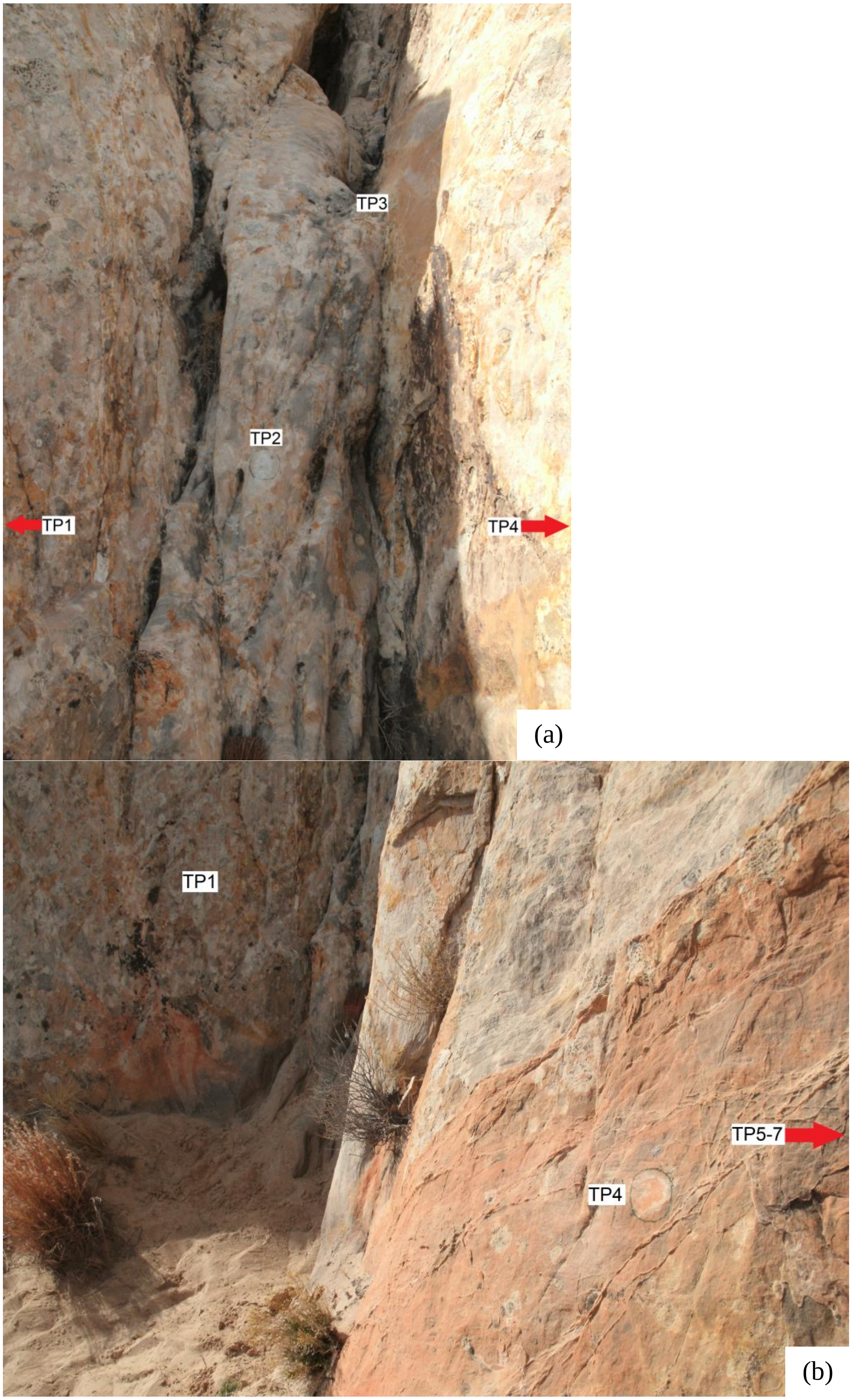
TP3
TP2
TP1
TP4
(a)
TP1
TP5-7
TP4
(b)

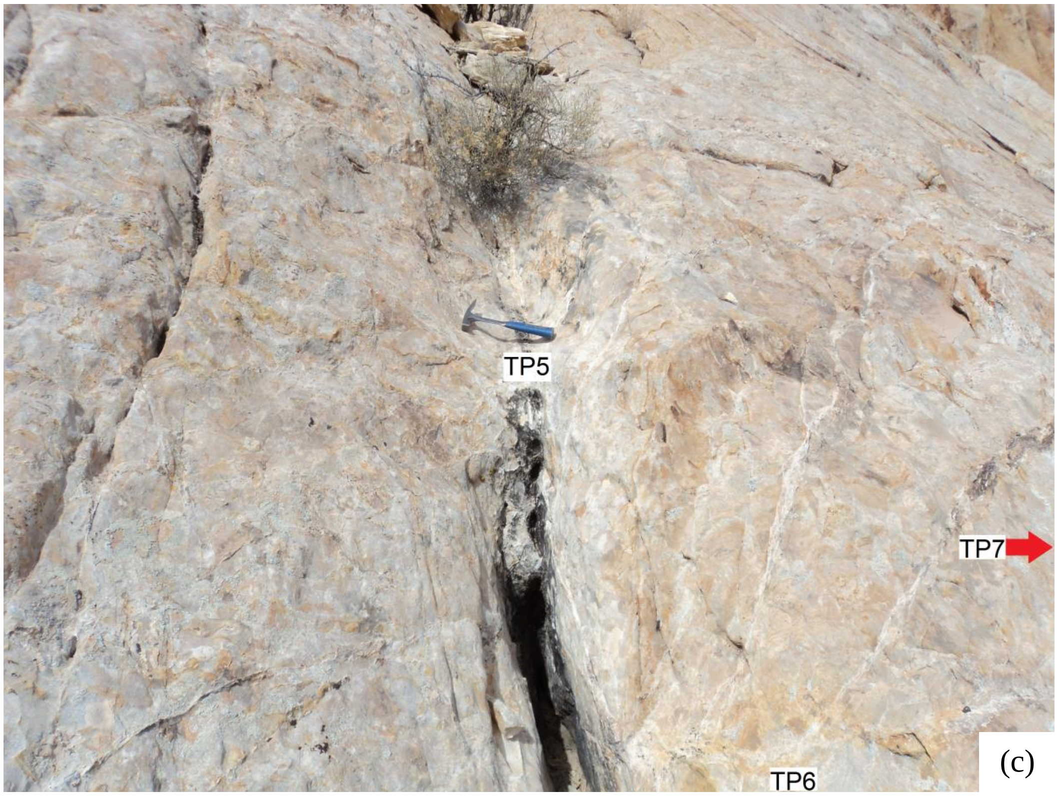

Figure B3. (abc) UMS-3 TinyPerm II measurement locations in the Navajo Sandstone.

Figure B4. UMS-3 TinyPerm II measurement locations in the Carmel Formation.

Table B2. UMS-3 TinyPerm II data.

Location	Raw TinyPerm II Data			Converted TinyPerm II Data (mD)			Corrected TinyPerm II Data (mD)			Deformation	Litho-
	Trial 1	Trial 2	Trial 3	Trial 1	Trial 2	Trial 3	Trial 1	Trial 2	Trial 3	Bands Present	facies
TP1	9.95	9.94	9.98	3654.94	3758.95	3359.87	1145.46	1174.56	1062.94		Def.
TP2	10.92	10.73	10.98	240.34	409.60	203.10	190.44	237.78	180.02	x	Def.
TP3	11.52	11.53	11.48	44.63	43.40	49.93	32.70	31.80	36.59	x	Def.
TP4	10.19	10.25	10.17	1863.85	1575.05	1971.44	644.52	563.74	674.61		Def.
TP5	11.67	11.48	11.73	29.30	49.93	24.76	21.47	36.59	18.14	x	Def.
TP6	10.75	10.73	10.80	387.24	409.60	336.55	231.52	237.78	217.35		Def.
TP7	10.62	10.65	10.69	557.71	512.68	458.25	279.20	266.61	251.38		Def.
TP8	12.03	11.06	11.62	10.67	162.26	33.71	7.82	168.60	24.70		Sand.
TP9	11.96	12.06	11.47	12.99	9.81	51.35	9.52	7.19	37.63		Sand.

Raw Data = (-0.8206)*log(Converted TinyPerm II Value in mD) + 12.8737
Samples >100 mD: Converted TinyPerm II Value in mD = 3.5754*(Corrected TinyPerm II value in mD) - 440.55 mD
Samples <100 mD: Converted TinyPerm II Value in mD = 1.3647*(Corrected TinyPerm II value in mD)

Def. = Deformed Sandstone Lithofacies
Sand. = Sandstone Lithofacie

Samples with deformation bands present were not included within the
average permeability assigned to the deformed and cross-bedded sandstone lithofacies

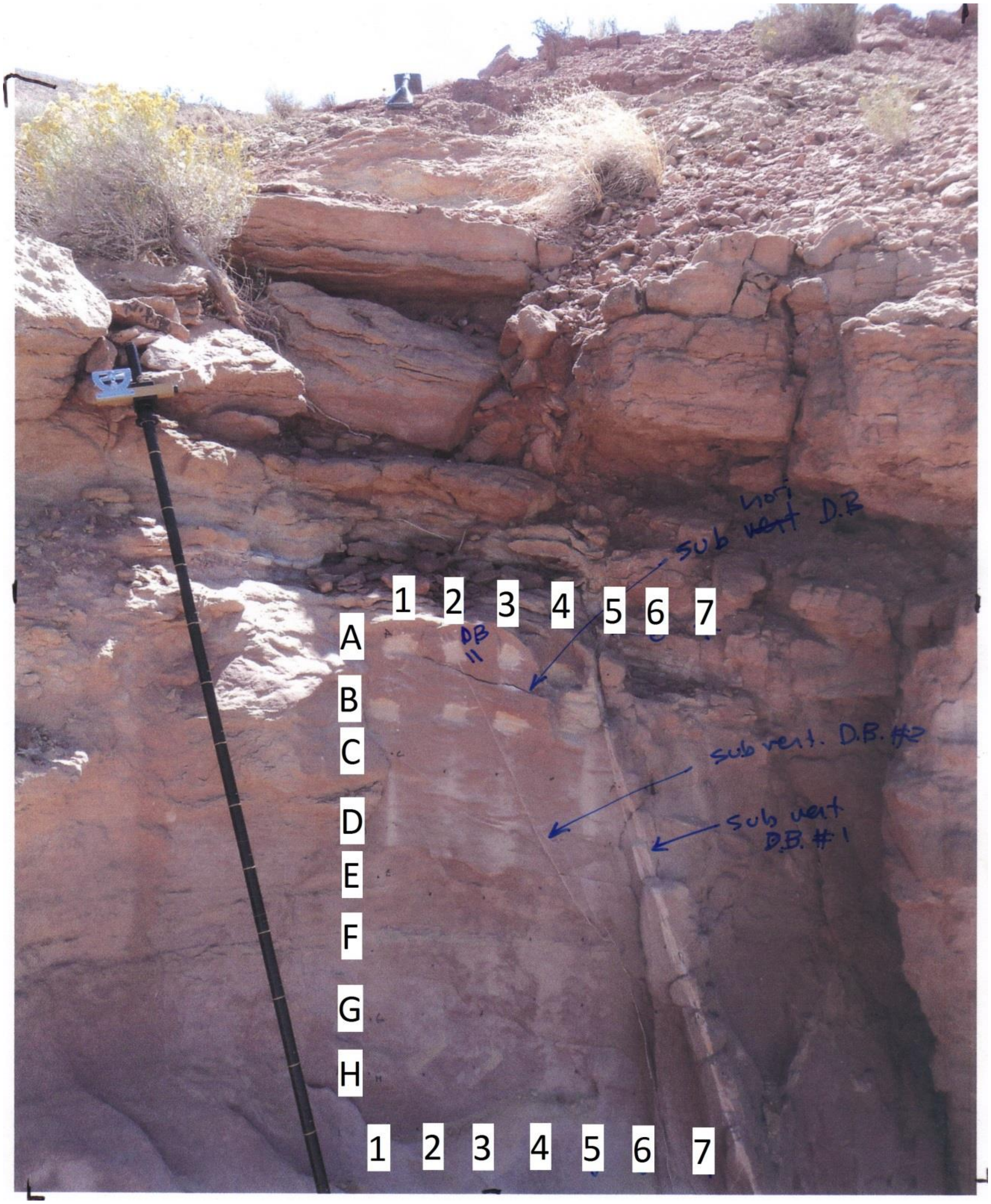

Figure B5. ISS-1 TinyPerm II measurement locations of the Slick Rock Member of the Entrada Sandstone.

Table B3. ISS-1 TinyPerm II data of the Slick Rock Member of the Entrada Sandstone.

Location	Raw TinyPerm II Data			Converted TinyPerm II Data (mD)			Corrected TinyPerm II Data (mD)			Deformation Bands Present	Litho-facies
	Trial 1	Trial 2	Trial 3	Trial 1	Trial 2	Trial 3	Trial 1	Trial 2	Trial 3		
A1	9.59	9.81	9.82	10036.54	5413.62	5263.83	2930.33	1637.35	1595.45		Def.
A2	9.90	9.90	9.79	4205.44	4205.44	5726.12	1299.43	1299.43	1724.75	x	Def.
A3	10.05	10.07	10.07	2760.70	2610.04	2610.04	895.35	853.22	853.22		Def.
A4	9.26	8.86	8.64	25335.47	77835.40	144302.45	7209.27	21892.92	40483.02		Def.
A5	10.27	10.52	10.51	1489.09	738.36	759.37	539.70	329.73	335.60	x	Def.
A6	9.42	9.08	8.87	16171.48	41983.70	75681.72	4646.20	11865.59	21290.56	x	Def.
A7	10.05	9.73	10.32	2760.70	6776.06	1294.17	895.35	2018.41	485.18	x	Def.
B1	10.38	10.39	9.24	1093.64	1063.38	26797.94	429.10	420.63	7618.31		Def.
B2	10.47	10.29	10.38	849.57	1407.83	1093.64	360.83	516.97	429.10		Def.
B3	10.15	10.13	10.26	2085.24	2205.61	1531.47	706.44	740.10	551.55	x	Def.
B4	10.30	9.90	10.12	1368.87	4205.44	2268.38	506.08	1299.43	757.66		Def.
B5	10.35	10.18	10.28	1189.69	1916.89	1447.89	455.96	659.35	528.18	x	Def.
B6	10.05	9.98	10.01	2760.70	3359.87	3088.61	895.35	1062.94	987.07		Def.
B7	9.83	9.55	9.95	5118.18	11228.69	3654.94	1554.71	3263.76	1145.46	x	Def.
C1	10.22	10.24	10.15	1713.38	1619.87	2085.24	602.43	576.28	706.44	x	Def.
C2	10.05	10.18	10.19	2760.70	1916.89	1863.85	895.35	659.35	644.52		Def.
C3	9.86	9.92	9.93	4704.97	3975.94	3865.92	1439.14	1235.24	1204.47		Def.
C4	10.06	10.11	10.14	2684.31	2332.93	2144.58	873.99	775.71	723.03		Def.
C5	10.90	10.32	10.38	254.21	1294.17	1093.64	194.32	485.18	429.10	x	Def.
C6	9.89	9.20	9.19	4325.12	29981.01	30834.18	1332.91	8508.57	8747.20	x	Def.
C7	9.37	9.43	9.32	18607.19	15724.02	21409.76	5327.44	4521.05	6111.29		Def.
D1	9.42	9.48	9.54	16171.48	13665.72	11548.22	4646.20	3945.37	3353.13		Def.
D2	9.11	9.18	9.10	38594.20	31711.63	39692.48	10917.59	8992.61	11224.77		Def.
D3	9.10	9.12	9.11	39692.48	37526.31	38594.20	11224.77	10618.91	10917.59	x	Def.
D4	9.27	9.34	9.25	24634.44	20241.34	26056.45	7013.20	5784.50	7410.92	x	Def.
D5	9.23	9.21	9.24	27560.53	29151.44	26797.94	7831.59	8276.55	7618.31		Def.
D6	10.24	10.25	10.15	1619.87	1575.05	2085.24	576.28	563.74	706.44	x	Def.
D7	10.41	10.34	10.36	1005.35	1223.54	1156.77	404.40	465.43	446.75	x	Cross.
E1	9.41	9.45	9.44	16631.67	14865.90	15288.94	4774.91	4281.04	4399.36		Cross.
E2	9.28	9.29	9.20	23952.82	23290.05	29981.01	6822.56	6637.19	8508.57		Cross.
E3	9.23	9.33	9.33	27560.53	20817.35	20817.35	7831.59	5945.60	5945.60	x	Cross.
E4	9.14	9.24	9.21	35478.35	26797.94	29151.44	10046.12	7618.31	8276.55		Cross.
E5	9.55	9.67	9.46	11228.69	8018.53	14454.56	3263.76	2365.91	4166.00	x	Cross.
E6	9.97	10.05	10.01	3455.48	2760.70	3088.61	1089.68	895.35	987.07	x	Cross.
E7	10.28	10.32	10.28	1447.89	1294.17	1447.89	528.18	485.18	528.18	x	Cross.
F1	9.38	9.40	9.46	18092.33	17104.96	14454.56	5183.44	4907.29	4166.00		Cross.
F2	9.54	9.48	9.48	11548.22	13665.72	13665.72	3353.13	3945.37	3945.37		Cross.
F3	9.55	9.53	9.52	11228.69	11876.85	12214.84	3263.76	3445.04	3539.57	x	Cross.
F4	9.27	9.36	9.40	24634.44	19136.69	17104.96	7013.20	5475.54	4907.29		Cross.
F5	9.87	9.90	9.64	4574.78	4205.44	8722.75	1402.73	1299.43	2562.87		Cross.
F6	11.19	11.53	11.40	112.67	43.40	62.50	154.73	135.35	140.70	x	Cross.
F7	9.40	9.30	9.43	17104.96	22645.62	15724.02	4907.29	6456.95	4521.05		Cross.
G1	9.45	9.43	9.45	14865.90	15724.02	14865.90	4281.04	4521.05	4281.04		Cross.
G2	9.42	9.47	9.45	16171.48	14054.61	14865.90	4646.20	4054.14	4281.04		Cross.
G3	9.28	9.32	9.32	23952.82	21409.76	21409.76	6822.56	6111.29	6111.29		Cross.
G6	9.36	9.36		19136.69	19136.69		5475.54	5475.54		x	Cross.
G7	10.69	10.28	10.43	458.25	1447.89	950.48	251.38	528.18	389.06	x	Cross.
H7	9.43	9.65	9.82	15724.02	8481.39	5263.83	4521.05	2495.37	1595.45		Cross.

Raw Data = (-0.8206)*log(Converted TinyPerm II Value in mD) + 12.8737
Samples >100 mD: Converted TinyPerm II Value in mD = 3.5754*(Corrected TinyPerm II value in mD) - 440.55 mD
Samples <100 mD: Converted TinyPerm II Value in mD = 1.3647*(Corrected TinyPerm II value in mD)

Def. = Deformed Sandstone Lithofacies
Cross. = Cross-bedded Sandstone Lithofacies

Samples with deformation bands present were not included within the
average permeability assigned to the deformed and cross-bedded sandstone lithofacies

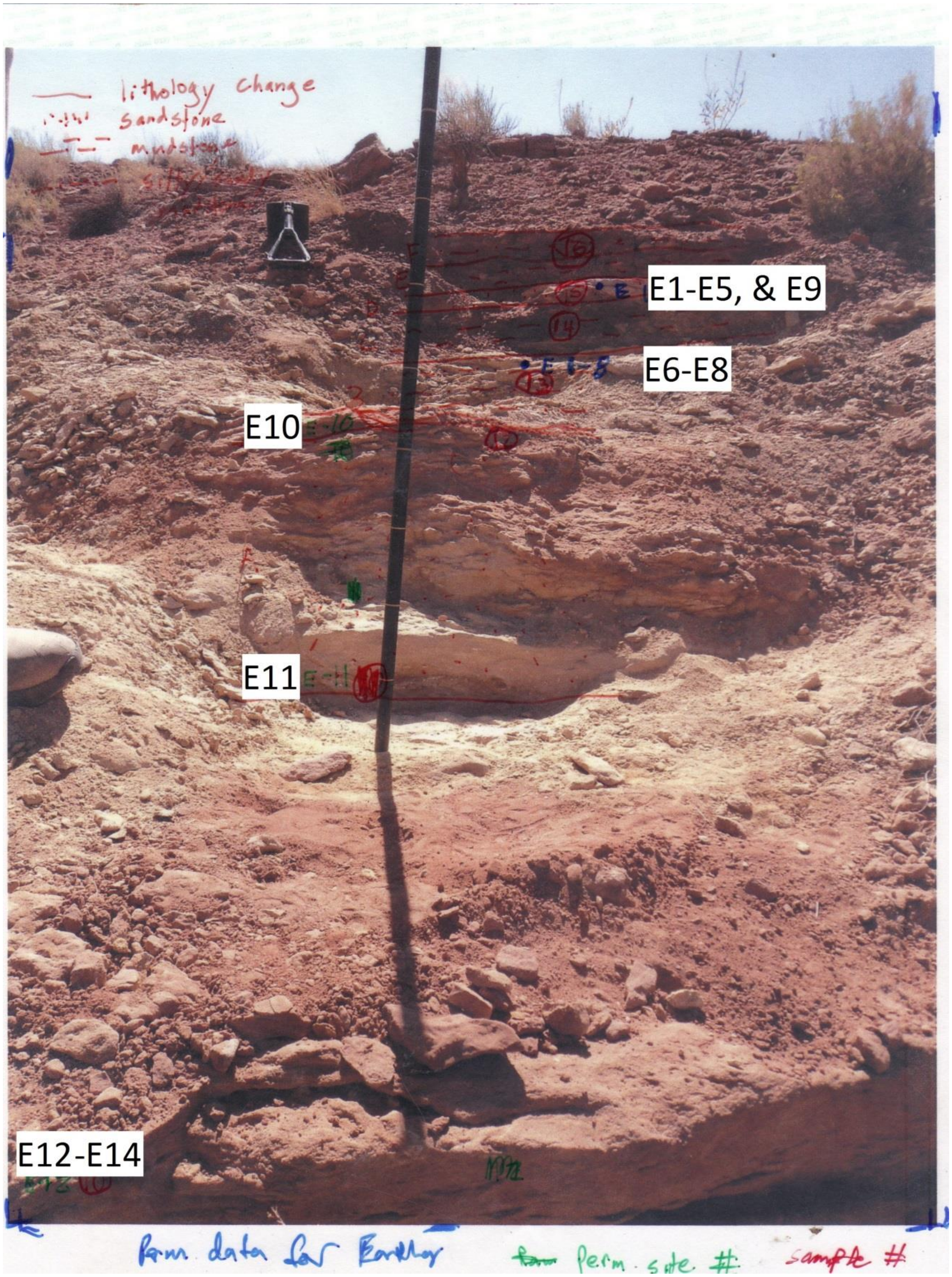

Figure B6. ISS-1 TinyPerm II measurement locations of the Earthy Member of the Entrada Sandstone.

Table B4. ISS-1 TinyPerm II data of the Earthy Member of the Entrada Sandstone.

Location	Raw TinyPerm II Data			Converted TinyPerm II Data (mD)			Corrected TinyPerm II Data (mD)			Litho-facies
	Trial 1	Trial 2	Trial 3	Trial 1	Trial 2	Trial 3	Trial 1	Trial 2	Trial 3	
E1	10.55	11.84	10.75	678.75	18.18	387.24	313.06	13.32	231.52	Sand.
E2	12.13			8.06			5.91			Sand.
E3	12.32			4.73			3.47			Sand.
E4	11.04	11.11		171.63	141.02		171.22	162.66		Sand.
E5	12.07			9.54			6.99			Sand.
E6	11.66	12.24		30.13	5.92		22.08	4.34		Sand.
E7	11.58			37.72			27.64			Sand.
E8	11.52			44.63			32.70			Sand.
E9	11.00			192.01			176.92			Sand.
E10	11.87	11.46	11.02	16.72	52.82	181.53	12.25	38.70	173.99	Sand.
E11	11.03	10.88	10.96	176.51	268.88	214.82	172.59	198.42	183.30	Sand.
E12	12.17	12.24	12.65	7.20	5.92	1.87	5.28	4.34	1.37	Sand.
E13*	10.88			268.88			198.42			Sand.
E14	11.36	11.26	11.15	69.92	92.57	126.05	51.24	67.83	158.47	Sand.

Raw Data = (-0.8206)*log(Converted TinyPerm II Value in mD) + 12.8737

Samples >100 mD: Converted TinyPerm II Value in mD = 3.5754*(Corrected TinyPerm II value in mD) - 440.55 mD

Samples <100 mD: Converted TinyPerm II Value in mD = 1.3647*(Corrected TinyPerm II value in mD)

Sand. = Sandstone Lithofacie

*E13 was not a good site and was not included within the average permeability assigned to the sandstone lithofacie

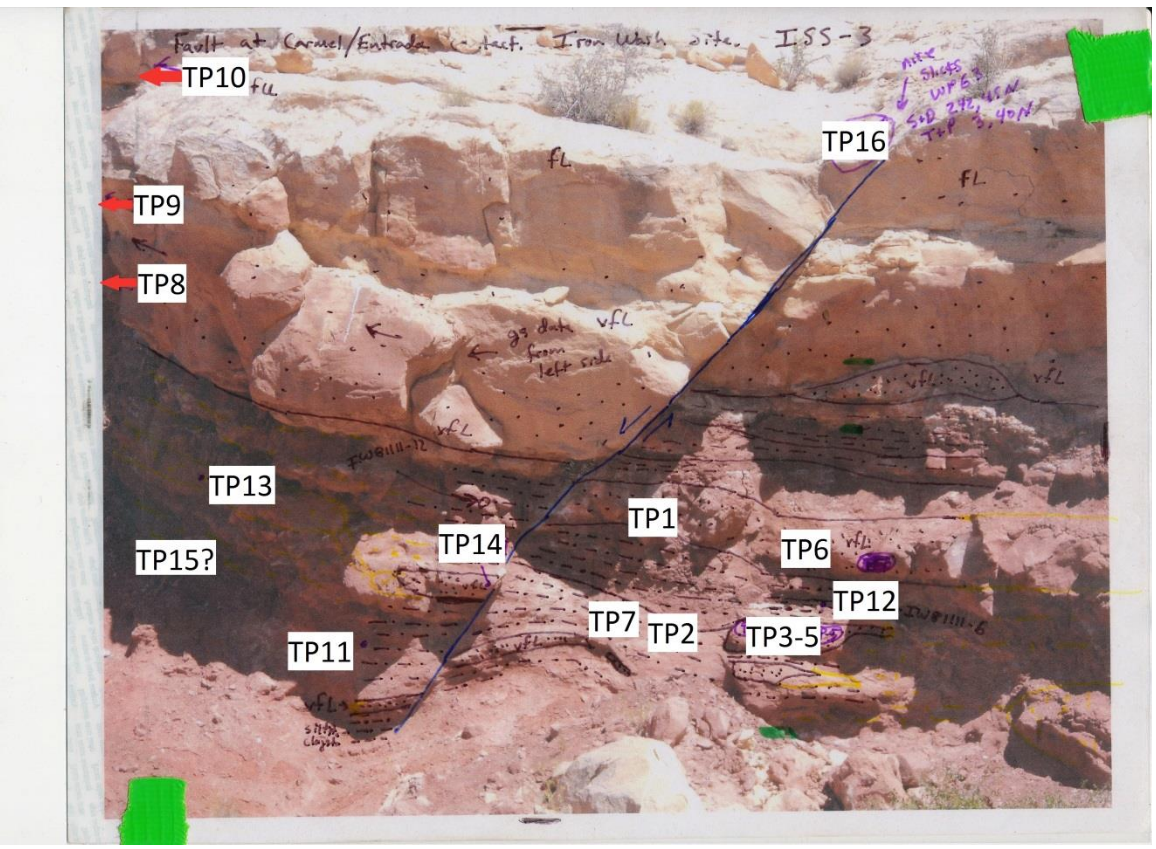

Figure B7. ISS-3 TinyPerm II measurement locations.

Table B5. ISS-3 TinyPerm II data.

Location	Raw TinyPerm II Data			Converted TinyPerm II Data (mD)			Corrected TinyPerm II Data (mD)			Litho-facies
	Trial 1	Trial 2	Trial 3	Trial 1	Trial 2	Trial 3	Trial 1	Trial 2	Trial 3	
TP-1	12.25			5.76			4.22			Sand.
TP-2	11.36	12.60	12.42	69.92	2.16	3.57	51.24	1.58	2.62	Silt.*
TP-3	12.01			11.29			8.27			Sand.
TP-4	12.40			3.78			2.77			Sand.
TP-5	12.27			5.44			3.99			Sand.
TP-6	12.48			3.02			2.21			Sand.
TP-7	11.89			15.80			11.58			Silt.
TP-8	12.46			3.19			2.34			Def.
TP-9	12.22			6.26			4.59			Def.
TP-10	10.21	10.35	10.28	1762.14	1189.69	1447.89	616.07	455.96	528.18	Cross.
TP11	12.01	11.78	12.23	11.29	21.52	6.09	8.27	15.77	4.46	Silt.
TP12	11.84	11.85	12.06	18.18	17.68	9.81	13.32	12.96	7.19	Silt.
TP13	12.45	11.41	12.77	3.28	60.77	1.34	2.41	44.53	0.98	Sand.
TP14	12.12	12.13	11.96	8.29	8.06	12.99	6.07	5.91	9.52	Sand.
TP15	11.65	12.30	12.11	30.99	5.00	8.52	22.71	3.67	6.25	Silt.
TP16	10.33	10.38	10.38	1258.36	1093.64	1093.64	475.17	429.10	429.10	Cross.

Raw Data = (-0.8206)*log(Converted TinyPerm II Value in mD) + 12.8737
Samples >100 mD: Converted TinyPerm II Value in mD = 3.5754*(Corrected TinyPerm II value in mD) - 440.55 mD
Samples <100 mD: Converted TinyPerm II Value in mD = 1.3647*(Corrected TinyPerm II value in mD)

Sand. = Sandstone Lithofacie
Silt. = Siltstone Lithofacie
Def. = Deformed Sandstone Lithofacies
Cross. = Cross-bedded Sandstone Lithofacies

*Measurements from the siltstone lithofacie are not considered accurate as the actual permeability of the siltstones is likely below the lower measuring range of TinyPerm II

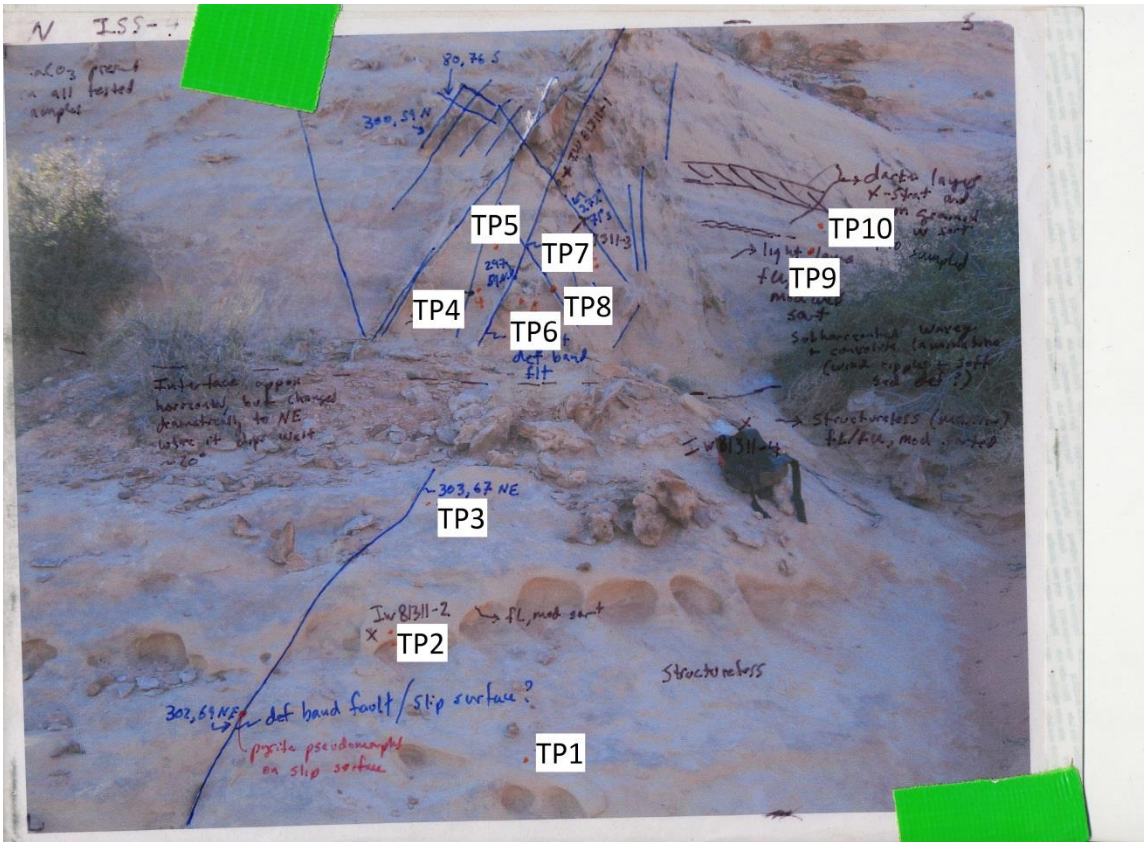

Figure B8. ISS-4 TinyPerm II measurement locations.

Table B6. ISS-4 TinyPerm II data.

Location	Raw TinyPerm II Data			Converted TinyPerm II Data (mD)			Corrected TinyPerm II Data (mD)			Deformation Bands Present	Litho-facies
	Trial 1	Trial 2	Trial 3	Trial 1	Trial 2	Trial 3	Trial 1	Trial 2	Trial 3		
TP1	10.94	11.04	11.28	227.22	171.63	87.52	186.77	171.22	64.13		Def.
TP2	10.99	10.95	10.95	197.48	220.93	220.93	178.45	185.01	185.01		Def.
TP3	10.52	10.72	10.62	738.36	421.25	557.71	329.73	241.04	279.20		Def.
TP4	9.83	9.89	9.82	5118.18	4325.12	5263.83	1554.71	1332.91	1595.45		Cross.
TP5	9.18	9.23	9.17	31711.63	27560.53	32614.06	8992.61	7831.59	9245.01		Cross.
TP6	9.02	9.28	9.30	49681.87	23952.82	22645.62	14018.69	6822.56	6456.95		Cross.
TP7	9.62	9.63	9.62	9226.26	8970.97	9226.26	2703.70	2632.30	2703.70		Cross.
TP8	11.44	11.14	11.15	55.86	129.64	126.05	138.84	159.47	158.47	x	Cross.
TP9	9.49	9.43	9.41	13287.59	15724.02	16631.67	3839.61	4521.05	4774.91		Cross.
TP10	9.95	9.80	9.91	3654.94	5567.68	4089.08	1145.46	1680.43	1266.89		Cross.

Raw Data = (-0.8206)*log(Converted TinyPerm II Value in mD) + 12.8737
Samples >100 mD: Converted TinyPerm II Value in mD = 3.5754*(Corrected TinyPerm II value in mD) - 440.55 mD
Samples <100 mD: Converted TinyPerm II Value in mD = 1.3647*(Corrected TinyPerm II value in mD)

Def. = Deformed Sandstone Lithofacies
Cross. = Cross-bedded Sandstone Lithofacies

Samples with deformation bands present were not included within the average permeability assigned to the cross-bedded sandstone lithofacies

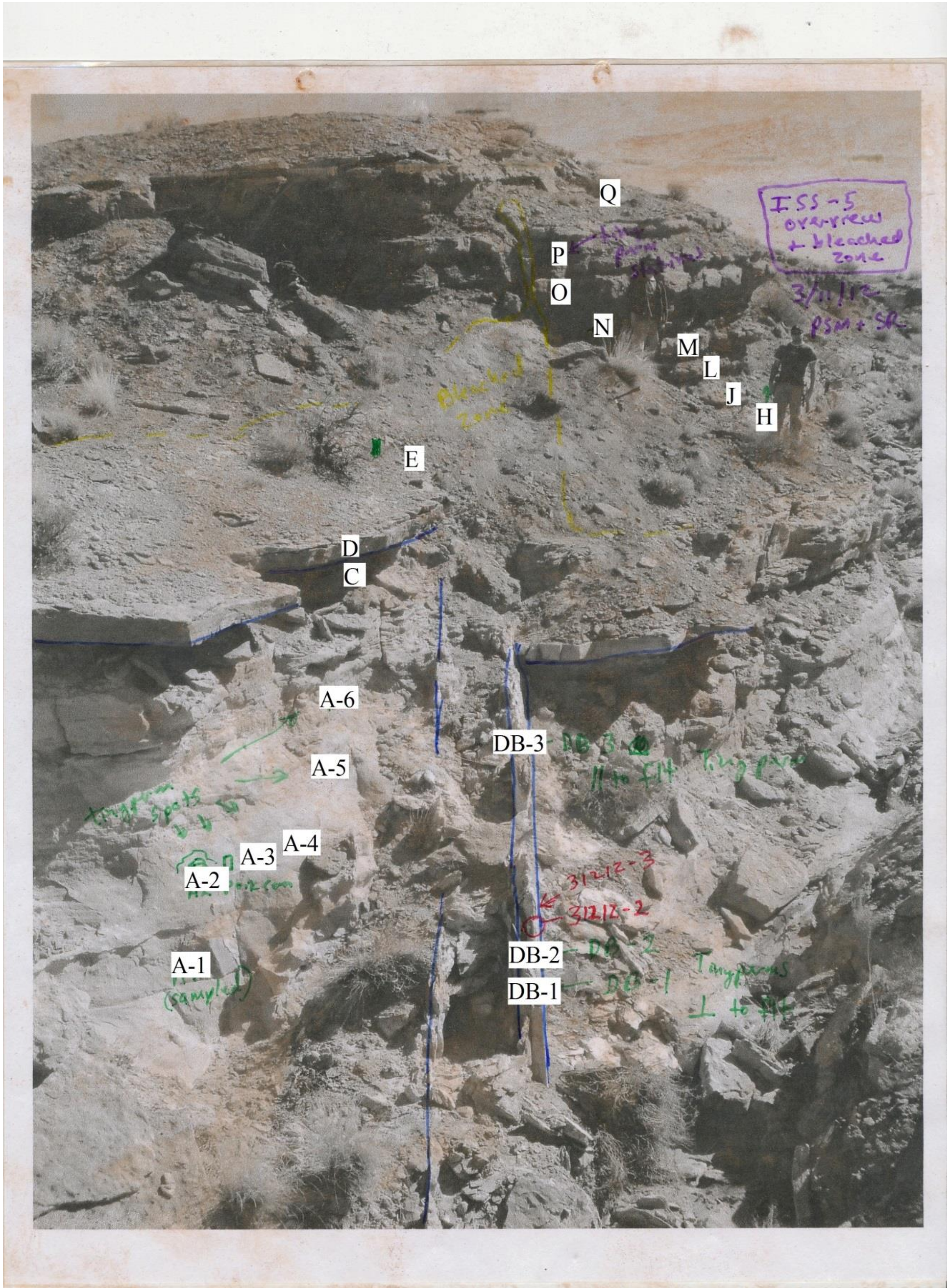

Figure B9. ISS-5 TinyPerm II measurement locations.

Table B7. ISS-5 TinyPerm II data.

Location	Raw TinyPerm II Data			Converted TinyPerm II Data (mD)			Corrected TinyPerm II Data (mD)			Deformation	Litho-
	Trial 1	Trial 2	Trial 3	Trial 1	Trial 2	Trial 3	Trial 1	Trial 2	Trial 3	Bands Present	facies
A-1	9.37	9.42	9.46	18607.19	16171.48	14454.56	5327.44	4646.20	4166.00		Cross.
A-2	9.18	9.23	9.26	31711.63	27560.53	25335.47	8992.61	7831.59	7209.27		Cross.
A-3	9.33	9.40	9.38	20817.35	17104.96	18092.33	5945.60	4907.29	5183.44		Cross.
A-4	9.20	9.36	9.32	29981.01	19136.69	21409.76	8508.57	5475.54	6111.29		Cross.
A-5	9.85	9.89	9.92	4838.86	4325.12	3975.94	1476.59	1332.91	1235.24		Def.
A-6	9.85	9.57	10.11	4838.86	10615.90	2332.93	1476.59	3092.37	775.71		Def.
B											Shale.*
C	9.44	8.83	9.29	15288.94	84671.22	23290.05	4399.36	23804.82	6637.19		Sand.
D	11.89	12.01	12.63	15.80	11.29	1.98	11.58	8.27	1.45		Sand.
E	11.26	10.91	11.35	92.57	247.18	71.91	67.83	192.35	52.70		Sand.
F											Shale.
G											Shale.
H	11.91	11.86	12.02	14.94	17.19	10.97	10.95	12.60	8.04		Sand.
I											Shale.
J	12.38	12.42	11.97	4.00	3.57	12.63	2.93	2.62	9.25		Silt.*
K											Shale
L	12.20	12.48	12.09	6.62	3.02	9.02	4.85	2.21	6.61		Silt.
M	11.85	11.90	11.50	17.68	15.37	47.21	12.96	11.26	34.59		Sand.
N											Shale.
O	12.28	12.40	12.51	5.29	3.78	2.77	3.88	2.77	2.03		Sand.
P	11.09	10.94	11.19	149.16	227.22	112.67	164.94	186.77	154.73		Sand.
Q	12.05	11.76	12.38	10.09	22.76	4.00	7.39	16.68	2.93		Sand.
DB-1	11.92	12.27	11.65	14.53	5.44	30.99	10.65	3.99	22.71	x	Cross.
DB-2	12.54			2.55			1.87			x	Cross.
DB-3	12.26			5.60			4.10			x	Cross.

Raw Data = (-0.8206)*log(Converted TinyPerm II Value in mD) + 12.8737
Samples >100 mD: Converted TinyPerm II Value in mD = 3.5754*(Corrected TinyPerm II value in mD) - 440.55 mD
Samples <100 mD: Converted TinyPerm II Value in mD = 1.3647*(Corrected TinyPerm II value in mD)

Def. = Deformed Sandstone Lithofacies
Cross. = Cross-bedded Sandstone Lithofacies
Sand. = Sandstone Lithofacie
Silt. = Siltstone Lithofacie
Shale. = Shale Lithoface

Samples with deformation bands present were not included within the average permeability assigned to the deformed and cross-bedded sandstone lithofacies

*Measurements from the siltstone and shale lithofacies are not considered accurate as the actual permeability of the siltstones is likely below the lower measuring range of TinyPerm II

APPENDIX C. THIN SECTION INVENTORY

Table C1. Thin section inventory.

	Thin Section	Formation	Member	Study Site	Polished	Deformation Band Present	Mineralized Fracture Present
1	SPR-1	Entrada	Slick Rock	N/A	X	X	X
2	SPR-2	Entrada	Slick Rock	N/A	X	X	
3	SPR-3a	Entrada	Slick Rock	N/A	X		
4	SPR-3b	Entrada	Slick Rock	N/A			
5	WP52 float	Entrada	Slick Rock	N/A	X	X	X
6	WP55 float	Entrada	Slick Rock	N/A	X	X	X
7	IW80811-1psm	Entrada	Slick Rock	N/A	X		
8	IW8911-1	Entrada	Slick Rock	ISS-1			
9	IW8911-3	Entrada	Slick Rock	ISS-1	X	X	
10	IW8911-5	Entrada	Slick Rock	ISS-1	X	X	
11	IW8911-6	Entrada	Slick Rock	ISS-1			
12	IW8911-9a	Entrada	Earthy	ISS-1	X		X
13	IW8911-9b	Entrada	Earthy	ISS-1	X		
14	IW8911-10	Entrada	Earthy	ISS-1	X		
15	IW8911-11	Entrada	Earthy	ISS-1	X		
16	IW8911-12	Entrada	Earthy	ISS-1	X		
17	IW8911-13	Entrada	Earthy	ISS-1	X		
18	IW8911-14	Entrada	Earthy	ISS-1	X		
19	IW8911-15	Entrada	Earthy	ISS-1	X		
20	IW8911-16	Entrada	Earthy	ISS-1	X		
21	IW81011-3	Entrada	Slick Rock	N/A	X	X	
22	IW81011-4	Entrada	Slick Rock	N/A	X	X	
23	IW81011-5	Entrada	Slick Rock	N/A	X	X	
24	IW81011-6	Entrada	Slick Rock	N/A	X		
25	IW81111-1	Entrada	Slick Rock	N/A	X	X	
26	IW81111-2	Entrada	Slick Rock	N/A	X		
27	IW81111-3a	Carmel	Winsor	ISS-3	X		X
28	IW81111-3b	Entrada	Slick Rock	ISS-2		X	
29	IW81111-4a	Carmel	Winsor	ISS-3	X		X
30	IW81111-4b	Entrada	Slick Rock	ISS-2	X		
31	IW81111-5	Carmel	Winsor	ISS-3	X		X
32	IW81111-6	Carmel	Winsor	ISS-3			
33	IW81111-7	Carmel	Winsor	ISS-3			
34	IW81111-8	Entrada	Slick Rock	ISS-3	X		
35	IW81111-9	Entrada	Slick Rock	ISS-3	X		
36	IW81111-10	Entrada	Slick Rock	ISS-3	X		
37	IW81111-11	Carmel	Winsor	ISS-3			
38	IW81111-12	Carmel	Winsor	ISS-3	X		
39	IW81111-13	Carmel	Winsor	ISS-3			
40	IW81111-14	Carmel	Winsor	ISS-3			
41	IW81111-15	Carmel	Winsor	ISS-3	X		
42	IW81211-1	Entrada	Slick Rock	N/A	X		
43	IW81211-2	Entrada	Slick Rock	N/A	X		
44	IW81211-3	Entrada	Slick Rock	N/A	X	X	
45	IW81211-4	Entrada	Slick Rock	N/A	X		

Table C1. Thin section inventory continued…

	Thin Section Name	Formation	Member	Study Site	Polished	Deformation Band Present	Mineralized Fracture Present
46	IW81311-1	Entrada	Slick Rock	ISS-4	X	X	
47	IW81311-2	Entrada	Slick Rock	ISS-4	X		
48	IW81311-3	Entrada	Slick Rock	ISS-4	X	X	
49	IW81311-4	Entrada	Slick Rock	ISS-4			
50	IW-Float-1	Entrada	Slick Rock	N/A	X		
51	UM-102211-A	Navajo	N/A	UMS-1		X	
52	UM-102211-B	Navajo	N/A	UMS-1		X	
53	UM-102211-C	Navajo	N/A	UMS-1	X		X
54	UM-102211-D	Navajo	N/A	UMS-1	X	X	
55	UM-102211-E	Carmel	Co-op Creek	UMS-1			
56	UM-102211-F	Carmel	Co-op Creek	UMS-1	X		
57	UM-102311-A	Carmel	Co-op Creek	UMS-1	X		
58	UM-102311-C	Carmel	Co-op Creek	UMS-1	X		
59	UM-102311-D	Carmel	Co-op Creek	UMS-1	X		
60	UM-102311-E	Carmel	Co-op Creek	UMS-1	X		
61	UM-102311-F	Carmel	Co-op Creek	UMS-1	X		
62	UM-102311-G	Carmel	Co-op Creek	UMS-1			X
63	UM-102311-H	Carmel	Co-op Creek	UMS-1			
64	UM-102311-I	Carmel	Co-op Creek	UMS-1	X		
65	UM-102311-J	Carmel	Co-op Creek	UMS-1	X		X
66	UM-102311-K	Carmel	Co-op Creek	UMS-1	X		X
67	UM-31312-16	Carmel	Co-op Creek	UMS-3	X		X
68	UM-31312-17	Carmel	Co-op Creek	UMS-3	X		X
69	UM-31312-18	Carmel	Co-op Creek	UMS-3	X		X
70	UM-31312-19	Navajo	N/A	UMS-3		X	
71	UM-31312-20	Navajo	N/A	UMS-3			
72	IW-31112-1	Entrada	Earthy	ISS-1	X		X
73	IW-31112-2A	Entrada	Earthy	ISS-1	X		X

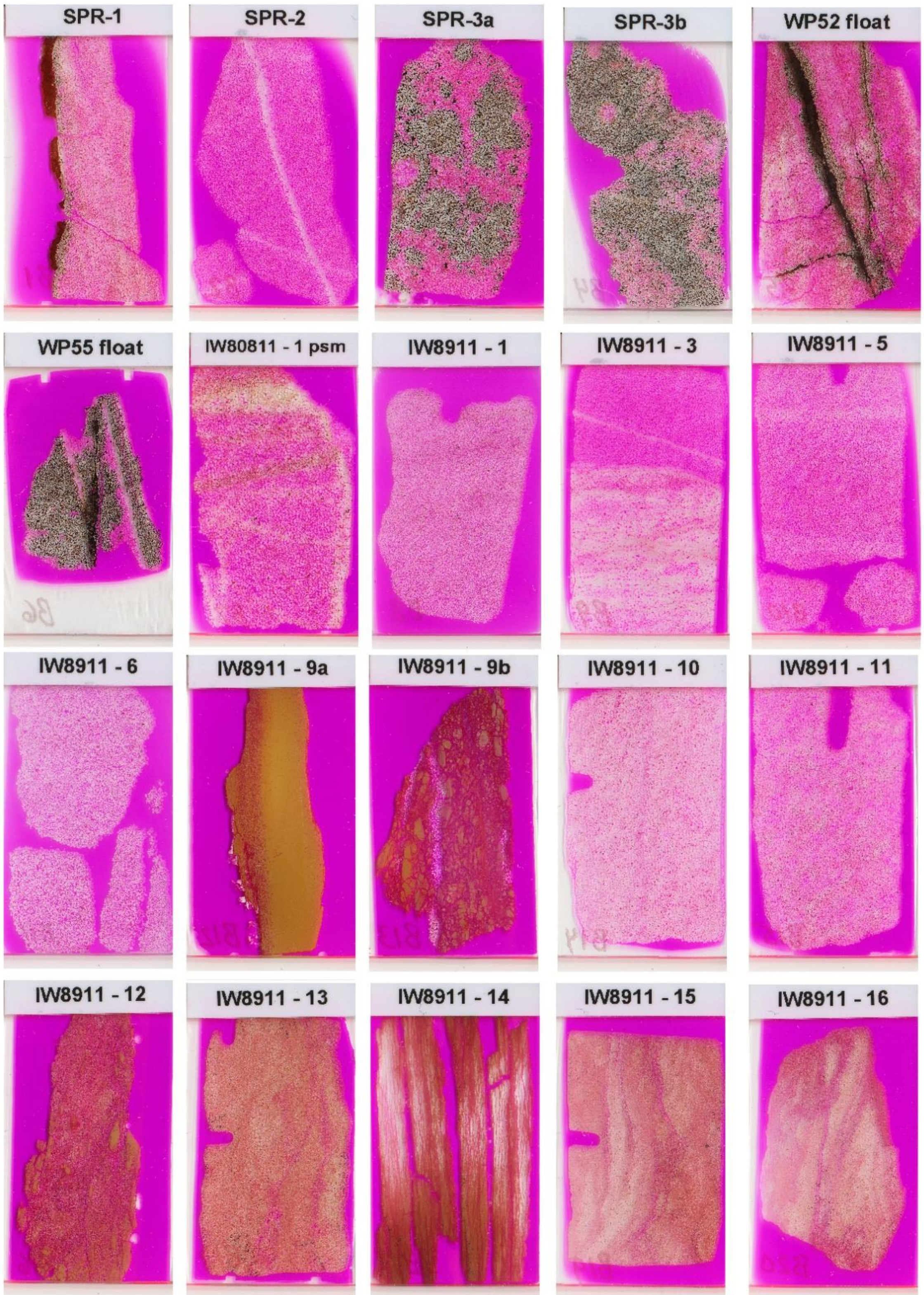

Figure C1. Thin section inventory.

Figure C1. Thin section inventory continued…

Figure C1. Thin section inventory continued…

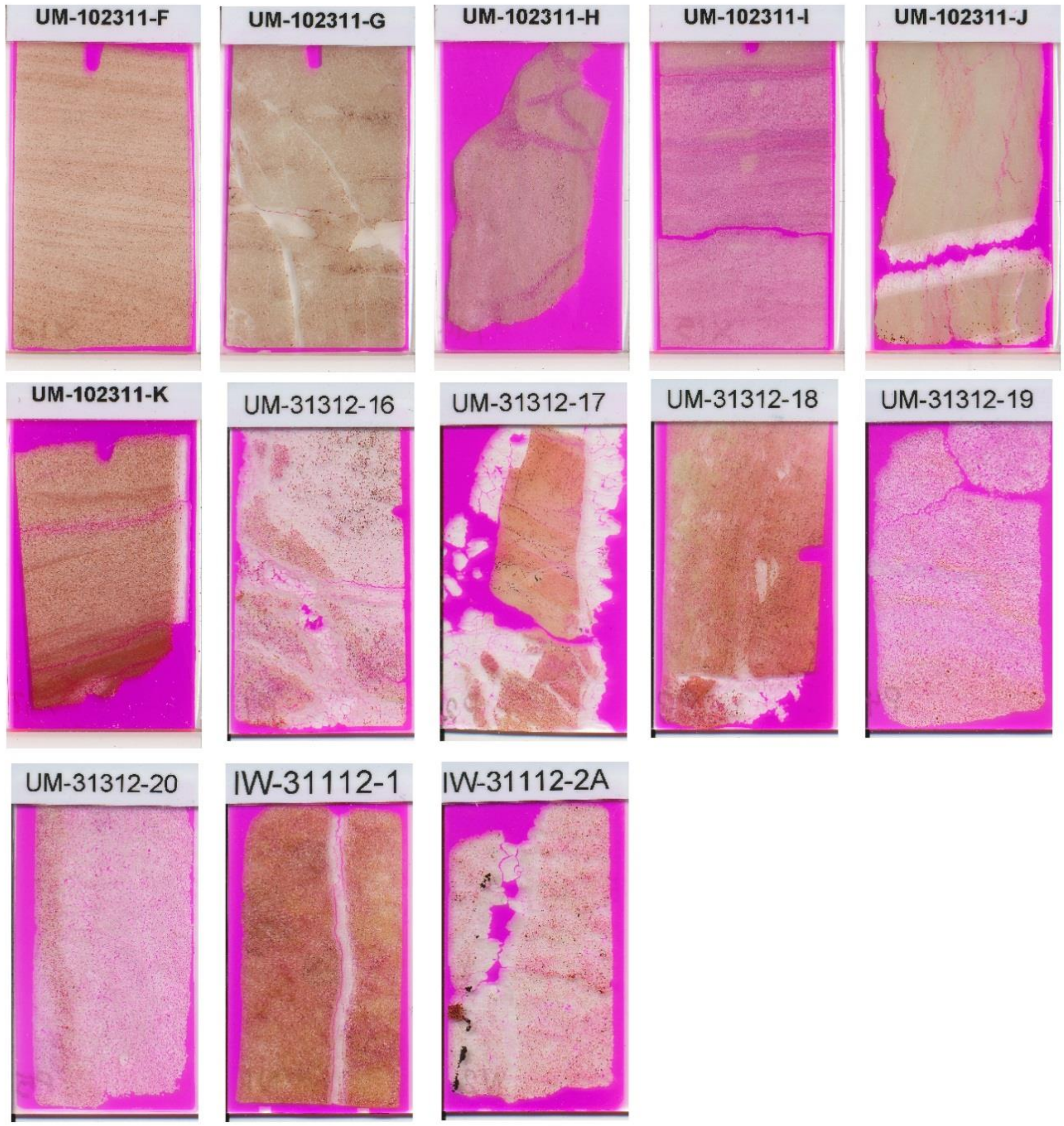

Figure C1. Thin section inventory continued…

APPENDIX D. X-RAY DIFFRACTION ANALYSIS

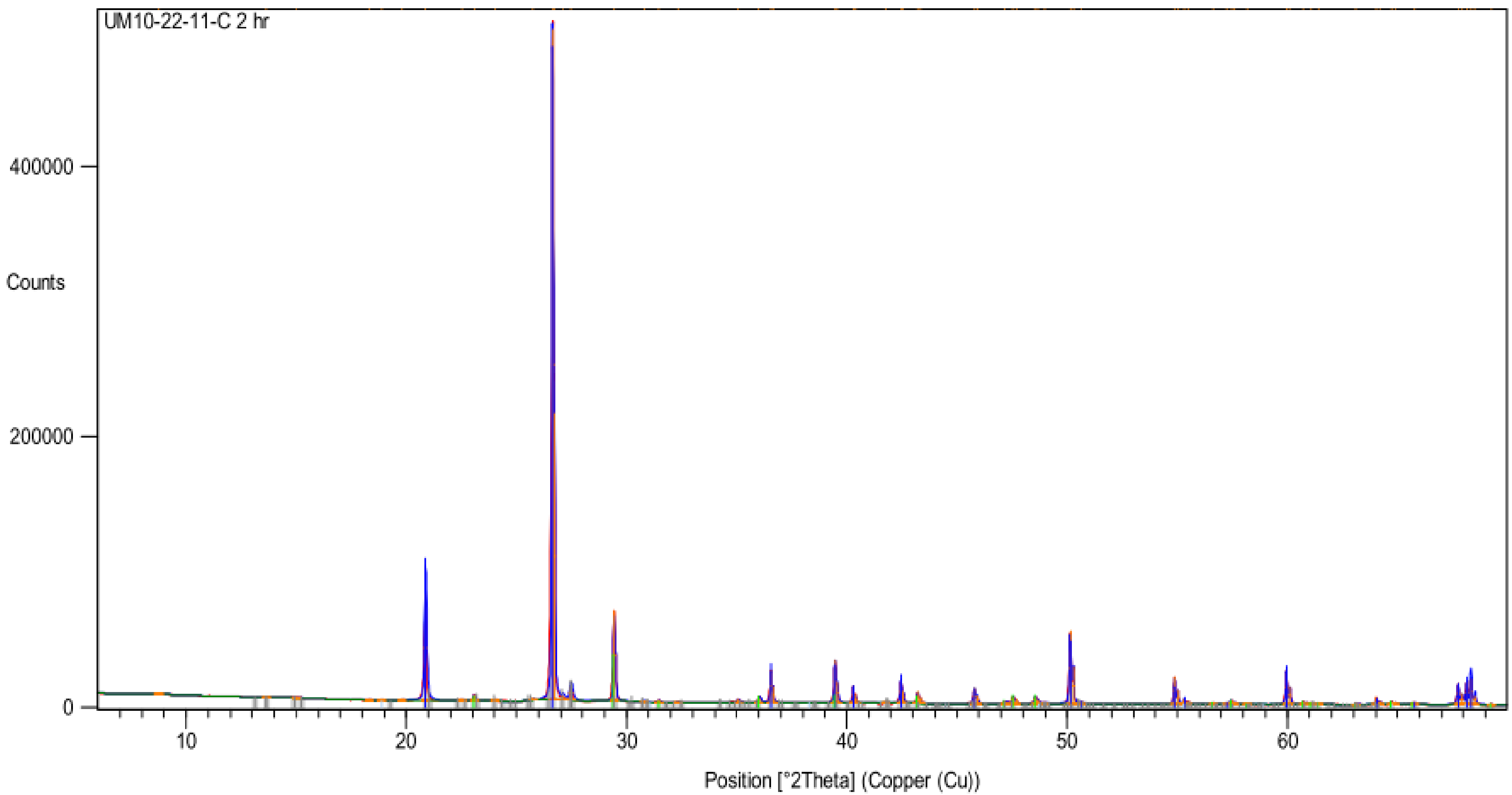

Figure D1. X-ray diffraction pattern of a powdered heavily iron oxide cemented sandstone. Lack of iron oxide mineral peaks suggests the iron oxide is amorphous. UM10-22-11-C, Navajo Sandstone, XRD pattern.

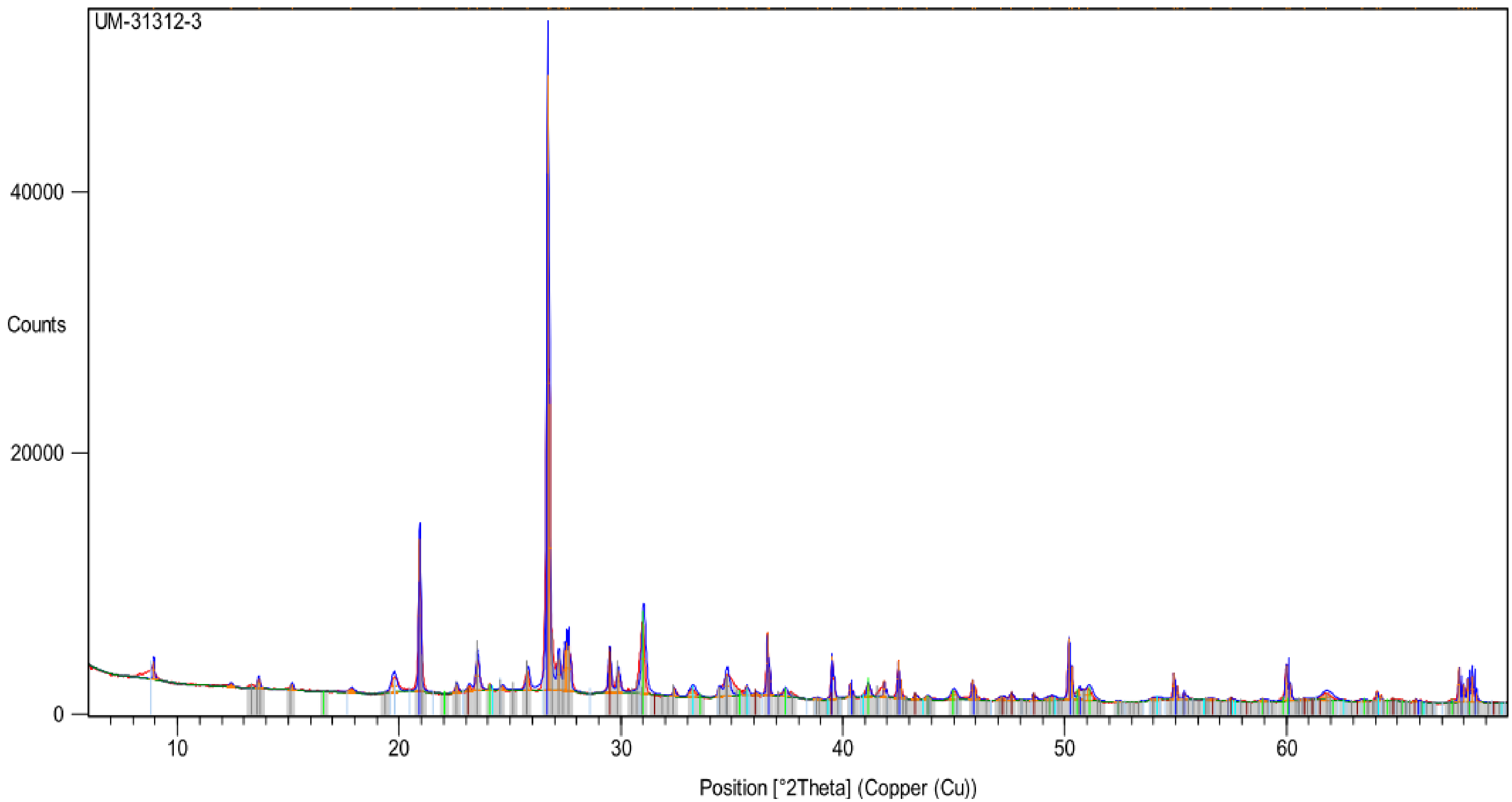

Figure D2. X-ray diffraction pattern of a powdered heavily iron oxide cemented sandstone. The presence of a peak at 33.2 °2θ suggests the iron oxide in this sample is hematite. UM-31312-3, Carmel Formation Co-op Creek Member, XRD pattern.

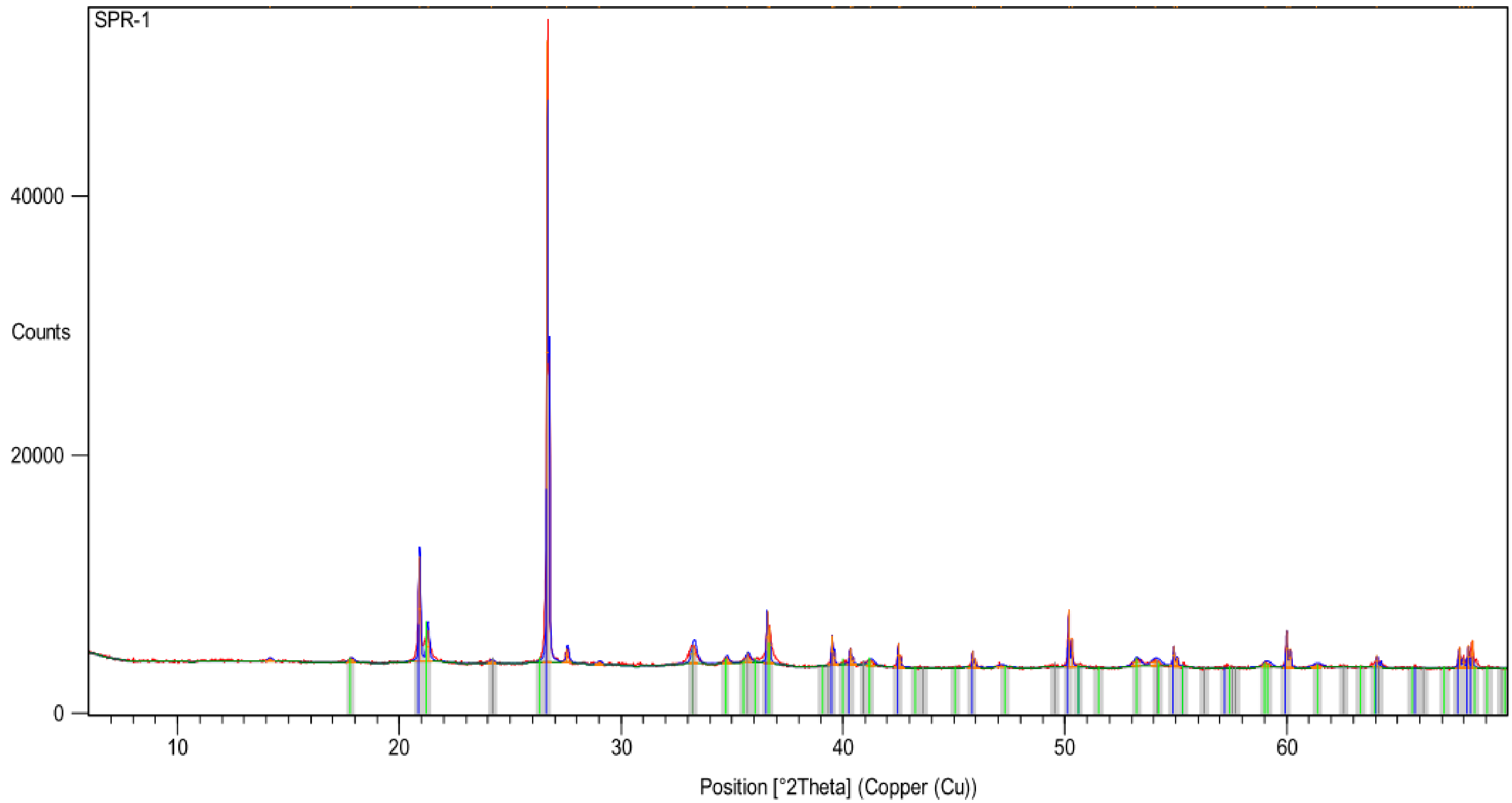

Figure D3. X-ray diffraction pattern of a powdered iron oxide mineralized fracture. The presence of a peak at 21.2 °2θ suggests the iron oxide in this sample is goethite. SPR-1, Entrada Sandstone Slick Rock Member, XRD pattern.

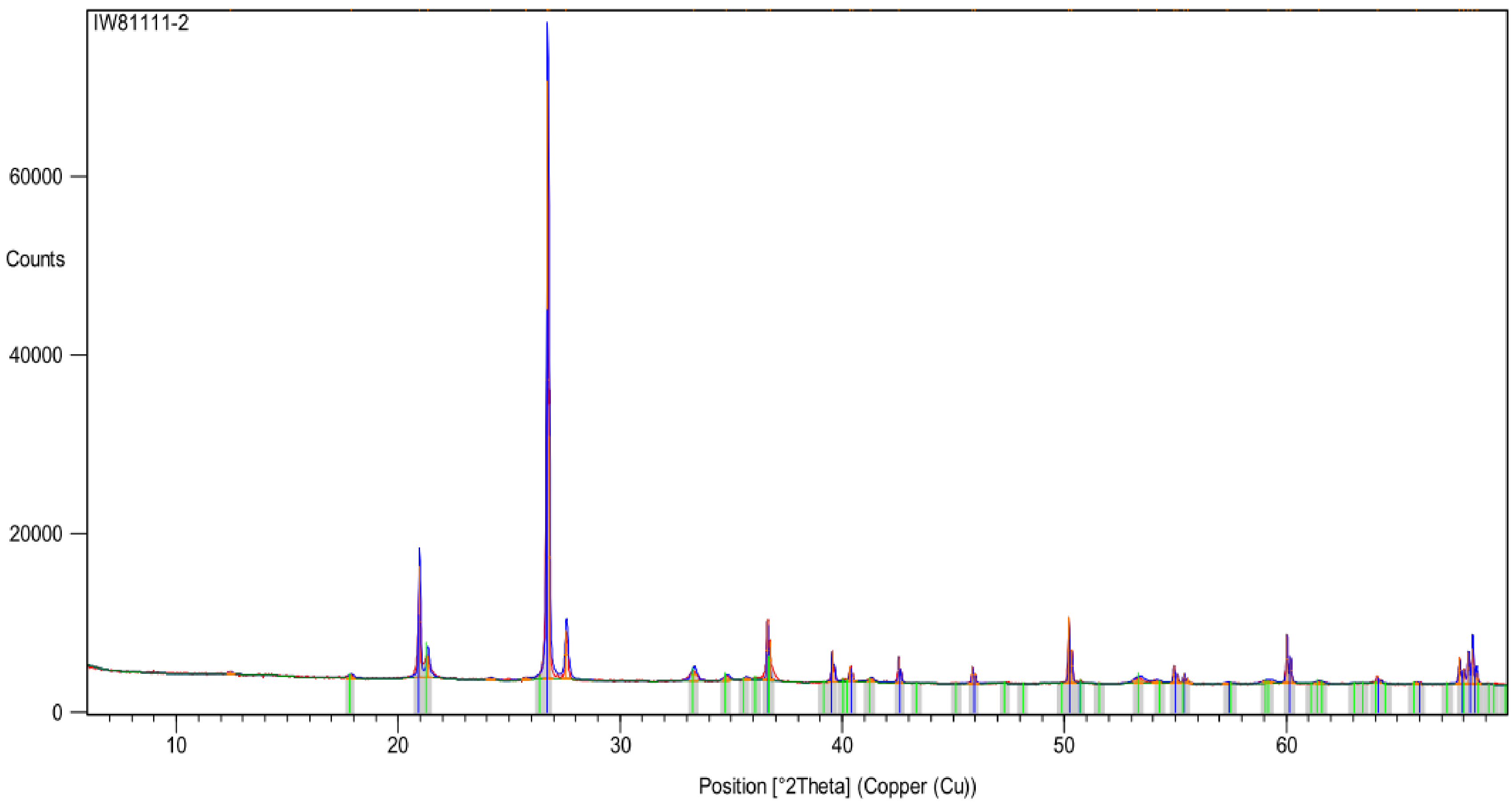

Figure D4. X-ray diffraction pattern of a powdered heavily iron oxide cemented sandstone. The presence of a peak at 21.2 °2θ suggests the iron oxide in this sample is goethite. IW81111-2, Entrada Sandstone Slick Rock Member, XRD pattern.

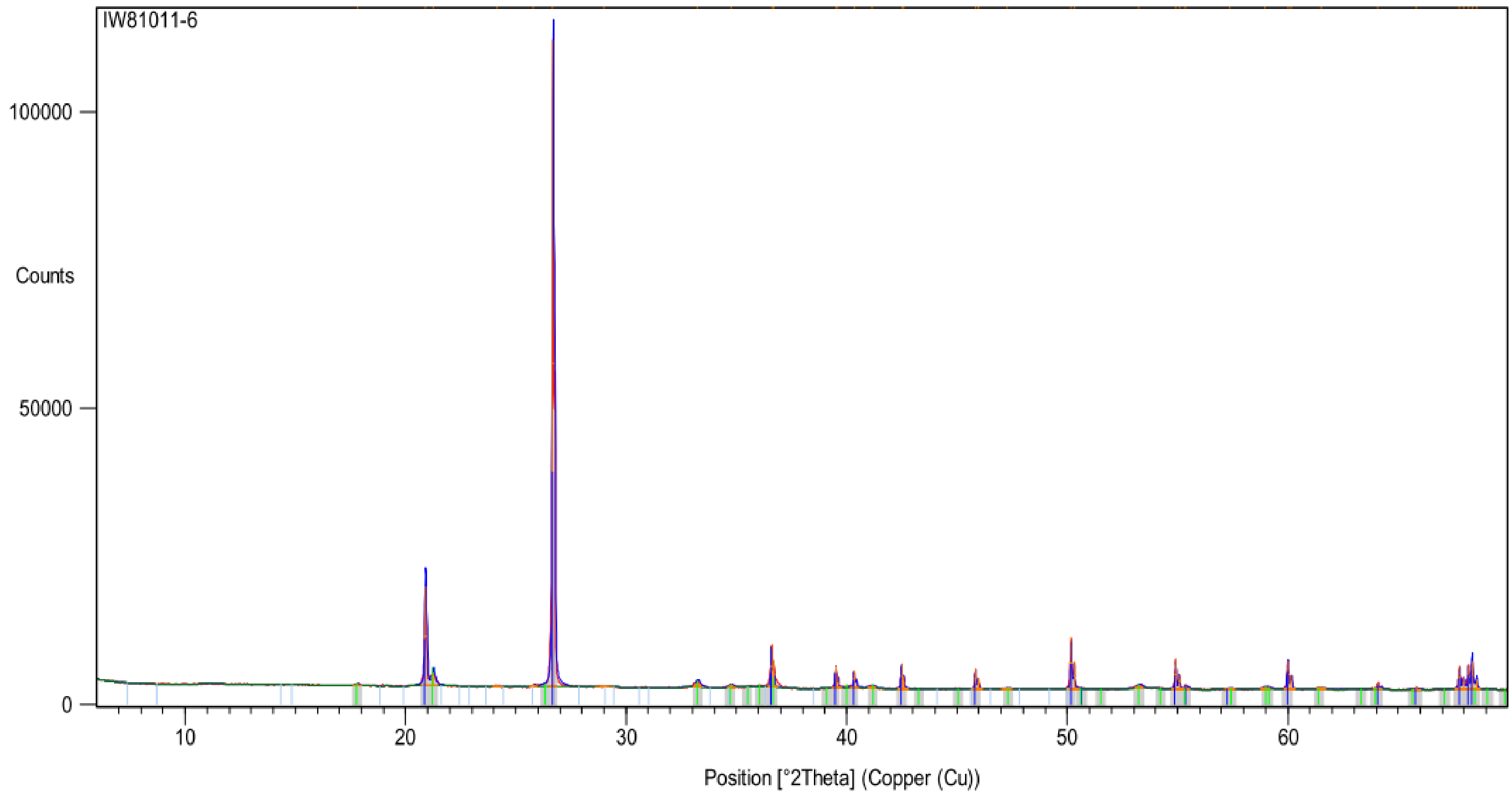

Figure D5. X-ray diffraction pattern of a powdered heavily iron oxide cemented sandstone. The presence of a peak at 21.2 °2θ suggests the iron oxide in this sample is goethite. IW81011-6, Entrada Sandstone Slick Rock Member, XRD pattern.

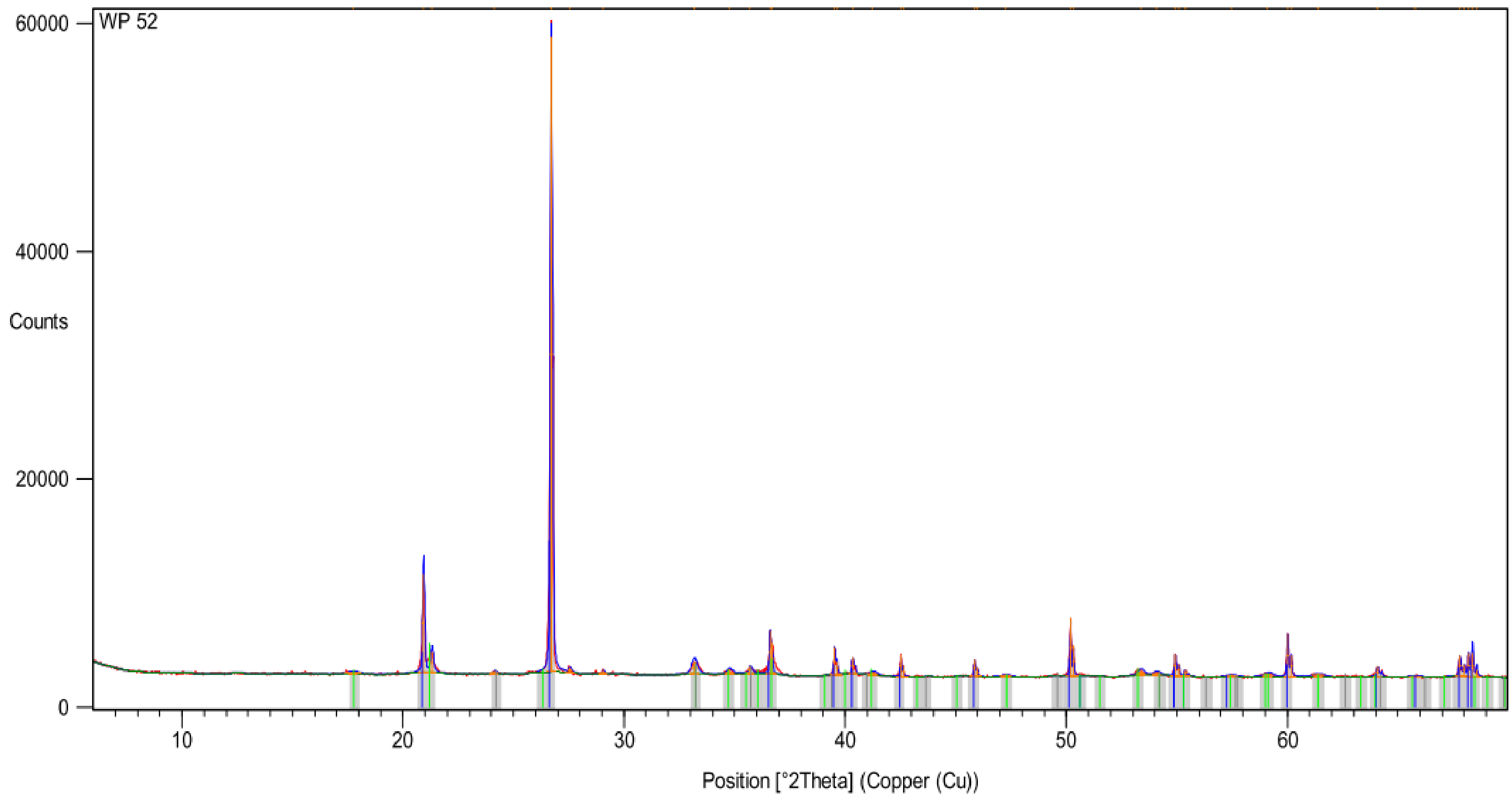

Figure D6. X-ray diffraction pattern of a powdered iron oxide mineralized fracture. The presence of a peak at 21.2 °2θ suggests the iron oxide in this sample is goethite. WP-52, Entrada Sandstone Slick Rock Member, XRD pattern.

APPENDIX E. MERCURY INJECTION CAPILARY PRESSURE

Table E1. IW8911-3-Pa-He-1 MICP Data.

Int Pres psia	Pore Dia microns	Inc Int mL/gm	Cum Int mL/gm	Cum Int %PV(bc)	Cum Int %BV	Inc Int %PV(ac)	Cum Int %PV(ac)	Pore Rad microns	W.P. Sat %PV(ac)	Lev "J" Funct.	G/B Pc psia	G/O Pc psia	O/B Pc psia	Ht FWL,ft G/B	Ht FWL,ft O/B	Swanson's Sb/Pc(ac)
5.94	35.9276	0	0	0.0708	0	0	0	17.9638	100	0.011	0.80784	0.3861	0.48708	2.0493	4.32432	-0.0441595
6.43	33.2016	0	0.0001	0.2125	0.02623	0	0	16.6008	100	0.012	0.87448	0.41795	0.52726	2.21835	4.68104	-0.0367149
6.95	30.6876	0.0001	0.0001	0.3744	0.02623	0	0	15.3438	100	0.013	0.9452	0.45175	0.5699	2.39775	5.0596	-0.0339679
7.52	28.3592	0	0.0002	0.5262	0.05246	0	0	14.1796	100	0.014	1.02272	0.4888	0.61664	2.5944	5.47456	-0.027905
8.14	26.2089	0	0.0002	0.6375	0.05246	0	0	13.1045	100	0.015	1.10704	0.5291	0.66748	2.8083	5.92592	-0.0257796
8.81	24.2251	0.0001	0.0003	0.8095	0.07869	0	0	12.1126	100	0.016	1.19816	0.57265	0.72242	3.03945	6.41368	-0.0208417
9.53	22.3852	0	0.0003	0.9208	0.07869	0	0	11.1926	100	0.017	1.29608	0.61945	0.78146	3.28785	6.93784	-0.0192671
10.31	20.6918	0	0.0003	1.022	0.07869	0	0	10.3459	100	0.019	1.40216	0.67015	0.84542	3.55695	7.50568	-0.0178094
11.16	19.1186	0.0001	0.0004	1.3458	0.10492	0	0	9.5593	100	0.020	1.51776	0.7254	0.91512	3.8502	8.12448	-0.0141025
12.07	17.6698	0.0001	0.0005	1.5381	0.13115	0	0	8.8349	100	0.022	1.64152	0.78455	0.98974	4.16415	8.78696	-0.0108661
13.06	16.3286	0	0.0005	1.6899	0.13115	0	0	8.1643	100	0.024	1.77616	0.8489	1.07092	4.5057	9.50768	-0.0100424
14.13	15.0965	0.0001	0.0006	1.8518	0.15738	0	0	7.54825	100	0.026	1.92168	0.91845	1.15866	4.87485	10.28664	-0.0074255
15.29	13.9517	0.0001	0.0006	2.0643	0.15738	0	0	6.97585	100	0.028	2.07944	0.99385	1.25378	5.27505	11.13112	-0.0068622
16.55	12.8926	0	0.0007	2.2161	0.18362	0	0	6.4463	100	0.030	2.2508	1.07575	1.3571	5.70975	12.0484	-0.0047548
17.9	11.9173	0.0001	0.0007	2.378	0.18362	0	0	5.95865	100	0.032	2.4344	1.1635	1.4678	6.1755	13.0312	-0.0043962
19.37	11.0139	0.0001	0.0008	2.555911	0.20985	0	0	5.50695	100	0.035	2.63432	1.25905	1.58834	6.68265	14.10136	-0.0027084
20.96	10.1782	0.0001	0.0009	2.875399	0.23608	0	0	5.0891	100	0.038	2.85056	1.3624	1.71872	7.2312	15.25888	-0.0012515
22.68	9.4076	0.0001	0.001	3.194888	0.26231	0	0	4.7038	100	0.041	3.08448	1.4742	1.85976	7.8246	16.51104	0
24.54	8.694	0.0006	0.0016	5.111821	0.41969	1.98019802	1.980198	4.347	98.0198	0.044	3.33744	1.5951	2.01228	8.4663	17.86512	0.00641338
26.55	8.0355	0.0002	0.0018	5.750799	0.47215	0.66006601	2.640264	4.01775	97.35974	0.048	3.6108	1.72575	2.1771	9.15975	19.3284	0.0079038
28.72	7.4266	0.0003	0.0021	6.709265	0.55085	0.99009901	3.630363	3.7133	96.36964	0.052	3.90592	1.8668	2.35504	9.9084	20.90816	0.01004659
31.08	6.8635	0.0006	0.0027	8.626198	0.70823	1.98019802	5.610561	3.43175	94.38944	0.056	4.22688	2.0202	2.54856	10.7226	22.62624	0.01434757
33.63	6.3424	0.0012	0.0039	12.46006	1.023	3.96039604	9.570957	3.1712	90.42904	0.061	4.57368	2.18595	2.75766	11.60235	24.48264	0.02261943
36.39	5.8627	0.0008	0.0047	15.01597	1.23284	2.64026403	12.21122	2.93135	87.78878	0.066	4.94904	2.36535	2.98398	12.55455	26.49192	0.02667044
39.37	5.4177	0.0008	0.0055	17.57188	1.44269	2.64026403	14.85149	2.70885	85.14851	0.071	5.35432	2.55905	3.22834	13.58265	28.66136	0.0299818
42.6	5.0075	0.0007	0.0062	19.80831	1.62631	2.31023102	17.16172	2.50375	82.83828	0.077	5.7936	2.769	3.4932	14.697	31.0128	0.03201874
46.45	4.5924	0.0006	0.0068	21.72524	1.78369	1.98019802	19.14191	2.2962	80.85809	0.084	6.3172	3.01925	3.8089	16.02525	33.8156	0.03275313
49.29	4.3282	0.0005	0.0073	23.32268	1.91484	1.65016502	20.79208	2.1641	79.20792	0.089	6.70344	3.20385	4.04178	17.00505	35.88312	0.03352681
56.06	3.8055	0.0006	0.0079	25.23962	2.07223	1.98019802	22.77228	1.90275	77.22772	0.102	7.62416	3.6439	4.59692	19.3407	40.81168	0.03228543
60.48	3.5269	0.0005	0.0084	26.83706	2.20338	1.65016502	24.42244	1.76345	75.57756	0.110	8.22528	3.9312	4.95936	20.8656	44.02944	0.03209449
64.75	3.2946	0.0004	0.0088	28.11502	2.30831	1.32013201	25.74257	1.6473	74.25743	0.117	8.806	4.20875	5.3095	22.33875	47.138	0.03159842
71.56	2.9809	0.0005	0.0093	29.71246	2.43946	1.65016502	27.39274	1.49045	72.60726	0.130	9.73216	4.6514	5.86792	24.6882	52.09568	0.03042414
77.62	2.7484	0.0006	0.0099	31.62939	2.59684	1.98019802	29.37294	1.3742	70.62706	0.141	10.55632	5.0453	6.36484	26.7789	56.50736	0.03007647
83.27	2.5619	0.0004	0.0103	32.90735	2.70177	1.32013201	30.69307	1.28095	69.30693	0.151	11.32472	5.41255	6.82814	28.72815	60.62056	0.02929577
90.38	2.3602	0.0005	0.0108	34.50479	2.83292	1.65016502	32.34323	1.1801	67.65677	0.164	12.29168	5.8747	7.41116	31.1811	65.79664	0.02844227
97.26	2.1933	0.0004	0.0112	35.78275	2.93784	1.32013201	33.66337	1.09665	66.33663	0.176	13.22736	6.3219	7.97532	33.5547	70.80528	0.0275091
105.84	2.0156	0.0005	0.0117	37.38019	3.069	1.65016502	35.31353	1.0078	64.68647	0.192	14.39424	6.8796	8.67888	36.5148	77.05152	0.02651823
116.16	1.8364	0.0006	0.0123	39.29712	3.22638	1.98019802	37.29373	0.9182	62.70627	0.210	15.79776	7.5504	9.52512	40.0752	84.56448	0.02551716
125.47	1.7002	0.0005	0.0128	40.89457	3.35753	1.65016502	38.94389	0.8501	61.05611	0.227	17.06392	8.15555	10.28854	43.28715	91.34216	0.02466906
134.91	1.5812	0.0006	0.0134	42.8115	3.51492	1.98019802	40.92409	0.7906	59.07591	0.244	18.34776	8.76915	11.06262	46.54395	98.21448	0.02410949
146.96	1.4515	0.0005	0.0139	44.40895	3.64607	1.65016502	42.57426	0.72575	57.42574	0.266	19.98656	9.5524	12.05072	50.7012	106.9869	0.02302508
159.76	1.3353	0.0006	0.0145	46.32588	3.80346	1.98019802	44.55446	0.66765	55.44554	0.289	21.72736	10.3844	13.10032	55.1172	116.3053	0.02216543
173.46	1.2298	0.0006	0.0151	48.24281	3.96084	1.98019802	46.53465	0.6149	53.46535	0.314	23.59056	11.2749	14.22372	59.8437	126.2789	0.02132212
188.94	1.1291	0.0006	0.0157	50.15974	4.11823	1.98019802	48.51485	0.56455	51.48515	0.342	25.69584	12.2811	15.49308	65.1843	137.5483	0.02040817
202.42	1.0539	0.0005	0.0162	51.75719	4.24938	1.65016502	50.16502	0.52695	49.83498	0.367	27.52912	13.1573	16.59844	69.8349	147.3618	0.01969703
219.73	0.9709	0.0006	0.0168	53.67412	4.40676	1.98019802	52.14521	0.48545	47.85479	0.398	29.88328	14.28245	18.01786	75.80685	159.9634	0.01886159
238.27	0.8953	0.0006	0.0174	55.59105	4.56415	1.98019802	54.12541	0.44765	45.87459	0.432	32.40472	15.48755	19.53814	82.20315	173.4606	0.01805448
257.08	0.8298	0.0005	0.0179	57.1885	4.6953	1.65016502	55.77558	0.4149	44.22442	0.466	34.96288	16.7102	21.08056	88.6926	187.1542	0.01724364
278.6	0.7657	0.0005	0.0184	58.78594	4.82646	1.65016502	57.42574	0.38285	42.57426	0.505	37.8896	18.109	22.8452	96.117	202.8208	0.01638244
301.54	0.7074	0.0005	0.0189	60.38339	4.95761	1.65016502	59.07591	0.3537	40.92409	0.546	41.00944	19.6001	24.72628	104.0313	219.5211	0.01557108
326.44	0.6535	0.0004	0.0193	61.66134	5.06253	1.32013201	60.39604	0.32675	39.60396	0.591	44.39584	21.2186	26.76808	112.6218	237.6483	0.01470477
355.74	0.5997	0.0004	0.0197	62.9393	5.16746	1.32013201	61.71617	0.29985	38.28383	0.644	48.38064	23.1231	29.17068	122.7303	258.9787	0.01378858
383.15	0.5568	0.0004	0.0201	64.21725	5.27238	1.32013201	63.0363	0.2784	36.9637	0.694	52.1084	24.90475	31.4183	132.1868	278.9332	0.013076
415.64	0.5132	0.0004	0.0205	65.49521	5.3773	1.32013201	64.35644	0.2566	35.64356	0.753	56.52704	27.0166	34.08248	143.3958	302.5859	0.01230631
450.3	0.4737	0.0004	0.0209	66.77316	5.48222	1.32013201	65.67657	0.23685	34.32343	0.816	61.2408	29.2695	36.9246	155.3535	327.8184	0.01159209
487.64	0.4375	0.0004	0.0213	68.05112	5.58715	1.32013201	66.9967	0.21875	33.0033	0.883	66.31904	31.6966	39.98648	168.2358	355.0019	0.01091961
528.05	0.404	0.0004	0.0217	69.32907	5.69207	1.32013201	68.31683	0.202	31.68317	0.956	71.8148	34.32325	43.3001	182.1773	384.4204	0.01028267
570.36	0.374	0.0003	0.022	70.28754	5.77076	0.99009901	69.30693	0.187	30.69307	1.033	77.56896	37.0734	46.76952	196.7742	415.2221	0.00965786
617.3	0.3456	0.0003	0.0223	71.24601	5.84945	0.99009901	70.29703	0.1728	29.70297	1.118	83.9528	40.1245	50.6186	212.9685	449.3944	0.00905094
670.18	0.3183	0.0003	0.0226	72.20447	5.92815	0.99009901	71.28713	0.15915	28.71287	1.214	91.14448	43.5617	54.95476	231.2121	487.891	0.00845421
724.52	0.2944	0.0003	0.0229	73.16294	6.00684	0.99009901	72.27723	0.1472	27.72277	1.312	98.53472	47.0938	59.41064	249.9594	527.4506	0.00792874
783.37	0.2723	0.0003	0.0232	74.12141	6.08553	0.99009901	73.26733	0.13615	26.73267	1.419	106.5383	50.91905	64.23634	270.2627	570.2934	0.00743356
848.08	0.2515	0.0003	0.0235	75.07987	6.16422	0.99009901	74.25743	0.12575	25.74257	1.536	115.3389	55.1252	69.54256	292.5876	617.4022	0.00695915
920	0.2319	0.0003	0.0238	76.03834	6.24292	0.99009901	75.24752	0.11595	24.75248	1.666	125.12	59.8	75.44	317.4	669.76	0.00650066
992.79	0.2149	0.0002	0.024	76.67732	6.29538	0.66006601	75.90759	0.10745	24.09241	1.798	135.0194	64.53135	81.40878	342.5126	722.7511	0.00607688
1076.04	0.1982	0.0002	0.0242	77.31629	6.34784	0.66006601	76.56766	0.0991	23.43234	1.949	146.3414	69.9426	88.23528	371.2338	783.3571	0.00565549
1163.1	0.1834	0.0002	0.0244	77.95527	6.4003	0.66006601	77.22772	0.0917	22.77228	2.107	158.1816	75.6015	95.3742	401.2695	846.7368	0.00527727
1258.16	0.1696	0.0002	0.0246	78.59425	6.45276	0.66006601	77.88779	0.0848	22.11221	2.279	171.1098	81.7804	103.1691	434.0652	915.9405	0.00492024
1361.84	0.1566	0.0002	0.0248	79.23323	6.50522	0.66006601	78.54785	0.0783	21.45215	2.467	185.2102	88.5196	111.6709	469.8348	991.4195	0.00458418
1475.32	0.1446	0.0002	0.025	79.8722	6.55768	0.66006601	79.20792	0.0723	20.79208	2.672	200.6435	95.8958	120.9762	508.9854	1074.033	0.00426713
1596.14	0.1336	0.0002	0.0252	80.51118	6.61015	0.66006601	79.86799	0.0668	20.13201	2.891	217.075	103.7491	130.8835	550.6683	1161.99	0.00397699
1726.68	0.1235	0.0002	0.0254	81.15016	6.66261	0.66006601	80.52805	0.06175	19.47195	3.128	234.8285	112.2342	141.5878	595.7046	1257.023	0.00370671
1866.72	0.1143	0.0002	0.0256	81.78914	6.71507	0.66006601	81.18812	0.05715	18.81188	3.381	253.8739	121.3368	153.071	644.0184	1358.972	0.00345674
2020.52	0.1056	0.0002	0.0258	82.42812	6.76753	0.66006601	81.84818	0.0528	18.15182	3.660	274.7907	131.3338	165.6826	697.0794	1470.939	0.00321958
2186.48	0.0976	0.0002	0.026	83.06709	6.81999	0.66006601	82.50825	0.0488	17.49175	3.961	297.3613	142.1212	179.2914	754.3356	1591.757	0.0029992
2366.77	0.0901	0.0002	0.0262	83.70607	6.87245	0.66006601	83.16832	0.04505	16.83168	4.287	321.8807	153.8401	194.0751	816.5357	1723.009	0.0027929
2560.41	0.0833	0.0001	0.0263	84.02556	6.89868	0.330033	83.49835	0.04165	16.50165	4.638	348.2158	166.4267	209.9536	883.3415	1863.978	0.00259192
2770.78	0.077	0.0001	0.0264	84.34505	6.92492	0.330033	83.82838	0.0385	16.17162	5.019	376.8261	180.1007	227.204	955.9191	2017.128	0.0024046
2995.64	0.0712	0.0001	0.0265	84.66454	6.95115	0.330033	84.15842	0.0356	15.84158	5.426	407.407	194.7166	245.6425	1033.496	2180.826	0.00223286
3244.97	0.0657	0.0001	0.0266	84.98403	6.97738	0.330033	84.48845	0.03285	15.51155	5.878	441.3159	210.9231	266.0875	1119.515	2362.338	0.00206938
3507.55	0.0608	0.0001	0.0267	85.30351	7.00361	0.330033	84.81848	0.0304	15.18152	6.353	477.0268	227.9908	287.6191	1210.105	2553.496	0.00192194
3797.1	0.0562	0.0001	0.0268	85.623	7.02984	0.330033	85.14851	0.0281	14.85149	6.878	516.4056	246.8115	311.3622	1310	2764.289	0.00178229
4108.57	0.0519	0.0001	0.0269	85.94249	7.05607	0.330033	85.47855	0.02595	14.52145	7.442	558.7655	267.0571	336.9027	1417.457	2991.039	0.00165356
4440.11	0.048	0.0001	0.027	86.26198	7.0823	0.330033	85.80858	0.024	14.19142	8.043	603.855	288.6072	364.089	1531.838	3232.4	0.001536
4804.42	0.0444	0.0001	0.0271	86.58147	7.10853	0.330033	86.13861	0.0222	13.86139	8.703	653.4011	312.2873	393.9624	1657.525	3497.618	0.00142498
5200.84	0.041	0.0001	0.0272	86.90096	7.13476	0.330033	86.46865	0.0205	13.53135	9.421	707.3142	338.0546	426.4689	1794.29	3786.212	0.00132141
5626.43	0.0379	0.0001	0.0273	87.22045	7.16099	0.330033	86.79868	0.01895	13.20132	10.192	765.1945	365.718	461.3673	1941.118	4096.041	0.00122612
6086.79	0.035	0.0001	0.0274	87.53994	7.18722	0.330033	87.12871	0.0175	12.87129	11.025	827.8034	395.6414	499.1168	2099.943	4431.183	0.0011377
6588.33	0.0324	0.0001	0.0275	87.85942	7.21345	0.330033	87.45875	0.0162	12.54125	11.934	896.0129	428.2415	540.2431	2272.974	4796.304	0.00105507

Table E1. IW8911-3-Pa-He-1 MICP data continued…

Int Pres psia	Pore Dia microns	Inc Int mL/gm	Cum Int mL/gm	Cum Int %PV(bc)	Cum Int %BV	Inc Int %PV(ac)	Cum Int %PV(ac)	Pore Rad microns	W.P. Sat %PV(ac)	Lev "J" Funct.	G/B Pc psia	G/O Pc psia	O/B Pc psia	Ht FWL,ft G/B	Ht FWL,ft O/B	Swanson's Sb/Pc(ac)
7125.32	0.0299	0.0001	0.0276	88.17891	7.23968	0.330033	87.78878	0.01495	12.21122	12.907	969.0435	463.1458	584.2762	2458.235	5187.233	0.00097924
7709.81	0.0277	0.0001	0.0277	88.4984	7.26591	0.330033	88.11881	0.01385	11.88119	13.965	1048.534	501.1377	632.2044	2659.884	5612.742	0.0009084
8348.25	0.0256	0.0001	0.0278	88.81789	7.29215	0.330033	88.44884	0.0128	11.55116	15.122	1135.362	542.6363	684.5565	2880.146	6077.526	0.00084207
9033.35	0.0236	0.0002	0.028	89.45687	7.34461	0.66006601	89.10891	0.0118	10.89109	16.363	1228.536	587.1678	740.7347	3116.506	6576.279	0.00078402
9771.29	0.0218	0.0001	0.0281	89.77636	7.37084	0.330033	89.43894	0.0109	10.56106	17.699	1328.895	635.1339	801.2458	3371.095	7113.499	0.00072749
10574.7	0.0202	0.0001	0.0282	90.09585	7.39707	0.330033	89.76898	0.0101	10.23102	19.155	1438.163	687.3575	867.1279	3648.282	7698.403	0.0006747
11444.1	0.0186	0.0001	0.0283	90.41534	7.4233	0.330033	90.09901	0.0093	9.90099	20.730	1556.398	743.8665	938.4162	3948.215	8331.305	0.00062574
12381.9	0.0172	0.0001	0.0284	90.73482	7.44953	0.330033	90.42904	0.0086	9.570957	22.428	1683.937	804.8229	1015.315	4271.752	9014.016	0.00058046
13401	0.0159	0.0001	0.0285	91.05431	7.47576	0.330033	90.75908	0.00795	9.240924	24.274	1822.532	871.0631	1098.88	4623.335	9755.906	0.00053828
14512.8	0.0147	0.0001	0.0286	91.3738	7.50199	0.330033	91.08911	0.00735	8.910891	26.288	1973.746	943.3346	1190.053	5006.93	10565.35	0.00049885
15690.7	0.0136	0.0001	0.0287	91.69329	7.52822	0.330033	91.41914	0.0068	8.580858	28.422	2133.934	1019.895	1286.637	5413.288	11422.82	0.00046307
16979.8	0.0126	0.0001	0.0288	92.01278	7.55445	0.330033	91.74917	0.0063	8.250825	30.757	2309.246	1103.684	1392.34	5858.014	12361.26	0.00042946
18387.2	0.0116	0.0001	0.0289	92.33227	7.58068	0.330033	92.07921	0.0058	7.920792	33.306	2500.663	1195.17	1507.753	6343.594	13385.9	0.00039801
19883.5	0.0107	0.0001	0.029	92.65176	7.60691	0.330033	92.40924	0.00535	7.590759	36.016	2704.155	1292.427	1630.446	6859.804	14475.18	0.00036938
21523.2	0.0099	0.0001	0.0291	92.97125	7.63315	0.330033	92.73927	0.00495	7.260726	38.987	2927.157	1399.009	1764.903	7425.507	15668.9	0.00034246
23293.8	0.0092	0.0001	0.0292	93.29073	7.65938	0.330033	93.06931	0.0046	6.930693	42.194	3167.953	1514.095	1910.089	8036.351	16957.86	0.00031756
25203.1	0.0085	0.0001	0.0293	93.61022	7.68561	0.330033	93.39934	0.00425	6.60066	45.652	3427.619	1638.2	2066.653	8695.063	18347.84	0.00029454
27279.8	0.0078	0.0002	0.0295	94.2492	7.73807	0.66006601	94.05941	0.0039	5.940594	49.414	3710.046	1773.184	2236.94	9411.514	19859.66	0.00027404
29506	0.0072	0.0001	0.0296	94.56869	7.7643	0.330033	94.38944	0.0036	5.610561	53.446	4012.817	1917.891	2419.493	10179.57	21480.38	0.00025425
31929.7	0.0067	0.0001	0.0297	94.88818	7.79053	0.330033	94.71947	0.00335	5.280528	57.837	4342.442	2075.432	2618.237	11015.75	23244.84	0.00023577
34542.4	0.0062	0.0001	0.0298	95.20767	7.81676	0.330033	95.0495	0.0031	4.950495	62.569	4697.76	2245.253	2832.473	11917.11	25146.83	0.0002187
37372.3	0.0057	0.0002	0.03	95.84665	7.86922	0.66006601	95.70957	0.00285	4.290429	67.695	5082.638	2429.202	3064.532	12893.46	27207.06	0.00020354
40410.7	0.0053	0.0001	0.0301	96.16613	7.89545	0.330033	96.0396	0.00265	3.960396	73.199	5495.85	2626.693	3313.674	13941.68	29418.96	0.00018889
43739.3	0.0049	0.0002	0.0303	96.80511	7.94791	0.66006601	96.69967	0.00245	3.30033	79.228	5948.538	2843.051	3586.619	15090.04	31842.17	0.00017571
47327.3	0.0045	0.0002	0.0305	97.44409	8.00038	0.66006601	97.35974	0.00225	2.640264	85.728	6436.517	3076.276	3880.841	16327.93	34454.3	0.0001635
51198.7	0.0042	0.0001	0.0306	97.76358	8.02661	0.330033	97.68977	0.0021	2.310231	92.740	6963.027	3327.917	4198.296	17663.56	37272.68	0.00015165
55399.4	0.0039	0.0001	0.0307	98.08307	8.05284	0.330033	98.0198	0.00195	1.980198	100.349	7534.312	3600.958	4542.747	19112.78	40330.73	0.00014062
59942.4	0.0036	0.0001	0.0308	98.40256	8.07907	0.330033	98.34983	0.0018	1.650165	108.578	8152.166	3896.256	4915.277	20680.13	43638.07	0.0001304

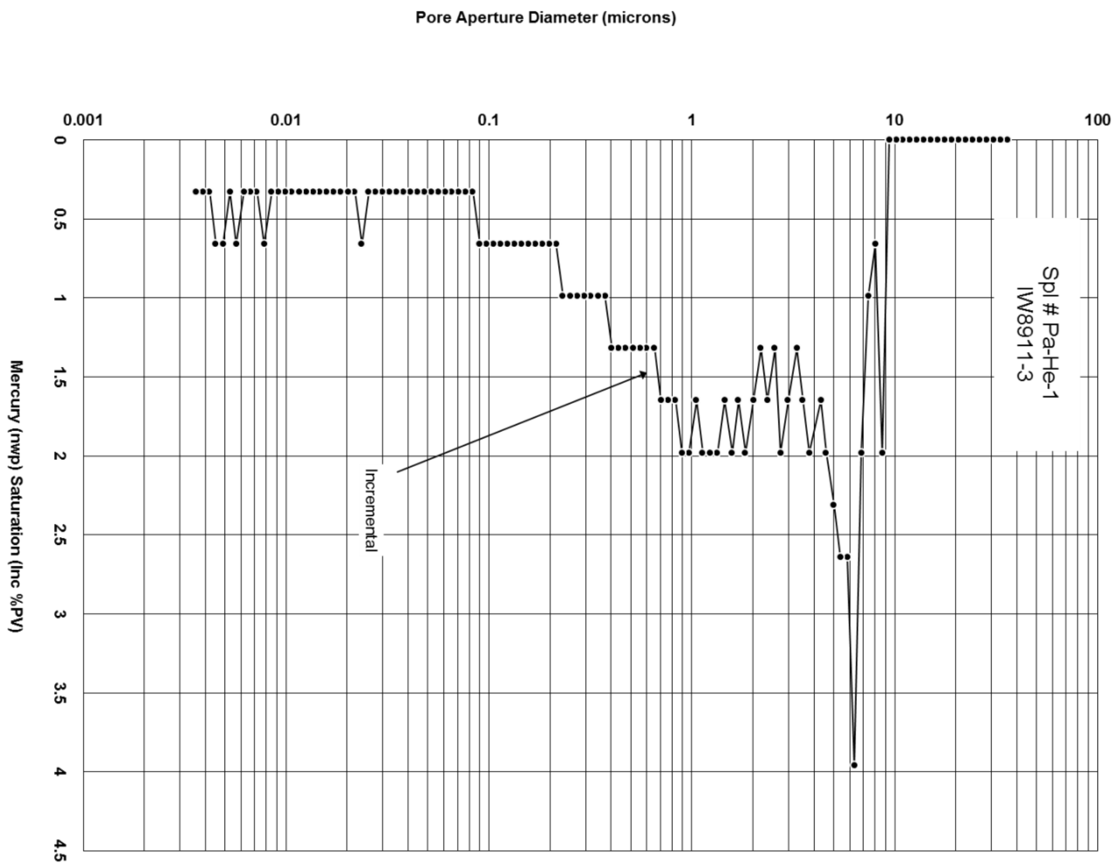

Figure E1. IW8911-3-Pa-He-1 pore aperture vs. mercury saturation.

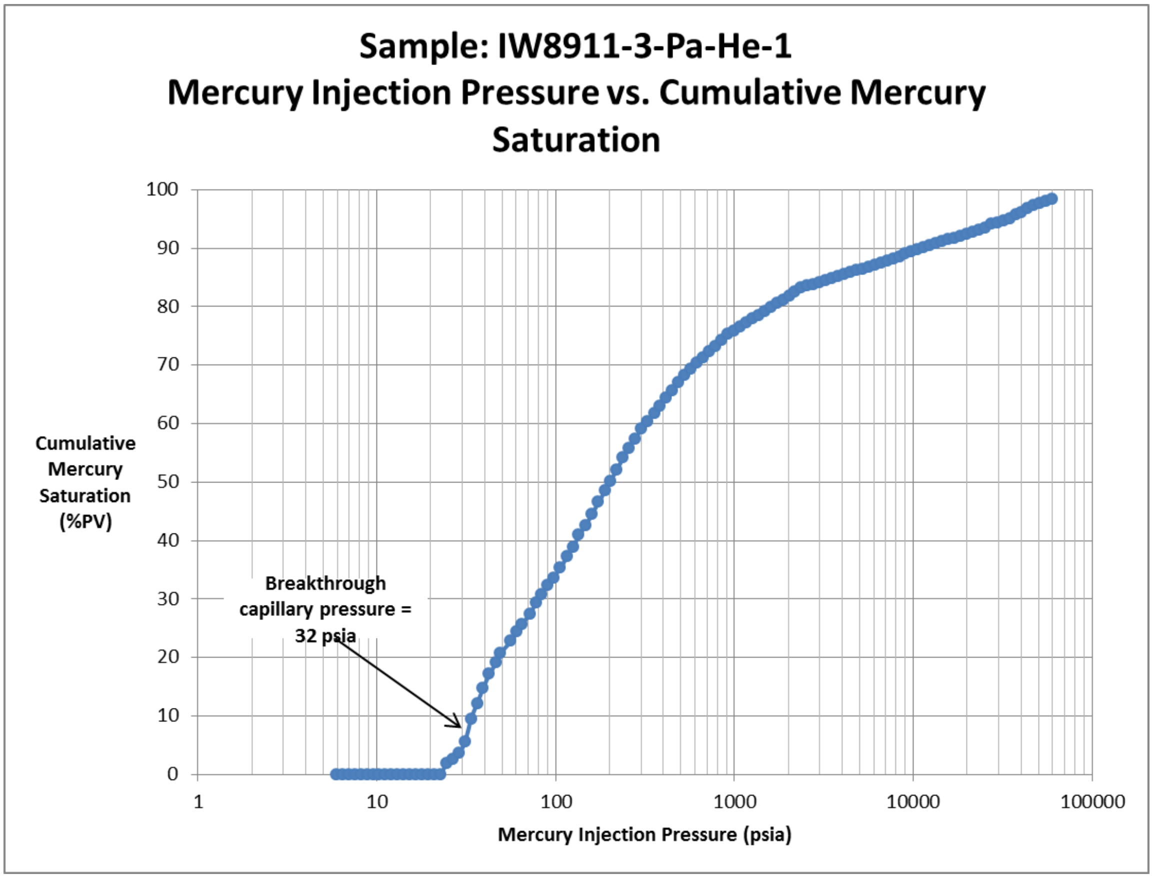

Figure E2. IW8911-3-Pa-He-1 mercury injection pressure vs. cumulative mercury saturation.

Table E2. IW8911-3-Pe-He-2 MICP Data

Int Pres psia	Pore Dia microns	Inc Int mL/gm	Cum Int mL/gm	Cum Int %PV(bc)	Cum Int %BV	Inc Int %PV(ac)	Cum Int %PV(ac)	Pore Rad microns	W.P. Sat %PV(ac)	Lev "J" Funct.	G/B Pc psia	G/O Pc psia	O/B Pc psia	Ht FWL,ft G/B	Ht FWL,ft O/B	Swanson's Sb/Pc(ac)
5.94	35.9299	0	0	0.0331	0	0	0	17.965	100	0.0178	0.80784	0.3861	0.48708	2.0493	4.32432	-0.0303168
6.43	33.1974	0	0.0001	0.1488	0.02573	0	0	16.5987	100	0.0193	0.87448	0.41795	0.52726	2.21835	4.68104	-0.0240056
6.95	30.6831	0	0.0001	0.2562	0.02573	0	0	15.3416	100	0.0209	0.9452	0.45175	0.5699	2.39775	5.0596	-0.0222095
7.52	28.3545	0	0.0001	0.3306	0.02573	0	0	14.1773	100	0.0226	1.02272	0.4888	0.61664	2.5944	5.47456	-0.0205261
8.14	26.2082	0	0.0002	0.4298	0.05145	0	0	13.1041	100	0.0244	1.10704	0.5291	0.66748	2.8083	5.92592	-0.0158022
8.81	24.216	0	0.0002	0.5538	0.05145	0	0	12.108	100	0.0264	1.19816	0.57265	0.72242	3.03945	6.41368	-0.0146005
9.53	22.3855	0	0.0003	0.6612	0.07718	0	0	11.1928	100	0.0286	1.29608	0.61945	0.78146	3.28785	6.93784	-0.0107979
10.31	20.6931	0.0001	0.0003	0.7935	0.07718	0	0	10.3466	100	0.0309	1.40216	0.67015	0.84542	3.55695	7.50568	-0.009981
11.16	19.1216	0.0001	0.0004	0.9671	0.1029	0	0	9.5608	100	0.0335	1.51776	0.7254	0.91512	3.8502	8.12448	-0.0069156
12.07	17.6725	0.0001	0.0005	1.256281	0.12863	0	0	8.83625	100	0.0362	1.64152	0.78455	0.98974	4.16415	8.78696	-0.0042628
13.06	16.3326	0.0001	0.0005	1.256281	0.12863	0	0	8.1663	100	0.0392	1.77616	0.8489	1.07092	4.5057	9.50768	-0.0039397
14.13	15.0947	0.0001	0.0006	1.507538	0.15436	0	0	7.54735	100	0.0424	1.92168	0.91845	1.15866	4.87485	10.28664	-0.0018207
15.29	13.9532	0.0001	0.0007	1.758794	0.18008	0	0	6.9766	100	0.0459	2.07944	0.99385	1.25378	5.27505	11.13112	0
16.54	12.8939	0.0003	0.001	2.512563	0.25726	0.76726343	0.767263	6.44695	99.23274	0.0496	2.24944	1.0751	1.35628	5.7063	12.04112	0.00466614
17.9	11.9171	0.0002	0.0012	3.015075	0.30871	0.51150895	1.278772	5.95855	98.72123	0.0537	2.4344	1.1635	1.4678	6.1755	13.0312	0.00718603
19.37	11.0129	0.0001	0.0013	3.266332	0.33444	0.25575448	1.534527	5.50645	98.46547	0.0581	2.63432	1.25905	1.58834	6.68265	14.10136	0.00796882
20.96	10.1784	0.0001	0.0014	3.517588	0.36016	0.25575448	1.790281	5.0892	98.20972	0.0629	2.85056	1.3624	1.71872	7.2312	15.25888	0.0085917
22.68	9.4071	0.0001	0.0015	3.768844	0.38589	0.25575448	2.046036	4.70355	97.95396	0.068	3.08448	1.4742	1.85976	7.8246	16.51104	0.00907443
24.54	8.6933	0.0002	0.0017	4.271357	0.43734	0.51150895	2.557545	4.34665	97.44246	0.0736	3.33744	1.5951	2.01228	8.4663	17.86512	0.01048329
26.55	8.0348	0.0002	0.0019	4.773869	0.48879	0.51150895	3.069054	4.0174	96.93095	0.0797	3.6108	1.72575	2.1771	9.15975	19.3284	0.01162757
28.75	7.4194	0.0024	0.0043	10.80402	1.10622	6.13810742	9.207161	3.7097	90.79284	0.0863	3.91	1.86875	2.3575	9.91875	20.93	0.03221343
31.09	6.862	0.0009	0.0052	13.06533	1.33775	2.30179028	11.50895	3.431	88.49105	0.0933	4.22824	2.02085	2.54938	10.72605	22.63352	0.0372361
33.65	6.34	0.0022	0.0074	18.59296	1.90372	5.62659847	17.13555	3.17	82.86445	0.101	4.5764	2.18725	2.7593	11.60925	24.4972	0.05122266
36.39	5.862	0.0011	0.0085	21.35678	2.18671	2.81329923	19.94885	2.931	80.05115	0.1092	4.94904	2.36535	2.98398	12.55455	26.49192	0.0551423
39.38	5.4167	0.0016	0.0101	25.37688	2.59833	4.09207161	24.04092	2.70835	75.95908	0.1182	5.35568	2.5597	3.22916	13.5861	28.66864	0.06140794
42.62	5.0055	0.0016	0.0117	29.39698	3.00994	4.09207161	28.13299	2.50275	71.86701	0.1279	5.79632	2.7703	3.49484	14.7039	31.02736	0.06639748
45.46	4.6925	0.0014	0.0131	32.91457	3.37011	3.58056266	31.71355	2.34625	68.28645	0.1364	6.18256	2.9549	3.72772	15.6837	33.09488	0.07017212
50.3	4.2411	0.0012	0.0143	35.92965	3.67882	3.06905371	34.78261	2.12055	65.21739	0.1509	6.8408	3.2695	4.1246	17.3535	36.6184	0.06955739
56.27	3.7909	0.001	0.0153	38.44221	3.93608	2.55754476	37.34015	1.89545	62.65985	0.1688	7.65272	3.65755	4.61414	19.41315	40.96456	0.06674954
59.18	3.6047	0.0009	0.0162	40.70352	4.16761	2.30179028	39.64194	1.80235	60.35806	0.1776	8.04848	3.8467	4.85276	20.4171	43.08304	0.0673797
65	3.2818	0.0009	0.0171	42.96482	4.39915	2.30179028	41.94373	1.6409	58.05627	0.195	8.84	4.225	5.33	22.425	47.32	0.06490869
70.24	3.0371	0.001	0.0181	45.47739	4.65641	2.55754476	44.50128	1.51855	55.49872	0.2107	9.55264	4.5656	5.75968	24.2328	51.13472	0.063729
77.5	2.7526	0.001	0.0191	47.98995	4.91367	2.55754476	47.05882	1.3763	52.94118	0.2325	10.54	5.0375	6.355	26.7375	56.42	0.06107852
83.85	2.5442	0.0009	0.02	50.25126	5.1452	2.30179028	49.36061	1.2721	50.63939	0.2516	11.4036	5.45025	6.8757	28.92825	61.0428	0.0592143
88.58	2.4083	0.0006	0.0206	51.75879	5.29956	1.53452685	50.89514	1.20415	49.10486	0.2658	12.04688	5.7577	7.26356	30.5601	64.48624	0.05779493
97.18	2.195	0.0009	0.0215	54.0201	5.53109	2.30179028	53.19693	1.0975	46.80307	0.2916	13.21648	6.3167	7.96876	33.5271	70.74704	0.05506286
107.25	1.9891	0.0009	0.0224	56.28141	5.76263	2.30179028	55.49872	0.99455	44.50128	0.3218	14.586	6.97125	8.7945	37.00125	78.078	0.05205168
114.12	1.8693	0.0008	0.0232	58.29146	5.96843	2.04603581	57.54476	0.93465	42.45524	0.3424	15.52032	7.4178	9.35784	39.3714	83.07936	0.05072162
124.33	1.7158	0.0006	0.0238	59.79899	6.12279	1.53452685	59.07928	0.8579	40.92072	0.373	16.90888	8.08145	10.19506	42.89385	90.51224	0.04779785
136.53	1.5625	0.0007	0.0245	61.55779	6.30287	1.79028133	60.86957	0.78125	39.13043	0.4096	18.56808	8.87445	11.19546	47.10285	99.39384	0.04484574
146.07	1.4604	0.0006	0.0251	63.06533	6.45723	1.53452685	62.40409	0.7302	37.59591	0.4383	19.86552	9.49455	11.97774	50.39415	106.339	0.04297354
157.34	1.3558	0.0006	0.0257	64.57286	6.61158	1.53452685	63.93862	0.6779	36.06138	0.4721	21.39824	10.2271	12.90188	54.2823	114.5435	0.04087645
171.89	1.241	0.0005	0.0262	65.82915	6.74021	1.27877238	65.21739	0.6205	34.78261	0.5157	23.37704	11.17285	14.09498	59.30205	125.1359	0.03816471
186.33	1.1449	0.0005	0.0267	67.08543	6.86884	1.27877238	66.49616	0.57245	33.50384	0.559	25.34088	12.11145	15.27906	64.28385	135.6482	0.03589739
201.35	1.0595	0.0005	0.0272	68.34171	6.99747	1.27877238	67.77494	0.52975	32.22506	0.6041	27.3836	13.08775	16.5107	69.46575	146.5828	0.03385841
217.7	0.9799	0.0005	0.0277	69.59799	7.1261	1.27877238	69.05371	0.48995	30.94629	0.6532	29.6072	14.1505	17.8514	75.1065	158.4856	0.03190639
238.69	0.8937	0.0005	0.0282	70.85427	7.25473	1.27877238	70.33248	0.44685	29.66752	0.7161	32.46184	15.51485	19.57258	82.34805	173.7663	0.0296395
256.89	0.8304	0.0004	0.0286	71.8593	7.35764	1.0230179	71.3555	0.4152	28.6445	0.7708	34.93704	16.69785	21.06498	88.62705	187.0159	0.02794019
278.16	0.7669	0.0004	0.029	72.86432	7.46054	1.0230179	72.37852	0.38345	27.62148	0.8346	37.82976	18.0804	22.80912	95.9652	202.5005	0.02617364
302.13	0.7061	0.0004	0.0294	73.86935	7.56345	1.0230179	73.40153	0.35305	26.59847	0.9065	41.08968	19.63845	24.77466	104.2349	219.9506	0.0244377
325.84	0.6547	0.0004	0.0298	74.87437	7.66635	1.0230179	74.42455	0.32735	25.57545	0.9776	44.31424	21.1796	26.71888	112.4148	237.2115	0.02297529
354.09	0.6025	0.0004	0.0302	75.8794	7.76925	1.0230179	75.44757	0.30125	24.55243	1.0624	48.15624	23.01585	29.03538	122.1611	257.7775	0.02143289
382.55	0.5576	0.0004	0.0306	76.88442	7.87216	1.0230179	76.47059	0.2788	23.52941	1.1478	52.0268	24.86575	31.3691	131.9798	278.4964	0.02010737
415.87	0.5129	0.0004	0.031	77.88945	7.97506	1.0230179	77.49361	0.25645	22.50639	1.2477	56.55832	27.03155	34.10134	143.4752	302.7534	0.01874379
448.32	0.4758	0.0003	0.0313	78.64322	8.05224	0.76726343	78.26087	0.2379	21.73913	1.3451	60.97152	29.1408	36.76224	154.6704	326.377	0.01755924
485.73	0.4392	0.0003	0.0316	79.39698	8.12942	0.76726343	79.02813	0.2196	20.97187	1.4573	66.05928	31.57245	39.82986	167.5769	353.6114	0.01636575
525.99	0.4056	0.0003	0.0319	80.15075	8.2066	0.76726343	79.7954	0.2028	20.2046	1.5781	71.53464	34.18935	43.13118	181.4666	382.9207	0.01525982
571	0.3736	0.0003	0.0322	80.90452	8.28377	0.76726343	80.56266	0.1868	19.43734	1.7132	77.656	37.115	46.822	196.995	415.688	0.0141921
617.61	0.3454	0.0003	0.0325	81.65829	8.36095	0.76726343	81.32992	0.1727	18.67008	1.853	83.99496	40.14465	50.64402	213.0755	449.6201	0.01324601
668.52	0.3191	0.0003	0.0328	82.41206	8.43813	0.76726343	82.09719	0.15955	17.90281	2.0058	90.91872	43.4538	54.81864	230.6394	486.6826	0.01235273
722.22	0.2954	0.0002	0.033	82.91457	8.48958	0.51150895	82.6087	0.1477	17.3913	2.1669	98.22192	46.9443	59.22204	249.1659	525.7762	0.0115055
783.77	0.2722	0.0002	0.0332	83.41709	8.54103	0.51150895	83.1202	0.1361	16.8798	2.3516	106.5927	50.94505	64.26914	270.4007	570.5846	0.01066761
847.24	0.2518	0.0002	0.0334	83.9196	8.59249	0.51150895	83.63171	0.1259	16.36829	2.542	115.2246	55.0706	69.47368	292.2978	616.7907	0.00992919
916.77	0.2327	0.0002	0.0336	84.42211	8.64394	0.51150895	84.14322	0.11635	15.85678	2.7506	124.6807	59.59005	75.17514	316.2857	667.4086	0.00923226
994.11	0.2146	0.0002	0.0338	84.92462	8.69539	0.51150895	84.65473	0.1073	15.34527	2.9826	135.199	64.61715	81.51702	342.968	723.7121	0.00856576
1075.61	0.1983	0.0002	0.034	85.42714	8.74684	0.51150895	85.16624	0.09915	14.83376	3.2272	146.283	69.91465	88.20002	371.0855	783.0441	0.00796456
1162.99	0.1834	0.0002	0.0342	85.92965	8.79829	0.51150895	85.67775	0.0917	14.32225	3.4893	158.1666	75.59435	95.36518	401.2316	846.6567	0.00741039
1257.33	0.1697	0.0002	0.0344	86.43216	8.84975	0.51150895	86.18926	0.08485	13.81074	3.7724	170.9969	81.72645	103.1011	433.7789	915.3362	0.0068953
1360.61	0.1568	0.0002	0.0346	86.93467	8.9012	0.51150895	86.70077	0.0784	13.29923	4.0823	185.043	88.43965	111.57	469.4105	990.5241	0.00640971
1473.69	0.1448	0.0002	0.0348	87.43719	8.95265	0.51150895	87.21228	0.0724	12.78772	4.4215	200.4218	95.78985	120.8426	508.4231	1072.846	0.00595279
1594.3	0.1338	0.0002	0.035	87.9397	9.0041	0.51150895	87.72379	0.0669	12.27621	4.7834	216.8248	103.6295	130.7326	550.0335	1160.65	0.00553473
1724.33	0.1237	0.0002	0.0352	88.44221	9.05555	0.51150895	88.23529	0.06185	11.76471	5.1735	234.5089	112.0815	141.3951	594.8939	1255.312	0.0051472
1867.1	0.1143	0.0001	0.0353	88.69347	9.08128	0.25575448	88.49105	0.05715	11.50895	5.6019	253.9256	121.3615	153.1022	644.1495	1359.249	0.00476739
2021.97	0.1055	0.0001	0.0354	88.94472	9.10701	0.25575448	88.7468	0.05275	11.2532	6.0666	274.9879	131.4281	165.8015	697.5797	1471.994	0.00441496
2181.87	0.0978	0.0001	0.0355	89.19598	9.13273	0.25575448	89.00256	0.0489	10.99744	6.5463	296.7343	141.8216	178.9133	752.7452	1588.401	0.0041032
2365.7	0.0902	0.0001	0.0356	89.44724	9.15846	0.25575448	89.25831	0.0451	10.74169	7.0979	321.7352	153.7705	193.9874	816.1665	1722.23	0.00379523
2560.84	0.0833	0.0001	0.0357	89.69849	9.18418	0.25575448	89.51407	0.04165	10.48593	7.6833	348.2742	166.4546	209.9889	883.4898	1864.292	0.00351607
2769.97	0.077	0.0001	0.0358	89.94975	9.20991	0.25575448	89.76982	0.0385	10.23018	8.3108	376.7159	180.0481	227.1375	955.6397	2016.538	0.0032599
2997.51	0.0712	0.0001	0.0359	90.20101	9.23564	0.25575448	90.02558	0.0356	9.974425	8.9935	407.6614	194.8382	245.7958	1034.141	2182.187	0.00302103
3242.62	0.0658	0.0001	0.036	90.45226	9.26136	0.25575448	90.28133	0.0329	9.71867	9.7289	440.9963	210.7703	265.8948	1118.704	2360.627	0.0028006
3509.27	0.0608	0.0001	0.0361	90.70352	9.28709	0.25575448	90.53708	0.0304	9.462916	10.529	477.2607	228.1026	287.7601	1210.698	2554.749	0.00259513
3797.94	0.0562	0.0001	0.0362	90.95477	9.31281	0.25575448	90.79284	0.0281	9.207161	11.395	516.5198	246.8661	311.4311	1310.289	2764.9	0.00240465
4104.34	0.052	0.0001	0.0363	91.20603	9.33854	0.25575448	91.04859	0.026	8.951407	12.314	558.1902	266.7821	336.5559	1415.997	2987.96	0.00223141
4443.19	0.048	0.0001	0.0364	91.45729	9.36427	0.25575448	91.30435	0.024	8.695652	13.331	604.2738	288.8074	364.3416	1532.901	3234.642	0.00206702
4803.11	0.0444	0.0001	0.0365	91.70854	9.38999	0.25575448	91.5601	0.0222	8.439898	14.411	653.223	312.2022	393.855	1657.073	3496.664	0.00191749
5199.08	0.041	0.0001	0.0366	91.9598	9.41572	0.25575448	91.81586	0.0205	8.184143	15.599	707.0749	337.9402	426.3246	1793.683	3784.93	0.0017764
5626.14	0.0379	0.0001	0.0367	92.21106	9.44144	0.25575448	92.07161	0.01895	7.928389	16.88	765.155	365.6991	461.3435	1941.018	4095.83	0.00164613
6086.09	0.0351	0.0001	0.0368	92.46231	9.46717	0.25575448	92.32737	0.01755	7.672634	18.26	827.7082	395.5959	499.0594	2099.701	4430.674	0.00152595
6587.66	0.0324	0.0001	0.0369	92.71357	9.4929	0.25575448	92.58312	0.0162	7.41688	19.765	895.9218	428.1979	540.1881	2272.743	4795.816	0.00141368

Table E2. IW8911-3-Pe-He-2 MICP data continued…

Int Pres psia	Pore Dia microns	Inc Int mL/gm	Cum Int mL/gm	Cum Int %PV(bc)	Cum Int %BV	Inc Int %PV(ac)	Cum Int %PV(ac)	Pore Rad microns	W.P. Sat %PV(ac)	Lev "J" Funct.	G/B Pc psia	G/O Pc psia	O/B Pc psia	Ht FWL,ft G/B	Ht FWL,ft O/B	Swanson's Sb/Pc(ac)
7127.66	0.0299	0.0001	0.037	92.96482	9.51862	0.25575448	92.83887	0.01495	7.161125	21.385	969.3618	463.2979	584.4681	2459.043	5188.936	0.00131018
7709	0.0277	0.0001	0.0371	93.21608	9.54435	0.25575448	93.09463	0.01385	6.905371	23.129	1048.424	501.085	632.138	2659.605	5612.152	0.00121472
8344.88	0.0256	0.0001	0.0372	93.46734	9.57007	0.25575448	93.35038	0.0128	6.649616	25.037	1134.904	542.4172	684.2802	2878.984	6075.073	0.00112524
9028.08	0.0236	0.0001	0.0373	93.71859	9.5958	0.25575448	93.60614	0.0118	6.393862	27.087	1227.819	586.8252	740.3026	3114.688	6572.442	0.00104294
9769.84	0.0218	0.0001	0.0374	93.96985	9.62153	0.25575448	93.86189	0.0109	6.138107	29.313	1328.698	635.0396	801.1269	3370.595	7112.444	0.00096639
10574.9	0.0202	0.0001	0.0375	94.22111	9.64725	0.25575448	94.11765	0.0101	5.882353	31.728	1438.18	687.3653	867.1377	3648.323	7698.491	0.00089525
11442.6	0.0186	0.0001	0.0376	94.47236	9.67298	0.25575448	94.3734	0.0093	5.626598	34.332	1556.199	743.7716	938.2965	3947.711	8330.242	0.00082961
12382.6	0.0172	0.0001	0.0377	94.72362	9.6987	0.25575448	94.62916	0.0086	5.370844	37.152	1684.034	804.869	1015.373	4271.997	9014.533	0.00076871
13399.7	0.0159	0.0001	0.0378	94.97487	9.72443	0.25575448	94.88491	0.00795	5.11509	40.203	1822.361	870.9812	1098.776	4622.9	9754.989	0.00071228
14497.2	0.0147	0.0001	0.0379	95.22613	9.75016	0.25575448	95.14066	0.00735	4.859335	43.496	1971.616	942.3167	1188.769	5001.527	10553.95	0.00066013
15691.6	0.0136	0.0001	0.038	95.47739	9.77588	0.25575448	95.39642	0.0068	4.603581	47.08	2134.056	1019.953	1286.71	5413.599	11423.48	0.00061153
16977.6	0.0126	0.0001	0.0381	95.72864	9.80161	0.25575448	95.65217	0.0063	4.347826	50.938	2308.958	1103.546	1392.166	5857.282	12359.71	0.00056672
18369.9	0.0116	0.0001	0.0382	95.9799	9.82733	0.25575448	95.90793	0.0058	4.092072	55.116	2498.305	1194.043	1506.331	6337.612	13373.28	0.00052517
19875.8	0.0107	0.0001	0.0383	96.23116	9.85306	0.25575448	96.16368	0.00535	3.836317	59.634	2703.107	1291.926	1629.815	6857.148	14469.58	0.00048667
21520.4	0.0099	0.0001	0.0384	96.48241	9.87879	0.25575448	96.41944	0.00495	3.580563	64.568	2926.773	1398.825	1764.672	7424.535	15666.84	0.00045068
23290	0.0092	0.0001	0.0385	96.73367	9.90451	0.25575448	96.67519	0.0046	3.324808	69.877	3167.433	1513.847	1909.776	8035.033	16955.08	0.00041754
25203	0.0085	0.0001	0.0386	96.98492	9.93024	0.25575448	96.93095	0.00425	3.069054	75.617	3427.605	1638.194	2066.644	8695.028	18347.77	0.00038687
27272.3	0.0078	0.0001	0.0387	97.23618	9.95596	0.25575448	97.1867	0.0039	2.813299	81.826	3709.03	1772.698	2236.327	9408.937	19854.22	0.00035845
29498.8	0.0072	0.0001	0.0388	97.48744	9.98169	0.25575448	97.44246	0.0036	2.557545	88.506	4011.83	1917.419	2418.898	10177.07	21475.09	0.00033227
31929.9	0.0067	0.0001	0.0389	97.73869	10.0074	0.25575448	97.69821	0.00335	2.30179	95.8	4342.468	2075.444	2618.253	11015.82	23244.97	0.00030778
34539.1	0.0062	0.0001	0.039	97.98995	10.0331	0.25575448	97.95396	0.0031	2.046036	103.63	4697.311	2245.038	2832.202	11915.97	25144.43	0.00028527
37365.1	0.0057	0.0002	0.0392	98.49246	10.0846	0.51150895	98.46547	0.00285	1.534527	112.11	5081.655	2428.732	3063.939	12890.96	27201.8	0.00026507
40408.5	0.0053	0.0001	0.0393	98.74372	10.1103	0.25575448	98.72123	0.00265	1.278772	121.24	5495.553	2626.551	3313.495	13940.93	29417.37	0.00024575
43748.7	0.0049	0.0001	0.0394	98.99497	10.136	0.25575448	98.97698	0.00245	1.023018	131.26	5949.826	2843.667	3587.395	15093.31	31849.07	0.00022757
47312.1	0.0045	0.0001	0.0395	99.24623	10.1618	0.25575448	99.23274	0.00225	0.767263	141.95	6434.443	3075.285	3879.591	16322.67	34443.19	0.00021098
51197.8	0.0042	0.0001	0.0396	99.49749	10.1875	0.25575448	99.48849	0.0021	0.511509	153.61	6962.901	3327.857	4198.22	17663.24	37272	0.00019547
55400.7	0.0039	0.0001	0.0397	99.74874	10.2132	0.25575448	99.74425	0.00195	0.255754	166.22	7534.488	3601.042	4542.853	19113.22	40331.67	0.0001811
59947.7	0.0036	0.0001	0.0398	100	10.239	0.25575448	100	0.0018	-3.3E-13	179.86	8152.886	3896.6	4915.711	20681.95	43641.92	0.00016779

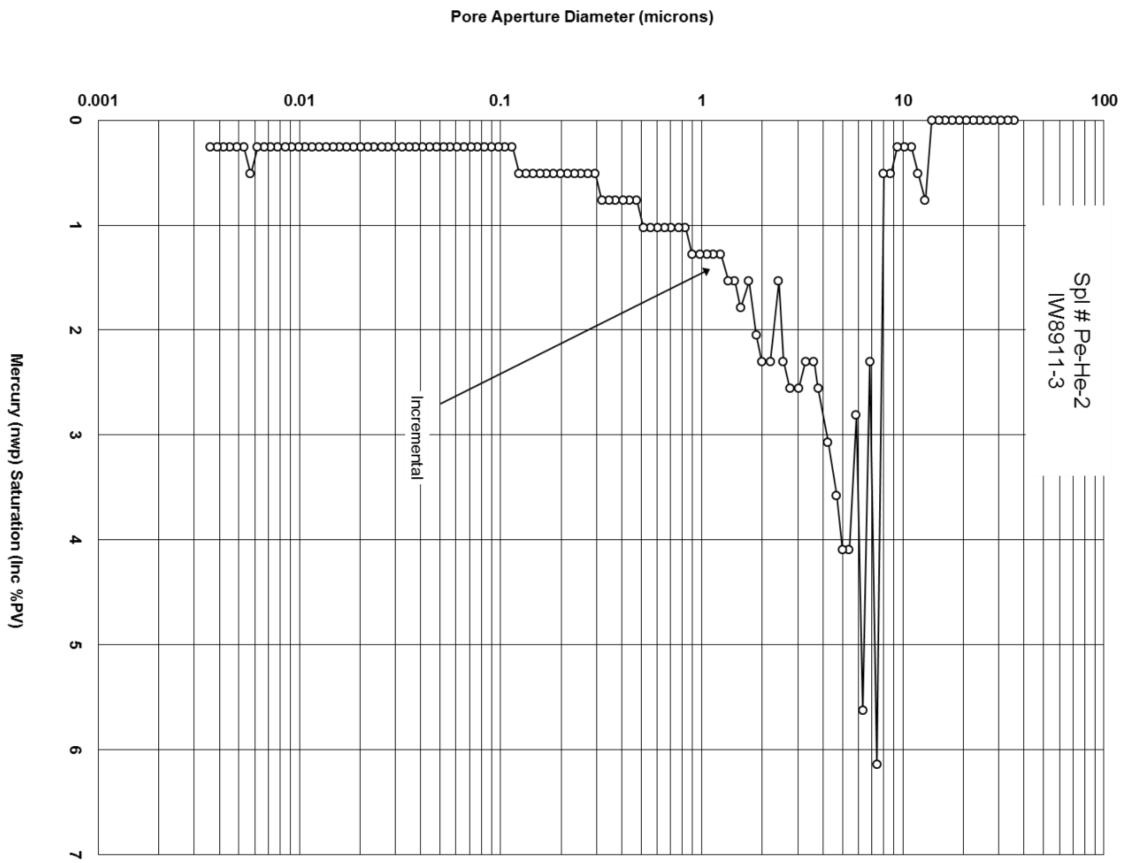

Figure E3. IW8911-3-Pe-He-2 pore aperture vs. mercury saturation.

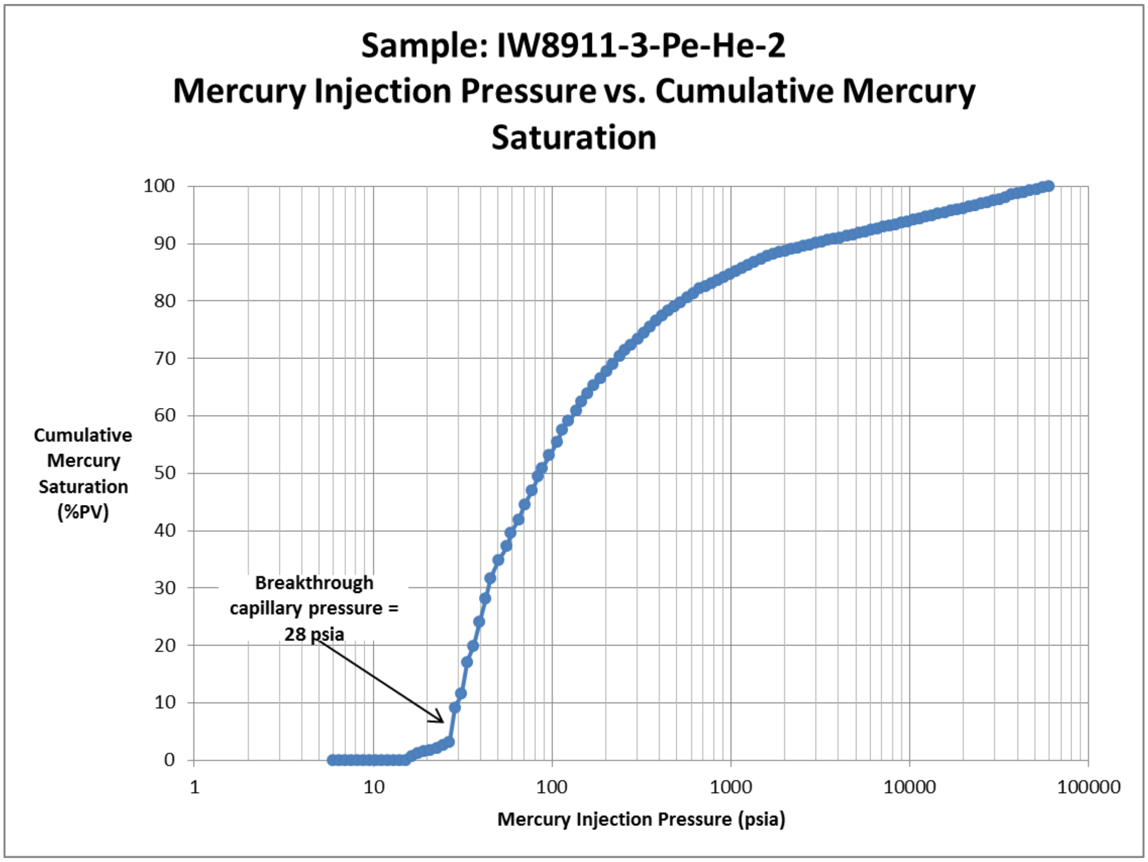

Figure E4. IW8911-3-Pe-He-2 mercury injection pressure vs. cumulative mercury saturation.

Table E3. IW8911-3-Pa-Ho-3 MICP data.

Int Pres psia	Pore Dia microns	Inc Int mL/gm	Cum Int mL/gm	Cum Int %PV(bc)	Cum Int %BV	Inc Int %PV(ac)	Cum Int %PV(ac)	Pore Rad microns	W.P. Sat %PV(ac)	Lev "J" Funct.	G/B Pc psia	G/O Pc psia	O/B Pc psia	Ht FWL,ft G/B	Ht FWL,ft O/B	Swanson's Sb/Pc(ac)
5.94	35.9276	0	0	0.0434	0	0	0	17.9638	100	0.0322	0.80784	0.3861	0.48708	2.0493	4.32432	-0.0042971
6.43	33.2016	0	0	0.1085	0	0	0	16.6008	100	0.0349	0.87448	0.41795	0.52726	2.21835	4.68104	-0.0039697
6.95	30.6876	0	0.0001	0.1881	0.02552	0	0	15.3438	100	0.0377	0.9452	0.45175	0.5699	2.39775	5.0596	0
7.52	28.3592	0	0.0001	0.228833	0.02552	0	0	14.1796	100	0.0408	1.02272	0.4888	0.61664	2.5944	5.47456	0
8.14	26.2089	0.0001	0.0002	0.457666	0.05105	0.2293578	0.229358	13.1045	99.77064	0.0442	1.10704	0.5291	0.66748	2.8083	5.92592	0.00313574
8.81	24.2251	0.0003	0.0005	1.144165	0.12762	0.68807339	0.917431	12.1126	99.08257	0.0478	1.19816	0.57265	0.72242	3.03945	6.41368	0.01158908
9.53	22.3852	0.0007	0.0012	2.745995	0.3063	1.60550459	2.522936	11.1926	97.47706	0.0517	1.29608	0.61945	0.78146	3.28785	6.93784	0.02946216
10.31	20.6918	0.0011	0.0023	5.263158	0.58707	2.52293578	5.045872	10.3459	94.95413	0.056	1.40216	0.67015	0.84542	3.55695	7.50568	0.05446641
11.16	19.1186	0.0021	0.0044	10.06865	1.1231	4.81651376	9.862385	9.5593	90.13761	0.0606	1.51776	0.7254	0.91512	3.8502	8.12448	0.09834879
12.07	17.6698	0.0015	0.0059	13.50114	1.50597	3.44036697	13.30275	8.8349	86.69725	0.0655	1.64152	0.78455	0.98974	4.16415	8.78696	0.12265507
13.06	16.3286	0.0011	0.007	16.01831	1.78675	2.52293578	15.82569	8.1643	84.17431	0.0709	1.77616	0.8489	1.07092	4.5057	9.50768	0.13485613
14.13	15.0965	0.001	0.008	18.30664	2.042	2.29357798	18.11927	7.54825	81.88073	0.0767	1.92168	0.91845	1.15866	4.87485	10.28664	0.14270845
15.29	13.9517	0.001	0.009	20.59497	2.29724	2.29357798	20.41284	6.97585	79.58716	0.083	2.07944	0.99385	1.25378	5.27505	11.13112	0.14857553
16.55	12.8926	0.0008	0.0098	22.42563	2.50144	1.83486239	22.24771	6.4463	77.75229	0.0898	2.2508	1.07575	1.3571	5.70975	12.0484	0.14960238
17.9	11.9173	0.0006	0.0104	23.79863	2.65459	1.37614679	23.62385	5.95865	76.37615	0.0972	2.4344	1.1635	1.4678	6.1755	13.0312	0.14687537
19.37	11.0139	0.0006	0.011	25.17162	2.80774	1.37614679	25	5.50695	75	0.1051	2.63432	1.25905	1.58834	6.68265	14.10136	0.14363545
20.96	10.1782	0.0005	0.0115	26.31579	2.93537	1.14678899	26.14679	5.0891	73.85321	0.1138	2.85056	1.3624	1.71872	7.2312	15.25888	0.13882841
22.68	9.4076	0.0005	0.012	27.45995	3.06299	1.14678899	27.29358	4.7038	72.70642	0.1231	3.08448	1.4742	1.85976	7.8246	16.51104	0.13392717
24.54	8.694	0.0005	0.0125	28.60412	3.19062	1.14678899	28.44037	4.347	71.55963	0.1332	3.33744	1.5951	2.01228	8.4663	17.86512	0.12897689
26.55	8.0355	0.0005	0.013	29.74828	3.31824	1.14678899	29.58716	4.01775	70.41284	0.1441	3.6108	1.72575	2.1771	9.15975	19.3284	0.1240195
28.72	7.4266	0.0005	0.0135	30.89245	3.44587	1.14678899	30.73394	3.7133	69.26606	0.1559	3.90592	1.8668	2.35504	9.9084	20.90816	0.1190927
31.08	6.8635	0.0007	0.0142	32.49428	3.62454	1.60550459	32.33945	3.43175	67.66055	0.1687	4.22688	2.0202	2.54856	10.7226	22.62624	0.11579848
33.63	6.3424	0.0007	0.0149	34.09611	3.80322	1.60550459	33.94495	3.1712	66.05505	0.1825	4.57368	2.18595	2.75766	11.60235	24.48264	0.112331
36.39	5.8627	0.0007	0.0156	35.69794	3.98189	1.60550459	35.55046	2.93135	64.44954	0.1975	4.94904	2.36535	2.98398	12.55455	26.49192	0.10872124
39.37	5.4177	0.0006	0.0162	37.07094	4.13504	1.37614679	36.92661	2.70885	63.07339	0.2137	5.35432	2.55905	3.22834	13.58265	28.66136	0.10438191
42.6	5.0075	0.0005	0.0167	38.2151	4.26267	1.14678899	38.07339	2.50375	61.92661	0.2312	5.7936	2.769	3.4932	14.697	31.0128	0.09946339
43.41	4.9146	0.0004	0.0171	39.13043	4.36477	0.91743119	38.99083	2.4573	61.00917	0.2356	5.90376	2.82165	3.55962	14.97645	31.60248	0.09995946
46.38	4.5999	0.0005	0.0176	40.2746	4.49239	1.14678899	40.13761	2.29995	59.86239	0.2517	6.30768	3.0147	3.80316	16.0011	33.76464	0.09631015
50.44	4.2289	0.0005	0.0181	41.41876	4.62001	1.14678899	41.2844	2.11445	58.7156	0.2738	6.85984	3.2786	4.13608	17.4018	36.72032	0.09108822
55.8	3.823	0.0008	0.0189	43.24943	4.82421	1.83486239	43.11927	1.9115	56.88073	0.3029	7.5888	3.627	4.5756	19.251	40.6224	0.08599801
59.59	3.58	0.0008	0.0197	45.08009	5.02841	1.83486239	44.95413	1.79	55.04587	0.3234	8.10424	3.87335	4.88638	20.55855	43.38152	0.08395517
66.45	3.2105	0.0007	0.0204	46.68192	5.20709	1.60550459	46.55963	1.60525	53.44037	0.3607	9.0372	4.31925	5.4489	22.92525	48.3756	0.07797688
70.86	3.0105	0.0007	0.0211	48.28375	5.38576	1.60550459	48.16514	1.50525	51.83486	0.3846	9.63696	4.6059	5.81052	24.4467	51.58608	0.07564547
76.13	2.802	0.0008	0.0219	50.11442	5.58996	1.83486239	50	1.401	50	0.4132	10.35368	4.94845	6.24266	26.26485	55.42264	0.07309126
83.25	2.5625	0.0006	0.0225	51.48741	5.74311	1.37614679	51.37615	1.28125	48.62385	0.4519	11.322	5.41125	6.8265	28.72125	60.606	0.06867973
89.49	2.3837	0.0006	0.0231	52.86041	5.89626	1.37614679	52.75229	1.19185	47.24771	0.4857	12.17064	5.81685	7.33818	30.87405	65.14872	0.06560215
98.07	2.1752	0.0007	0.0238	54.46224	6.07494	1.60550459	54.3578	1.0876	45.6422	0.5323	13.33752	6.37455	8.04174	33.83415	71.39496	0.06168463
105	2.0317	0.0005	0.0243	55.60641	6.20256	1.14678899	55.50459	1.01585	44.49541	0.5699	14.28	6.825	8.61	36.225	76.44	0.05882892
113.73	1.8756	0.0006	0.0249	56.97941	6.35571	1.37614679	56.88073	0.9378	43.11927	0.6173	15.46728	7.39245	9.32586	39.23685	82.79544	0.05565977
123.99	1.7205	0.0006	0.0255	58.3524	6.50886	1.37614679	58.25688	0.86025	41.74312	0.673	16.86264	8.05935	10.16718	42.77655	90.26472	0.05228918
134.92	1.5811	0.0006	0.0261	59.7254	6.66201	1.37614679	59.63303	0.79055	40.36697	0.7323	18.34912	8.7698	11.06344	46.5474	98.22176	0.0491883
146.51	1.4561	0.0005	0.0266	60.86957	6.78963	1.14678899	60.77982	0.72805	39.22018	0.7952	19.92536	9.52315	12.01382	50.54595	106.6593	0.04616825
158.37	1.347	0.0006	0.0272	62.24256	6.94278	1.37614679	62.15596	0.6735	37.84404	0.8596	21.53832	10.29405	12.98634	54.63765	115.2934	0.04367784
171.74	1.2421	0.0005	0.0277	63.38673	7.07041	1.14678899	63.30275	0.62105	36.69725	0.9322	23.35664	11.1631	14.08268	59.2503	125.0267	0.04102064
186.35	1.1448	0.0005	0.0282	64.53089	7.19803	1.14678899	64.44954	0.5724	35.55046	1.0115	25.3436	12.11275	15.2807	64.29075	135.6628	0.03848945
200.55	1.0637	0.0005	0.0287	65.67506	7.32566	1.14678899	65.59633	0.53185	34.40367	1.0886	27.2748	13.03575	16.4451	69.18975	146.0004	0.03640057
219.58	0.9715	0.0006	0.0293	67.04805	7.47881	1.37614679	66.97248	0.48575	33.02752	1.1918	29.86288	14.2727	18.00556	75.7551	159.8542	0.03394336
236.6	0.9016	0.0004	0.0297	67.96339	7.58091	0.91743119	67.88991	0.4508	32.11009	1.2842	32.1776	15.379	19.4012	81.627	172.2448	0.03193315
257.58	0.8282	0.0005	0.0302	69.10755	7.70853	1.14678899	69.0367	0.4141	30.9633	1.3981	35.03088	16.7427	21.12156	88.8651	187.5182	0.02982766
277.38	0.7691	0.0005	0.0307	70.25172	7.83616	1.14678899	70.18349	0.38455	29.81651	1.5056	37.72368	18.0297	22.74516	95.6961	201.9326	0.0281586
301.34	0.7079	0.0005	0.0312	71.39588	7.96378	1.14678899	71.33028	0.35395	28.66972	1.6356	40.98224	19.5871	24.70988	103.9623	219.3755	0.02634319
326.33	0.6537	0.0005	0.0317	72.54005	8.09141	1.14678899	72.47706	0.32685	27.52294	1.7713	44.38088	21.21145	26.75906	112.5839	237.5682	0.02471695
354.27	0.6021	0.0005	0.0322	73.68421	8.21903	1.14678899	73.62385	0.30105	26.37615	1.9229	48.18072	23.02755	29.05014	122.2232	257.9086	0.02312786
383.3	0.5565	0.0004	0.0326	74.59954	8.32113	0.91743119	74.54128	0.27825	25.45872	2.0805	52.1288	24.9145	31.4306	132.2385	279.0424	0.02164259
415.19	0.5138	0.0004	0.033	75.51487	8.42323	0.91743119	75.45872	0.2569	24.54128	2.2536	56.46584	26.98735	34.04558	143.2406	302.2583	0.02022618
448.48	0.4757	0.0004	0.0334	76.43021	8.52533	0.91743119	76.37615	0.23785	23.62385	2.4343	60.99328	29.1512	36.77536	154.7256	326.4934	0.01895247
486.41	0.4386	0.0004	0.0338	77.34554	8.62743	0.91743119	77.29358	0.2193	22.70642	2.6402	66.15176	31.61665	39.88562	167.8115	354.1065	0.01768448
526.57	0.4051	0.0003	0.0341	78.03204	8.70401	0.68807339	77.98165	0.20255	22.01835	2.8581	71.61352	34.22705	43.17874	181.6667	383.343	0.01648115
570.82	0.3737	0.0003	0.0344	78.71854	8.78058	0.68807339	78.66972	0.18685	21.33028	3.0983	77.63152	37.1033	46.80724	196.9329	415.557	0.01533768
616.82	0.3458	0.0003	0.0347	79.40503	8.85716	0.68807339	79.3578	0.1729	20.6422	3.348	83.88752	40.0933	50.57924	212.8029	449.045	0.014318
667.26	0.3197	0.0003	0.035	80.09153	8.93373	0.68807339	80.04587	0.15985	19.95413	3.6218	90.74736	43.3719	54.71532	230.2047	485.7653	0.01335043
723.27	0.2949	0.0003	0.0353	80.77803	9.0103	0.68807339	80.73394	0.14745	19.26606	3.9258	98.36472	47.01255	59.30814	249.5282	526.5406	0.01242244
782.16	0.2727	0.0003	0.0356	81.46453	9.08688	0.68807339	81.42202	0.13635	18.57798	4.2455	106.3738	50.8404	64.13712	269.8452	569.4125	0.01158504
847.56	0.2517	0.0003	0.0359	82.15103	9.16345	0.68807339	82.11009	0.12585	17.88991	4.6004	115.2682	55.0914	69.49992	292.4082	617.0237	0.01078145
915.88	0.2329	0.0002	0.0361	82.6087	9.2145	0.4587156	82.56881	0.11645	17.43119	4.9713	124.5597	59.5322	75.10216	315.9786	666.7606	0.01003295
994.44	0.2145	0.0002	0.0363	83.06636	9.26555	0.4587156	83.02752	0.10725	16.97248	5.3977	135.2438	64.6386	81.54408	343.0818	723.9523	0.00929169
1074.24	0.1986	0.0002	0.0365	83.52403	9.3166	0.4587156	83.48624	0.0993	16.51376	5.8308	146.0966	69.8256	88.08768	370.6128	782.0467	0.00864898
1162.98	0.1834	0.0002	0.0367	83.98169	9.36765	0.4587156	83.94495	0.0917	16.05505	6.3125	158.1653	75.5937	95.36436	401.2281	846.6494	0.00803292
1258.73	0.1695	0.0002	0.0369	84.43936	9.4187	0.4587156	84.40367	0.08475	15.59633	6.8322	171.1873	81.81745	103.2159	434.2619	916.3554	0.00746243
1360.82	0.1568	0.0002	0.0371	84.89703	9.46975	0.4587156	84.86239	0.0784	15.13761	7.3863	185.0715	88.4533	111.5872	469.4829	990.677	0.0069401
1471.44	0.145	0.0002	0.0373	85.35469	9.5208	0.4587156	85.3211	0.0725	14.6789	7.9868	200.1158	95.6436	120.6581	507.6468	1071.208	0.00645305
1594.56	0.1338	0.0002	0.0375	85.81236	9.57185	0.4587156	85.77982	0.0669	14.22018	8.655	216.8602	103.6464	130.7539	550.1232	1160.84	0.00598681
1725.44	0.1236	0.0002	0.0377	86.27002	9.6229	0.4587156	86.23853	0.0618	13.76147	9.3654	234.6598	112.1536	141.4861	595.2768	1256.12	0.00556228
1868.07	0.1142	0.0002	0.0379	86.72769	9.67395	0.4587156	86.69725	0.0571	13.30275	10.14	254.0575	121.4246	153.1817	644.4842	1359.955	0.00516492
2020.47	0.1056	0.0002	0.0381	87.18535	9.725	0.4587156	87.15596	0.0528	12.84404	10.967	274.7839	131.3306	165.6785	697.0622	1470.902	0.0048006
2186.12	0.0976	0.0001	0.0382	87.41419	9.75053	0.2293578	87.38532	0.0488	12.61468	11.866	297.3123	142.0978	179.2618	754.2114	1591.495	0.00444852
2363.28	0.0903	0.0001	0.0383	87.64302	9.77605	0.2293578	87.61468	0.04515	12.38532	12.828	321.4061	153.6132	193.789	815.3316	1720.468	0.00412585
2561.09	0.0833	0.0001	0.0384	87.87185	9.80158	0.2293578	87.84404	0.04165	12.15596	13.901	348.3082	166.4709	210.0094	883.5761	1864.474	0.00381715
2768.27	0.0771	0.0001	0.0385	88.10069	9.8271	0.2293578	88.07339	0.03855	11.92661	15.026	376.4847	179.9376	226.9981	955.0532	2015.301	0.00354069
2995.99	0.0712	0.0001	0.0386	88.32952	9.85263	0.2293578	88.30275	0.0356	11.69725	16.262	407.4546	194.7394	245.6712	1033.617	2181.081	0.00328009
3240.68	0.0658	0.0001	0.0387	88.55835	9.87815	0.2293578	88.53211	0.0329	11.46789	17.59	440.7325	210.6442	265.7358	1118.035	2359.215	0.0030403
3508.4	0.0608	0.0001	0.0388	88.78719	9.90368	0.2293578	88.76147	0.0304	11.23853	19.043	477.1424	228.046	287.6888	1210.398	2554.115	0.00281557
3796.54	0.0562	0.0001	0.0389	89.01602	9.9292	0.2293578	88.99083	0.0281	11.00917	20.607	516.3294	246.7751	311.3163	1309.806	2763.881	0.00260861
4105.73	0.052	0.0001	0.039	89.24485	9.95473	0.2293578	89.22018	0.026	10.77982	22.285	558.3793	266.8725	336.6699	1416.477	2988.971	0.00241838
4439.5	0.0481	0.0001	0.0391	89.47368	9.98025	0.2293578	89.44954	0.02405	10.55046	24.097	603.772	288.5675	364.039	1531.628	3231.956	0.00224231
4809.04	0.0444	0.0001	0.0392	89.70252	10.0058	0.2293578	89.6789	0.0222	10.3211	26.103	654.0294	312.5876	394.3413	1659.119	3500.981	0.00207531
5200.44	0.041	0.0001	0.0393	89.93135	10.0313	0.2293578	89.90826	0.0205	10.09174	28.227	707.2598	338.0286	426.4361	1794.152	3785.92	0.00192403
5626.74	0.0379	0.0001	0.0394	90.16018	10.0568	0.2293578	90.13761	0.01895	9.862385	30.541	765.2366	365.7381	461.3927	1941.225	4096.267	0.00178279
6087.69	0.035	0.0001	0.0395	90.38902	10.0824	0.2293578	90.36697	0.0175	9.633028	33.043	827.9258	395.6999	499.1906	2100.253	4431.838	0.00165199

Table E3. IW8911-3-Pa-Ho-3 MICP data continued.

Int Pres psia	Pore Dia microns	Inc Int mL/gm	Cum Int mL/gm	Cum Int %PV(bc)	Cum Int %BV	Inc Int %PV(ac)	Cum Int %PV(ac)	Pore Rad microns	W.P. Sat %PV(ac)	Lev "J" Funct.	G/B Pc psia	G/O Pc psia	O/B Pc psia	Ht FWL,ft G/B	Ht FWL,ft O/B	Swanson's Sb/Pc(ac)
6590.35	0.0324	0.0001	0.0396	90.61785	10.1079	0.2293578	90.59633	0.0162	9.40367	35.771	896.2876	428.3728	540.4087	2273.671	4797.775	0.00152987
7130.56	0.0299	0.0001	0.0397	90.84668	10.1334	0.2293578	90.82569	0.01495	9.174312	38.704	969.7562	463.4864	584.7059	2460.043	5191.048	0.00141754
7709.43	0.0277	0.0001	0.0398	91.07551	10.1589	0.2293578	91.05505	0.01385	8.944954	41.846	1048.482	501.113	632.1733	2659.753	5612.465	0.00131442
8350.85	0.0255	0.0001	0.0399	91.30435	10.1845	0.2293578	91.2844	0.01275	8.715596	45.327	1135.716	542.8053	684.7697	2881.043	6079.419	0.00121651
9030.37	0.0236	0.0001	0.04	91.53318	10.21	0.2293578	91.51376	0.0118	8.486239	49.016	1228.13	586.9741	740.4903	3115.478	6574.109	0.0011278
9781.39	0.0218	0.0001	0.0401	91.76201	10.2355	0.2293578	91.74312	0.0109	8.256881	53.092	1330.269	635.7904	802.074	3374.58	7120.852	0.00104382
10586.6	0.0202	0.0001	0.0402	91.99085	10.261	0.2293578	91.97248	0.0101	8.027523	57.463	1439.779	688.1297	868.102	3652.38	7707.052	0.00096683
11452.6	0.0186	0.0001	0.0403	92.21968	10.2866	0.2293578	92.20183	0.0093	7.798165	62.163	1557.552	744.4184	939.1124	3951.144	8337.486	0.00089596
12386.4	0.0172	0.0001	0.0404	92.44851	10.3121	0.2293578	92.43119	0.0086	7.568807	67.232	1684.554	805.118	1015.687	4273.318	9017.321	0.00083047
13400.1	0.0159	0.0001	0.0405	92.67735	10.3376	0.2293578	92.66055	0.00795	7.33945	72.734	1822.41	871.0046	1098.806	4623.024	9755.251	0.00076955
14503.8	0.0147	0.0001	0.0406	92.90618	10.3631	0.2293578	92.88991	0.00735	7.110092	78.725	1972.52	942.7483	1189.313	5003.818	10558.78	0.00071275
15704.5	0.0136	0.0001	0.0407	93.13501	10.3887	0.2293578	93.11927	0.0068	6.880734	85.242	2135.813	1020.793	1287.77	5418.056	11432.88	0.00065988
16995.6	0.0126	0.0002	0.0409	93.59268	10.4397	0.4587156	93.57798	0.0063	6.422018	92.249	2311.396	1104.711	1393.636	5863.468	12372.77	0.00061276
18386.7	0.0116	0.0002	0.0411	94.05034	10.4908	0.4587156	94.0367	0.0058	5.963303	99.8	2500.587	1195.134	1507.707	6343.401	13385.5	0.00056917
19882.5	0.0107	0.0001	0.0412	94.27918	10.5163	0.2293578	94.26606	0.00535	5.733945	107.92	2704.024	1292.364	1630.367	6859.473	14474.48	0.00052764
21518.9	0.0099	0.0001	0.0413	94.50801	10.5418	0.2293578	94.49541	0.00495	5.504587	116.8	2926.564	1398.725	1764.546	7424.003	15665.72	0.0004887
23297.8	0.0092	0.0002	0.0415	94.96568	10.5929	0.4587156	94.95413	0.0046	5.045872	126.46	3168.505	1514.359	1910.422	8037.751	16960.82	0.00045358
25203.2	0.0085	0.0001	0.0416	95.19451	10.6184	0.2293578	95.18349	0.00425	4.816514	136.8	3427.631	1638.206	2066.66	8695.094	18347.91	0.0004203
27269.4	0.0078	0.0002	0.0418	95.65217	10.6694	0.4587156	95.6422	0.0039	4.357798	148.01	3708.644	1772.514	2236.094	9407.957	19852.15	0.00039032
29506.8	0.0072	0.0002	0.042	96.10984	10.7205	0.4587156	96.10092	0.0036	3.899083	160.16	4012.918	1917.939	2419.554	10179.83	21480.91	0.00036246
31930.7	0.0067	0.0002	0.0422	96.56751	10.7715	0.4587156	96.55963	0.00335	3.440367	173.32	4342.57	2075.493	2618.314	11016.08	23245.52	0.00033654
34534.4	0.0062	0.0001	0.0423	96.79634	10.7971	0.2293578	96.78899	0.0031	3.211009	187.45	4696.674	2244.734	2831.818	11914.36	25141.02	0.00031191
37365.8	0.0057	0.0002	0.0425	97.254	10.8481	0.4587156	97.24771	0.00285	2.752294	202.82	5081.745	2428.775	3063.993	12891.19	27202.28	0.00028964
40421.3	0.0053	0.0002	0.0427	97.71167	10.8992	0.4587156	97.70642	0.00265	2.293578	219.4	5497.29	2627.381	3314.543	13945.33	29426.67	0.00026901
43720	0.0049	0.0001	0.0428	97.9405	10.9247	0.2293578	97.93578	0.00245	2.06422	237.31	5945.917	2841.799	3585.038	15083.39	31828.15	0.00024929
47339.4	0.0045	0.0003	0.0431	98.627	11.0013	0.68807339	98.62385	0.00225	1.376147	256.95	6438.156	3077.06	3881.829	16332.09	34463.07	0.00023185
51206.1	0.0042	0.0002	0.0433	99.08467	11.0523	0.4587156	99.08257	0.0021	0.917431	277.94	6964.026	3328.395	4198.898	17666.09	37278.02	0.00021534
55432.4	0.0038	0.0003	0.0436	99.77117	11.1289	0.68807339	99.77064	0.0019	0.229358	300.88	7538.805	3603.105	4545.456	19124.17	40354.78	0.0002003
59935.7	0.0036	0.0001	0.0437	100	11.1544	0.2293578	100	0.0018	-1.6E-13	325.32	8151.25	3895.818	4914.724	20677.8	43633.16	0.00018568

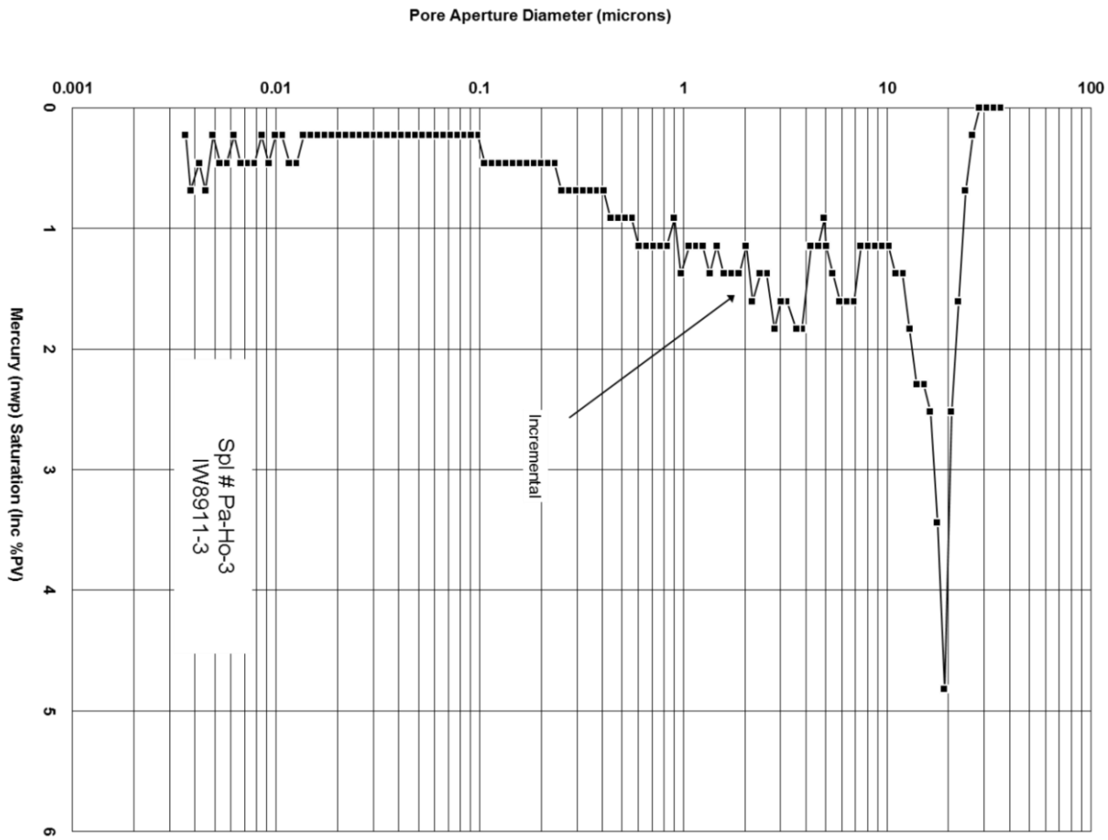

Figure E5. IW8911-3-Pa-Ho-3 pore aperture vs. mercury saturation.

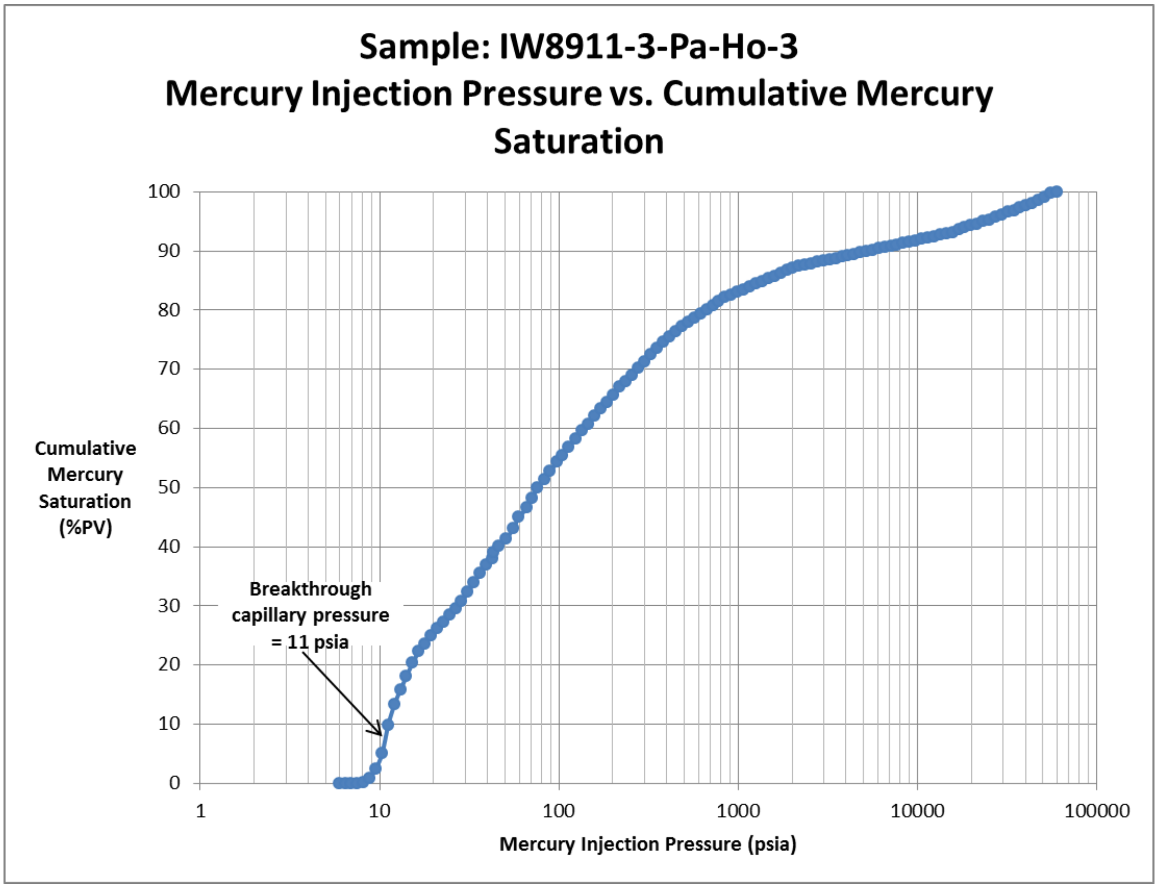

Figure E6. IW8911-3-Pa-Ho-3 Mercury injection pressure vs. cumulative mercury saturation.

Table E4. IW8911-3-Pe-Ho-4 MICP data.

Int Pres psia	Pore Dia microns	Inc Int mL/gm	Cum Int mL/gm	Cum Int %PV(bc)	Cum Int %BV	Inc Int %PV(ac)	Cum Int %PV(ac)	Pore Rad microns	W.P. Sat %PV(ac)	Lev "J" Funct.	G/B Pc psia	G/O Pc psia	O/B Pc psia	Ht FWL,ft G/B	Ht FWL,ft O/B	Swanson's Sb/Pc(ac)
5.94	35.9299	0	0	0.0316	0	0	0	17.965	100	0.0063	0.80784	0.3861	0.48708	2.0493	4.32432	-0.0361678
6.43	33.1974	0	0	0.0738	0	0	0	16.5987	100	0.0068	0.87448	0.41795	0.52726	2.21835	4.68104	-0.0334116
6.95	30.6831	0	0	0.116	0	0	0	15.3416	100	0.0074	0.9452	0.45175	0.5699	2.39775	5.0596	-0.0309117
7.52	28.3545	0	0.0001	0.1898	0.02685	0	0	14.1773	100	0.008	1.02272	0.4888	0.61664	2.5944	5.47456	-0.0249976
8.14	26.2082	0	0.0001	0.2319	0.02685	0	0	13.1041	100	0.0087	1.10704	0.5291	0.66748	2.8083	5.92592	-0.0230936
8.81	24.216	0	0.0001	0.3163	0.02685	0	0	12.108	100	0.0094	1.19816	0.57265	0.72242	3.03945	6.41368	-0.0213373
9.53	22.3855	0.0001	0.0001	0.5166	0.02685	0	0	11.1928	100	0.0101	1.29608	0.61945	0.78146	3.28785	6.93784	-0.0197253
10.31	20.6931	0	0.0002	0.6326	0.05371	0	0	10.3466	100	0.011	1.40216	0.67015	0.84542	3.55695	7.50568	-0.0156283
11.16	19.1216	0.0001	0.0002	0.8329	0.05371	0	0	9.5608	100	0.0119	1.51776	0.7254	0.91512	3.8502	8.12448	-0.0144379
12.07	17.6725	0	0.0003	0.9594	0.08056	0	0	8.83625	100	0.0128	1.64152	0.78455	0.98974	4.16415	8.78696	-0.0111245
13.06	16.3326	0	0.0003	1.0753	0.08056	0	0	8.1663	100	0.0139	1.77616	0.8489	1.07092	4.5057	9.50768	-0.0102812
14.13	15.0947	0	0.0003	1.1913	0.08056	0	0	7.54735	100	0.015	1.92168	0.91845	1.15866	4.87485	10.28664	-0.0095027
15.29	13.9532	0.0001	0.0004	1.3811	0.10742	0	0	6.9766	100	0.0163	2.07944	0.99385	1.25378	5.27505	11.13112	-0.0070254
16.54	12.8939	0	0.0004	1.5076	0.10742	0	0	6.44695	100	0.0176	2.24944	1.0751	1.35628	5.7063	12.04112	-0.0064945
17.9	11.9171	0.0001	0.0005	1.74216	0.13427	0	0	5.95855	100	0.019	2.4344	1.1635	1.4678	6.1755	13.0312	-0.0045008
19.37	11.0129	0.0001	0.0006	2.090592	0.16113	0	0	5.50645	100	0.0206	2.63432	1.25905	1.58834	6.68265	14.10136	-0.0027728
20.96	10.1784	0.0001	0.0006	2.090592	0.16113	0	0	5.0892	100	0.0223	2.85056	1.3624	1.71872	7.2312	15.25888	-0.0025625
22.68	9.4071	0.0001	0.0007	2.439024	0.18798	0	0	4.70355	100	0.0241	3.08448	1.4742	1.85976	7.8246	16.51104	-0.0011841
24.54	8.6933	0.0001	0.0008	2.787456	0.21484	0	0	4.34665	100	0.0261	3.33744	1.5951	2.01228	8.4663	17.86512	-1.131E-18
26.55	8.0348	0.0003	0.0011	3.832753	0.2954	1.07526882	1.075269	4.0174	98.92473	0.0282	3.6108	1.72575	2.1771	9.15975	19.3284	0.00303441
28.75	7.4194	0.0003	0.0014	4.878049	0.37596	1.07526882	2.150538	3.7097	97.84946	0.0306	3.91	1.86875	2.3575	9.91875	20.93	0.00560443
31.09	6.862	0.0001	0.0015	5.226481	0.40282	0.35842294	2.508961	3.431	97.49104	0.0331	4.22824	2.02085	2.54938	10.72605	22.63352	0.00604638
33.65	6.34	0.0001	0.0016	5.574913	0.42967	0.35842294	2.867384	3.17	97.13262	0.0358	4.5764	2.18725	2.7593	11.60925	24.4972	0.00638444
36.39	5.862	0.0002	0.0018	6.271777	0.48338	0.71684588	3.584229	2.931	96.41577	0.0387	4.94904	2.36535	2.98398	12.55455	26.49192	0.00737966
39.38	5.4167	0.0002	0.002	6.968641	0.53709	0.71684588	4.301075	2.70835	95.69892	0.0419	5.35568	2.5597	3.22916	13.5861	28.66864	0.00818321
42.62	5.0055	0.001	0.003	10.45296	0.80564	3.58422939	7.885305	2.50275	92.1147	0.0453	5.79632	2.7703	3.49484	14.7039	31.02736	0.01386205
46.16	4.6213	0.0004	0.0034	11.84669	0.91306	1.43369176	9.318996	2.31065	90.681	0.0491	6.27776	3.0004	3.78512	15.9252	33.60448	0.01512606
50.63	4.2132	0.0003	0.0037	12.89199	0.99362	1.07526882	10.39427	2.1066	89.60573	0.0538	6.88568	3.29095	4.15166	17.46735	36.85864	0.01538184
56.07	3.8046	0.0004	0.0041	14.28571	1.10104	1.43369176	11.82796	1.9023	88.17204	0.0596	7.62552	3.64455	4.59774	19.34415	40.81896	0.01580526
59.32	3.5962	0.0003	0.0044	15.33101	1.1816	1.07526882	12.90323	1.7981	87.09677	0.0631	8.06752	3.8558	4.86424	20.4654	43.18496	0.01629744
65.42	3.2606	0.0004	0.0048	16.72474	1.28902	1.43369176	14.33692	1.6303	85.66308	0.0696	8.89712	4.2523	5.36444	22.5699	47.62576	0.01641979
72.43	2.9451	0.0004	0.0052	18.11847	1.39644	1.43369176	15.77061	1.47255	84.22939	0.077	9.85048	4.70795	5.93926	24.98835	52.72904	0.01631369
76.68	2.7819	0.0004	0.0056	19.5122	1.50386	1.43369176	17.2043	1.39095	82.7957	0.0815	10.42848	4.9842	6.28776	26.4546	55.82304	0.01681037
83.37	2.5588	0.0004	0.006	20.90592	1.61127	1.43369176	18.63799	1.2794	81.36201	0.0887	11.33832	5.41905	6.83634	28.76265	60.69336	0.01674988
91.9	2.3213	0.0007	0.0067	23.34495	1.79926	2.50896057	21.14695	1.16065	78.85305	0.0977	12.4984	5.9735	7.5358	31.7055	66.9032	0.01724069
98.19	2.1725	0.0004	0.0071	24.73868	1.90667	1.43369176	22.58065	1.08625	77.41935	0.1044	13.35384	6.38235	8.05158	33.87555	71.48232	0.01723024
105.55	2.0211	0.0004	0.0075	26.1324	2.01409	1.43369176	24.01434	1.01055	75.98566	0.1122	14.3548	6.86075	8.6551	36.41475	76.8404	0.01704648
114.92	1.8563	0.0004	0.0079	27.52613	2.12151	1.43369176	25.44803	0.92815	74.55197	0.1222	15.62912	7.4698	9.42344	39.6474	83.66176	0.01659132
125.48	1.7	0.0005	0.0084	29.26829	2.25578	1.7921147	27.24014	0.85	72.75986	0.1334	17.06528	8.1562	10.28936	43.2906	91.34944	0.01626512
136.47	1.5632	0.0006	0.009	31.35889	2.41691	2.15053763	29.39068	0.7816	70.60932	0.1451	18.55992	8.87055	11.19054	47.08215	99.35016	0.01613596
146.92	1.4519	0.0006	0.0096	33.44948	2.57804	2.15053763	31.54122	0.72595	68.45878	0.1562	19.98112	9.5498	12.04744	50.6874	106.9578	0.01608496
158.96	1.342	0.0007	0.0103	35.8885	2.76602	2.50896057	34.05018	0.671	65.94982	0.169	21.61856	10.3324	13.03472	54.8412	115.7229	0.01604922
173.43	1.23	0.0007	0.011	38.32753	2.954	2.50896057	36.55914	0.615	63.44086	0.1844	23.58648	11.27295	14.22126	59.83335	126.257	0.01579407
186.2	1.1456	0.0006	0.0116	40.41812	3.11513	2.15053763	38.70968	0.5728	61.29032	0.198	25.3232	12.103	15.2684	64.239	135.5536	0.01557622
203.5	1.0483	0.0006	0.0122	42.50871	3.27626	2.15053763	40.86022	0.52415	59.13978	0.2164	27.676	13.2275	16.687	70.2075	148.148	0.01504384
219.06	0.9738	0.0005	0.0127	44.25087	3.41053	1.7921147	42.65233	0.4869	57.34767	0.233	29.79216	14.2389	17.96292	75.5757	159.4757	0.01458821
238.21	0.8955	0.0005	0.0132	45.99303	3.5448	1.7921147	44.44444	0.44775	55.55556	0.2533	32.39656	15.48365	19.53322	82.18245	173.4169	0.01397912
256.97	0.8302	0.0004	0.0136	47.38676	3.65222	1.43369176	45.87814	0.4151	54.12186	0.2733	34.94792	16.70305	21.07154	88.65465	187.0742	0.0133766
279.2	0.7641	0.0004	0.014	48.78049	3.75964	1.43369176	47.31183	0.38205	52.68817	0.2969	37.9712	18.148	22.8944	96.324	203.2576	0.01269628
302.41	0.7054	0.0004	0.0144	50.17422	3.86706	1.43369176	48.74552	0.3527	51.25448	0.3216	41.12776	19.65665	24.79762	104.3315	220.1545	0.01207705
326.01	0.6543	0.0004	0.0148	51.56794	3.97448	1.43369176	50.17921	0.32715	49.82079	0.3467	44.33736	21.19065	26.73282	112.4735	237.3353	0.01153228
353.95	0.6027	0.0004	0.0152	52.96167	4.08189	1.43369176	51.6129	0.30135	48.3871	0.3764	48.1372	23.00675	29.0239	122.1128	257.6756	0.01092543
384.59	0.5547	0.0004	0.0156	54.3554	4.18931	1.43369176	53.04659	0.27735	46.95341	0.409	52.30424	24.99835	31.53638	132.6836	279.9815	0.01033432
416.1	0.5127	0.0004	0.016	55.74913	4.29673	1.43369176	54.48029	0.25635	45.51971	0.4425	56.5896	27.0465	34.1202	143.5545	302.9208	0.00980989
451.11	0.4729	0.0004	0.0164	57.14286	4.40415	1.43369176	55.91398	0.23645	44.08602	0.4797	61.35096	29.32215	36.99102	155.633	328.4081	0.00928668
487.02	0.438	0.0004	0.0168	58.53659	4.51157	1.43369176	57.34767	0.219	42.65233	0.5179	66.23472	31.6563	39.93564	168.0219	354.5506	0.00882249
525.78	0.4057	0.0003	0.0171	59.58188	4.59213	1.07526882	58.42294	0.20285	41.57706	0.5591	71.50608	34.1757	43.11396	181.3941	382.7678	0.00832533
571.23	0.3734	0.0003	0.0174	60.62718	4.67269	1.07526882	59.49821	0.1867	40.50179	0.6075	77.68728	37.12995	46.84086	197.0744	415.8554	0.00780396
617.46	0.3455	0.0004	0.0178	62.02091	4.78011	1.43369176	60.9319	0.17275	39.0681	0.6566	83.97456	40.1349	50.63172	213.0237	449.5109	0.00739364
668.61	0.3191	0.0003	0.0181	63.0662	4.86068	1.07526882	62.00717	0.15955	37.99283	0.711	90.93096	43.45965	54.82602	230.6705	486.7481	0.0069485
724.94	0.2943	0.0003	0.0184	64.1115	4.94124	1.07526882	63.08244	0.14715	36.91756	0.7709	98.59184	47.1211	59.44508	250.1043	527.7563	0.00651972
784.3	0.272	0.0003	0.0187	65.15679	5.0218	1.07526882	64.15771	0.136	35.84229	0.8341	106.6648	50.9795	64.3126	270.5835	570.9704	0.00612899
847.85	0.2516	0.0003	0.019	66.20209	5.10237	1.07526882	65.23297	0.1258	34.76703	0.9017	115.3076	55.11025	69.5237	292.5083	617.2348	0.00576462
917.71	0.2325	0.0003	0.0193	67.24739	5.18293	1.07526882	66.30824	0.11625	33.69176	0.976	124.8086	59.65115	75.25222	316.61	668.0929	0.00541358
994.42	0.2145	0.0003	0.0196	68.29268	5.26349	1.07526882	67.38351	0.10725	32.61649	1.0575	135.2411	64.6373	81.54244	343.0749	723.9378	0.00507699
1074.77	0.1985	0.0003	0.0199	69.33798	5.34406	1.07526882	68.45878	0.09925	31.54122	1.143	146.1687	69.86005	88.13114	370.7957	782.4326	0.00477239
1163.02	0.1834	0.0003	0.0202	70.38328	5.42462	1.07526882	69.53405	0.0917	30.46595	1.2368	158.1707	75.5963	95.36764	401.2419	846.6786	0.00447953
1258.96	0.1694	0.0003	0.0205	71.42857	5.50519	1.07526882	70.60932	0.0847	29.39068	1.3389	171.2186	81.8324	103.2347	434.3412	916.5229	0.00420216
1362.65	0.1565	0.0003	0.0208	72.47387	5.58575	1.07526882	71.68459	0.07825	28.31541	1.4491	185.3204	88.57225	111.7373	470.1143	992.0092	0.00394152
1473.75	0.1447	0.0003	0.0211	73.51916	5.66631	1.07526882	72.75986	0.07235	27.24014	1.5673	200.43	95.79375	120.8475	508.4438	1072.89	0.00369905
1596.09	0.1337	0.0003	0.0214	74.56446	5.74688	1.07526882	73.83513	0.06685	26.16487	1.6974	217.0682	103.7459	130.8794	550.6511	1161.954	0.003466
1723.67	0.1238	0.0003	0.0217	75.60976	5.82744	1.07526882	74.91039	0.0619	25.08961	1.8331	234.4191	112.0386	141.3409	594.6662	1254.832	0.00325619
1866.47	0.1143	0.0002	0.0219	76.30662	5.88115	0.71684588	75.62724	0.05715	24.37276	1.9849	253.8399	121.3206	153.0505	643.9322	1358.79	0.00303584
2020.22	0.1056	0.0002	0.0221	77.00348	5.93486	0.71684588	76.34409	0.0528	23.65591	2.1484	274.7499	131.3143	165.658	696.9759	1470.72	0.00283139
2187.58	0.0975	0.0002	0.0223	77.70035	5.98857	0.71684588	77.06093	0.04875	22.93907	2.3264	297.5109	142.1927	179.3816	754.7151	1592.558	0.00263932
2365.75	0.0902	0.0002	0.0225	78.39721	6.04228	0.71684588	77.77778	0.0451	22.22222	2.5159	321.742	153.7738	193.9915	816.1838	1722.266	0.00246325
2560.79	0.0833	0.0002	0.0227	79.09408	6.09599	0.71684588	78.49462	0.04165	21.50538	2.7233	348.2674	166.4514	209.9848	883.4726	1864.255	0.00229662
2771.2	0.077	0.0002	0.0229	79.79094	6.1497	0.71684588	79.21147	0.0385	20.78853	2.9471	376.8832	180.128	227.2384	956.064	2017.434	0.00214162
2997.59	0.0712	0.0002	0.0231	80.4878	6.2034	0.71684588	79.92832	0.0356	20.07168	3.1878	407.6722	194.8434	245.8024	1034.169	2182.246	0.00199779
3242.71	0.0658	0.0002	0.0233	81.18467	6.25711	0.71684588	80.64516	0.0329	19.35484	3.4485	441.0086	210.7762	265.9022	1118.735	2360.693	0.00186334
3507.89	0.0608	0.0002	0.0235	81.88153	6.31082	0.71684588	81.36201	0.0304	18.63799	3.7305	477.073	228.0129	287.647	1210.222	2553.744	0.00173779
3798.18	0.0562	0.0002	0.0237	82.5784	6.36453	0.71684588	82.07885	0.0281	17.92115	4.0392	516.5525	246.8817	311.4508	1310.372	2765.075	0.00161912
4110.77	0.0519	0.0002	0.0239	83.27526	6.41824	0.71684588	82.7957	0.02595	17.2043	4.3717	559.0647	267.2001	337.0831	1418.216	2992.641	0.00150906
4444.46	0.048	0.0002	0.0241	83.97213	6.47195	0.71684588	83.51254	0.024	16.48746	4.7265	604.4466	288.8899	364.4457	1533.339	3235.567	0.00140785
4806	0.0444	0.0002	0.0243	84.66899	6.52566	0.71684588	84.22939	0.0222	15.77061	5.111	653.616	312.39	394.092	1658.07	3498.768	0.00131311
5198.27	0.041	0.0001	0.0244	85.01742	6.55251	0.35842294	84.58781	0.0205	15.41219	5.5282	706.9647	337.8876	426.2581	1793.403	3784.341	0.00121919
5628.51	0.0379	0.0002	0.0246	85.71429	6.60622	0.71684588	85.30466	0.01895	14.69534	5.9857	765.4774	365.8532	461.5378	1941.836	4097.555	0.00113554
6089.74	0.035	0.0001	0.0247	86.06272	6.63308	0.35842294	85.66308	0.0175	14.33692	6.4762	828.2046	395.8331	499.3587	2100.96	4433.331	0.00105394
6587.38	0.0324	0.0001	0.0248	86.41115	6.65993	0.35842294	86.02151	0.0162	13.97849	7.0054	895.8837	428.1797	540.1652	2272.646	4795.613	0.0009784

Table E4. IW8911-3-Pe-Ho-4 MICP data continued…

Int Pres psia	Pore Dia microns	Inc Int mL/gm	Cum Int mL/gm	Cum Int %PV(bc)	Cum Int %BV	Inc Int %PV(ac)	Cum Int %PV(ac)	Pore Rad microns	W.P. Sat %PV(ac)	Lev "J" Funct.	G/B Pc psia	G/O Pc psia	O/B Pc psia	Ht FWL,ft G/B	Ht FWL,ft O/B	Swanson's Sb/Pc(ac)
7125.18	0.0299	0.0001	0.0249	86.75958	6.68679	0.35842294	86.37993	0.01495	13.62007	7.5774	969.0245	463.1367	584.2648	2458.187	5187.131	0.00090832
7711.86	0.0277	0.0001	0.025	87.10801	6.71364	0.35842294	86.73835	0.01385	13.26165	8.2013	1048.813	501.2709	632.3725	2660.592	5614.234	0.0008427
8344.56	0.0256	0.0001	0.0251	87.45645	6.7405	0.35842294	87.09677	0.0128	12.90323	8.8741	1134.86	542.3964	684.2539	2878.873	6074.84	0.00078203
9030.83	0.0236	0.0002	0.0253	88.15331	6.79421	0.71684588	87.81362	0.0118	12.18638	9.604	1228.193	587.004	740.5281	3115.636	6574.444	0.00072855
9771.24	0.0218	0.0001	0.0254	88.50174	6.82106	0.35842294	88.17204	0.0109	11.82796	10.391	1328.889	635.1306	801.2417	3371.078	7113.463	0.00067609
10576.5	0.0202	0.0002	0.0256	89.19861	6.87477	0.71684588	88.88889	0.0101	11.11111	11.248	1438.407	687.4738	867.2746	3648.899	7699.707	0.00062969
11448.2	0.0186	0.0002	0.0258	89.89547	6.92848	0.71684588	89.60573	0.0093	10.39427	12.175	1556.952	744.1317	938.7508	3949.622	8334.275	0.00058644
12383.7	0.0172	0.0001	0.0259	90.2439	6.95533	0.35842294	89.96416	0.0086	10.03584	13.17	1684.179	804.9386	1015.461	4272.366	9015.312	0.00054431
13397.9	0.0159	0.0001	0.026	90.59233	6.98219	0.35842294	90.32258	0.00795	9.677419	14.248	1822.109	870.8609	1098.625	4622.262	9753.642	0.00050511
14498	0.0147	0.0001	0.0261	90.94077	7.00904	0.35842294	90.681	0.00735	9.318996	15.418	1971.723	942.3674	1188.833	5001.796	10554.51	0.00046863
15691.9	0.0136	0.0001	0.0262	91.2892	7.0359	0.35842294	91.03943	0.0068	8.960573	16.688	2134.104	1019.976	1286.739	5413.719	11423.73	0.00043469
16976.2	0.0126	0.0001	0.0263	91.63763	7.06275	0.35842294	91.39785	0.0063	8.602151	18.054	2308.763	1103.453	1392.048	5856.789	12358.67	0.00040338
18371.9	0.0116	0.0001	0.0264	91.98606	7.08961	0.35842294	91.75627	0.0058	8.243728	19.538	2498.58	1194.174	1506.497	6338.309	13374.75	0.0003742
19880.7	0.0107	0.0001	0.0265	92.33449	7.11646	0.35842294	92.1147	0.00535	7.885305	21.142	2703.775	1292.246	1630.217	6858.842	14473.15	0.00034715
21518.8	0.0099	0.0001	0.0266	92.68293	7.14331	0.35842294	92.47312	0.00495	7.526882	22.885	2926.561	1398.724	1764.544	7423.996	15665.71	0.00032197
23290.8	0.0092	0.0002	0.0268	93.37979	7.19702	0.71684588	93.18996	0.0046	6.810036	24.769	3167.542	1513.899	1909.842	8035.309	16955.67	0.00029978
25204.2	0.0085	0.0001	0.0269	93.72822	7.22388	0.35842294	93.54839	0.00425	6.451613	26.804	3427.777	1638.276	2066.748	8695.463	18348.69	0.00027809
27271.5	0.0078	0.0001	0.027	94.07666	7.25073	0.35842294	93.90681	0.0039	6.09319	29.002	3708.919	1772.645	2236.26	9408.654	19853.62	0.00025799
29501.3	0.0072	0.0002	0.0272	94.77352	7.30444	0.71684588	94.62366	0.0036	5.376344	31.374	4012.174	1917.583	2419.105	10177.94	21476.93	0.00024032
31918	0.0067	0.0001	0.0273	95.12195	7.3313	0.35842294	94.98208	0.00335	5.017921	33.944	4340.845	2074.669	2617.274	11011.7	23236.29	0.00022296
34532.4	0.0062	0.0001	0.0274	95.47038	7.35815	0.35842294	95.3405	0.0031	4.659498	36.724	4696.405	2244.605	2831.656	11913.67	25139.58	0.00020686
37345.5	0.0057	0.0001	0.0275	95.81882	7.38501	0.35842294	95.69892	0.00285	4.301075	39.716	5078.989	2427.458	3062.332	12884.2	27187.53	0.000192
40408.5	0.0053	0.0002	0.0277	96.51568	7.43871	0.71684588	96.41577	0.00265	3.584229	42.973	5495.551	2626.55	3313.494	13940.92	29417.36	0.00017877
43734.9	0.0049	0.0002	0.0279	97.21254	7.49242	0.71684588	97.13262	0.00245	2.867384	46.51	5947.944	2842.767	3586.26	15088.53	31838.99	0.0001664
47332.1	0.0045	0.0002	0.0281	97.90941	7.54613	0.71684588	97.84946	0.00225	2.150538	50.336	6437.171	3076.589	3881.235	16329.59	34457.8	0.00015489
51194.9	0.0042	0.0002	0.0283	98.60627	7.59984	0.71684588	98.56631	0.0021	1.433692	54.444	6962.505	3327.668	4197.981	17662.24	37269.88	0.00014425
55434.3	0.0038	0.0002	0.0285	99.30314	7.65355	0.71684588	99.28315	0.0019	0.716846	58.952	7539.07	3603.232	4545.616	19124.85	40356.2	0.00013419
59942.7	0.0036	0.0002	0.0287	100	7.70726	0.71684588	100	0.0018	0	63.747	8152.209	3896.276	4915.302	20680.23	43638.29	0.00012499

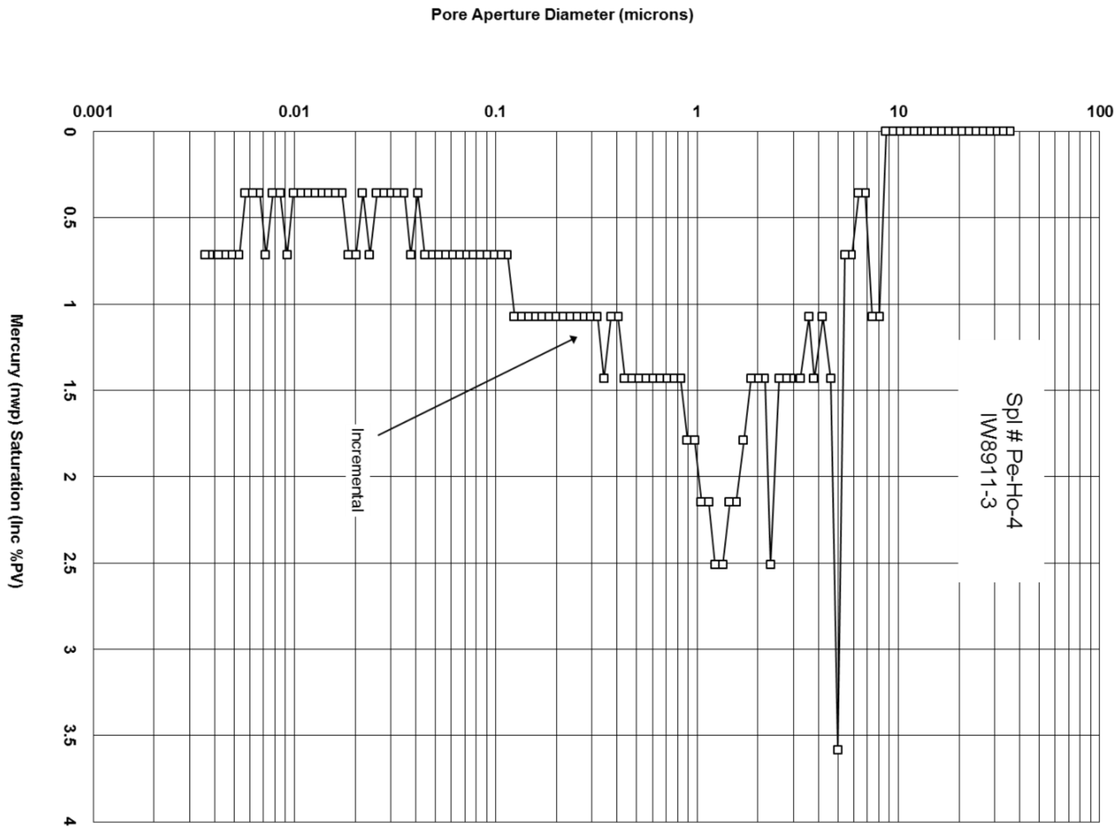

Figure E7. IW8911-3-Pe-Ho-4 pore aperture vs. mercury saturation.

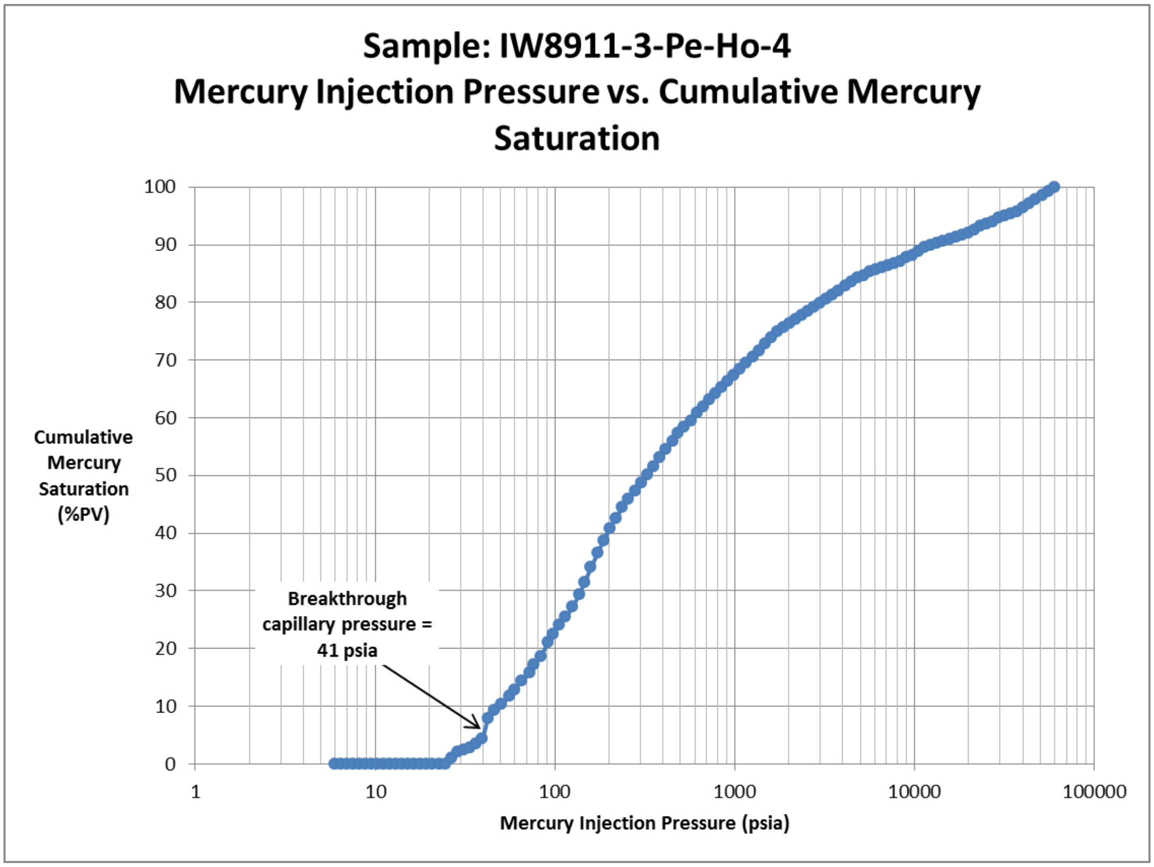

Figure E8. IW8911-3-Pe-Ho-4 mercury injection pressure vs. cumulative mercury saturation.

New Mexico Institute of Mining and Technology
Center For Graduate Studies

Student's Full Name: Stefan P. Raduha
Title: Influence of Mesoscale features of the Reservoir – caprock interface on fluid transmission into and through caprock
Degree: ☒MS ☐PhD Department: Earth & Environmental Science Graduation Date May 2013

NMT Copyright Agreement

I hereby certify that this is my original work and I have the authority to grant the non-exclusive right and license specified herein. I further certify that, if appropriate, I have obtained and attached hereto a written permission statement from the owner(s) of each third party copyrighted matter to be included in my thesis, dissertation, or record of study, allowing distribution as specified below.

I certify that the version I submitted is the same as the approved by my advisory committee.

I hereby grant in perpetuity, without restriction, royalty free to New Mexico Tech or its agents the non-exclusive right and license to archive and make accessible, under the conditions specified below, my thesis, dissertation, or record of study in while or in part in all forms of media, now or hereafter known. This agreement shall survive assignment of any and all exclusive rights provided to copyright holders in Section 106 or the United States copyright law.

FERPA. To the extent this thesis, dissertation, or record of study is an educational record as defined in the Family Educational Rights and Privacy Act (FERPA) (20 USC 1232g), I consent to disclosure of it to anyone who requests a copy.

I retain all other ownership rights to the copyright of the thesis, dissertation, or record of study. I also retain the right to use in future works (such as articles or books) all or part of this thesis, dissertation, or record of study.

Availability Option (check one)

☒ Release the work immediately for **worldwide access on the Internet.**
☐ (*Patent Hold*) Secure the work temporarily for patent and/or proprietary purposes, then release the work for **worldwide access on the Internet.**
☐ (*Journal Hold*) Hold the work for one year, then release the work for **worldwide access on the Internet.** (*One-year extension on request, if needed*)

Chair/Co-Chair Certification

I have discussed the availability choices with my student and I am aware of the choice my student has made.

Chair/Co-Chair's Signature: Gary J Axen
(*Only one Chair or Co-Chair signature is required*).

Student Copyright Agreement

I have read and fully agree to the NMT copyright agreement regarding my thesis/dissertation. I agree to the thesis/dissertation availability option I selected above. I understand that the availability option is my choice and that there may be publishing consequences to my selection.

Student's Signature: Stefan P. Raduha

Approval ____________ Effective Date ________